Photophysics of Quantum Confinement in Novel Semiconductors



Karim Amr Elmestekawy

St Cross College

University of Oxford

A thesis submitted for the degree of

Doctor of Philosophy

Trinity 2024

الي **أمي** ،

لعلها تكون شيئاً يستدعي فخرك لي.

Acknowledgements

This thesis and all the projects within it, any accomplishment I have achieved, any successes I have reached, or any personal development or growth in the past 4 years would have never been possible without the support, encouragement, and the company of the many amazing people I have met in my PhD. I hold all these friendships so close to my heart and I hope they will last a lifetime.

Before I can get to thanking the people I have met during my PhD, I want to acknowledge all the people who have helped me reach that point in the first place. I would not have been able to even dream of applying for my PhD without the foundation I had established in my undergraduate degree, and so I would like to thank: **Professor Alfons Weber**, and **Professor Tim Woollings** for asking easy questions in my interview :), and for being my undergraduate physics tutors, and **Mr. Simon Li** and **Mrs. June Li** for setting up an Oxford scholarship for international undergraduates. I still vividly remember meeting both Simon and June Li and feeling amazed at their willingness to set up these scholarships. It was the main reason I applied to Oxford in the first place, and it has had a huge impact on my life, and facilitated my entire adult experience - I will forever be grateful for this scholarship and will always strive to be worthy of it.

For my time during my PhD, I would first like to deeply thank the University of Oxford and the Mohammed bin Rashid Al Maktoum Knowledge Foundation (MBRF) for financially supporting my PhD degree through an **Oxford Graduate Scholarship**. Beyond funding, I would like to sincerely thank my supervisor: **Professor Laura Herz** for her guidance throughout my PhD, support from before I even started this degree by applying for an Oxford graduate scholarship on my behalf, and for her great life and work advice. I would also like to thank all my colleagues in the 'Semiconductors' and 'Terahertz Photonics' groups for their advice, and constant willingness to help throughout my PhD. I want to especially thank Dr. Aleksander Ulatowski, Dr. Marcello Righetto, Dr. Silvia Motti, and Dr. Adam Wright for all their invaluable mentorship, guidance in the lab, and help with writing papers and discussions.

More importantly, I would like to thank all my friends in the Herz and Johnston groups for making spending time in the lab a more enjoyable activity. In particular, I want to give a special thanks to: Dr. **Marcello Righetto** for your companionship in runs, your kind words in moments of grief, your willingness to always listen, and your caring and friendly personality, Dr. **Aleksander Ulatowski** for your life advice, jokes, perfect sentence structure and making the office a better place to be in, **Vincent Lim** for our partnership in starting and ending this journey together and for your codependent tendencies when going to the post office and refilling your water bottle, **Jae Eun Lee** for being incredibly kind, always putting a smile on my face, and of course the gym sessions, **Siyu Yan** for being the best desk neighbour I could ask for, **Snigdha Lal** for always making me laugh, for our interesting conversations, and for being the best Snogdha that I know, **Ford Wagner** for the squash sessions, and for allowing your home to be the first of many homes I stalk, and Dr. **Jay Patel** for unintentionally being one of the funniest and most unpredictable people that I know.

I would like to thank my close friends from the departments and degrees more interesting

than mine. In particular, I would like to thank: **Emma Tobin** for being a great and an incredibly reliable friend, for allowing me to get to know you and your family better, and for our deep and interesting conversations, Dr. **Julia-Sophia Bellingrath** for being an incredibly caring friend, and for your comforting words and listening ear throughout my degree and throughout my mother's cancer treatment. I am truly grateful for being able to call you close friends! I would also like to thank **Sharvi Maheshwari**, **Anna Geatrell**, for being great house mates, and Dr. **Teoman Taskesen**, and **Guopeng Chen** for being my tennis and squash partners throughout my degree.

Importantly, I would like to thank all the friends I have made from rowing at the Wolfson College Boat Club, especially Coach **Rory Copus** for making me find my "swag". I can confidently say that it is the single thing I am most grateful for during my PhD and what has caused the most change in my confidence levels, physical and mental health and overall personality - it has truly been the highlight of my degree.

I hold all these friendship close to my heart and they are what made this PhD worth it. I love all of you and thank you from the bottom of my heart!

Finally and most importantly: Thank you to everyone in my immediate and extended family. Everything pales in comparison to the gratitude, appreciation and love I have for everyone in my family. **Asser**, Shokran for taking care of us and for standing next to mama when we were younger; without you none of us would have considered moving to the UK, so Shokran for everything. **Gedo Atef**, Shokran for how reliable and caring you were to all of us. I will always try to follow in your footsteps by copying how you treated everyone in your life and being a dahr for everyone to yestened 3aleh. **Anna Samia**, I am grateful to have had you as a loving and caring grandmother. Shokran for showing me how important it is to have close family members, and for your gebna be tamatam every night at 2am when I was studying, and for your class and manners that I will always to try to replicate. **Baba**, Shokran for giving me life. Atamana eny kont 2abeltak, all my life I have been trying to follow in your footsteps and I would be honoured to end up with the same som3a and 7osn el zekra that you left us. **Rana**, Shokran ya Rana for everything. You are one of the closest people to my heart, w mn aktar el nas el shabahee. Shokran for always looking out for me and for paving the way for me and Shady. I have always been inadvertently taking the same path in life as you, and it would be my honour to keep following you in the path you forge in life. W Shokran for saving my life in el ma3moora. **Shady**, Shokran ya Makka for being my twin. We have always been together and shared everything starting from el ra7em and isA until the end of our lives. We have always been responsible for each other so Shokran for wo2ofak ma3aya in everything and for being a sanad to the entire family.

Mama, *La3alaha!* Shokran will never be enough to repay the debt I owe you and all the sacrifices you made for me. Everything I have ever achieved in my life and any good qualities and attributes I have are all because of your sacrifices, influence, and love. I never fully understood or appreciated how you could have so much unconditional love to me until you were gone and I will forever strive to make sure all that love was not misplaced and that you will continue live on with me as promised! Asef eny ma7adantekeesh aktar w eny ma2oltelkeesh ad eh ana ba7ebak. Atamana en I could have spent more time with you and I will try to live up to your expectations and forever hold up your memory. Ba7ebak ad el donya w bab3atlak 3asafeer kol youm 3ashan netkalem. Atmana enek tekony mabsoota w fakhora bya w dayman has3ah eny a3eesh 7ayaty be qodowaky.

Abstract

The intersection between quantum confinement and metal halide perovskites is a new and exciting avenue for breakthrough research. Metal halide perovskite already hold tremendous potential for numerous optoelectronic applications, which can be enhanced if the effects of quantum confinement and precise control over its presence can be achieved. This thesis explores and discusses this tantalising possibility.

The tendency of one of the most well-known and promising metal halide perovskite compositions ($FAPbI_3$) to self assemble into confined nanodomains is investigated. Successful control over the peculiar features associated with this intrinsic quantum confinement phenomenon is demonstrated through stoichiometric engineering. This demonstrated that precise control and eventual suppression of quantum confinement is possible, shed light on some key fundamental physics governing this quantum confinement, and cemented the link between the observable peculiar absorption features and the presence of quantum confinement. This corroboration was further supported by the observation of photon emission from the confined nanodomains when a $FAPbI_3$ film is lowered to cryogenic temperatures.

The possibility of controlling the intrinsic quantum confinement while still retaining the $FAPbI_3$ composition is explored by studying films made using different fabrication methods. The successful control over the quantum confinement therefore shows the importance of the crystallization dynamics in influencing the quantum confinement behaviour manifesting in the final film. Subsequently, the relationship between the presence of quantum confinement and charge-carrier extraction and photovoltaic (PV) performance is explored. Experimental evidence demonstrated a good correlation between both reduced PV performance and extractable charge carriers in the presence of quantum confinement - a correlation that was corroborated by a meta-study of the field and further extended by observing that a power conversion efficiency ceiling of 20% exists for such films.

Finally, quantum confinement in its different forms and its effects on charge-carrier transport properties is investigated. The compositional similarity between $FAPbI_3$ films ensured that the local intrinsic optoelectronic properties stayed the same, while the huge difference in quantum confinement behaviour and other extrinsic differences ensured that the charge-carrier lifetimes and transport properties were poorer for the fabrication method that supported quantum confinement. A similar analysis on 2-dimensional perovskite semiconductors of orthogonal preferential growth orientations demonstrated that charge-carrier transport properties agree with predictions based on the geometry of the confined structures. This therefore confirms that the 2-dimensional semiconductor was grown in orthogonal directions, confirms that charge-carrier transport in these confined semiconductors is within the conductive regions instead of across the insulating layers, and demonstrates the huge potential of oriented 2-dimensional semiconductors in PV devices.

Contents

List of Publications ix

List of Abbreviations x

1 Introduction 1

2 Background 5

2.1 Fundamentals: Semiconductor theory . . . 7

2.1.1 Band theory and energy levels . . . 7

2.1.2 Semiconductors . . . 12

2.1.3 Hybrid metal halide perovskites . . . 16

2.1.4 Charge-carrier dynamics . . . 19

2.1.5 Photovoltaic devices . . . 22

2.2 Focus: Lower dimensional metal halide perovskites . . . 24

2.2.1 Density of states . . . 24

2.2.2 Quantum confinement . . . 28

2.2.3 Nano structuring . . . 33

3 Experimental Methods 39

3.1 Low temperature measurements . . . 40

3.2 Absorption spectroscopy . . . 41

3.2.1 Experimental setup . . . 41

3.2.2 Data analysis . . . 43

3.2.3 Elliott fitting . . . 44

3.2.4 Extraction of the above-bandgap peaks . . . 45

3.3 Photoluminescence spectroscopy . . . 48

3.3.1 Time-integrated experimental setup . . . 48

3.3.2 Time-resolved (TR) experimental setup . . . 50

3.4 Terahertz (THz) spectroscopy . . . 54

3.4.1 Optical-pump terahertz-probe (OPTP) . . . 54

3.5 X-ray diffraction . . . 59

3.5.1 Theory . . . 59

3.5.2 Experimental setup . . . 61

4 Control of intrinsic quantum confinement in formamidinium lead triiodide 63
4.1 Motivation . . . 65
4.2 Results and discussion . . . 68
4.2.1 Cesium incorporation into the crystal structure . . . 68
4.2.2 Effect of cesium incorporation on quantum confinement . . . 76
4.2.3 Photoluminescence spectrum . . . 87
4.3 Conclusion . . . 100

5 Photovoltaic Performance of $FAPbI_3$ Perovskite is Hampered by Intrinsic Quantum Confinement 102
5.1 Motivation . . . 104
5.2 Results and discussion . . . 108
5.2.1 Effect of fabrication method on thin film quality, crystallinity and quantum confinement . . . 108
5.2.2 Effect of quantum confinement on photovoltaic performance . . . 120
5.3 Conclusion . . . 132

6 Charge-carrier dynamics in quantum confined perovskites 134
6.1 Motivation . . . 136
6.2 Results and discussion . . . 138
6.2.1 3-dimensional $FAPbI_3$ . . . 138
6.2.2 2-dimensional perovskites . . . 147
6.3 Conclusion . . . 158

7 Conclusion and Outlook 159

Appendices

A Supplementary Analysis of Control of intrinsic quantum confinement in formamidinium lead triiodide 4 165
A.1 Sample fabrication . . . 166
A.2 X-ray diffraction . . . 167
A.2.1 XRD spectra . . . 167
A.3 Steady-state photoluminescence . . . 169
A.4 Absorption measurements . . . 171
A.4.1 Elliott fitting . . . 173
A.4.2 Tauc plots . . . 176
A.4.3 Baseline fitting and peak indexing . . . 178
A.4.4 Temperature-dependent study of the absorbance spectra . . . 179
A.5 Theoretical models . . . 182

A.5.1 Infinite quantum well . . . 182
A.5.2 Krönig-Penney potential . . . 183
A.6 Temperature-dependent study of steady-state PL . . . 184
A.6.1 $FA_{0.57}Cs_{0.43}PbI_3$ . . . 186
A.7 Time-resolved PL (TRPL) . . . 189

B Supplementary Analysis of Photovoltaic Performance of $FAPbI_3$ Perovskite is Hampered by Intrinsic Quantum Confinement 5 193
B.1 Materials . . . 195
B.2 Fabrication . . . 196
B.2.1 For material characterization: . . . 196
B.2.2 For perovskite solar cell fabrication: . . . 196
B.3 X-ray diffraction (XRD) . . . 200
B.3.1 Synchrotron X-ray data . . . 201
B.4 Scanning electron microscopy (SEM) . . . 203
B.5 Absorption measurements . . . 205
B.5.1 Elliott fitting . . . 207
B.5.2 Baseline fitting . . . 209
B.5.3 Temperature dependence of the absorbance spectra . . . 209
B.5.4 Definitions . . . 210
B.6 Photoluminescence . . . 211
B.7 Photovoltaic performance . . . 212
B.8 meta-analysis of literature reports . . . 217
B.8.1 Additional figures displaying results of meta-analysis: . . . 219

C Supplementary Analysis of charge-carrier dynamics in quantum confined perovskites 6 227
C.1 2-dimensional perovskites . . . 228
C.1.1 Fabrication . . . 228
C.1.2 Absorption measurements . . . 229
C.1.3 Grazing incidence wide-angle X-ray scattering (GIWAXS) . . . 231
C.1.4 Photoluminescence (PL) . . . 234

References 235

List of Publications

- **Elmestekawy, K.A.**, Wright, A.D., Lohmann, K.B., Borchert, J., Johnston, M.B. and Herz, L.M. 'Controlling Intrinsic Quantum Confinement in Formamidinium Lead Triiodide Perovskite through Cs Substitution'. *ACS Nano*, **2022** 16(6), 9640–9650.
- **Elmestekawy, K.A.**, Gallant, B.M., Wright, A.D., Holzhey, P., Noel, N.K., Johnston, M.B., Snaith, H.J. and Herz L.M. 'Photovoltaic Performance of $FAPbI_3$ Perovskite Is Hampered by Intrinsic Quantum Confinement'. *ACS Energy Letters*, **2023** 8(6), 2543–2551.
- Lohmann, K.B., Motti, S.G., Oliver, R.D.J., Ramadan, A.J., Sansom, H.C., Yuan, Q., **Elmestekawy, K.A.**, Patel, J.B., Ball, J.M., Herz, L.M., Snaith, H.J. and Johnston, M.B. 'Solvent-Free Method for Defect Reduction and Improved Performance of p-i-n Vapor-Deposited Perovskite Solar Cells'. *ACS Energy Letters*, **2022** 7(6), 1903–1911.
- Shen, X., Gallant, B.M., Holzhey, P., Smith, J.A., **Elmestekawy, K.A.**, Yuan, Z., Rathnayake, P.V.G.M., Bernardi, S., Dasgupta, A., Kasparavicius, E., Malinauskas, T., Caprioglio, P., Shargaieva, O., Lin, Y-H., McCarthy, M.M., Unger, E., Getautis, V., Widmer-Cooper, A., Herz, L.M. and Snaith, H.J. 'Chloride-Based Additive Engineering For Efficient and Stable Wide-Bandgap Perovskite Solar Cells'. *Advanced Materials*, **2023** 35(30), 2211742.
- Yan, S., Patel, J.B., Lee, J.E., **Elmestekawy, K.A.**, Ratnasingham, S.R., Yuan, Q., Herz, L.M., Noel, N.K. and Johnston, M.B. 'A Templating Approach to Controlling the Growth of Coevaporated Halide Perovskites'. *ACS Energy Letters*, **2023** 8(10), 4008–4015
- Righetto, M., Wang, Y., **Elmestekawy, K.A.**, Xia, C.Q., Johnston, M.B., Konstantatos, G. and Herz, L.M. 'Cation-Disorder Engineering Promotes Efficient Charge-Carrier Transport in $AgBiS_2$'. *Advanced Materials*, **2023** 35(48), 2305009.
- Ulatowski, A.M., **Elmestekawy, K.A.**, Patel, J.B., Noel, N.K., Yan, S., Kraus, H., Huggard, P.G., Johnston, M.B., Herz, L.M. 'Contrasting Charge-Carrier Dynamics across Key Metal-Halide Perovskite Compositions through In Situ Simultaneous Probes'. *Advanced Functional Materials*, **2023** 33(51), 2305283.

List of Abbreviations

DFT	Density functional theory
FWHM	Full width at half maximum
STEM	Scanning transmission electron microscope
XRD	X-ray diffraction
GIWAXS	Grazing incidence wide-angle scattering
MHP	Metal halide perovskite
FA	Formamidinium $CH(NH_2)_2$
FACs	Formamidinium-cesium alloy
MA	Methylammonium CH_3NH_3
DoS	Density of states
QC	Quantum confinement
PCE	Power conversion efficiency
PV	Photovoltaic
J_{SC}	Short-circuit current density
V_{OC}	Open-circuit voltage
FTIR	Fourier-transform infrared
PL	Photoluminescence
TRPL	Time-resolved photoluminescence
TCSPC	Time-correlated single-photon counting
CCD	Charge-coupled device
MCP	Microchannel plate
PMT	Photomultiplier tube
SPAD	Single-photon avalanche diode
THz	Terahertz
OPTP	Optical-pump terahertz-probe

1

Introduction

As the global human population continues to grow to its projected peak of 10.4 billion people in the 2080s, and as communities continue to urbanise and populations are lifted from poverty, the world's energy demand will surely follow this unsustainable increase. [1, 2] In order to be able to address the scarcity, volatility and global inequality of energy, while still focusing on the climate crisis and limiting global warming to 1.5°C, clean and renewable energy sources such as photovoltaics needs to be further invested in and better incorporated into the energy landscape. [3] After all, the sun provides the Earth with an inexhaustible source of free energy that is solely capable of more than adequately fulfilling all the world's energy demands. [4]

In the photovoltaic industry, crystalline silicon has so far been the most dominant semiconductor used. The first silicon solar cell was reported in 1954 with a PCE of 6%, [5] and research into the further development of these cells has been ongoing ever since. The culmination of this 70-year long history is the champion silicon solar cell with a 26.8% PCE. [6, 7] However, progress on further improving the efficiency of silicon in photovoltaic devices have slowed down massively. [8] Instead, other novel semiconductors such as metal halide perovskites have emerged over the last decade as both potential

rivals [9] and complementary aides [10, 11] to the silicon solar cell. These semiconductors can be used to address all the main global problems humanity is facing in the form of the current climate crisis, energy scarcity, and globally equally-accessible energy sources. [12]

The versatile utility of these novel semiconductors in various optoelectronic applications can be further enhanced when the excellent optoelectronic properties of these semiconductors are precisely tuned and modified through the inclusion of quantum confinement behaviour in these semiconductors. Therefore, the work presented in this thesis addresses some of the key fundamental features related to quantum confinement in these novel semiconductors and how they can be modified and controlled depending on our need and the possible future applications for such novel semiconductors.

Thesis overview

Chapter 2 contextualises the work presented in this thesis and provides the foundational knowledge needed to understand the work presented later on in the experimental chapters. The chapter begins by introducing the basic theory behind the electronic wavefunction and its evolution from isolated atoms to periodic crystals, to eventually being able to fully describe band formation and semiconductor theory. The chapter then follows by introducing and focusing on the type of semiconductor being investigated in this thesis; namely metal halide perovskites, and continues to lay the foundation for the analysis of charge-carrier dynamics and photovoltaic performance within such semiconductors. Chapter 2 then transitions to explain the focus of this thesis by introducing the theory behind some different types of quantum confinement, the different forms they can take, and how they affect the optoelectronic properties of the emerging semiconductor.

Chapter 3 introduces the various experimental techniques used throughout this thesis, delving into the underlying theory behind each technique and providing details about the specific experimental setups used. This includes low-temperature cryogenics experiments,

absorption spectroscopy measurements and data analysis - which is used extensively throughout this thesis, both time-resolved and time-integrated photoluminescence (PL) spectroscopy, X-ray diffraction (XRD) measurements, and photo-induced conductivity measurements through optical-pump terahertz-probe (OPTP) spectroscopy.

Chapter 4 is the first experimental chapter in this thesis and it addresses the potential ability to control intrinsic quantum confinement within the formamidinium lead triiodide ($FAPbI_3$) perovskite composition. Successful control of the quantum confinement and suppression of the absorption features associated with this phenomenon is demonstrated through the partial substitution of FA with cesium (Cs). The gradual inclusion of Cs within the perovskite structure affects the bandstructure, the strain within the system, and the tendency for other crystallographic phases and $FAPbI_3$ polyomorphs to form, all of which might be partial reasons for the gradual elimination of quantum confinement effects with increasing Cs substitution. The chapter also examines the possibility of light emission from such confined nanodomains at cryogenic temperatures, which highlights the importance of further control over such features in order for its amplification or suppression depending on its need in future application either in light-emitting devices or photovoltaic devices respectively.

Chapter 5 shares the same theme as Chapter 4 in further investigating ways of controlling the intrinsic quantum confinement in $FAPbI_3$, and shows that compositionally-similar films experiencing different crystallization processes exhibit drastically different quantum confinement tendencies. This chapter then extends this investigation by examining the relationship between this intrinsic quantum confinement in $FAPbI_3$ films with their extractable charge-carrier current density (J_{SC}), power conversion efficiency (PCE) and general photovoltaic (PV) performance, through both experiments and a meta-study of the literature. This study finds that an inherent barrier of 20% PCE exists for $FAPbI_3$ and FA-rich perovskite films exhibiting quantum confinement behaviour,

which suggests that a first point of investigation for the validity of a fabrication method in making highly-efficient FA-rich PV devices should be an investigation into the presence or absence of any above-bandgap features in its absorption spectrum.

Chapter 6 investigates the effects of quantum confinement in its different forms on optoelectronic and charge-carrier transport properties of the semiconductor. In the first half of this chapter, the charge-carrier dynamics of the same $FAPbI_3$ sample set studied in Chapter 5 is investigated to explore the relationship between the intrinsic quantum confinement and charge-carrier transport properties in these films. While, in the second half of this chapter, the same experimental techniques and analyses are extended to 2-dimensional perovskite semiconductors with orthogonal preferential growth orientations. The comparison of the extracted effective sum mobilities between the orthogonal orientations and their agreement with what is expected based on geometry, proved the strong preferential orientation of the 2-dimensional conductive slabs, and strongly suggests that band-like intra-slab charge-carrier transport dominates over inter-slab charge-carrier transport across the insulating layers.

Finally, Chapter 7 presents the conclusion and overview of the entire thesis and provides an outlook for future research that can build on this work.

2

Background

Contents

2.1 Fundamentals: Semiconductor theory 7
2.1.1 Band theory and energy levels 7
Isolated wavefunctions 7
Bloch's theorem 8
Band theory and tight binding model 9
2.1.2 Semiconductors 12
2.1.3 Hybrid metal halide perovskites 16
Crystal lattice 16
2.1.4 Charge-carrier dynamics 19
2.1.5 Photovoltaic devices 22
2.2 Focus: Lower dimensional metal halide perovskites 24
2.2.1 Density of states 24
2.2.2 Quantum confinement 28
Quantum confinement models 28
Band-like vs hopping-like transport 30
2.2.3 Nano structuring 33
Intrinsic quantum confinement 33
Quasi 2-dimensional structures 37

This chapter outlines the important physical concepts behind the work presented in this thesis. First, I outline the fundamental concepts behind semiconductor theory, the evolution of metal halide perovskites as promising semiconducting material with great optoelectronic properties, and the necessary foundation for the understanding of

photovoltaic devices and the important parameters to gauge photovoltaic performance. Second, I delve deeper into the theory of quantum confinement by outlining the accompanying effects of an increase in confinement dimensionality on the density of states, bandstructure, and optoelectronic and charge-carrier transport properties of the confined semiconductor. Finally, I outline how certain semiconductors studied in this thesis can be structured in order to achieve quantum confinement.

2.1 Fundamentals: Semiconductor theory

2.1.1 Band theory and energy levels

Isolated wavefunctions

Before attempting to explain band theory and the theory behind semiconductors, I begin my explanation with a single isolated atom. An outer-shell electron can approximately be described as a Hydrogen atom due to it experiencing a net positive charge from the positively-charged nucleus and the totality of the inner-shell electrons. Therefore, its Hamiltonian can be described similarly to a Hydrogen atom as follows:

$$\hat{H}\left(r,\theta,\phi\right)\psi\left(r,\theta,\phi\right)=E\psi\left(r,\theta,\phi\right)=\left(-\frac{\hbar}{2\mu}\nabla^{2}-\frac{Ze^{2}}{4\pi\epsilon_{0}r}\right)\psi\left(r,\theta,\phi\right), \tag{2.1}$$

where $\hbar$ is the reduced plank's constant, μ is the reduced effective mass of the electron and isolated atom, Z is the net atomic charge on the nucleus and inner shell electrons, e is the electron charge, and ϵ_0 is the vacuum permittivity. The Hamiltonian has spherical symmetry around the center of mass, so the orbital wavefunction ψ can be written in terms of a product of a radial component and spherical harmonics as the angular component, and can be entirely described using three good quantum numbers. The single electron orbital wavefunction is therefore described as follows:

$$\psi_{n,l,m}\left(r,\theta,\phi\right)=R_{n,l}\left(r\right)\cdot Y_{l}^{m}\left(\theta,\phi\right), \tag{2.2}$$

where $R_{n,l}\left(r\right)$ is the radial component describing how far away the electron is from the nucleus and is described using the principal quantum number (n) and the azimuthal quantum number (l). While, $Y_{l}^{m}\left(\theta,\phi\right)$ is the spherical harmonic solution to the angular component of the Hamiltonian, and is described using the azimuthal quantum number (l), and the magnetic quantum number (m). The eigenvalues of the single-electron Hamiltonian are only described using the principal quantum number and represent

discrete energy levels that are quantized as follows:

$$E_n = -\frac{\mu e^4}{32\pi^2\epsilon_0^2\hbar^2 \cdot n^2} = -\frac{e^2}{8\pi\epsilon_0 a_0 \cdot n^2}, \tag{2.3}$$

where a_0 is the bohr radius. [13, 14]

Bloch's theorem

A crystal lattice can be defined in terms of its primitive unit cell, which forms the foundational configuration of atoms that needs to be infinitely repeated in 3-dimensions to form the overall crystal lattice. This repetition creates an intrinsic periodicity in the crystal lattice that can be utilised to simplify both the Hamiltonian and the description of the electronic eigen-wavefunctions. Therefore, the Hamiltonian of the orbital electrons in a periodic crystal will be invariant under a translation vector corresponding to a linear combination of primitive lattice vectors. Accordingly, Bloch's theorem states that the solutions to the Hamiltonian of a periodic crystal (described in Equation 2.8) are plane waves modified by functions with the same periodicity as that of the crystal, mathematically written as:

$$\psi(\boldsymbol{r}) = e^{i\boldsymbol{k}\cdot\boldsymbol{r}}u(\boldsymbol{r}); \qquad u(\boldsymbol{r}) = u(\boldsymbol{r} + \boldsymbol{R_n}), \tag{2.4}$$

where ψ is the wavefunction, $\boldsymbol{r}$ is the position, $\boldsymbol{k}$ is the crystal wave vector, $u(\boldsymbol{r})$ is the periodic function, and $\boldsymbol{R_n}$ is a linear combination of primitive lattice vectors.

The expected periodicity, based on the definition of a unit cell within a crystal lattice, can be applied to the Bloch wavefunction as follows:

$$\psi\left(\boldsymbol{r} + \boldsymbol{R_n}\right) = e^{i\boldsymbol{k}\cdot(\boldsymbol{R_n})}\psi\left(\boldsymbol{r}\right) = \psi\left(\boldsymbol{r}\right), \tag{2.5}$$

which yields the boundary conditions expressed as:

$$\boldsymbol{k} \cdot (n_i\boldsymbol{a_i}) = 2m_i\pi; \qquad m_i \in \mathbb{Z}, \tag{2.6}$$

where $\boldsymbol{a}$ are the primitive lattice vectors. This in turn allows for the expression of the permitted k-states mathematically described as:

$$\boldsymbol{k} = \sum_{i=1}^{\dim} \frac{m_i}{n_i} \boldsymbol{b_i}, \tag{2.7}$$

where dim is the dimensionality, and $\boldsymbol{b}$ are the reciprocal primitive lattice vectors. [13, 14]

Band theory and tight binding model

Now, to be able to figure out the bandstructure of electrons in a crystal lattice, the energy dispersion relationship in reciprocal space needs to be mapped, and the periodic crystal potential needs to be taken into consideration. There are many possible ways to calculate the bandstructure, such as using the tight-binding model, the nearly free electron model, or even density functional theorem (DFT). However, in this thesis, I utilise a simplified tight binding model as the explanatory model due to its relevance to the material used throughout this thesis, which are crystals with narrower bandgaps and where electrons experience strong localisation. This is ultimately to demonstrate the proof of principle and not to derive a wavefunction for an all encompassing Hamiltonian.

In the simplified tight binding model (assuming a one-atom basis in the unit cell with no hybridisation and minimal wavefunction overlap between nearest neighbouring sites), the electron experiences the Coulombic attractive potential from all lattice sites, therefore the Hamiltonian can be written as:

$$\hat{H} = \left(\frac{\hat{\boldsymbol{P}}^2}{2m} + V(\boldsymbol{r}) \right) + \sum_{\boldsymbol{R_n} \neq 0} V\left(\boldsymbol{r} - \boldsymbol{R_n}\right) = \hat{H}_{\text{atomic}} + \Delta\hat{H}, \tag{2.8}$$

where $\hat{H}_{\text{atomic}}$ represents the Hamiltonian of an isolated atom, while $\Delta\hat{H}$ represents all the extra Coulombic interactions between the electron and the nuclei at all other sites in the crystal structure.

In accordance with this Hamiltonian, the isolated atomic orbitals (which are the eigenfunctions for the isolated Hamiltonian, and are described in Equation 2.2) can

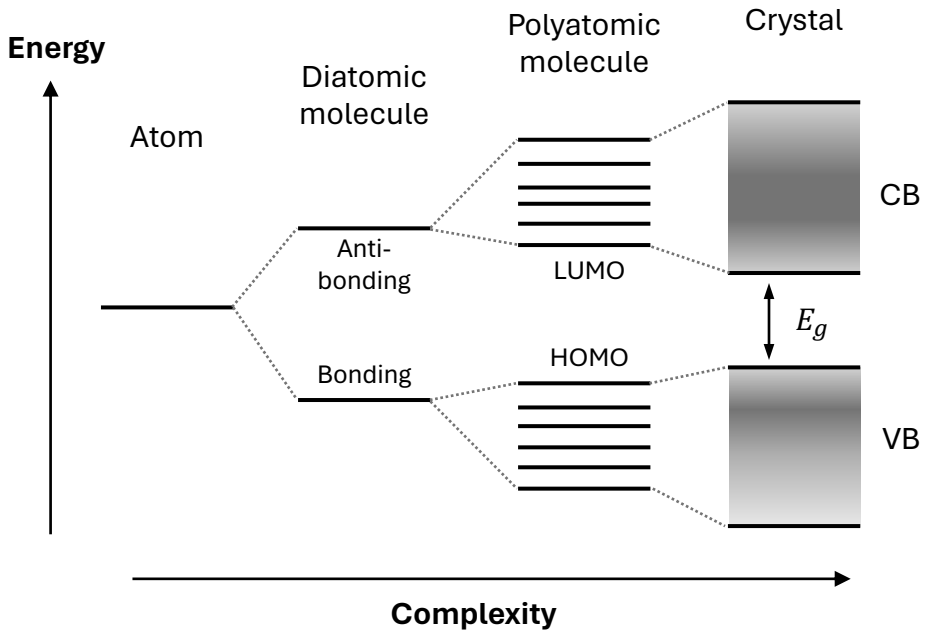


Figure 2.1: Schematic of the evolution of the electronic energy states from isolated atom to a crystal. LUMO and HOMO represent the 'lowest unoccupied molecular orbit' and 'highest occupied molecular orbit' respectively. While, CB, VB and E_g represent the 'conduction band', 'valence band' and 'band gap' in a semiconductor.

form a basis to be used for the true eigenfunctions of the new electronic Hamiltonian in a crystal. This linear combination of atomic orbitals (LCAO) can be mathematically expressed in Equation 2.9, achieved after using the translational symmetry of Bloch's theorem (shown in Equation 2.4) and a normalization requirement.

$$\psi(\boldsymbol{r}) = \frac{1}{\sqrt{N}} \sum_{\boldsymbol{R_n}} e^{i\boldsymbol{k}\cdot\boldsymbol{R_n}} \phi\left(\boldsymbol{r} + \boldsymbol{R_n}\right), \tag{2.9}$$

where ψ is the wavefunction, N is the number of sites in the crystal, and ϕ is the atomic orbital.

Subsequently, solving the Hamiltonian will result in the acquisition of a dispersion relationship in the following form:

$$E(\boldsymbol{k}) = \left(E_{\text{atomic}} + E_{\text{shift}}\right)_{\text{constant}} + E_{\text{transfer}}(\boldsymbol{k}), \tag{2.10}$$

where E_{atomic} is the energy eigenvalues for the Hamiltonian of an isolated atom, the E_{shift} is the central atom energy shift due to the extra potential of the surrounding atoms, while E_{transfer} is the energy dispersion related to the transfer integral quantitatively representing the hopping or transfer probability to a neighbouring site. [13, 15]

In the end, this model converts the discrete energy levels (used to describe singular atomic orbitals) into multiple energetic bands separated by an energy gap (used to describe a periodic crystal). A schematic of the evolution of the energy states from an isolated atom to a crystal is visualized in Figure 2.1.

This model also importantly creates a transfer integral variable to parameterise and efficiently describe the bandstructure. Such that a small (large) transfer integral implies weak (strong) orbital wavefunction overlap, a wide (narrow) bandgap, a narrow (wide) bandwidth, and heavy (light) charge carriers.

I additionally note that the tight binding model can be further extended with a multiple-atom basis, or with the inclusion of multiple orbitals available per atom to increase complexity and accuracy, and create more bands in the bandstructure.

2.1.2 Semiconductors

Classifications based on bandstructure Once the bands are formed, the crystal can be categorised as a metal, semiconductor or an insulator depending on its bandgap and bandstructure. If there is a continuous availability of higher-energy states that the electrons can occupy, then the crystal is classified as a metal. Otherwise it is considered a semiconductor or an insulator depending on the energetic gap between the two bands. The difference between a semiconductor and an insulator is purely based on convention, as semiconductors are usually defined by a comparatively surpassable band gap of a few eVs. For a typical semiconductor, the band gap is the pivotal parameter that represents the energetic range where no states exist and the energetic gap between the top of the entirely filled band (valence band) and the bottom of the empty band (conduction band). Semicondcutors can additionally be classified as either direct or indirect semiconductor depending on the alignment of the momentum positions of the minimum of the conduction band and maximum of the valence band with respect to each other (k-space alignment). Direct semiconductors have the extremes of their valence and conduction bands aligned, allowing for radiative optical transitions between the extremes. On the other hand, indirect semiconductors have misaligned extremes for the valence and conduction bands, forcing the emission or absorption of lattice vibrations (phonons) to be involved in any transition between the two bands in order to conserve momentum, and yet the probability of such 'forbidden' transitions is comparatively small. [13, 15]

Photo-generation of charge carriers In an intrinsic (undoped) semiconductor (with minimal thermal energy available), all the electrons fill the entirety of the valence band leaving no unfilled energy state in that band and making the semiconductor behave as an insulator. However, the semiconductor can be converted into a conductive state when the electrons are promoted to unfilled energy states in the conduction band by

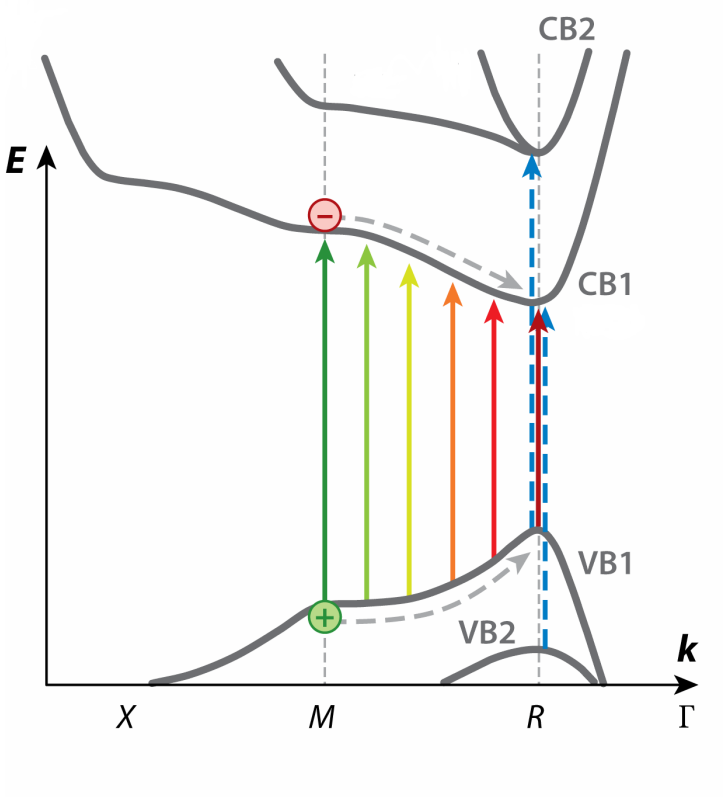


Figure 2.2: Bandstructure of a direct semiconductor. The coloured arrows between the valence band (VB) and the conduction band (CB) represent allowed optical transition where the photo-generation of an electron-hole pair is possible. The grey arrows represent the charge-carrier relaxation process to the band edge post photo-generation. While the blue dashed lines are other allowed transitions between different bands. Figure is adapted from [16].

providing enough energy either thermally or through a non-resonant (i.e. above bandgap) photo-excitation to the valence band electrons. The newly generated charge carriers rapidly relax to the band edge through carrier-carrier scattering to establish a thermalized charge-carrier Maxwell distribution defined by a gas temperature (thermalization process). The discrepancy between the charge-carrier gas temperature and lattice temperature is then resolved by interactions between the charge carriers and lattice vibrations (phonons) (cooling process). [17, 18] To complete the photo-generation picture, the electronic promotion to the conduction band also leaves a vacant state in the valence band that the other electrons feel an attraction to and try to occupy. The apparent movement of this unoccupied state can be equivalently seen as a positively-charged particle freely moving in the valence band with an effective mass reflective of the energy-momentum dispersion relationship in the valence band. Therefore, a photo-excitation that promotes an electron into the conduction band and leaves a vacant state in the valence band, is effectively photo-generating a pair of free charge carriers and creating an availability of higher-energy free states that they can freely occupy. [17, 18] A schematic of the bandstructure of a typical direct semiconductor with the photo-generation process is displayed in Figure 2.2.

Excitons Coulombic attraction between the photo-generated electrons and holes can result in the formation of electron-hole bound states (excitons) with binding energy that vary. The binding energy represents the ease with which excitons dissociate to form free charge carriers. When the binding energy is minimal such that they can easily thermally dissociate at room temperature, then the photo-excitation is effectively generating a pair of free charge carriers as explained above. However, for more strongly bound excitons, the excitonic effects may lead to the hampering of charge-carrier extraction and a reduction in the generation of a photocurrent. For a weakly bound (Wannier-Mott) exciton, the energy levels can be treated as that of a hydrogen-like species with

electron and hole effective masses in a dielectric medium with a relative permittivity that encapsulates all the additional complexities to a simple hydrogen atom. [19] For a strongly-bound exciton (Frenkel exciton), the energy levels and binding energy will have a much more complicated dependency, and the exciton can be delocalised depending on the disorder present in the structure. [19]

Trap states Finally, an additional electronic transition available for valence electrons to get promoted into are trap or defect states within the bandgap. Point defects for example (which are the most common defects for perovskite films) [20] are local disturbance to the crystal structure due to a missing or misplaced atom resulting in a variation in the energetic landscape and the creation of trap states within the bandgap that usually increase both the scattering rate and propensity for localisation, and consequently reduce the charge-carrier mobility and the current density of extractable charge carriers. [15, 18, 19]

2.1.3 Hybrid metal halide perovskites

Originally, 'perovskite' exclusively referred to a particular calcium titanium oxide mineral ($CaTiO_3$). [21] However, it is now used to refer to any crystal structure adopting the same ABX_3 structure shown schematically in Figure 2.3. In fact, there is a plethora of materials that can result in the formation of the generic ABX_3 perovskite structure. However, that pool of materials is significantly restricted by the requirements of attaining excellent optoelectronic properties, long-range and efficient charge-carrier transport, and long-term operational stability against the elements. A specific subset of perovskites with such qualities are metal halide perovskites (MHP), [16] where the B-site cation is a divalent metal cation (usually Pb^{+2} or Sn^{+2}), and the X-site anions are halides (usually I^-, Br^-, or Cl^-). The ideal perovskite structure will only form for certain sizes of ions at each site, [9, 22] and hence the choice of cations can have significant influence over the structural and optoelectronic properties of the emergent crystal. [16, 23] For standard high-quality 3-dimensional MHPs, the A-site cation is a small monovalent cation, usually an organic molecule such as formamidinium $H_2NCHNH_2^+$ (FA^+) or methylamonium $CH_3NH_3^+$ (MA^+), or a small inorganic cation such as cesium$^+$ (Cs^+), or a mixture thereof. [23] Alternatively, much larger organic cation can be used as the A-site cation to reduce the electronic dimensionality of the system, as these large spacer molecules act as insulating layers between the conductive perovskite octahedra, resulting in films ranging from purely 2-dimensional to quasi 2-dimensional to 3-dimensional, depending on the ratio of large organic spacer molecules to small A-site typical molecules. [24–27]

Crystal lattice

One of the key defining structural factors of MHPs is their facile ionic movement and soft lattice properties. [28] This allows them to accommodate large amounts of disorder within their crystal structure and allow a mixture of ionic species to coexist and occupy

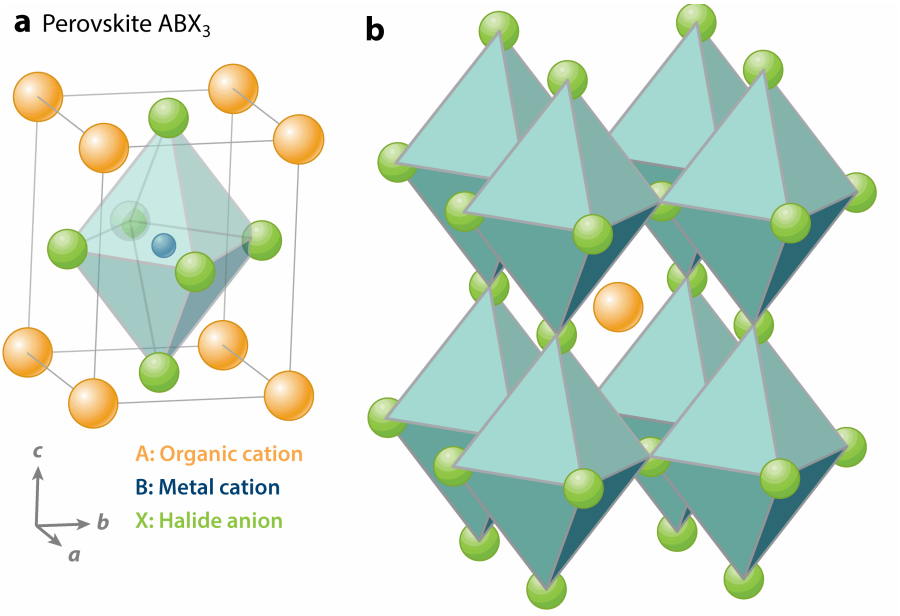


Figure 2.3: Perovskite structure. a: A unit cell of the ABX_3 perovskite structure, with the A-site cation usually occupied by a small organic molecule (e.g. FA^+ or MA^+) or an inorganic element (e.g. Cs^+), the B-site cation usually occupied by a divalent metal (e.g. Pb^{2+} or Sn^{2+}), and the X-site anion usually occupied by a halide (e.g. I^-, Br^-, or Cl^-). **b**: A representation of the 3-dimensional perovskite lattice structure. The legend in **a** also applies to **b**. Figure is adapted from [16].

similar lattice sites, permitting stoichiometric engineering to be one of the plausible avenues for the controlling and fine tuning of the bandstructure and final optoelectronic properties of the emergent crystal. [29–31]

Additionally, the soft lattice MHP property partly influences and aids in the formation of high-quality films from such an easy and low-cost fabrication method such as spin-coating: The random ionic movement in the lattice leads to the acquisition of the 'self-healing' ability in MHPs, where the crystal can correct imperfections, recover from degradation, and ease any extra lattice strain or massive distortions in the lattice through this random lattice movement. [32] This however is a double-edged sword as it leads to the formation of other defects and the creation of other low-energy barrier degradation routes that quicken degradation or inhibits the maximum photovoltaic potential of the perovskite photo-absorber layer. [33] For example, any lattice mismatch between the substrate and the growing perovskite structure, or between two different compositions or phases in the crystal, or other similar external pressures that introduce large-enough amounts of strain in the system will force the lattice to reorder itself and potentially result in many unexpected outcomes. [34–36]

2.1.4 Charge-carrier dynamics

In general, charge-carrier dynamics within a typical semiconductor are governed by a handful of physical processes expressed in the following rate equation:

$$\frac{dn}{dt} = G - k_1 n - k_2 n^2 - k_3 n^3, \tag{2.11}$$

where n is the population density of the charge-carriers, G is the generation rate of charge-carriers caused by stimulated absorption, k_1 is the monomolecular recombination rate constant, k_2 is the bimolecular recombination rate constant, and k_3 is the Auger recombination rate constant. [16]

Charge carriers can be generated when an incident photon matches the energy of an optically allowed transition inducing the absorption of that photon in a process called 'stimulated absorption'. This process will depend on the available energy levels, the selection rules for such a transition, the density of states, and the spectral profile of the incident light. Therefore it is an intrinsic property of the semiconductor and represents the G term in Equation 2.11. [15, 37]

The other processes are all associated with the demotion of the excited electron back into the valence band. Trap-mediated recombination is one of these recombination pathways, and is initiated when free charge carriers are localised around a trap state, followed by recombination with the complementary free charge carrier, usually through the transferring of the excess energy to the lattice as extra phonons. However, the recombination can either be radiative or non-radiative depending on the selection rules for the transition between the trap state and the valence band. This recombination pathway depends on the population density of the traps and on one species of free charge carriers, therefore its contribution to the rate equation will be proportional to $n_T p + p_T n$ (n_T and p_T are the electron and hole trap densities respectively) or alternatively $k_1 n$ for an intrinsic (electron and hole populations are the same) semiconductor. [16, 19, 37] This

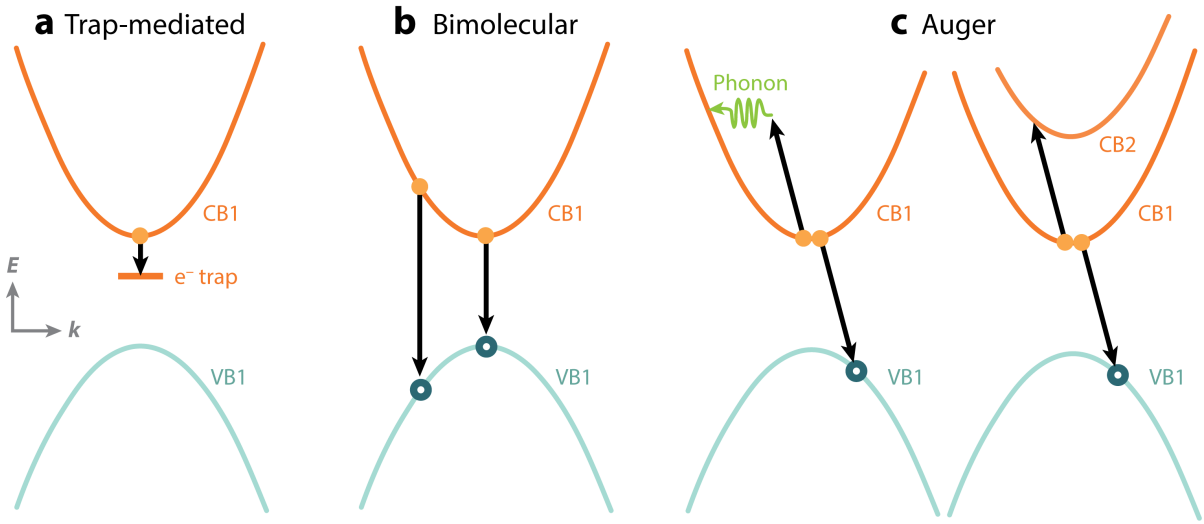


Figure 2.4: Schematic diagram of the recombination mechanisms. **a**: trap-mediated recombination, which usually involves the non-radiative recombination of a trapped charge carrier with a free charge-carrier, hence its monoloecular dependence on the density of free charge carriers ($k_1 n$). **b**: bimolecular recombination, which represents the intrinsic radiative recombination a free electron-hole pair, hence its bimolecular dependence on density of free charge carriers ($k_2 n^2$). **c**: Auger recombination, where the excess energy from the non-radiative recombination of a free electron-hole pair is given to another free charge carrier, hence its trimolecular dependence on the density of free charge carriers ($k_3 n^3$). Figure is taken from [16].

in turn implies that it is an extrinsic property of the semiconductor, where fabrication method, crystallinity, phase purity, grain size, trap passivation techniques and much more factors are able to influence the value of k_1 and the prominence of trap-mediated recombination pathways. It is worth noting that the limited availability of trap states, which could be entirely filled with a high-enough laser excitation fluence or by enough time passing, makes this process better described by a time-dependent rate constant. [16] There is an additional monomolecular recombination pathway that depends on a single mobile carrier species in the form of excitonic radiative recombination. However, it is only worth considering when excitons are long-lived and when they represent a significant fraction of the generated charge carriers, such as in strongly confined semiconductors or semiconductors that possess strong exciton binding energies.

Next, bimolecular recombination represents an intrinsic recombination pathway for a semiconductor and sets an intrinsic limit on charge-carrier lifetimes and diffusion lengths. This pathways can be viewed as the inverse process of absorption, as it involves the radiative annihilation of free electrons and holes and is therefore a permanent recombination mechanism for a semiconductor under light. The recombination probability will therefore depend on the square of the charge-carrier population density, and the recombination rate k_2 will depend on the bandstructure and density of states among other things. [15]

Finally, Auger recombination is the final demotion process considered in this simplified rate equation, and it involves a third charge carrier carrying away the excess energy and momentum from the non-radiative annihilation of an electron and a hole. Therefore, it can be represented by a cubic dependence on the charge-carrier population density in Equation 2.11, and would usually require a significantly large charge-carrier density to be present in the semiconductor for it to dominate the recombination pathways, and hence can be effectively ignored for the purpose of this thesis. [16, 37]

The recombination mechanisms are visually presented in Figure 2.4.

2.1.5 Photovoltaic devices

The key future application of metal halide perovskites is as the active photo-absorber layer in photovoltaic devices. Accordingly, for an effective operating photovoltaic device, the photo-generated free electrons and holes in the active layer need to be separated and extracted into an external electrical circuit. This can be achieved by sandwiching the 'intrinsic' active layer between a electron-doped 'n' ('electron transfer layer') and a hole-doped 'p' ('hole transfer layer') semiconductors to selectively promote the transfer of a specific species of free charge carriers.

The doping in the 'n' layer means that there exists a population of electrons in the conduction band of that layer, effectively raising its Fermi level closer to he conduction band. Analogously, there exists a hole population in the valence band of the 'p' layer, lowering its Fermi level closer to the valence band. When the 'n', 'i', and 'p' layers are brought in contact, electrons and holes from the 'n' and 'p' layers respectively, transverse the 'i' layer and recombine causing a build up of the opposing charge in each layer and creating a built-in electric field in the 'i' layer that will encourage charge-carrier separation post photo-generation. The system then equilibrates once the Fermi level across the device stack becomes constant and once the current from the built-in electric field and the current based on the charge-carrier population gradient cancel out (in the dark and with no applied bias). [37]

As hinted at in the above paragraph, two opposing electric current are created; a 'drift' and a 'diffusion' current. First, the 'diffusion' current is the current derived from the population gradient of the majority charge carriers within the device stack. This current is against the built-in electric field and runs from the 'p' to the 'n' layers. Therefore, it has a strong dependence on the strength of the built-in electric field and any externally applied electric field. Second, the 'drift' current is based on excited charge carriers in the 'i' layer (whether thermally excited into the conduction band or photo-generated) being

directed along the direction of the built-in electric field. This current runs from the 'n' to the 'p' layers, and is mostly dependent on the population of excited charge carriers which in turn depends on the Fermi level, the thermal energy available and the excitation fluence of the incident illumination (a forward applied bias opposing the built-in electric field would change the direction of the 'drift' current to be along the 'diffusion' current).

The total extractable current density (J) from the photovoltaic device under illumination and an applied bias can therefore be written as follows:

$$J(V) = J_{\mathrm{SC}} - J_{\mathrm{Dark}} = J_{\mathrm{SC}} - J_0 \left(e^{\frac{eV}{k_{\mathrm{B}}T}} - 1 \right), \tag{2.12}$$

where J_{SC} is the 'short-circuit' current density, J_{Dark} is the current density in the dark under an applied bias of V, K_{B} is the Boltzmann constant, and T is the temperature. The J_{Dark} is based on the ideal diode equation, and can be effectively seen as the enhancement to the 'diffusion' current due to an applied voltage. On the other hand, the J_{SC} is the maximum extractable current density, and can be effectively seen as the enhancement to the 'drift' current under illumination, and is the total extractable current density when there is no externally applied bias. This makes the J_{SC} an extremely useful parameter to gauge the ease with which charge carriers can overcome energetic obstacles and can be extracted, and to gain insights into the energetic landscape of a photovoltaic device. The applied voltage can be ramped up until the enhanced 'diffusion' current is strong enough to overcome the enhanced 'drift' current (J_{SC}), when this is achieved the externally applied voltage is labelled the 'open-circuit' voltage (V_{OC}), and it should approximately reflect the built-in potential in the device.

Finally, the power extracted from a photovoltaic device is the product of the extractable current density and voltage, and therefore the most important parameter used to assess the efficiency and feasibility of a photovoltaic device is its power conversion efficiency (PCE), which is defined as the electrical power output from the device as a percentage of the total power input. [37]

2.2 Focus: Lower dimensional metal halide perovskites

Reducing the electronic dimensionality of a semiconductor is an involved process that has the ability to yield drastically different structural and optoelectronic properties from a compositionally-similar 3-dimensional semiconductor. As the dimensionality of the semiconductor decreases, the quantum confinement increases until quantum phenomena start to manifest and quantum effects start becoming significant enough to necessitate taking them into consideration. This is usually achieved when the confinement length scale becomes comparable to the characteristic length scale of the material such as the exciton Bohr radius or the de Broglie wavelength. [15]

The introduction of quantum confinement as a controllable parameter in these semiconductors creates an additional dimension that can be used to fine tune the optoelectronic and transport properties of the emerging film. For example, precise control over the bandgap, photoluminescence profile and intensity, structural integrity, photovoltaic performance, nature of charge-carrier transport, and much more can be achieved through the choice of insulating ligands and spacer molecules, and through the control of the confinement length scale. [38]

2.2.1 Density of states

The density of states (DoS) describe the number of allowed states per unit energy range and is denoted by $g(E)$. The total number of allowed states would therefore become $g(E)dE$, which can equally be written in terms of the wavevector k, as $g(k)dk$.

$$g(k)dk = 2\left(\frac{\text{Total volume in } k\text{-space}}{k\text{-space volume per allowed state}}\right), \tag{2.13}$$

where the is a prefactor of 2, due to electrons being fermions, where 2 electrons of opposing spins are capable of occupying the same k-state before Pauli's exclusion principle needs to be enforced.

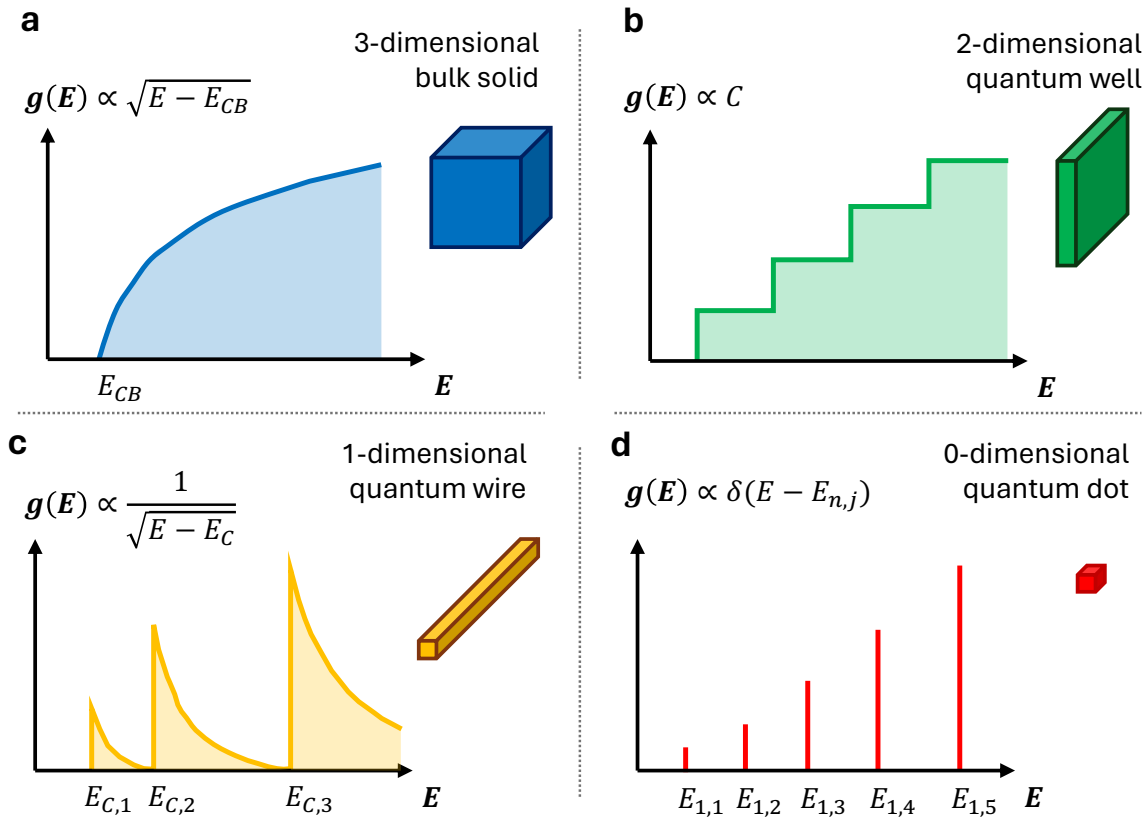


Figure 2.5: Density of States (DoS) under different electronic dimensionality. **a**: DoS for a 3-dimensional bulk solid with E_{CB} representing the conduction band energy. **b**: DoS for a 2-dimensional quantum well with C representing a constant. **c**: DoS for a 1-dimensional quantum wire with E_C representing the minimum energy of each band. **d**: DoS for a 0-dimensional quantum dot with $E_{n,j}$ representing the quantised energy levels of a 3-dimensionally confined system.

Using the boundary conditions defined earlier based on Bloch's theorem in Equation 2.6, the k-spacing per allowed state can be written as:

$$\delta k_i = \frac{2\pi}{n_i a_i}, \tag{2.14}$$

where $\boldsymbol{a_i}$ is the primitive lattice vector, and $n_i \boldsymbol{a_i}$ is $\boldsymbol{L_i}$ representing one of the dimensions of the semiconductor. Therefore, the k-space volume per allowed state is as follows:

$$\delta k = \frac{(2\pi)^{\dim}}{V_{\dim}}, \tag{2.15}$$

where dim is the dimensionality of the semiconductor, and $V_{\dim}$ is the total volume of the semiconductor in real space.

The total volume occupied in k-space for any number of dimensions is based in a known mathematical formula for a volume in dim dimensions, [39] which can be written as:

$$dV_k = \alpha k^{\dim-1} dk; \qquad \alpha = 2\left(\frac{\pi^{\left(\frac{\dim}{2}\right)}}{\Gamma\left(\frac{\dim}{2}\right)}\right), \tag{2.16}$$

where Γ is the gamma function defined such that $\Gamma(n) = (n-1)!$.

A final expression for the density of states as a function of energy in any number of dimensions can therefore be obtained by combining Equations 2.13, 2.15, and 2.16 into:

$$g(E) = 2\left(\frac{V_{\dim}}{2^{\dim-1}\pi^{\left(\frac{\dim}{2}\right)}\Gamma\left(\frac{\dim}{2}\right)}\right) k^{\dim-1}\frac{dk}{dE}. \tag{2.17}$$

To decipher what the density of states could look like for an electron in any medium, the dispersion relationship of free charge carriers can be used if all the bandstructure and non-parabolic behaviour is encapsulated into the equation by using a new effective mass for the charge carrier, which can be written as follows:

$$E(k) = \frac{\hbar k^2}{2m^*}; \qquad m^* = \hbar\frac{d^2k}{dE^2}, \tag{2.18}$$

where m^* is the effective mass of the charge carrier and can be visually deduced as the inverse of the curvature of the bandstructure in k-space.

By using Equations 2.17 and 2.18, the DoS for semiconductors with differing degrees of confinement can be roughly expressed in Equations 2.19-2.22. A schematic of the typical dispersion relationships and the corresponding density of states for semiconductors of different electronic dimensionality is plotted in Figure 2.5.

$$g(E) \propto \sqrt{E - E_{\mathrm{CB}}}\ ; \qquad \text{Bulk solid (3-dimensional)}, \tag{2.19}$$

$$g(E) \propto C\ ; \qquad \text{Quantum well (2-dimensional)}, \tag{2.20}$$

$$g(E) \propto \frac{1}{\sqrt{E - E_{\mathrm{C}}}}\ ; \qquad \text{Quantum wire (1-dimensional)}, \tag{2.21}$$

$$g(E) \propto \delta\left(E - E_{n,l}\right)\ ; \qquad \text{Quantum dot (0-dimensional)}, \tag{2.22}$$

where E_{CB} is the minimum energy of the conduction band, C is a constant, E_{C} is the minimum energy of each band, and $E_{n,l}$ is the discrete energy levels defined in Equation 2.3 for an isolated atom. [13, 15]

2.2.2 Quantum confinement

Quantum confinement models

In an isotropic (effective mass is the same within and outside of the quantum well) quantum well confinement model, the potential energy ($V(\boldsymbol{r})$) is either 0 within the quantum well or V_0 outside of the well, resulting in a Hamiltonian that can be written as follows:

$$\hat{H}\psi(\boldsymbol{r}) = \left(-\frac{\hbar^2}{2m^*}\nabla^2 + V(\boldsymbol{r})\right)\psi(\boldsymbol{r}) = E\psi(\boldsymbol{r}). \tag{2.23}$$

While the ansatz solution of the wavefunction can be written as follows:

$$\psi(\boldsymbol{r}) = Ae^{i\boldsymbol{\alpha}\cdot\boldsymbol{r}} + Be^{-i\boldsymbol{\alpha}\cdot\boldsymbol{r}}. \tag{2.24}$$

Substituting the ansatz solution into the Hamiltonian, yields:

$$\alpha_j^2(\boldsymbol{r}) = \frac{2m^*(E_j - V_j(\boldsymbol{r}))}{\hbar^2}, \qquad \forall j. \tag{2.25}$$

By applying the necessary boundary conditions and the requirement that the wavefunction has to be continuous ($\psi_{\text{outside}} = \psi_{\text{inside}}$) and smooth ($\nabla\psi_{\text{outside}} = \nabla\psi_{\text{inside}}$) at the quantum well boundary, the full dispersion relationship can be obtained. [17]

Infinite quantum well To gain some intuition into how the wavefunction and the energetic landscape is going to behave in the presence of quantum confinement, a simple yet non-physical model of an infinite quantum well can be studied. In an infinite quantum well, the wavefunction either does not exist for regions outside of the quantum well, or is that of a free particle inside the well, which can be mathematically expressed as:

$$\psi(\boldsymbol{r}) = \begin{cases} Ae^{i\boldsymbol{k}\cdot\boldsymbol{r}} + Be^{-i\boldsymbol{k}\cdot\boldsymbol{r}}, & \text{Inside the well,} \\ 0, & \text{Outside the well.} \end{cases} \tag{2.26}$$

The boundary condition for this model of $\psi(0) = \psi(L_i) = 0$ is what provides the approximate analytical solution to the energy levels for such a deeply confined system

with a near prefect parabolic dispersion relationship. The quantized energy levels take the following expression:

$$E_n = \frac{\hbar^2 \pi^2}{2m^*} \cdot \left(\sum_i^{\dim} \frac{n_i}{L_i} \right)^2, \tag{2.27}$$

where n_i is the integer quantum number representing the peak indices in the i^{th} dimension, and L_i represents the confinement length scale in the i^{th} dimension. [17]

Periodic finite quantum wells A more plausible physical model of a quantum-mechanical semiconductor is an infinitely periodic array of finite potential barriers (referred to as a Krönig-Penney potential), which can be a good approximate representation of periodic barriers in a periodic crystal.

In order to obtain an expression for the dispersion relationship, the model can be simplified for a 1-dimensional superlattice. In this assumption, the full wavefunction can be expressed as:

$$\psi(\boldsymbol{r}) = \psi_{\text{free}} \cdot \psi_{\text{conf}}, \tag{2.28}$$

where ψ_{free} is the free electron wavefunction in the non-confined dimensions ($\psi_{\text{free}} \propto e^{\pm i(k_y y + k_z z)}$), and ψ_x is the confined wavefunction expressed as:

$$\psi_{\text{conf}}(x) = \begin{cases} e^{ikx}\left(Ae^{i(\alpha-k)x} + Be^{-i(\alpha+k)x}\right), & \text{Inside the well} \\ e^{ikx}\left(Ce^{i(\beta-k)x} + De^{-i(\beta+k)x}\right), & \text{Outside the well,} \end{cases} \tag{2.29}$$

where α and β can be obtained from Equation 2.25. The boundary conditions for this model can therefore be expressed as:

$$\text{B.C.s} : \begin{cases} \psi_{\text{inside}}(x_0) = \psi_{\text{outside}}(x_0), & \text{Continuous wavefunction,} \\ \partial_x \psi_{\text{inside}}(x_0) = \partial_x \psi_{\text{outside}}(x_0), & \text{Smooth wavefunction,} \\ u_{\text{inside}}(x_0) = u_{\text{outside}}(x_0 + L), & \text{Periodic Bloch function,} \\ \partial_x u_{\text{inside}}(x_0) = \partial_x u_{\text{outside}}(x_0 + L), & \text{Periodic Bloch function,} \end{cases} \tag{2.30}$$

where x_0 is the boundary position, and L is the combined widths of the quantum well (L_1) and potential barrier (L_2). These boundary conditions can be re-written to yield a

matrix whose determinant has to be 0 for a non-trivial solution to exist.

$$\begin{vmatrix} 1 & 1 & -1 & -1 \\ \alpha & -\alpha & -\beta & \beta \\ e^{i(\alpha-k)x_0} & e^{-i(\alpha+k)x_0} & -e^{i(\beta-k)(x_0+L)} & -e^{-i(\beta+k)(x_0+L)} \\ (\alpha-k)e^{i(\alpha-k)x_0} & -(\alpha+k)e^{-i(\alpha+k)x_0} & -(\beta-k)e^{i(\beta-k)(x_0+L)} & (\beta+k)e^{-i(\beta+k)(x_0+L)} \end{vmatrix} = 0. \tag{2.31}$$

This leads to the following transcendental equations to describe the dispersion relationship:

$$\cos(kL) = \cos(\alpha L_1)\cosh(\gamma L_2) - \left(\frac{\alpha^2-\gamma^2}{2\alpha\gamma}\right)\sin(\alpha L_1)\sinh(\gamma L_2), \qquad E < V_0, \tag{2.32}$$

where $\gamma^2 = -\beta^2$. Equation 2.32 is reflective of electrons with energies less than the potential barrier. However, Similarly, the transcendental equation changes for electrons with energies higher than the potential barrier are instead reflected by the following transcendental equation:

$$\cos(kL) = \cos(\alpha L_1)\cos(\beta L_2) - \left(\frac{\alpha^2+\beta^2}{2\alpha\beta}\right)\sin(\alpha L_1)\sin(\beta L_2), \qquad E > V_0. \tag{2.33}$$

This simple model converts the simple discrete energy levels of the infinite quantum well model and broadens them into minibands. Importantly, as demonstrated in Equation 2.33, a perturbing influence will still exist for unbound electrons with energies higher than that of the confining potential barriers. [15]

Band-like vs hopping-like transport

A reduction in electronic dimensionality is always accompanied by drastic changes to the nature of charge-carrier transport within the semiconductor. Under strong quantum confinement such as in a 2-dimensional semiconductor with long-chained organic insulating molecules, charge-carrier transport within the conductive slabs (intra-slab charge-carrier transport) becomes a lot more prominent that any transport between the conductive slabs through the insulating layer (inter-slab charge-carrier transport). Similarly for a nanocrystal, the intra-particle charge-carrier transport become more prominent than any long-range inter-particle charge-carrier transport. Therefore, controlling the fabrication

method becomes a pivotal route to tip the scales one way or the other; towards more favourable long-range inter-slab over inter-particle charge-carrier transport, or towards strengthening the quantum confinement experienced by the charge carriers.

Intra-slab and intra-particle charge-carrier transport in a conductive medium is characterised by band-like transport, where the transport properties are determined by the bandstructure of the semiconductor, the wavefunctions are delocalised over the entire volume of the semiconductor, and the mobility decreases with increasing temperatures. [14, 15] On the other hand, long-range inter-slab and inter-particle charge-carrier transport can be instead characterised by hopping-like transport, where the transport efficiency is determined by the hopping distance, and where transport requires an activation energy and is therefore monotonically increasing with increasing temperature. [17] Hopping-like charge-carrier transport can either be through charge-carrier tunnelling or Förster resonance energy transfer (FRET). The probability for a charge carrier to tunnel through a potential barrier has an exponentially decaying dependence on the tunnelling distance, potential barrier height, and effective mass of the charge carrier. [13, 14] This implies that there is a near-zero probability for an electron to tunnel through a thick insulating layer, effectively removing tunnelling as a viable charge-carrier transport mechanism for the typical lower-dimensional perovskite semiconductors. Alternatively, energy transfer (FRET) offers a more realistic transport mechanism across a small-enough insulating layer. The energy transfer involves transitions between two localised states via non-radiative dipole-dipole coupling. The efficiency of the transition (coupling strength) depends on the spectral overlap between the excitation spectrum of the acceptor and the emission spectrum of the donor, on the relative orientation of the two dipoles, and on the spatial separation between the two dipoles with a particularly sensitive dependence. Therefore, FRET efficiencies can - similarly to the tunnelling efficiency, reach near-zero values for

long-chained insulating layers, as it is inversely proportional to the sixth power of the distance between the two dipoles (thickness of the insulating layer). [15]

2.2.3 Nano structuring

Intrinsic quantum confinement

Certain MHP compositions have a tendency to intrinsically form nanostructures and manifest quantum physical behaviour in their absorption spectrum. This has notably been most associated with the formamidinium lead triiodide ($FAPbI_3$) perovskite composition. The absorption spectrum of which possesses peculiar above-bandgap oscillatory features that has been linked to and used to parameterise the strength of the quantum confinement within such a composition. [40–42] An example of these peculiar above-bandgap features in the absorption spectrum of $FAPbI_3$ is displayed in Figure 2.6.

Evidence: The link between these above-bandgap absorption features and the presence of quantum confinement has been established through several experimental observations and a couple of theoretical simulations. First, after decoupling the oscillatory features from the underlying bulk-like absorption spectrum, the energetic positions of the decoupled peaks relative to the bandgap ($E_{\text{peak}} - E_{\text{g}}$) is found to have a temperature dependence that is different and independent to that of the bandgap or film thickness. Instead, their temperature dependence can be better understood when linked to changes in the reduced lattice parameter of $FAPbI_3$. Based on the simple infinite quantum well model in Equation 2.27, the confinement energy ($E_{\text{peak}} - E_{\text{g}}$) is inversely proportional to the square of the confinement length scale. Indeed, the inverse square of the reduced lattice parameter was experimentally found to have a very similar dependence on temperature to the confinement energy. [40]

Second, the energetic spacing between the decoupled peaks follows a quadratic dependence on the peak indices in a manner consistent with what is predicted based on both an infinite quantum well model and a Krönig-Penney superlattice potential. Third, the broadening of the decoupled peaks, and the excitonic peak and absorption onset

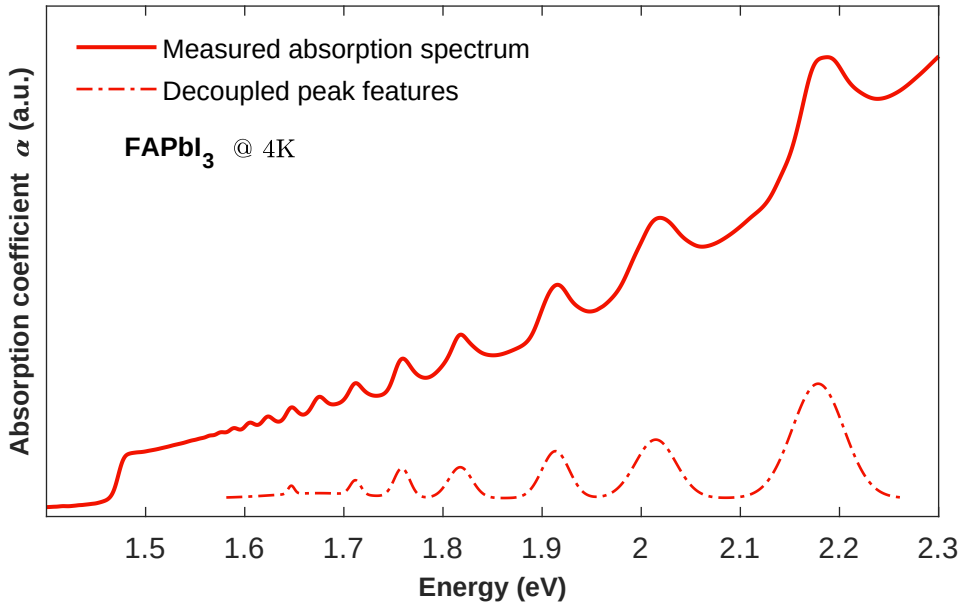


Figure 2.6: An absorption coefficient spectrum of $FAPbI_3$ at 4 K displaying the peculiar absorption features indicative of quantum confinement.

possess significantly different temperature trends, highlighting the inherent fundamental difference in the physical phenomena governing these features and their origins. This is again in agreement with a quantum confinement picture, as a reduction in the electronic coupling strength to optical phonons is expected following a reduction in electronic dimensionality in semiconductors. [43, 44]

In addition to the experimental evidence for the quantum confinement hypothesis, theoretical calculations and simulations further support this hypothesis. Both *ab initio* calculation on the bandstructure of $FAPbI_3$ under an infinite quantum well confinement, and simulations of the bandstructure and DoS of a superlattice of finite potential barriers correlate well with the measured absorption spectrum of $FAPbI_3$. [40]

Finally, the size of the intrinsically-occurring nanostructures was additionally inferred from both experiments and theoretical calculations. When the thickness of the film was reduced below 35 nm, the prominence of the above-bandgap absorption features massively decreased, implying that the film thickness was comparable to the intrinsic domain size, and that it disrupted the local ordering needed for this phenomenon to occur. This observation in tandem with the density functional theorem (DFT) calculations simulating absorption spectra of $FAPbI_3$ with different confinement length scale to match the measured spectrum, lead to an estimation of the confinement length scale to be $\sim$ 15 nm. [40]

It is worth noting that for a typical quantum confined state, the oscillator strength for a transition starts to decreases as the peak index n (and by association confinement energy) increases. [13, 17, 45] However, the overall density of states for a confined semiconductor like the $FAPbI_3$ composition will have additional layers of complexity due to the existence of multiple conduction bands - which will each be quantized due to the quantum confinement, and due to the smearing and broadening of the DoS - due to easily-accessible thermal energy or due to the dimensionality of the quantum

confinement. This explains the observed increase in both amplitude and width of the decoupled peaks with peak index and confinement energy.

Causes: The confinement theories and simulations that linked the observation of the oscillatory above-bandgap absorption features with quantum confinement were either based on an infinite quantum well model - where instances of the photo-active (α) phase of $FAPbI_3$ was 3-dimensionally confined, or a periodic array of a finite quantum well - where the α phase is comparatively weakly confined in a periodic arrangement. This intrinsic restructuring and self-assembly of nanostructures within a 3-dimensional semiconductor can be viewed as an extension of the 'self-healing' and 'soft lattice' properties of metal-halide perovskites as the lattice could be rearranging itself and inadvertently forming (easily-formable) potential barriers in an attempt to relieve the strain within the crystal structure, and yet the cause of such quantum confinement tendencies has to be exclusive to FA-rich MHPs to comply with the observation of these features only in FA-rich MHP compositions.

A possible explanation for the cause of the confinement could be the presence of one of the many photo-inactive $FAPbI_3$ polymorphs (such as the hexagonal δ phase). These polymorphs are usually thermodynamically stable, provide a degradation pathway (with minimal activation energy) for the $FAPbI_3$ α phase upon minimal exposure to moisture, [33] are usually present around grain boundaries and can form periodic arrangement, possess higher bandgaps than the α phase, and can suitably act as potential barriers. All of which make them plausible potential barriers for these nanostructures. Other crystallographic phases and superstructures of the $FAPbI_3$ composition could similarly act as potential barriers. The formation of these phases could be a result of twinning defects at grain boundaries, experienced strain within the film, and generally the fabrication and crystallization methods of the 3-dimensional film.

Quasi 2-dimensional structures

Layered perovskite structures can be achieved through the inclusion of large organic cations that are too large to fit as the A-site cations within the perovskite structure and thus act as spacers between the conductive metal halide octahedral planes. The resulting quasi 2-dimensional perovskite network consists of n planes of the corner-sharing octahedra confined between insulating planes of the large organic spacer molecules. [46] Varying n in this structure changes the dimensionality of the perovskite slabs and its optoelectronic properties including its bandgap and stability. $n = 1$ corresponds to the purely 2-dimensional state with only a layer of octahedras between each insulating plane, $n = \infty$ corresponds to the 3-dimensional perovskite structure and the integer values inbetween results in a quasi 2-dimensional structure.

These quasi 2-dimensional structures have managed to demonstrate superior moisture and air stability when compared to their 3-dimensional counterparts. [47] In fact, the incorporation of these large organic cations can also suppress the non-radiative recombination pathways throughout the film, by passivating the trap states and point defects, preventing a large number of degradation pathways, and providing a better electronic interface between the grains of the different dimensionality phases. [48] However, this enhancement in environmental stability and suppression of trap-mediated recombination appear to be counter-acted by the lower solar cell efficiency, higher exciton binding energies, shorter diffusion lengths, lower charge-carrier mobilities, and poorer photovoltaic performance. [49]

These systems are natural multiple-quantum wells, due to the offset in the energetic band alignment of the conductive perovskite slabs and the insulating organic layers, and the dielectric constant mismatch between these layers. The presence of this complicated and obstructive energetic landscape has the potential to inhibit any out-of-plane charge-carrier motion through the insulating layers to the electron and hole transport layers

and the electrical contacts of a photovoltaic device afterwards, leading to the obstruction of charge-carrier extraction, and the quantum wells being the main culprit behind the very poor photovoltaic performance and charge-carrier transport properties of such semiconductors. However, such a problem can be overcome if the preferential orientation of the insulating layers and conductive slabs can be tuned and controlled in such a way to promote strong out-of-plane charge-carrier transport properties.

3

Experimental Methods

Contents

3.1 Low temperature measurements 40
3.2 Absorption spectroscopy 41
3.2.1 Experimental setup 41
3.2.2 Data analysis 43
3.2.3 Elliott fitting 44
3.2.4 Extraction of the above-bandgap peaks 45
3.3 Photoluminescence spectroscopy 48
3.3.1 Time-integrated experimental setup 48
3.3.2 Time-resolved (TR) experimental setup 50
3.4 Terahertz (THz) spectroscopy 54
3.4.1 Optical-pump terahertz-probe (OPTP) 54
3.5 X-ray diffraction 59
3.5.1 Theory 59
3.5.2 Experimental setup 61

This chapter presents and discusses the methodology used throughout the thesis, with emphasis given to the underlying theory, working principle and specific experimental setup of each measurement technique. Absorption spectroscopy is the principal measurement technique used in Chapters 4 and 5, photoluminescence (PL) spectroscopy is mainly referring to experiments in Chapters 4 and 6, while terahertz spectroscopy solely focuses on Chapter 6.

3.1 Low temperature measurements

For all low-temperature measurements, a gas-exchange helium cryostat (Oxford Instruments, OptistatCF2) was used to control the temperature of the samples. The gas-exchange cryostat consists of a sample stick made out of thermally conductive metal with a resistor and the sample on its end, an inner chamber to house the sample, a radiation shield for insulation and better and more stable thermal performance, an outer chamber that is kept under vacuum to act as a thermally insulating layer, and an tube opening for the liquid helium to flow and surround the inner chamber using a transfer tube. After mounting the sample in the inner chamber of the cryostat, the chamber is then repeatedly purged and flushed with helium to ensure the presence of a helium atmosphere, and to prevent any condensation on the samples when the temperature is lowered. The helium atmosphere within the inner chamber and the liquid helium surrounding that inner chamber are what create the heat exchange, and by controlling both the flow rate of the liquid helium and the voltage across the resistor on the sample stick radiating heat, the temperature of the sample and the entire inner chamber can be controlled. To ensure stable thermal performance, the outer chamber of the cryostat is pumped down to low pressures ($< 5 \times 10^{-5}$ mbar) to provide an insulating layer for the temperature changes experienced in the inner chamber.

For temperature-dependent studies throughout this thesis, I vary the inner chamber temperature in increments of either 5 K or 10 K, in a thermal range from 4 K to 295 K.

3.2 Absorption spectroscopy

Absorption spectroscopy is a powerful measurement technique that provides the spectral dependence of the absorption properties of a material and gives information about the possible energetic transitions within such a material. These measured energetic transitions can be associated with vibronic transitions related to the crystal lattice and molecular bonds, alternatively they can be reflective of transitions between the energy levels of the core shell electrons, as the amount of light absorbed by a material will depend on the available higher-energy states, their density of states, and the spectral shape of the incident light. The broadening of the absorption features can provide additional properties on the physical phenomena of these induced transitions: The lifetime of the excited state is reflected in the natural broadening of an absorption feature, while energetic disorder in the form of structural and compositional heterogeneities can cause additional broadening of such features. [45] This technique measures spectra that mostly reflect the bulk properties of the material investigated. Therefore, throughout this thesis, absorption spectroscopy is used to gain insights into the energetic landscape of the semiconductor, identify the majority material composition in a film, probe energetic transition created from quantum confined states, and estimate values for useful intrinsic physical quantities of the material such as band gap (E_g), exciton binding energy (E_B), and the electron-phonon coupling strength (γ).

3.2.1 Experimental setup

The reflectance and transmittance of a material, and subsequently its absorbance, can be measured by using a fourier transform infrared (FTIR) spectrometer (Bruker Vertex 80v). The FTIR, in the configuration I use in this thesis, is essentially a Michelson interferometer that consists of a silicon detector, a tungsten halogen lamp as the illumination source, a CaF_2 beamsplitter that equally splits the incident beam into two paths and eventually

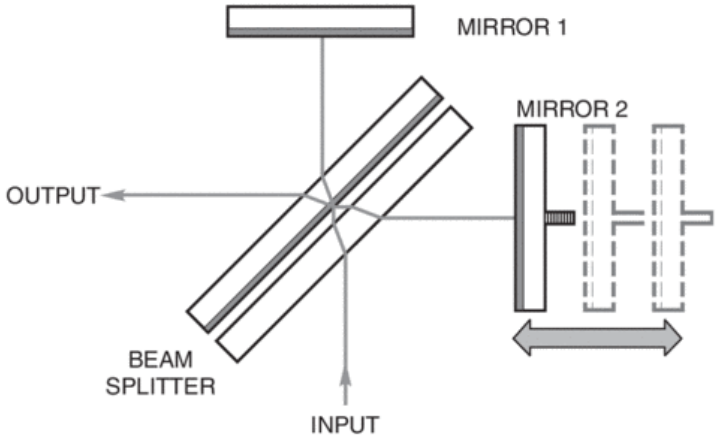


Figure 3.1: Operation of a Fourier transform infrared (FTIR) spectrometer. An incident light beam is split into two paths using a beamsplitter, where one of the split beams reaches a fixed mirror and is reflected back, while the other reaches a movable mirror on a translation stage. The moving of the second mirror changes the path length of one of the split beams, causing the formation of an interference pattern when both split beams are recombined. The interference pattern is then fourier transform to obtain the spectral information on how much light has been reflected of or transmitted through the sample. Figure is taken from [50].

recombines them, a fixed mirror, a movable mirror controlling the optical path length in one of the arms of the interferometer, and a HeNe laser used as a reference for precise control over the position and speed of the movable mirror. The resulting interference pattern (interferogram) depends on the optical path difference between the two arms of the interferometer, and can then be fourier transformed into a spectrum in the wavenumber domain. [50] A schematic of the experimental setup is shown in Figure 3.1.

3.2.2 Data analysis

The fractional reflectance and transmittance of a sample can be calculated after using reference measurements to account for what is approximately a 100% reflective (a silver mirror for the optical range) and 100% transmissive material (sample holder left empty), and is calculated as follows:

$$T(\nu) = \frac{T_{\text{Sample}} - T_{\text{Mirror}}}{T_{\text{Blank}} - T_{\text{Mirror}}}, \tag{3.1}$$

$$R(\nu) = \frac{R_{\text{Sample}} - R_{\text{Blank}}}{R_{\text{Mirror}} - R_{\text{Blank}}} \cdot \rho, \tag{3.2}$$

where T_{Mirror} represents the background transmission, and T_{Blank} represents the ideal transmissive material. Similarly, R_{Blank} represents the background reflection, and R_{Mirror} represents the ideal reflective material, while ρ is the reflectivity of the mirror.

The steady-state absorption coefficient spectrum can be calculated from the reflectance and transmittance values, as described by the Beer-Lambert law, [51] shown in Equation 3.3.

$$\alpha = -\frac{1}{d} \cdot \log_{10}\left(\frac{T}{1-R}\right), \tag{3.3}$$

where T and R are the fractional transmittance and reflectance of the sample respectively, α is the absorption coefficient, and d is the film thickness. It is worth pointing out that the reflection-transmission setup used here does not account for the light scattered of the sample, and therefore the measured absorption spectrum is slightly artificially

enhanced. This can be simply corrected for (for a direct semiconductor with minimal traps) by observing the absorption spectrum at energies significantly below the absorption onset and bandgap, where there should minimal absorption and any non-zero absorption indicative of the artificial enhancement due to scattering.

3.2.3 Elliott fitting

The onset in the absorption coefficient spectrum can be fitted using Elliott's model that describes the absorption of a semiconductor near its band edge. [52] This model offers a very realistic physical picture for semiconductors such as metal-halide perovskites close to their band edge, especially when compared to the Tauc relationships that were derived for amorphous semiconductors. The validity of Tauc plots is questionable, and the apparent close proximity of extracted bandgaps to the actual metal-halide perovskite bandgap is dependent on some of the errors from its assumptions cancelling out each other. [53]

The theory expresses the energy-dependent absorption as:

$$\alpha(E) = \alpha_{\mathrm{X}}(E) + \alpha_{\mathrm{C}}(E). \tag{3.4}$$

The bound exciton contribution α_{X} has the form:

$$\alpha_{\mathrm{X}}(E) = \frac{b_0}{E} \sum_{n=1}^{\infty} \frac{4\pi E_{\mathrm{b}}^{3/2}}{n^3} \delta\left(E - \left[E_{\mathrm{g}} - \frac{E_{\mathrm{b}}}{n^2}\right]\right), \tag{3.5}$$

where b_0 is a constant of proportionality that incorporates the electric dipole transition matrix element between the valence and conduction band. α_{X} is formed of the weighted sum of contributions from the exciton states with positive integer quantum number n and energies $E_{\mathrm{g}} - \frac{E_{\mathrm{b}}}{n^2}$, where E_{g} is the band gap energy and E_{b} is the exciton binding energy.

Here, the contribution from the electron-hole continuum states $\alpha_{\mathrm{C}}(E)$ has the form:

$$\alpha_{\mathrm{C}}(E) = \frac{b_0}{E} \left[\frac{2\pi\sqrt{\frac{E_{\mathrm{b}}}{E-E_{\mathrm{g}}}}}{1 - \exp(-2\pi\sqrt{\frac{E_{\mathrm{b}}}{E-E_{\mathrm{g}}}})}\right] c_0^{-1} \mathrm{JDoS}(E), \tag{3.6}$$

where the joint density of states is given by $\mathrm{JDoS}(E) = c_0\sqrt{E - E_\mathrm{g}}$ for $E > E_\mathrm{g}$ and 0 otherwise, and the joint density of states constant $c_0 = \frac{1}{(2\pi)^2}\left(\frac{2\mu}{\hbar^2}\right)^{3/2} \times\ 2$, where μ is the reduced effective mass of the electron-hole system. The term in square brackets is the Coloumbic enhancement factor, which increases the absorption from the continuum states above the square-root form of the JDoS for a direct-gap semiconductor as a result of the Coloumbic attraction between the unbound electrons and holes.

The linear combination of the contributions from the excitonic and continuum states, $\alpha(E)$, is then convolved with a broadening normal distribution function - representing the homogeneous broadening caused by electron-phonon coupling, disorder and local fluctuations of the stoichiometry of the material. The broadening is mathematically denoted by:

$$g(E) = \mathcal{N}(0, \sigma_\mathrm{T}^2) = \frac{1}{\sqrt{2\pi}\sigma_\mathrm{T}} e^{-\frac{x^2}{2\sigma_\mathrm{T}^2}}. \tag{3.7}$$

3.2.4 Extraction of the above-bandgap peaks

The Elliott fitting is only applicable to the absorption onset near the band edge, where the electronic band structure can be assumed to be parabolic and isotropic, transitions can be assumed to be between one valence and one conduction band, and the electric dipole transition matrix assumed to be independent of photon energy. [54] Therefore to decouple the peak features from the standard absorption coefficient spectrum at energies higher than the bandgap, I used a phenomenological fit to extract the peaks and quantify their behaviour.

The positions of the troughs in the experimental absorption coefficient data were obtained by subtracting a smoothed “central fit" line from the measured spectrum to result in a spectrum showing only the peak feature, from which the minimas (corresponding to the troughs) could be more readily extracted. Subsequently, interpolating a cubic spline between the experimental data at the energies of these troughs, resulted

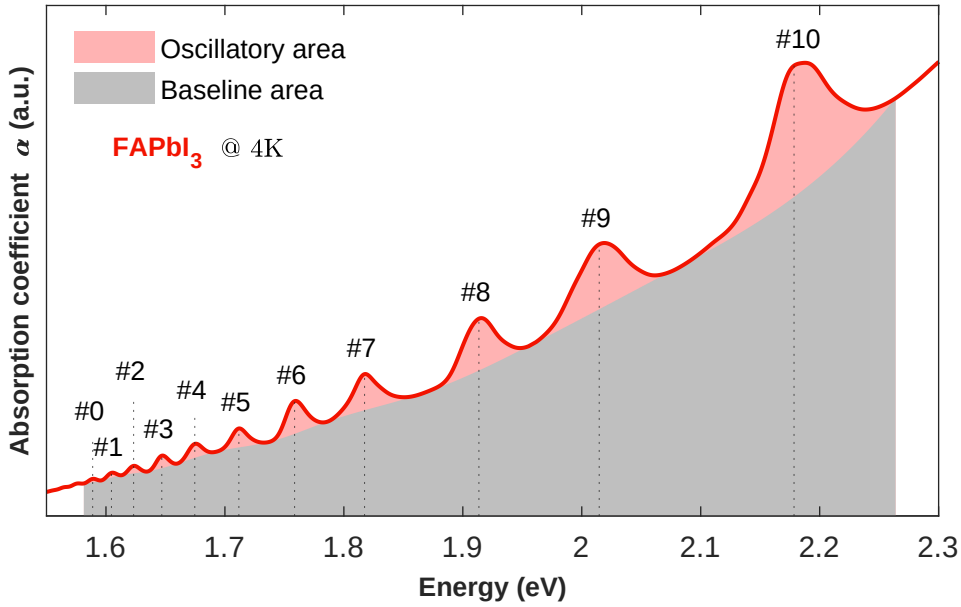


Figure 3.2: An absorption coefficient spectrum of $FAPbI_3$ with definitions of terms used in the analysis. Absorption coefficient spectrum of a $FAPbI_3$ film. The spectral area under the spline baseline (grey-shaded area) and spectral area between the measured absorption coefficient and spline baseline (pink-shaded area) - termed the peak area, used to calculate the percentage of spectral area under the peaks. The relevance of the spectral area under the peaks compared to the peak amplitude, is that it takes into account both the extracted amplitude and FWHM of the peaks, making it comparatively less susceptible to artificial changes caused by the narrowing and widening of the peaks as opposed to changes caused by the increase and decrease in strength of confinement. The peaks are identified by their peak index, with the lowest energy discernible peak labelled as peak #0.

in the spline baseline fit I used to decouple the peak features from the underlying absorption coefficient data.

It is worth noting that because the dimensionality of confinement has not been conclusively determined, the peak-decoupling procedure implemented in this study potentially eliminates any underlying density of state contributions that may be associated with the quantum confinement. For instance, for an infinite-quantum-well confinement in all three dimensions, the density of states will have peak-like behaviour similar to what I extract from the decoupling mechanism. Alternatively, for a one-dimensional or a two-dimensional electronic confinement, the density of states will have additional continuum states associated with the electronic free motion in the other non-confined dimensions, states that would be removed when using this decoupling mechanism and would result in the same peak-like features I observe. This makes an accurate estimate of the confinement dimensionality even more difficult.

In my quantitative analysis of the quantum confinement and behaviour of the peaks, I utilise the confinement energy and spectral area under the peaks. I define the confinement energy associated with a given peak as the Elliott fit-extracted band gap of the material subtracted from the peak energy position of the decoupled peak. Meanwhile, the spectral area under the peaks is defined as the spectral area between the experimental absorption coefficient data and baseline fit, stated as a percentage of the spectral area under my experimental data (integrated between the first and last detectable minima of the oscillatory peak features). An explanatory figure of the the parameters defined in this section and the algorithm for decoupling the peak features is displayed in Figure 3.2.

3.3 Photoluminescence spectroscopy

Photon emission from a semiconductor post photo-excitation is the reverse process of absorption, where all the induced transition can be reversed and the promoted charge carriers can be demoted back to their original states. Therefore, both steady-state and time-resolved photoluminescence measurements can be used in tandem with absorption measurements to gain deeper insights into the different charge-carrier recombination and relaxation mechanisms, into both the majority and dominant compositions or crystal phases in a semiconductor with heterogeneity, and estimate values for the optical band gap, trap densities, and Stokes shift. [19, 45]

3.3.1 Time-integrated experimental setup

Under steady-state conditions, the photoluminescence will be dominated by the lowest-energy radiative transition available for the charge carriers after they thermalize and cool to that lowest-energy available state. Therefore, this technique is important for the evaluation of the optical bandgap, and for gauging the phase purity of a semiconductor and the contextualisation of its trap densities. For example, a direct semiconductor with minimal traps lying within its bandgap, will have its PL dominated by band edge recombination, corresponding to its bandgap. While a trap density-heavy semiconductor with optically allowed transition, will have its PL dominated by the lowest-energy available trap state within its bandgap. Alternatively, for a mixed phase semiconductor (e.g. a metal mixed-halide perovskite, or a quasi 2-dimensional perovskite film), charge carriers will funnel into the lowest-energy phase of this complex heterogeneous film and dominate the PL emission. [23]

For all time-integrated PL measurements, a 398 nm diode laser (PicoHarp, LDH-D-C-405M) was used to photo-excite the samples, on a continuous wave setting at a chosen intensity. The resultant steady-state PL was collected and coupled into a

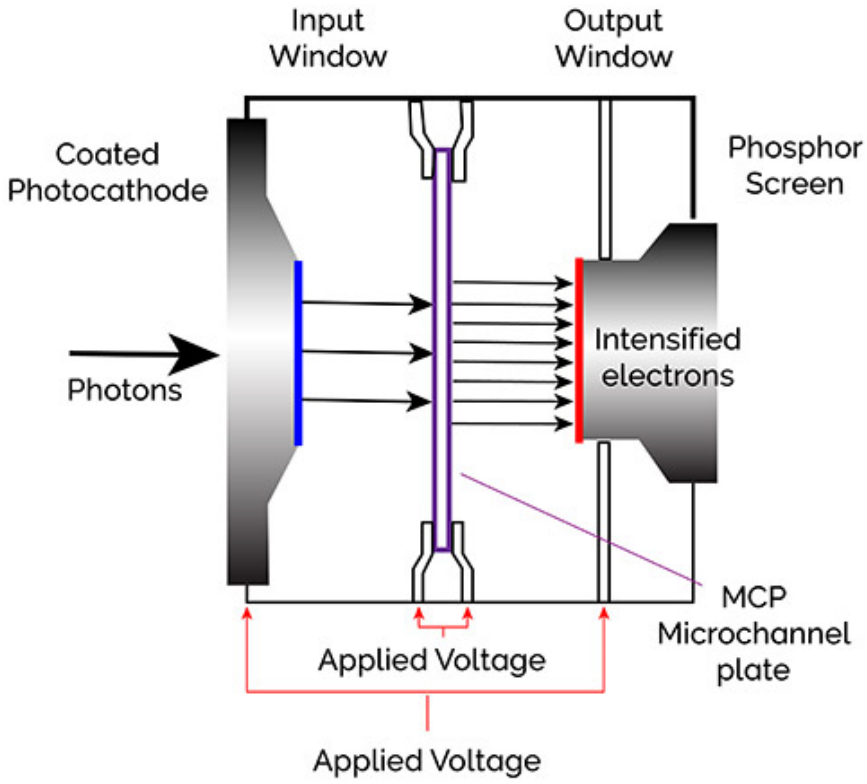


Figure 3.3: Operation of an intensified charge coupled device (iCCD). The intensifier in an iCCD works by first converting the collected photons from a sample into electrons, which are then either accelerated into a microchannel plate (MCP) or diverted away from the MCP using an applied voltage which effectively act as a shutter. Secondary electrons are generated through collisions within the MCP, which are then directed towards a fluorescent screen in order to convert the electrons back into photons, resulting in a substantial increase in the light sensitivity of the the entire iCCD. Figure is taken from [55].

grating spectrometer (Princeton Instruments, SP-2558), which directed the spectrally dispersed PL onto a silicon iCCD (intensified charge coupled device, PI-MAX4, Princeton Instruments). The iCCD is essentially an intensifier, which amplifies the light signal in front of a regular CCD. The intensifier consists of a photocathode that converts incoming photons into photo-electrons, an electric field which can either accelerate or block the photo-electrons from reaching the next component - effectively acting as a shutter, a microchannel plate (MCP) with an applied voltage that causes the generation of secondary electrons through collisions within its walls, and a fluorescent (phosphor) screen that reconverts all the electrons into photons. The emerging photons from the intensifier are then coupled by an optical fibre onto a regular CCD for detection. The setup in this configuration allows for the acquisition of spectrally and temporally resolved PL spectra from weakly luminescent samples. The time resolution of the setup will be determined by the time and duration of the accelerating electric field between the photocathode and the MCP, while the presence of an intensifier allows for high light sensitivity. [55] A schematic of the iCCD setup is shown in Figure 3.3.

The samples were always mounted in a vacuum cell under low pressure ($\sim 10^{-2}$ mbar).

3.3.2 Time-resolved (TR) experimental setup

This technique allows for the measurement of the temporal evolution of the intensity and the spectral shape of the photoluminescence spectrum. This allows for the study of charge-carrier dynamics for the determination of the dominant relaxation and recombination pathway, and allows for the resolution of the different structural and compositional phases present in a heterogeneous material. This is therefore naturally a very useful technique for measurements of mixed-phase films (whether they are quasi-2-dimensional films with different dimensionality phases, or films with compositional variation within the film with distinct bandgaps)

Time resolved photoluminescence (depending on the achievable time-resolution of the experimental setup) can provide valuable insights by probing the fast relaxation processes that charge carriers experience post photo-excitation. For example, immediately post photo-excitation, the charge carrier population will thermalize (where their energetic population density (density of states) matches a Maxwell-Boltzmann's distribution for a given temperature, achieved by carrier-carrier scattering), followed by charge-carrier cooling (where the temperature of the hot charge-carrier gas cools down and equilibrates with the lattice temperature, achieved by electron-phonon scattering). This is in turn followed by charge-carrier relaxation to the band edge or to the lowest-energy trap states within the bandgap. [13, 17] After these relaxation mechanisms, radiative recombination typically starts to compete with other recombination and relaxation mechanisms.

Some quantitative analysis can additionally be carried out on the measured PL transients to gain deeper insights on the charge-carrier dynamics based on Equation 3.8.

$$\frac{dn}{dt} = -k_1 n - k_2 n^2 - k_3 n^3. \tag{3.8}$$

In this thesis, TR-PL measurements are usually carried out under low laser excitation fluences resulting in a comparatively low charge-carrier density to be present within the film, which allows for the disregard of the bimolecular and Auger recombination terms while still accurately reflecting the recombination process which will be dominated by the trap-mediated recombination mechanism. [49, 56]

Charge-carrier lifetimes (τ), and diffusion lengths (L_D) are both essential in determining the quality of transport within a semiconductor. Both these quantities can be determined by measuring the temporal evolution of the PL spectrum and analysing the measured traces with the competing recombination pathways explained in Equation 2.11. The diffusion lengths is essentially the average distance a charge-carrier travels by diffusion before recombination occurs, and is characterised by Equation 3.9. Crucially,

the diffusion length is required to be larger than the penetration depths of the incident illumination to have efficient charge extraction. [9, 57]

$$L_D = \sqrt{D\tau} = \sqrt{\frac{D}{R_R}}\,; \qquad D = \frac{\mu K_B T}{e}, \tag{3.9}$$

Where D is the diffusion coefficient for the charge-carrier dynamics in the absence of an external electric field.

However, a fixed monoexponenetial decay rate is insufficient to fully encapsulate all the nuances of trap-mediated recombination within a metal-halide perovskite. Therefore, I use a stretched exponential function to fit the PL transients, mathematically described as follows:

$$I = I_0 e^{\left(\frac{t}{\tau_{\text{char}}}\right)^{\beta}}, \tag{3.10}$$

where I is the PL signal, τ_{char} is the characteristic lifetime corresponding to the time taken for the PL intensity to drop to I_0/e, and β is the distribution coefficient used to account for the higher-order recombination still present in the film, the time-dependent nature of the available trap density (as traps get filled and emptied over time, and as charge carriers diffuse and spread across the film), and the local distribution of different k_1 recombination rates (inhoomogeneously distribution of trap densities). [58, 59] The effective lifetime can therefore be written as follows:

$$\tau_{\text{eff}} = \frac{\tau_{\text{char}}}{\beta} \cdot \Gamma\left(\frac{1}{\beta}\right), \tag{3.11}$$

where Γ is the Gamma function defined such that $\Gamma(n) = (n-1)!$. The PL signal originates from radiative electron-hole recombination ($I \propto K_2 n^2$). Therefore, by combining Equations 3.8 and 3.10, the k_1 recombination rate can be assumed to be $k_1 = 1/(2\tau_{\text{eff}})$. [60, 61]

For all time-resolved PL measurements, time-correlated single photon counting (TCSPC) experiments were carried out following excitation by a 398 nm picosecond pulsed diode laser at a chosen fluence and repetition rate (PicoHarp, LDH-D-C-405M), chosen to avoid 'pile up' and 'wrap around' (when there is not enough time for the PL signal to die down before an upcoming excitation pulse) respectively. The resultant transient PL was collected and coupled into a grating spectrometer (Princeton Instruments, SP-2558), which directed the spectrally dispersed PL onto a photon-counting detector (PDM series from MPD), whose timing was controlled with a PicoHarp300 TCSPC event timer.

The signal obtained from a TCSPC measurement solely relies on the time duration for a single photon to reach the detector per laser excitation. This is achieved by splitting an electrical signal into two different parts. The first is used to trigger the laser pulse to photo-excite the sample, while the second is used to trigger a linear voltage ramp up with time. Subsequently, once a photon is emitted from the sample and directed onto an MCP, a photomultiplier tube (PMT), or a single photon avalanche diode (SPAD) detector, it can be detected and is used to stop the voltage ramp up. The produced voltage is proportional to the time delay and can be used to reconstruct a histogram of photon arrival times reflective of the true PL transient. [62] Importantly, TCSPC relies on detecting at most a single photon per excitation pulse. Therefore, for non-attenuated PL when multiple photons are being emitted per excitation pulse, the reconstructed photon time distribution will be biased towards shorter photon arrival times and will be artificially creating shorter PL transients (known as 'pile up'). The temporal resolution of the TCSPC is set by the instrument response function (IRF).

The PL transients were recorded at chosen wavelengths to probe a specific spectral range reflective of the charge-carrier dynamics corresponding to the relaxation mechanisms being studied.

3.4 Terahertz (THz) spectroscopy

THz radiation refers to the radiation in the frequency range between 100 GHz and 20 THz, and that radiation interacts strongly with free mobile charge carriers and lattice phonon modes in an investigated semiconductor. These measurements are extremely non-invasive and are optically gated resulting in the ability to obtain photo-induced conductivity measurements with high temporal resolution. All this make this technique ideal for investigating the frequency dependence of the absorption, dielectric function, and photoconductivity of the material.

3.4.1 Optical-pump terahertz-probe (OPTP)

The photo-induced conductivity ($\Delta\sigma$) of a semiconductor can be measured by first using an optical pump to photo-excite the semiconductor followed by THz probing radiation directed at the sample after a well-defined time delay. By measuring the relative change in the transmission of the THz field at different delay times from the optical pump pulse, I am able to non-invasively probe the local dielectric response of the semiconductor (the strength and frequency of the generated THz radiation determine the investigated spatial range, which corresponds to ~ 10 nm in this thesis), investigate the local charge-carrier dynamics and quantify the effective sum mobilities and bimolecular recombination rates of the photo-generated charge carriers at THz frequencies on the timescale of a couple of nanoseconds, with a temporal resolution of a few hundred femtoseconds. [63–66]

The time resolution possible in this experiment is primarily due to the very short laser pulses of the pump and gate beams of ~ 25 fs, used to optically excite the sample and for detection respectively. For detection of radiation in the THz range, electro-optical sampling techniques are used. This can be achieved by directing the THz field transmitted through the sample onto an electro-optic medium, so that it can induce a birefringence that is proportional to the strength of the THz field. Accordingly, the variation in the

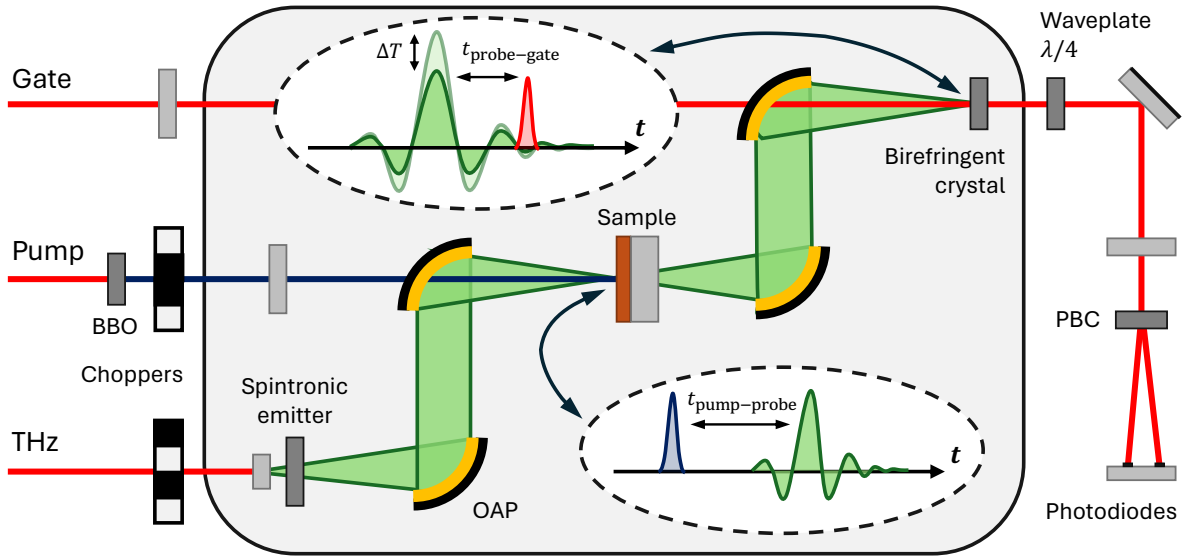


Figure 3.4: A schematic of the geometry of an optical-pump terahertz-probe (OPTP) experiment. A beta barium borate (BBO) crystal is used to double the frequency of the ultra-fast 800 nm laser pulse to obtain a similarly ultra fast optical pump beam (of $\sim$ 25 fs at 400 nm), which is used to photo-excite a semiconducting sample. After a controlled time-delay of $t_{\text{pump-probe}}$, a terahertz (THz) probing beam is directed on the sample to probe the photo-induced conductivity response of the sample. The THz beam is generated by shining an ultra fast 800 nm pulse at a spintronic emitter. [63, 64]. The transmitted THz can then be detected using electro-optical sampling in a birefringent crystal by overlapping the probe beam with an ultra-fast gate beam (of $\sim$ 25 fs) after another controlled time delay of $t_{\text{probe-gate}}$. The gate beam then passes through a quarter waveplate ("Waveplate $\lambda/4$") and a polarising beam cube (PBC) to split the gate beam into 2 photodiodes which can be measured. By doing so, I am able to measure different parts of the transmitted THz signal and construct both the temporal evolution of the photoconductiivty response and retain the spectral information of the THz pulse.

birefringence of the medium, and by association the strength of the transmitted THz field, can be entirely mapped and quantified by directing an optical beam onto the detection crystal (labelled gate beam) and measuring the degree of polarization rotation of that gate pulse using simple optical elements. [63–66] A schematic of the experimental setup and detection procedure are illustrated in Figure 3.4.

The duration of the gate pulse is much shorter than the expanded THz pulse, therefore, by changing the time delay between the THz and gate pulses ($t_{\text{probe-gate}}$) at the detection crystal, the entire THz pulse can be mapped. This implies that to obtain maximal signal during OPTP measurements, $t_{\text{probe-gate}}$ can be fixed such that the detection at the electro-optic medium is at the peak of the THz pulse ($t_{\text{probe-gate}} = 0$). At the peak of the THz pulse, the measured relative change in THz electric field transmission ($(\Delta T/T)$) is directly proportional to the photo-induced sheet conductivity ($\Delta S = (\Delta\sigma/d)$) of films whose thickness (d) is much smaller the THz wavelengths (λ_{THz}) used to probe the material's conductivity. This relationship is represented by:

$$\Delta S = -\epsilon_0 c\,(n_a + n_b)\,\frac{\Delta T\,(t_{\text{probe-gate}} = 0)}{T}, \tag{3.12}$$

where $\epsilon_0 c$ is the invert of the vacuum impedence, and n_a and n_b are the refractive indices of the mediums surrounding the sample (Vacuum and the substrate). The temporal evolution of this photo-induced sheet conductivity (ΔS) can then be mapped by controlling the time delay between the pump and probe pulses ($t_{\text{pump-probe}}$).

The THz conductivity signal will primarily be a result of either absorption by free charge carriers (as the charge-neutral and non-conductive excitons will not couple to THz radiation) or resonant coupling to lattice phonon modes (which can be ignored in photoconductivity experiments as no change will occur upon photo-excitation). Therefore, the intrinsic sum mobility of the free charge carriers (μ) can be extracted from OPTP

measurements by using the linear relationship described in Equation 3.13, which usually only holds for low charge-carrier densities and laser fluences $< 50\,\mu\mathrm{J/cm^2}$.

$$\mu = \frac{\Delta S\left(t_{\text{pump-probe}}\right) A_{\text{eff}}}{N\left(t_{\text{pump-probe}}\right) e}, \tag{3.13}$$

where A_{eff} is the effective area of overlap between the optical pump and THz probe, and N is the number of photo-generated free charge carriers. Thus, by focusing on the initial ΔS signal, which reflects charge-carrier dynamics closely after photo-generation ($t_{\text{pump-probe}} = 0$), N will then represent the total number of photo-generated charge carriers immediately post excitation, which can be calculated using:

$$N_0 = \Phi \frac{E\lambda}{hc}\left(1 - R_{\text{pump}} - T_{\text{pump}}\right), \tag{3.14}$$

where Φ is the branching ratio of free charge carriers to photons absorbed, $(1 - R_{\text{pump}} - T_{\text{pump}})$ is the fraction of the pump pulse absorbed by the sample, $\frac{hc}{\lambda}$ and E are the photon and pulse energy of the pump beam, such that $\frac{E\lambda}{hc} = N_{\text{photon}}$ is the number of photons in a pump pulse.

Subsequently, the effective intrinsic sum mobility of the photo-generated free electrons and holes ($\Phi\mu$), which reflects the true sum mobility when the photons absorbed are fully converted to free charge carriers ($\Phi = 1$), can be expressed by combining Equations 3.12, 3.13, and 3.14.

$$\Phi\mu = -\epsilon_0 c\left(n_a + n_b\right) \cdot \frac{A_{\text{eff}} hc}{Ee\lambda\left(1 - R_{\text{pump}} - T_{\text{pump}}\right)} \cdot \frac{\Delta T\left(t_{\text{probe-gate}}, t_{\text{pump-probe}} = 0\right)}{T}. \tag{3.15}$$

In the presence of an electric field, this effective sum mobility becomes the most important parameter to study for an accurate assessment of charge-carrier transport abilities. However, this can be supported by evaluating an estimate for the diffusion coefficient and the diffusion length within the semiconductor based on Equation 3.9 to obtain a clearer and full picture of its optoelectronic properties.

As a result of obtaining the decay transients of the photo-induced sheet conductivity, the temporal evolution of the free charge carriers within the semiconductor can be mapped, the charge-carrier dynamics can be fitted, and values for the recombination rate constants can be extracted as described in Equation 3.8 and in more details in Section2.1.4. The absorbed photon density is based on Equation 3.14 and given by:

$$\tilde{n}_0 = \frac{E\lambda}{hcdA_{\text{eff}}}(1 - R_{\text{pump}} - T_{\text{pump}}). \tag{3.16}$$

Therefore, the direct proportionality between charge-carrier density and photo-induced sheet conductivity (shown in Equation 3.13) can be extended in combination with Equations 3.8 and 3.16 to describe the temporal evolution of the photo-induced sheet conductivity in terms of the recombination rate constants as follows:

$$\frac{d\left(\Delta S\right)}{dt} = -k_1\left(\Delta S\right) - \Phi k_2 \cdot C\left(\Delta S\right)^2 - \Phi^2 k_3 \cdot C^2\left(\Delta S\right)^3, \tag{3.17}$$

where C is the proportionality constant given as $\tilde{n}_o \,/\, (\Delta S_0)$. [63–66]

3.5 X-ray diffraction

X-ray diffraction experiments are typically used to determine the different crystallographic phases within a material, the overall crystalline quality of the material, and possibly determine the orientation and size of the crystallites of the investigated phase. [67]

3.5.1 Theory

X-ray diffraction patterns emerge when a constructive interference of the X-rays can be formed from interactions with the lattice planes of the crystal structure, as illustrated in Figure 3.5, A constructive interference pattern will only emerge when the difference in path lengths for X-rays scattering of a set of parallel lattice planes is an integer multiple of the wavelength of the incident X-rays. This diffraction condition (Bragg condition) is represented by the Bragg equation shown below:

$$n\lambda = 2d\sin(2\theta), \tag{3.18}$$

where n is an integer, λ is the wavelength of the X-ray radiation, d is the lattice plane spacing, and 2θ is the deflection angle of the incident beam. [13, 67] This allows for the crystalline quality of the material, and its crystallographic purity to be assessed by measuring the material's X-ray diffraction patterns to detect and quantify any lattice distortions, expansions or contractions.

In the XRD patterns, each observed diffraction peak corresponds to a family of lattice planes (reflective of a certain periodicity within the crystal lattice) that is defined by a set of miller indices (hkl). The family of lattice planes are those orthogonal to the reciprocal lattice vector $\boldsymbol{g}$ defined as $h\boldsymbol{b_1} + k\boldsymbol{b_2} + l\boldsymbol{b_3}$, where $(\boldsymbol{b_1}\boldsymbol{b_2}\boldsymbol{b_3})$ are the primitive reciprocal lattice vectors. Alternatively, these planes can be defined as those which intersect the borders of the unit cell at a_1/h, a_2/k, and a_3/l, where $(\boldsymbol{a_1}\boldsymbol{a_2}\boldsymbol{a_3})$ are the primitive lattice vectors.

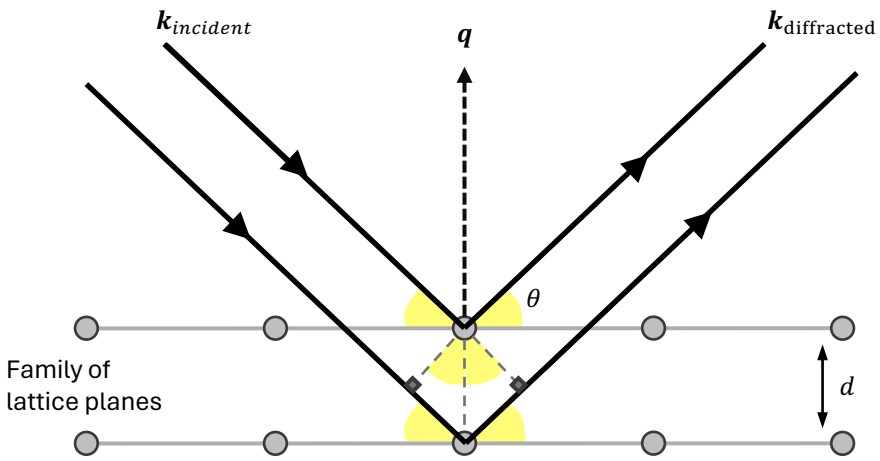


Figure 3.5: A schematic of X-ray diffraction in a crystal lattice. 2θ represents the deflection angle of the incident X-rays, d is the lattice spacing for the family of lattice planes responsible for the diffraction, $\boldsymbol{q}$ is the reciprocal lattice vector of that familly of lattice planes and $\boldsymbol{k}_{\text{incident}}$ and $\boldsymbol{k}_{\text{incident}}$ are the wavevectors of the incident and diffracted X-rays respectively.

A pollycrystalline film, like most 3-dimensional metal-halide perovskite films, will have no preferential growth orientation and will therefore possess all possible orientations of each family of lattice planes. Therefore, by association the reciprocal lattice vector of that set of lattice planes will be pointing in all the possible directions, resulting in a uniform ring-like XRD pattern. This implies that the measurement of a simpler 1-dimensional XRD diffraction pattern would encapsulate all the relevant crystallographic information for such a pollycrystalline film. This can be obtained by moving the X-ray source and detector to change the 2θ angle, while rotating the sample to ensure all orientation were accounted for and measured.

Unlike the pollycrystalline films, a lower-dimensional film with strong preferential growth orientation - by definition, will not accommodate all orientations of a family of lattice planes, and the reciprocal lattice vector of that set of lattice planes will have preferential directions. Therefore, to conserve momentum ($\boldsymbol{k}_{\text{incident}} = \boldsymbol{g} + \boldsymbol{k}_{\text{diffracted}}$) and to reflect that preferential orientation, the emerging XRD patterns will form sharp localised points instead of uniform rings. This necessitates 2-dimensional XRD detection for any highly-ordered film in order to retain the orientation information. [67]

To obtain quantitative values from the XRD patterns, the XRD peaks corresponding to the crystalline phase being investigated was fitted with a pseudo-voigt function [68] to extract the peak position and full widths at half maximum (FWHM) of the relevant peaks.

3.5.2 Experimental setup

The 1-dimensional XRD patterns throughout this thesis were measured in air using a Panalytical X'pert powder diffractometer with a copper X-ray source (Cu-Kα X-rays with a wavelength of 1.5418 Å). The XRD patterns were then corrected for tilt by shifting the 2θ-axis, such that the refrence peaks of the substrate used matched the expected

literature values. The main z-cut quartz reference peak is centered at $2\theta = 16.433°$, while the main sapphire reference peak is centered at $2\theta = 20.553°$.

The 2-dimensional XRD patterns were measured using a Rigaku Smartlab X-ray diffractometer using the Cu-Kα X-ray source and a HyPix-3000 2D X-ray detector in a Bragg-Brentano reflection geometry. For these measurements, the incidence angle of the X-rays is comparatively low to have a smaller penetration (probing) depth, and to increase the sensitivity of this experiment to the structural properties of the surface of the film, lending the experiment its name of 'grazing incidence wide angle X-ray scattering' (GIWAXS).

4

Control of intrinsic quantum confinement in formamidinium lead triiodide

Contents

4.1 Motivation 65
4.2 Results and discussion 68
4.2.1 Cesium incorporation into the crystal structure 68
4.2.2 Effect of cesium incorporation on quantum confinement 76
Absorption spectrum 76
4.2.3 Photoluminescence spectrum 87
Photon reabsorption and recycling events 90
PL Confinement energy 93
Charge-carrier dynamics with quantum confinement 96
4.3 Conclusion 100

In this chapter, I investigate the possible control of the intrinsic quantum confinement present in the formamidinium lead triiodide ($FAPbI_3$) perovskite composition. As explained in Chapter 2.2.3, the $FAPbI_3$ composition has a tendency to self-assemble and form quantum confined domains, apparent through above-bandgap oscillatory features in that composition's absorption spectrum. Here, I show that such nanoscale electronic effects can indeed be controlled through the partial replacement of the formamidinium

(FA^+) cation with cesium (Cs^+). I find that the Cs^+-cation exchange causes a weakening of the quantum confinement in $FAPbI_3$, arising from changes in the bandstructure, the length scale of confinement, or the presence of δ_H electronic barriers (or similar polymorphs that can act as potential barriers). I further observe photon emission from quantum-confined regions, highlighting their potential usefulness to light-emitting devices and single-photon sources. Importantly, this demonstrates the importance of perfecting control over the quantum confinement for either its suppression or enhancement according to need and future application.

The work presented in this chapter has been published in: **Elmestekawy, K.A.**, Wright, A.D., Lohmann, K.B., Borchert, J., Johnston, M.B., and Herz, L.M. 'Controlling Intrinsic Quantum Confinement in Formamidinium Lead Triiodide Perovskite through Cs Substitution', *ACS Nano*, **16(6)**, *9640–9650* (2022) (Ref. [41]).

4.1 Motivation

Metal halide perovskites have emerged as promising materials for photovoltaic cells with reported power conversion efficiencies (PCE) of single-junction cells improving from an initially reported 3.8%, [69] to over 26%, [6, 70] in just over a decade. Their excellent properties include high charge-carrier mobilities, [71] long diffusion lengths, [57, 72] low exciton binding energies, [16] broadly tunable absorption spectrum, [73] and facile fabrication. [74] In addition, promising light-emitting [75–79] and lasing applications [80–82] are rapidly emerging. In this context, perovskites with lowered electronic dimensionality are increasingly of interest, including two-dimensional perovskites [27, 49, 83, 84] and perovskite nanocrystals and quantum dots. [38, 78, 85–87] Such nanostructured materials tend to exhibit electronic properties substantially different from those of their three-dimensional counterparts, including altered emission color and bandwidth, [38, 86] improved photoluminescence quantum yield (PLQY), [88] more easily-achievable population inversion, [80–82] and photon recycling. [27, 87]. However, a major drawback is that nanostructured materials usually have additional complexities associated with their fabrication, [89] making facile new fabrication methods a highly-sought after goal.

One promising route to the facile generation of nanostructured domains is through the use of formamidinium lead triiodide ($FAPbI_3$), which has recently been shown to exhibit intrinsic electronic quantum confinement in a small subset of the volume of nominally bulk thin films. [40] This surprising property manifests through sharp above-bandgap features superimposed on the bulk absorbance spectra of $FAPbI_3$ films, which can be discerned in many published spectra, [9, 29, 90, 91] but had until recently gone unnoticed and unexplained. A recent report [40] provided experimental evidence and theoretical simulations to demonstrate that these sharp absorption features arise from intrinsic quantum confinement on the length scale of $\sim$10 nm occurring in sub-volumes of

nominally bulk $FAPbI_3$ films. However, the usefulness of intrinsic electronic confinement in $FAPbI_3$ will depend critically on the targeted application. On the one hand, $FAPbI_3$ in its three-dimensional cubic room-temperature phase (termed α-phase) is particularly well-suited for single-junction PV applications, with its bandgap of 1.55 eV close to the optimal theoretical value for monojunctions, [92] and PCEs achieving a record value of 26.2% for cells based on $FAPbI_3$. [6, 7, 70, 93, 94] For such photovoltaic applications, confinement domains exhibiting barriers to charge motion will to some extent hinder the passage of photocurrent through the bulk and towards charge-extraction layers, lowering efficiencies. On the other hand, intrinsic quantum confinement may allow for facile fabrication of efficient light-emitting devices, if emission from such domains can be observed. With targeted fabrication and processing, such as strain engineering, this system thus offers the possibility of self-assembled quantum-confined states being readily formed without the need for a cumbersome fabrication process, making it an intriguing candidate for light-emitting diodes, lasers and displays, and single photon emitters for use in quantum computing. [80–82, 95, 96]

The above considerations show that control over intrinsic quantum confinement in $FAPbI_3$ films is critical to its successful implementation in specific applications. Here in this chapter, I attempt such control through partial substitution of the FA cation with the much smaller Cs cation, because it has recently been postulated the the origin of intrinsic quantum confinement in $FAPbI_3$ could derive from the presence of trace amounts of the hexagonal non-perovskite δ_H-phase of $FAPbI_3$. [40] Since the δ_H-phase in its bulk form has an electronic bandgap near 2.3 eV, its presence even as thin layers will represent barriers to electronic motion through the black $FAPbI_3$ perovskite α-phase, leading to charge-carriers experiencing electronic confinement in quantum wells or periodic superlattices. [40, 97] Replacement of FA with Cs has been shown to stabilize the otherwise meta-stable α-phase of $FAPbI_3$ [9, 98] against deterioration into the δ_H-$FAPbI_3$ phase, which is

the thermodynamically-favoured phase at room temperature. [33] In general, A-cation engineering of ABX_3 metal halide perovskites has proven highly effective at improving performance, improving structural stability, [99–102] crystallinity, [29] and suppressing phase transitions in the material. [71, 101] Specifically, the large size of the FA A-cation in $FAPbI_3$ proves detrimental to its structural stability, which alloying with the much smaller Cs-cation has been shown to remedy. [29–31] Therefore, alloying with Cs may not only eliminate large crystallites of δ_H-phase $FAPbI_3$, but also potentially be able to suppress the smaller remnant inclusions that act as the potential barriers which lead to intrinsic quantum confinement in $FAPbI_3$.

In this thesis chapter, control over the intrinsic quantum confinement in $FAPbI_3$ is successfully reported through the partial A-cation substitution of FA with Cs. I probe the presence of such nanoscale domains through their impact on the electronic structure, evident from features superimposed on the absorption and emission spectra of the otherwise bulk semiconductor. The alloying of FA with Cs is proposed to reduce quantum confinement owing to the interplay between changes in bandstructure and confinement length scale, and the removal of trace layers of the hexagonal δ_H-phase. I observe that Cs percentages, x, in excess of 40% are required for the complete removal of intrinsic quantum confinement effects in $FA_{1-x}Cs_xPbI_3$ – significantly higher than those commonly reported to suffice for structural stabilization of $FAPbI_3$ [29, 33, 103–106]. Furthermore, a series of emission peaks with photon energy significantly above the bulk bandgap in $FAPbI_3$ are reported, which I show to be associated with radiative recombination of intrinsically confined charge carriers. Overall, I demonstrate that the degree of intrinsic nanoscale confinement in $FA_{1-x}Cs_xPbI_3$ may thus be controlled through simple stoichiometric engineering rather than intensive nanoscale processing.

4.2 Results and discussion

4.2.1 Cesium incorporation into the crystal structure

Absorption spectra of solution-processed $FAPbI_3$ films reported in the literature often exhibit the peculiar absorption features being investigated in this study, [9, 101, 106–109] though this is not typically commented on. However, to ensure surface uniformity and controllable composition, I based my investigation on vapor-deposited $FAPbI_3$ films of 100-nm thickness in which the partial substitution of FA with Cs had been induced through a solution-based cation exchange. $FAPbI_3$ films were evaporated onto either quartz or sapphire substrates through thermal co-evaporation of FAI and PbI_2 (performed by Juliane Borchert and Kilian B. Lohmann), [110–112] and subsequently dipped for three seconds in IPA solutions of differing cesium acetate ($CsCH_3COO$) concentrations, following the procedure outlined by Jiang et al. [113] Two control films were used for this study; an undipped neat $FAPbI_3$ film, and one dipped in an IPA solution. Five other $FAPbI_3$ films were subject to A-cation exchange through dipping in IPA solutions of 0.2, 0.5, 1, 5 and 7.5 mg/mL $CsCH_3COO$ concentrations. Further details on the fabrication method of the thin films are described in Appendix A.1.

I begin by determining the extent to which Cs has replaced FA in the as-grown $FAPbI_3$ films as a result of dipping in $CsCH_3COO$ solution. Figure 4.1 shows the crystallographic effects of Cs incorporation on the full X-ray diffraction (XRD) patterns. The main crystallographic trend that can be observed is the shifting of the (100) and (200) cubic $FAPbI_3$ peaks towards higher 2θ angles with higher $CsCH_3COO$ concentrations, a trend that is indicative of a crystal lattice contraction in accordance with Cs^+ ions replacing the bulkier FA in the perovskite. [31] (Excerpts XRD patterns centering on the (200) cubic $FAPbI_3$ peak are displayed in Figure 4.3a)

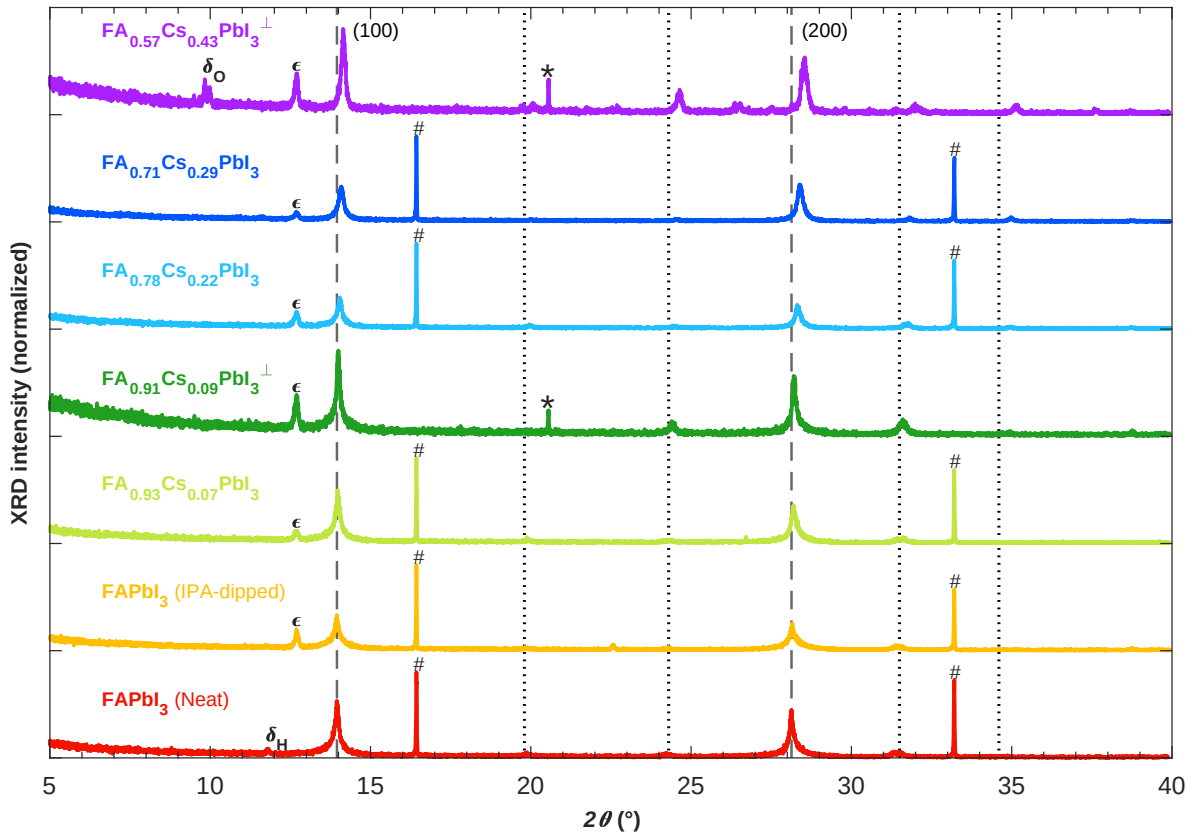


Figure 4.1: Full X-ray diffraction (XRD) pattern for the investigated $FA_{1-x}Cs_xPbI_3$ films. Substrate peaks are indexed with # and $*$ for quartz and sapphire substrates respectively. The main cubic (α) $FAPbI_3$ peaks ((100) and (200)) are represented by the vertical black dashed lines at the experimentally measured values of 14° and 28.2° respectively. The literature values [98] of the less prominent cubic α-$FAPbI_3$ peaks are indicated by vertical black dotted lines, at 2θ values of $19.8°, 24.3°, 31.5°$, and 34.6°. The PbI_2 peak can be seen for the films dipped in $CsCH_3COO$ IPA solution at 12.7°, and is indexed with ϵ. [114] The most prominent XRD peak for the non-perovskite δ_H-$FAPbI_3$ and δ_O-$CsPbI_3$ phases appear for the $FAPbI_3$ neat film and the film with highest Cs percentage at 11.8°, [98] and 9.9°, [98, 106, 114] respectively.

I utilize these crystallographic trends to determine the spatially-averaged incorporated Cs percentage by pursuing three different approaches which gave very similar results. In a previous study by Jiang et al. [113], which also introduced the fabrication procedure that I used, a linear relationship between the pseudo-cubic lattice parameter and Cs concentration within the film was extracted from the XRD patterns, X-ray fluorescence (XRF; which probes the bulk of the film) and X-ray photo-electron spectroscopy (XPS; which probes the surface of the film) measurements on similar films. Notably, the linear relationship between the lattice parameters and the Cs concentration obtained by Jiang et al. depends on the part of the film being probed. However this method of Cs incorporation through A-cation exchange leads to a certain non-uniformity and depth-dependence in the distribution of Cs content in these films as observed previously by Jiang et al. [113] and apparent from the broadening of the XRD peaks with increasing Cs content (see Figure 4.3a for XRD peaks and Figure A.2a for extracted values of peak widths). In this situation, the surface ultimately has a higher concentration of Cs as a result of more exposure to the cation exchange-inducing solution. As a consequence, the Cs concentration on the surface - probed by XPS measurements, and in the bulk - probed by XRF measurements, yields different linear relationships between Cs percentages and pseudo-cubic lattice parameter. I hereafter use the bulk linear relationship as the relationship that best represents the majority of the film and the approximate mean Cs concentration present throughout the film. In the first two approaches, I therefore calibrated the lattice parameters of the films used in this chapter to the linear relationship experimentally obtained by Jiang et al. [113]

In the first approach, I offset the measured XRD 2θ values of the films such that the (200) peak of the neat $FAPbI_3$ film measured in this chapter was aligned with the experimental (200) XRD peak of the $FAPbI_3$ film measured in the study by Jiang et al. [113] Subsequently, their linear relationship was directly applied to my calculated lattice parameters to obtain approximate Cs concentrations (the results of this method

are denoted "XRD offset", and displayed in Figure 4.2a). In the second approach, I attempted a physically more plausible method, in which the XRD patterns were only shifted such that the reference quartz and sapphire peaks matched their literature values. In this method, I directly calculated the lattice parameters from the measured XRD patterns, and offset the linear relationship obtained from Jiang et al. [113], such that it would estimate zero incorporation of Cs into the lattice for the lattice parameter value of the neat $FAPbI_3$ film used in this chapter (the results of this method are denoted "Fit offset", and displayed in Figure 4.2b). For the third approach, I implemented Vegard's law, which is a heuristic method that expects the pseudo-cubic lattice parameter of a solid solution to be the weighted mean of the lattice parameter of its constituents (the results of which are displayed in Figure 4.2c). The reference end points for this estimation were my measured pseudo-cubic lattice parameter for neat $FAPbI_3$ (of 6.339 Å), and the literature-extracted pseudo-cubic lattice parameter for $CsPbI_3$ (of 6.153 Å). [113, 115, 116]

The extracted spatially-averaged Cs concentration from all three methods is reassuringly similar and are presented in Table 4.1. Based on these findings, I determine here that the $FAPbI_3$ films dipped in IPA solutions of $CsCH_3COO$ of concentrations 0.2, 0.5, 1, 5, and 7.5 mg/mL resulted in $FA_{1-x}Cs_xPbI_3$ films with spatially-averaged 7%, 9%, 22%, 29%, and 43% Cs content.

I note that the δ_H-phase of $FAPbI_3$ is not particularly apparent in the patterns for all films except for the neat (undipped) $FAPbI_3$ film. XRD patterns magnified around the typical (100) peak of the δ_H-phase of $FAPbI_3$ at $2\theta = 11.8°$, [98] (see Figure A.1) show little diffraction signal, which is consistent with any incorporated electronic barriers arising from δ_H-phase inclusions being relatively thin, as had previously been postulated. [40]

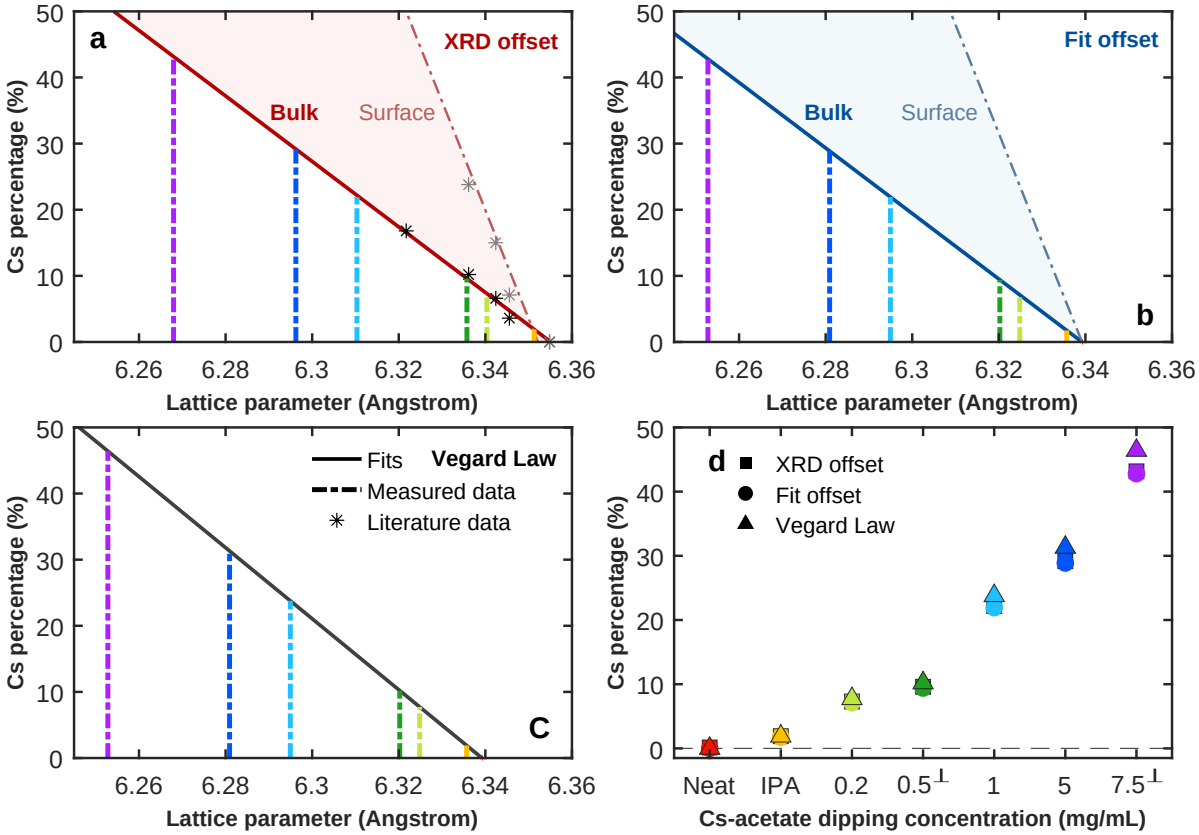


Figure 4.2: Extraction and calibration of Cs percentages in Cs-acetate dipped $FA_{1-x}Cs_xPbI_3$ films. (**a**) and (**b**) show the calibration method used to extract rough estimates for the Cs concentration of the films used in this study by either **a**: aligning the XRD patterns such that the pattern of the neat $FAPbI_3$ film matches that of the literature values, or **b**: offsetting the linear relationship between Cs concentration pseudo-cubic lattice parameter, to give the correct estimate for the $FAPbI_3$ film (0% Cs). The solid lines represent the extracted linear relationship between the pseudo-cubic lattice parameter and measured Cs content from Jiang et al. [113] both for the bulk and the surface, while the dashed lines correspond to the lattice parameter values calculated for the films used in this chapter. (**c**) shows the Cs concentration estimates from Vegard's law. The reference end points for this heuristic estimation were my measured pseudo-cubic lattice parameter for neat $FAPbI_3$ (of 6.339 Å), and the literature-extracted pseudo-cubic lattice parameter for $CsPbI_3$ (of 6.153 Å). [113, 115, 116] (The legend in (**c**) also applies to (**a**), and (**b**)). (**d**) shows the extracted Cs concentration from each of these different methods. (Films are evaporated on quartz or sapphire (indicated by $^{\perp}$) substrates).

Cs-acetate concentration	XRD (200)	Lattice parameter	Cs XRD Offset	Cs Fit Offset	Cs Vegard
Neat	28.13°	6.339 Å	0%	**0%**	0%
IPA-dipped	28.15°	6.336 Å	0%	**0%**	0%
0.2 mg/mL	28.20°	6.325 Å	7.3%	**7.1%**	7.7%
0.5 mg/mL$^{\perp}$	28.22°	6.320 Å	9.6%	**9.4%**	10.2%
1 mg/mL	28.33°	6.295 Å	22.2%	**21.9%**	23.8%
5 mg/mL	28.40°	6.281 Å	29.2%	**28.9%**	31.3%
7.5 mg/mL$^{\perp}$	28.53°	6.253 Å	43.2%	**42.8%**	46.4%

Table 4.1: Parameters extracted from XRD patterns of $FA_{1-x}Cs_xPbI_3$ films. The (200) XRD 2θ peak position and corresponding calculated pseudo-cubic lattice parameter for films dipped in IPA solutions with differing Cs-acetate concentrations. The Cs concentration is extracted using either the XRD offset method, Fit offset method, or Vegard's law - as explained and discussed in Section A.2. (Films are evaporated on either quartz or sapphire (indicated by $^{\perp}$) substrates).

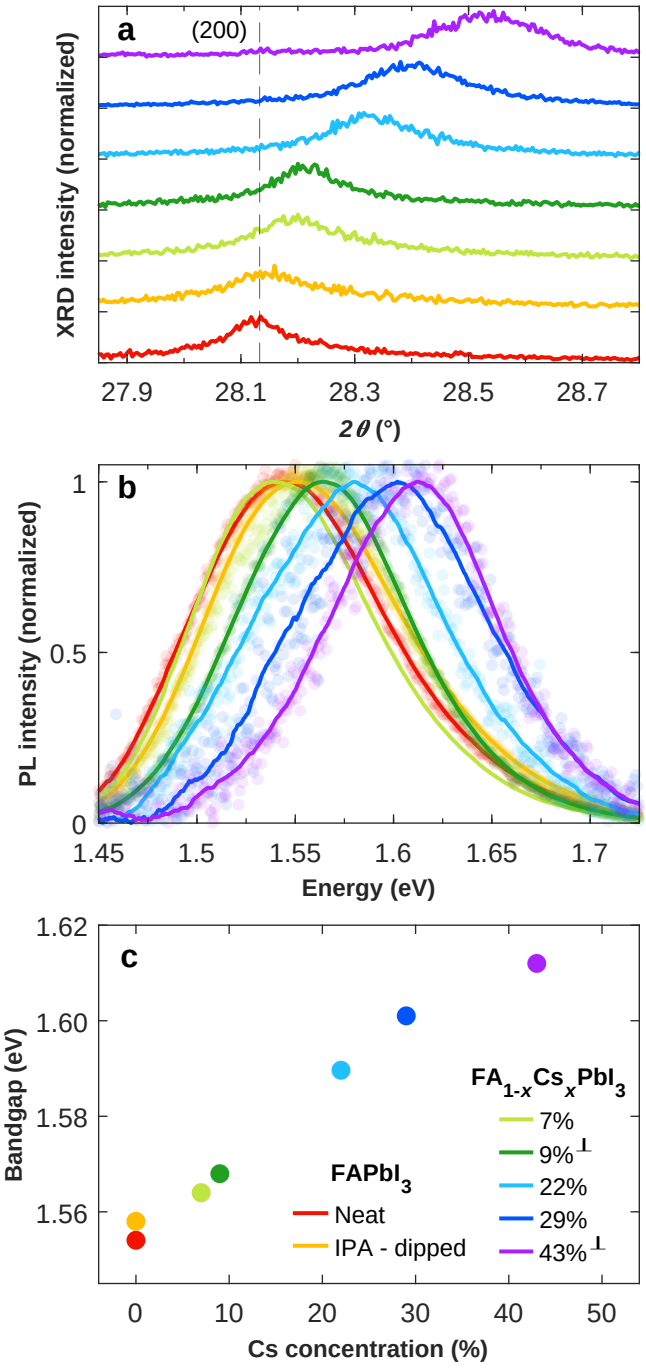


Figure 4.3: Structural and optical characterization of $FA_{1-x}Cs_xPbI_3$ films. **a**: Excerpts from recorded X-ray diffraction (XRD) patterns centring on the pseudo-cubic (200) peak of $FA_{1-x}Cs_xPbI_3$. The vertical dotted line represents the (200) peak position of the $FAPbI_3$ neat film. For visual clarity, the XRD patterns are successively vertically offset. **b**: Normalized, smoothed, room-temperature photoluminescence (PL) spectra of the $FA_{1-x}Cs_xPbI_3$ films represented by solid lines, while the raw data is represented by the scatter points. **c**: Relationship between the optical bandgap extracted from Elliott fits to the absorption onset and the Cs content x evaluated based on the XRD peak positions (as described in Figure 4.2). (The legend in (**c**), also applies to (**a**), and (**b**).)

Figure 4.3b, c show the rest of the effects of Cs incorporation on the photoluminescence (PL) spectra and bandgap determined from absorption onsets respectively. I note that since quantum confined domains in these films tend to occupy only a few percent of the total film volume, [40] the recorded spectra mostly reflect bulk $FA_{1-x}Cs_xPbI_3$ properties. The incorporation of Cs resulting from dipping of $FAPbI_3$ films in $CsCH_3COO$ solutions can also be evident in these measurements based on the the blue-shifts in the room-temperature PL spectra (Figure 4.3b) and the bandgap energies (Figure 4.3c) in accordance with general observations for $FA_{1-x}Cs_xPbI_3$ with increasing x. [9, 117] The bandgap values were determined through fitting of absorption coefficient onsets with Elliott theory, which accurately accounts for both the excitonic feature and Coulombic contribution to the absorption continuum. [52, 54] A simpler procedure based on commonly used Tauc fits [29, 30, 117] yields similar trends (see Figure A.6) but is somewhat less accurate, in particular for polycrystalline films. [53] I note that a direct determination of Cs content from optical spectra rather than XRD patterns is however cumbersome as the linear relationship generally expected to hold between the pseudo-cubic lattice parameters of a set of materials and their alloying fraction (Vegard's law) does not necessarily translate to a linear relationship for the electronic bandgap, as indeed we see in Figure 4.3c. Bandgap values relatively rarely relate to a weighted mean of their constituents' values leading to the well-know effect of "bandgap bowing", [117–119] which in the case of $FA_{1-x}Cs_xPbI_3$, may for example arise from significant ionic size mismatch between the FA^+ and Cs^+ ions inducing strain in the material. [71, 101, 106]

4.2.2 Effect of cesium incorporation on quantum confinement

Absorption spectrum

The absorption coefficient spectra of $FA_{1-x}Cs_xPbI_3$ films clearly reveal that the incorporation of Cs affects the prevalence of domains exhibiting quantum confinement. Figure 4.4 shows that the room-temperature absorption coefficient spectra display above-bandgap peak features whose prominence declines with increasing Cs content. To visualize these features more readily, they were decoupled from the spectrum using a phenomenological spline baseline connecting all the troughs of the features together, and subtracting this baseline to produce the plot in Figure 4.4b (full details of method provided in Appendix A.4.3). As Cs replaces FA, two trends are clearly apparent: the band-edge blue-shifts, as incorporation of the smaller Cs increases the bandgap (Figure 4.3), and the prominence and widths of the peak features gradually change until they effectively disappear for the $FA_{1-x}Cs_xPbI_3$ film containing 43% Cs. These observations therefore demonstrate conclusively that introducing Cs into the perovskite stoichiometry can reduce and control intrinsic quantum confinement.

I note that the almost-complete elimination of quantum confinement features for sufficiently high Cs content (43%) is also evident in the low temperature (4 K) absorption spectrum (see inset in Figure 4.4a, and Figure A.8 for decoupled peaks). This absence is particularly interesting because such features have previously been shown [40] to be enhanced with reduction in temperature (as also evident from Figure 4.4a). The determination of the absorption coefficient spectra and decoupled peaks across a range of different temperatures for the neat $FAPbI_3$ film, and $FA_{1-x}Cs_xPbI_3$ films with 22%, 29%, and 43% Cs (Figures A.7 and A.8 respectively) shows that this trend of enhanced features with lowered temperature clearly holds for a range of Cs contents. Such enhancement of quantum confinement at reduced temperature may arise from lattice contraction and subsequent reduction in confinement length scale, and a decrease in electron-phonon

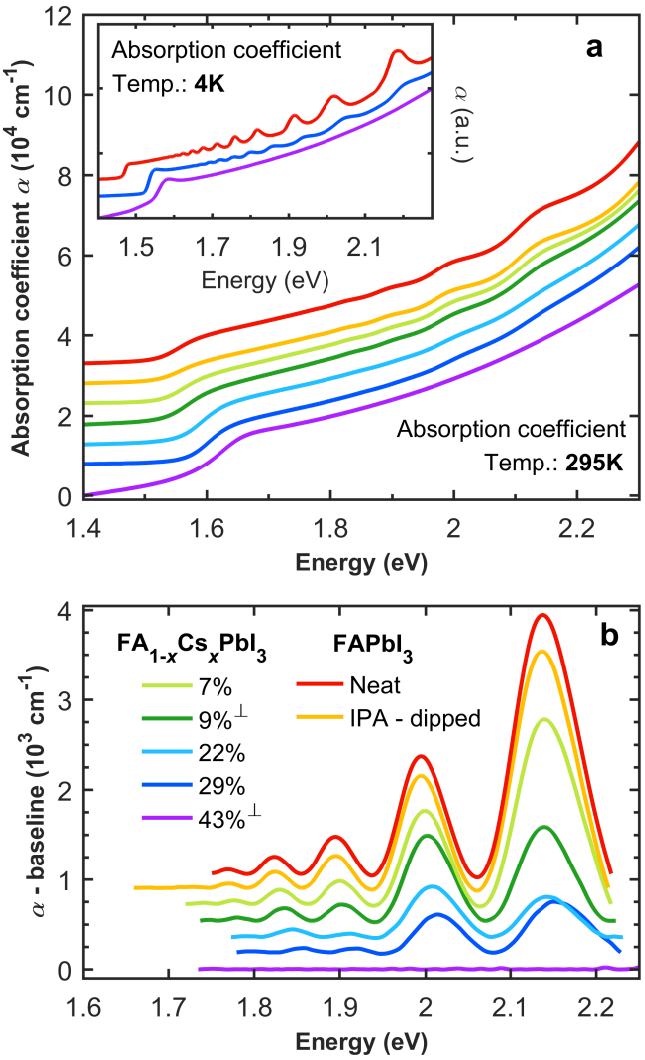


Figure 4.4: Absorption coefficient spectra and decoupled peaks. **a**: Absorption coefficient spectra of $FA_{1-x}Cs_xPbI_3$ films with different Cs content x at room temperature (295 K, main panel) and 4 K (inset). **b**: Peak features decoupled from the rest of the bulk-like absorption spectra at room temperature. For visual clarity, the absorption coefficient spectra and peak features are successively vertically offset by $0.5 \times 10^4 \mathrm{cm}^{-1}$ and $0.15 \times 10^3 \mathrm{cm}^{-1}$ respectively. (The legend in (**b**) also applies to (**a**). Films are evaporated on either quartz or sapphire (indicated by $^{\perp}$) substrates, indicating that trends are independent of substrate choice.

coupling and thermal fluctuations, which may strengthen the quantum confinement, enhancing the amplitude and reducing the width of the associated peaks, making them clearly discernible. [40] In addition, the increased prominence may derive from a growth in the material volume experiencing confinement as δ_{H}-phase formation becomes more prominent at lower temperatures. [33]

However, I note that phase transitions from the α-phase to other polymorphs of $FAPbI_3$ including the δ_{H}-phase can be severely suppressed and the film can be effectively kinetically trapped in the α-phase even at cryogenic temperatures by thermally quenching the film and rapidly decreasing the temperature. [33, 120] This is indeed what is achieved experimentally here, as the films experience a rapid reduction in temperature from 295 K to 4 K within the sample chamber of the cryostat in 10 minutes or less. Therefore, the majority of the film is presumed to be kinetically trapped in the α-phase, and most of the phase transitions during the cooling process are presumed to be heavily suppressed. This has been experimentally observed in elastic neutron scattering experiments - observed by Chen et al. [33] and visualized in Figure 4.5, and observed experimentally through the lack of phase transitions when $FAPbI_3$ films are heated from cryogenic temperatures up to room temperature after they have been thermally quenched. [121]

However, to narrow down the origin of this enhancement of quantum confinement, more in-depth quantitative analysis is required. To that end, I first define and calculate from my data two useful parameters. First, I define the spectral area under the peaks as the area between the experimental absorption coefficient spectrum and the spline baseline connecting the troughs (i.e. the integral over curves such as those shown in Figure 4.4b, and the red-shaded area in Figure 4.6), stated as a percentage of the overall area under the absorption spectrum (i.e. the sum of the red- and grey-shaded areas in Figure 4.6), between the first and last detectable minima of the peak features. Such data indicate a

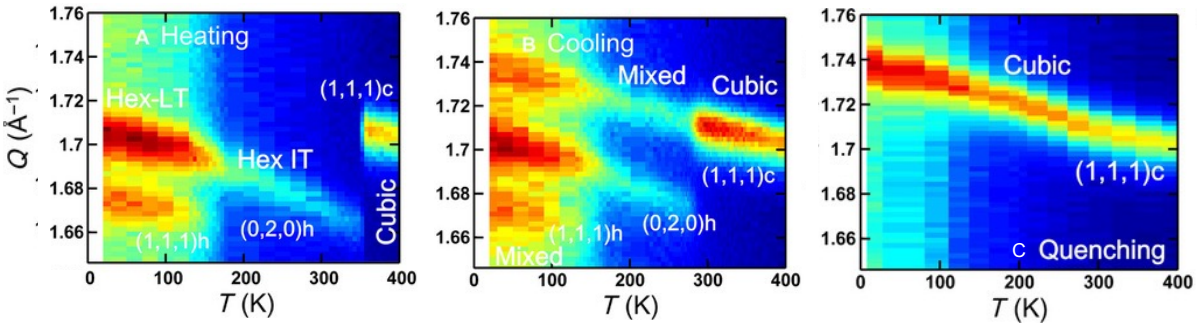


Figure 4.5: Thermal contour map of the elastic neutron scattering data of $FAPbI_3$. Elastic neutron scattering data of $FAPbI_3$ under **a**: heating, **b**: cooling, and **c**: rapid temperature quenching. Figure is adapted from [33].

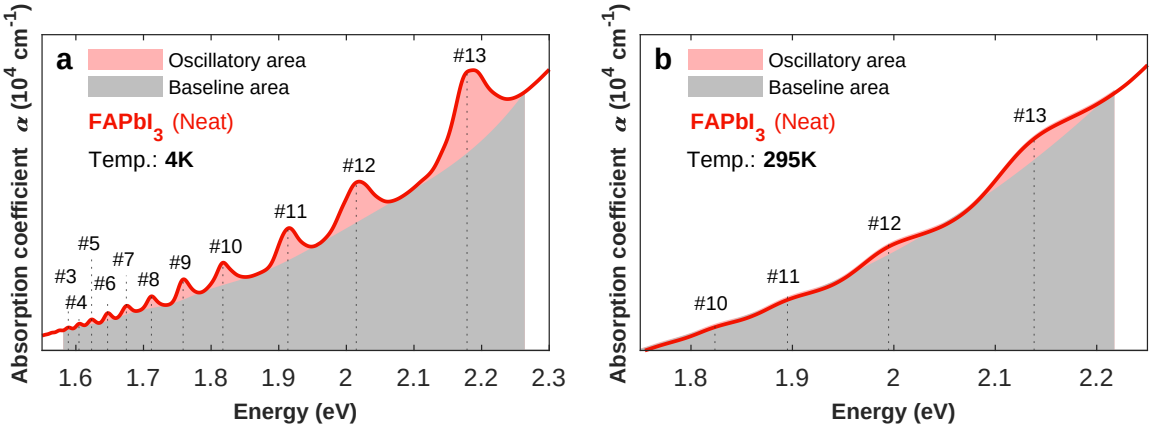


Figure 4.6: Absorption coefficient spectrum of $FAPbI_3$ with definitions of terms used in the analysis. Absorption coefficient spectrum of the neat $FAPbI_3$ film, **a**: at 4 K, and **b**: at room temperature. The spectral area under the spline baseline (grey-shaded area) and spectral area between the measured absorption coefficient and spline baseline (pink-shaded area) - termed the peak area, used to calculate the percentage of spectral area under the peaks in Figure 4.7a, and Figure 4.7a, are visually represented. The relevance of the spectral area under the peaks compared to the peak amplitude, is that it takes into account both the extracted amplitude and FWHM of the peaks, making it comparatively less susceptible to artificial changes caused by the narrowing and widening of the peaks as opposed to changes caused by the increase and decrease in strength of confinement. The peaks in Figure 4.7c, and Figure 4.7d are identified by their peak index, with the lowest energy discernible peak labelled as peak #0.

relative prominence of the features in the absorption spectra and are displayed in Figure 4.7a and Figure 4.7b for different Cs contents and temperatures. Second, I calculate the confinement energy for a given absorption peak feature by simply subtracting from each peak energy E_{peak} the bandgap values E_{g} previously extracted from Elliott fits (Figure 4.3c). Subsequent peaks were numbered incrementally towards higher energy, with peak index value $n = 0$ referring to the lowest-energy discernible peak in the absorbance spectra for a $FAPbI_3$ film at 4 K. [40] Accordingly, the highest-energy discernible peaks of all the films have the same highest peak index. Figure 4.7c and Figure 4.7d display the changes in confinement energy $E_{\text{peak}} - E_{\text{g}}$ for different Cs content and temperatures. Appendix A.4.3 provides further details on the peak indexing method, definitions and extraction of both parameters.

I first explore how substitution of FA with Cs affects the confinement energy $E_{\text{peak}} - E_{\text{g}}$. As Figure 4.7c indicates, increasing Cs content in $FA_{1-x}Cs_xPbI_3$ leads to a decline in confinement energy, a trend opposite to that of the blue-shift of the bandgap. It has previously been postulated that intrinsic quantum confinement in $FAPbI_3$ may be linked with the spontaneous formation of electronic barriers in the material deriving from relatively thin, and potentially periodic inclusions of δ_{H}-phase, or possibly ferroelectric domain walls. [40] It has further been shown that the quadratic dependence of the confinement energy on the peak index was compatible with energy levels deriving from a superlattice structure (Krönig-Penney model) whose energy levels may approach those of an infinite quantum well. As discussed in Appendix A.5, in this approximation, the confinement energy E_n follows:

$$E_n = \frac{\hbar^2}{8\mu^* L^2} \sum_{i=1}^{d_{\text{conf}}} n_i^2,$$

where d_{conf} is the dimensionality of confinement. Accordingly, it depends on the square of the peak index ($\propto n_i^2$), and is inversely proportional to the electron-hole reduced effective

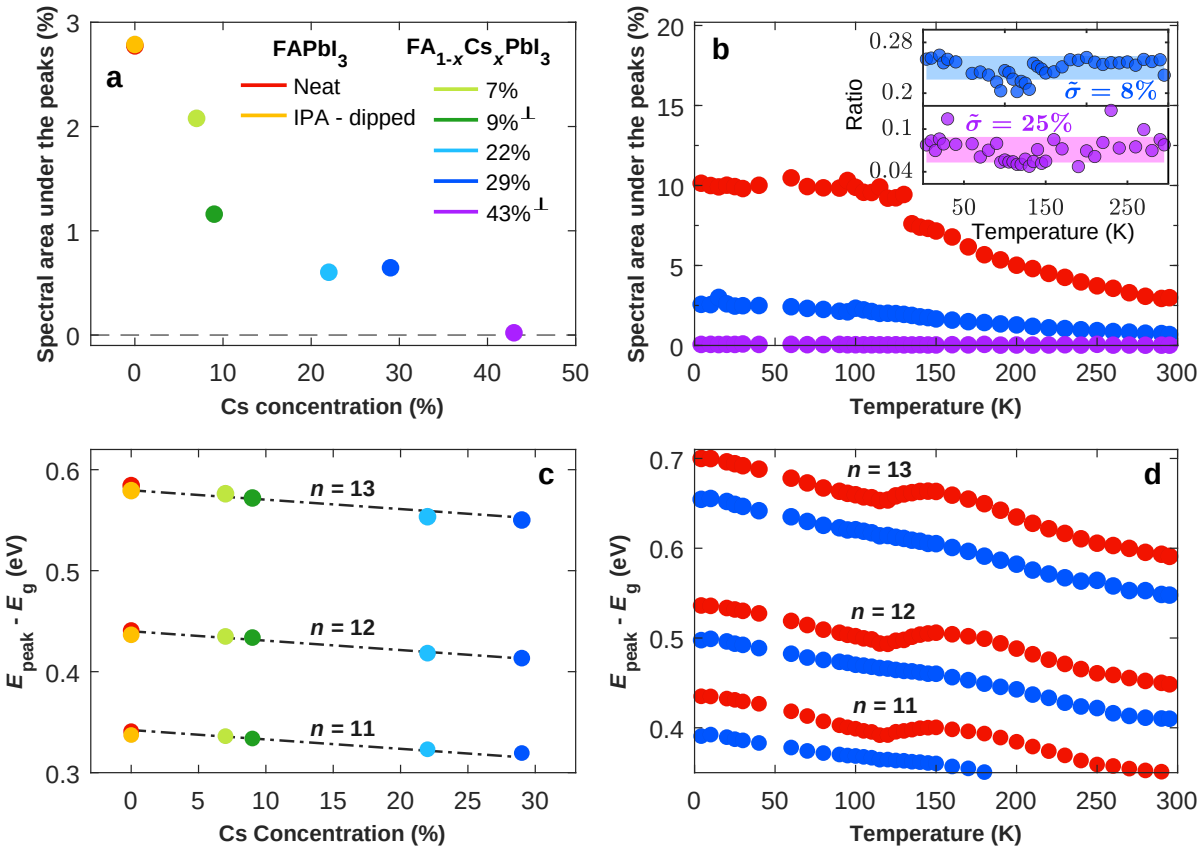


Figure 4.7: Quantitative analysis of the prominence of absorption peak features, and the derived energy of quantum confinement. **a**, **b**: Spectral area underneath the absorption peaks, given as a percentage of the total area under the absorption coefficient spectrum, used to parameterize the occurrence of quantum confinement. (**a**) shows values at 295 K as a function of Cs content x in $FA_{1-x}Cs_xPbI_3$, and (**b**) displays values as a function of temperature for the compositions: $FAPbI_3$ (red circles), $FA_{0.71}Cs_{0.29}PbI_3$ (blue circles), and $FA_{0.57}Cs_{0.43}PbI_3$ (purple circles). The inset in (**b**) shows the spectral areas under the absorption peaks for $FA_{0.71}Cs_{0.29}PbI_3$ (blue circles) and $FA_{0.57}Cs_{0.43}PbI_3$ (purple circles) divided by the values for $FAPbI_3$, indicating a temperature-independent ratio (within a standard deviation of the mean, as visualized with the shaded areas). The value of $\tilde{\sigma}$ shown indicates the standard deviation divided by the mean value, parameterizing the spread. **c**, **d**: Confinement energy, calculated as the difference between the absorption peak position E_{peak} and the bandgap E_g extracted from Elliott fits to absorption onsets. (**c**) shows the confinement energy extracted from peaks with index numbers $n = 11$, 12, 13 at room temperature as a function of Cs content across the $FA_{1-x}Cs_xPbI_3$ film series, with lines showing a global linear fit of identical gradient yielding 0.93 meV change per Cs fraction. (**d**) shows the confinement energy as a function of temperature for $FAPbI_3$ (blue circles) and $FA_{0.71}Cs_{0.29}PbI_3$ (red circles). (The legend in **a** also applies to **b**, **c**, and **d**. Films are evaporated on quartz or sapphire (indicated by $^{\perp}$) substrates)

mass ($\propto 1/\mu^*$) and the square of the length scale (or periodicity) of electronic confinement ($\propto 1/L^2$). By fitting, as a crude first-order approximation, a global linear regression to the confinement energy $E_{\text{peak}} - E_{\text{g}}$ at room temperature for peak indices $n = 11$, 12, 13 (see Figure 4.7c) I determine a gradual decline in confinement energy by 0.93 meV per Cs fraction up until 29% Cs content. These linear fits indicate that within this Cs content range, the confinement energy falls by 270 meV, corresponding to a fractional fall of around 6.2%. Based on the known trends in the literature for a lattice contraction and an increase in the electron-hole reduced effective mass μ^* with increasing Cs content for FA-based perovskites, such a decline in confinement energy with increasing Cs content could thus be caused by a combination of a small decrease in the confinement length scale L, and a considerably larger counteracting increase in the reduced effective mass. My analysis of the XRD patterns provided in Table 4.1 indicates a fractional reduction in lattice parameter by 0.92% between 0% and 29% Cs content, which would induce an analogous relative contraction of the associated intrinsic confinement length scales. Similarly, the electron-hole reduced effective mass has been shown to increase from $FAPbI_3$ to $CsPbI_3$ from $0.09m_e$, [122] to $0.114m_e$, [123] respectively, as expected from changes to the electronic band structure. [113, 117, 123–125] Assuming a linear relationship for the change in reduced effective mass with Cs concentration, [122, 123] the fractional increase in μ^* would correspond to 7.73% between 0% and 29% Cs concentration films. Therefore, this percentage increase in μ^* (by 7.73%) is more than sufficient to counterbalance the reduction in confinement energy caused by a decline in L^2 (by $2 \times 0.92\%$) accompanying the increase in Cs content, which, taken together, would be expected to decrease the confinement energy ($\propto 1/(\mu L^2)$) by $\sim 5.4\%$, similar to what is actually observed in Figure 4.7c. Even though this quantitative analysis is not sufficient on its own to conclusively correlate the differences observed in confinement energies and quantum physical behaviour with changes to the bandstructure and lattice parameter as more Cs is progressively

incorporated into the lattice, it is still able to demonstrate that the simple confinement models used here do not directly contradict with these observed changes and predict changes of the same order of magnitude as those observed experimentally.

It is worth noting that additionally, as can be seen in Figure 4.8, the confinement energies at 4 K extracted from the absorbance spectra of the neat $FAPbI_3$ and the $FA_{0.71}CS_{0.29}PbI_3$ film can both be fitted against their peak indices using a one-dimensional infinite quantum well model given by

$$E_n = A(n - n_0)^2 + B,$$

where A is a constant of proportionality $\left(\frac{\hbar^2}{8\mu^* L^2}\right)$, n_0 is the peak index at which the quadratic relation starts (lowest discernible peak $n_0 = 0$ for the neat $FAPbI_3$ film at 4 K), and B is the energy shift of the confined ground state from the bulk bandgap, which could be a result of a different bandgap within the confined regions owing to the lattice strain, and was fixed to the freely fitted value obtained from the $FAPbI_3$ fit across the different samples. Between the neat $FAPbI_3$ film (0% Cs) and the $FA_{0.71}Cs_{0.29}PbI_3$ film (29% Cs), the factor A changes by 9.6%, a change that is roughly consistent with what is observed from the global linear regression for the confinement energies at room temperature (6.2%) and what is expected from the changes to the reduced effective mass μ^* and lattice parameter (5.4%).

As a second step, I proceed by analysing the extent to which Cs incorporation affects the prevalence of peak features in the absorption of the $FA_{1-x}Cs_xPbI_3$ films. First, I note that the spectral area under the peaks (Figure 4.7a) and the peak amplitude (Figure 4.4) gradually decrease with increasing Cs content until they mostly vanish for the film with 43% Cs content, commensurate with almost-complete elimination of quantum confinement effects. The accompanying gentle decline in confinement energy discussed above is clearly

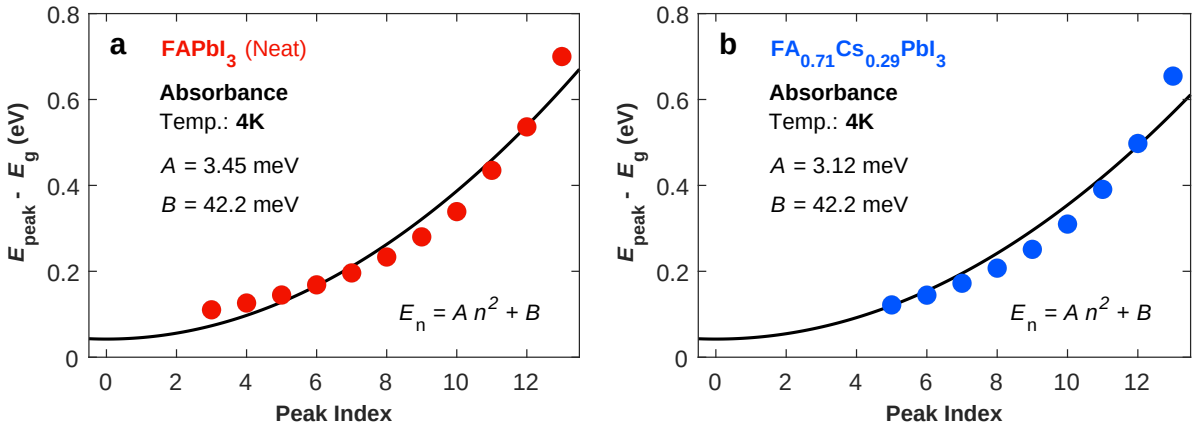


Figure 4.8: Quadratic confinement models for the infinite potential well using the absorbance peak features for $\mathbf{FA_{1-x}Cs_xPbI_3}$ films. The confinement energies from the absorbance spectra of **a**: $FAPbI_3$ (Neat) film, and **b**: $FA_{0.71}Cs_{0.29}PbI_3$ film are fitted with a quadratic model according to the infinite quantum well model.

too small to be the main cause of the fading peak features in the absorption spectra. I therefore propose that instead, much of the amplitude decline is caused by a reduction in the volume fraction supporting such quantum confined domains. This hypothesis is also supported by the observation of a constant ratio of peak amplitudes for films with different Cs content as a function of temperature (see inset in Figure 4.7b), suggesting that the films of different Cs content share a mechanism of amplitude decline, whose temperature dependence is common between them. It is additionally worth noting that due to the rapid thermal quenching experienced by the films to first reach cryogenic temperatures before starting measurements (see Figure 4.5), the films are kinetically trapped in the α-phase irrespective of temperature. This is in agreement with the observed constant ratio of the peak amplitude as a function of temperature across my sample set. Phase transitions or other major restructuring of the crystal lattice that is exclusive to a specific composition at a threshold temperature, would have caused a similarly abrupt discontinuity in the ratio of the peak amplitude at said threshold temperature. Accordingly, the lack of a discontinuity in the peak amplitude ratio suggests that this experimental data does not contradict my hypothesis that the quantum confinement is experienced by the majority α-phase of $FAPbI_3$ - possibly confined by other minority polymorphs created by the lattice due to grain boundaries, thermodynamic arguments, or in an effort to relieve some strain.

I propose two possible reasons why substituting FA for Cs may cause fewer confinement domains to be present in the film volume. First, I note that incorporation of Cs into $FAPbI_3$ has been shown to reduce the formation of large δ_H-phase domains (apparent in literature XRD patterns with (100) peak around $2\theta = 11.8°$) [98] for addition of as little as 5% Cs. [29, 33, 103–106] It has previously been postulated that periodic inclusions of thin layers of δ_H-phase, for example as a result of strain, may lead to the quantum confinement effects observed in $FAPbI_3$ [40]. Such thin electronic barriers with widths of less than 10% of the well width are capable of inducing prominent effects in

the absorption spectrum [40] while not necessarily generating noticeable XRD diffraction amplitude at $2\theta = 11.8°$. I note that the amount of Cs content required to almost entirely remove quantum confinement effects ($\geq 40\%$) is significantly larger than that ($\sim$5%) [29, 33, 103–106] needed to eliminate extended domains of bulk crystalline δ_{H}-phase, which may relate to their differing thermodynamics of formation.

4.2.3 Photoluminescence spectrum

My observations clearly demonstrate that Cs substitution in $FAPbI_3$ is able to control the presence of domains exhibiting intrinsic quantum confinement, leading to their almost-complete elimination at high Cs content. Alternatively, this same level of control could potentially be achieved through the incorporation of different additives, or through strain engineering or templating during the fabrication process, which has in the past been shown to affect the formation of δ_H-phase in $FAPbI_3$. [33, 35, 36, 99, 126] An argument could then be made, that quantum confinement in $FAPbI_3$ could instead also be enhanced, possibly through strain engineering or nucleation agents, capable of controlling and stabilizing the self-assembled nanostructures. Indeed, absorption and PL features of lower-dimensional phases associated with $MAPbI_3$ films were previously reported to have been enhanced and stabilized using stoichiometric and additive engineering. [127] Such enhancement of nanoscale effects through facile bulk processing techniques could provide a future pathway for efficient light emission and single-photon sources for quantum applications. To test the tantalising possibility of emission emerging from these nanostructures (i.e. from electronically confined states) I performed photoluminescence measurements on $FAPbI_3$ at low temperatures, for which non-radiative recombination is suppressed because of thermal depopulation of the available phonons to mediate such recombination, [128, 129] and for which radiative recombination is enhanced as a result of the sharpening of the Fermi distribution function. [54, 121]

Notably I am indeed able to observe photoluminescence peak features at energies above the bandgap for $FAPbI_3$ at 4 K, at energetically similar positions to those observed in the absorption coefficient spectra. As shown in Figure 4.9a, such features are weak but clearly apparent in an IPA-dipped $FAPbI_3$ film, however, they disappear when 43% of FA has been substituted for Cs in $FA_{0.57}Cs_{0.43}PbI_3$. Such dependence on Cs incorporation is

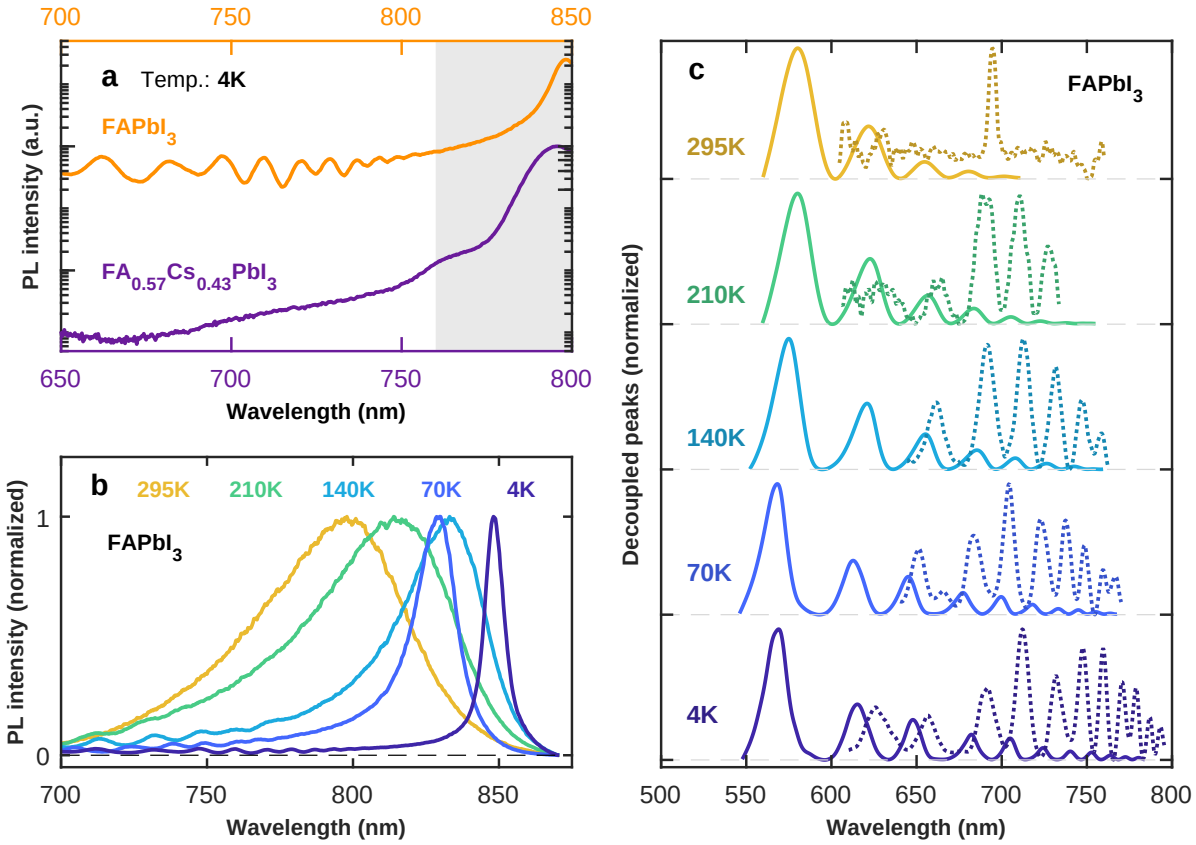


Figure 4.9: Photoluminescence spectra. **a**: Photoluminescence (PL) spectra on a log scale, of an $FAPbI_3$ (IPA dipped) and a $FA_{0.57}Cs_{0.43}PbI_3$ film at a temperature of 4 K showcasing the presence and absence, respectively, of above-bandgap peak features. The two spectra are vertically offset for visual clarity. (The full PL spectra of both films on a linear scale are shown in Figure A.10.) **b**: Temperature dependence of the normalised PL spectra for an $FAPbI_3$ film (IPA-dipped control). **c**: Normalized spectra of the decoupled absorption and emission peak features for the $FAPbI_3$ film, recorded at different temperatures. Peak features were decoupled from the absorption (represented by solid lines) and photoluminescence (represented by dotted lines) spectra using a spline phenomenological baseline fitting method in both cases. The PL spectra are collected following excitation by a 398 nm wavelength diode laser under continuous-wave operation.

similar to that observed for the absorption peak features, leading me to attribute these observed PL peak features to the same quantum phenomenon. It therefore appears that a subset of photo-generated charge carriers spends sufficient time in quantum-confined domains to yield emission from the associated states.

To further explore the fundamental physics behind the PL peak features and the quantum confinement, I examine the temperature dependence of the emission from quantum confined domains. Figure 4.9b shows that the PL peak features gradually broaden and progressively become less discernible from the underlying main PL spectrum as the temperature increases, similar to the temperature trends observed in the absorbance spectra. To quantitatively analyse this observation and unmask the relationship between these features in both the PL and absorbance spectra, I decoupled the PL peak features from the underlying spectra in a manner analogous to that utilized for the absorption spectra (see Figures A.10 and 4.6).

The overlaid decoupled peaks from the PL and absorbance spectra (shown in Figure 4.9c) clearly demonstrate that these indeed occupy the same energetic range and similar wavelength position patterns. However, two clear differences are worth noting. First, a slight Stokes shift is evident between absorption and emission peaks. Such shifts may arise e.g. from migration of charge carriers to domains with weaker confinement within the confined bands that emerge from the Krönig-Penney model, or within the slightly disordered density of states available in a domain, evidenced by the non-zero broadening that is present even at low temperature and may derive, for example, from well width fluctuations. The apparent Stokes shift may also partly be related to weak photon reabsorption effects, though I note that such reabsorption alone cannot explain the modulations observed in the PL spectra, as discussed in detail below and visualized in Figure 4.14. Ultimately, the quantum confinement will create different electronic bands, and the relaxation of the photo-generated charge-carriers in each band to their local

minima will define each band's Stokes shift. That Stokes shift will naturally be very different to the shift observed for the main PL peak, owing to the differing curvature and band structure between the band edge and higher up in the band. Second, and more importantly, the peak amplitude trends with energy markedly differ between the absorption and emission features. For the absorption peaks, the amplitude progressively increases with higher energy (shorter wavelength), as observed previously and attributed to a higher density of states available at higher energies that generates strong transition densities [40]. For the photoluminescence peaks, however, an opposite trend is observed with the lower-energy confined states having the largest PL amplitude. This cross-over in trends is most likely caused by fast charge-carrier relaxation from higher-energy to lower-energy quantum-confined states. I note that such relaxation through the internal states of a quantum structure is generally relatively rapid, such that the observation of emission from higher-lying states depends on a competitive trade-off with the time scale for radiative recombination.

Photon reabsorption and recycling events

To conclusively refute the plausibility of photon recycling and reabsorption events modulating the PL spectra and artificially generating the PL peak features, I point out three main arguments. First, the PL spectra at room temperature are thermally broadened because the distribution function governing the occupation of states near the band edge will tend to a Maxwell-Boltzmann thermal distribution, which would then be truncated on the high-energy end if photon absorption were prevalent. However, when I overlay the PL spectra of the IPA-dipped $FAPbI_3$ film on top of the corresponding absorbance spectra at different temperatures, as can be seen in Figure 4.10, the PL spectra

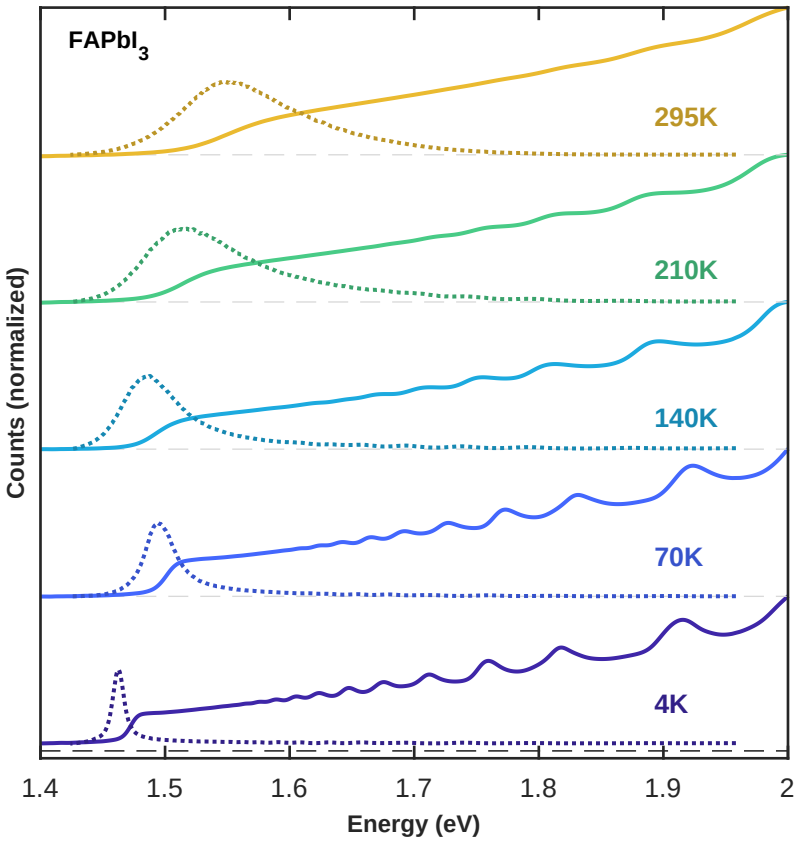


Figure 4.10: Photoluminescence and absorbance spectra of $FAPbI_3$ at different temperatures. Solid lines represent the absorption coefficient spectra, and dashed lines represent the photoluminescence spectra.

can be seen to clearly still possess a high-energy tail that extends well into the highly-absorbing regions in the absorbance spectrum. This is unlike what would be expected in the case that photon reabsorption and recycling events were prevalent, in which case the PL spectra would have been red-shifted beyond the absorbance onset and an asymmetric PL spectrum with a low-energy tail would have artificially emerged. Second, the very small film thickness - of around 100 nm, limits the amount of photon recycling occurring in the films and the degree to which the PL can be modulated by the absorbance spectrum. The penetration depth for the IPA-dipped $FAPbI_3$ film starts to decline below 100 nm for energies above 2.7 eV, highlighting the complete absorption of the excitation laser and the inability of the film to efficiently modulate the PL being emitted. Specifically, the penetration depth for the energetic range associated with the absorbance and PL features investigated in this study (between 1.55 eV and 2.25 eV) ranges from 3.2 μm to 220 nm.

Finally, I simulate the hypothetical shape of an originally smooth PL spectrum that has been filtered by (i.e. modulated by the absorption spectrum of) the entire IPA-dipped $FAPbI_3$ film. I then compare this spectrum with what I observed experimentally. I considered two possible baselines to represent the smooth PL emission spectrum: a smoothed baseline and a baseline that goes through the most prominent PL peak features as the hypothetical high-energy PL tails (see Figure 4.11a). By multiplying these hypothetical tails with the transmittance function of the entire film (displayed in Figure 4.11b), I obtained the filtered PL that would have been emitted if no PL peak features were present (see Figure 4.11c). A couple of observations can be made from this attempted imitation. First, the generated PL tail has significantly less prominent peak features, even though this model is clearly the most extreme case, in which all the PL is assumed to pass through the entire film before collection. This highlights the need for substantially stronger and more prominent transmittance features to exist for PL peak features similar to what is observed to emerge - even for a model that over-exaggerates

the effects of photon reabsorption. Second and more importantly, the amplitude of the absorbance features is highest for higher energies, which would naturally cause a similar amplitude variation with energy for the PL features if they indeed originated from photon recycling and absorbance modulations of the PL spectra as seen for the artificially generated PL peak features (displayed in Figure 4.11d). However, I observe the opposite amplitude dependence with energy for the actually observed PL peak features, in which the lower-energy confined states seem to have the largest PL amplitude. This amplitude variation can instead be understood in terms of charge-carrier relaxation, where charge carriers from the higher-energy confined states relax into the lower-energy confined states at a rate slightly faster than other de-excitation pathways, including funnelling to bulk regions, explaining the higher intensity at lower energies.

PL Confinement energy

According to my primary model, these emissions should originate from transitions between confined levels. Such emissions from higher-lying quantum confined states bands have been observed before for zero-dimensional quantum dots, [130–134] where they typically exhibit a spectral dependence on excitation intensity as they ultimately emerge from the slowing down of the relaxation dynamics due to either ground-state filling or hot phonon bottlenecks. [135, 136] I however do not observe such an excitation intensity dependence (see Figure 4.12 and 4.13), ruling out ground-state filling as a cause of these emissions. I instead argue that these emissions are observed as a snap-shot of early times after photo-excitation, when charge carriers experience competing fast radiative recombination, funnelling out of regions experiencing confined domains to surrounding regions with solely bulk phase material, and internal relaxation within the confined bands. This can be due to some possible hindrance to the fast internal relaxation mechanism

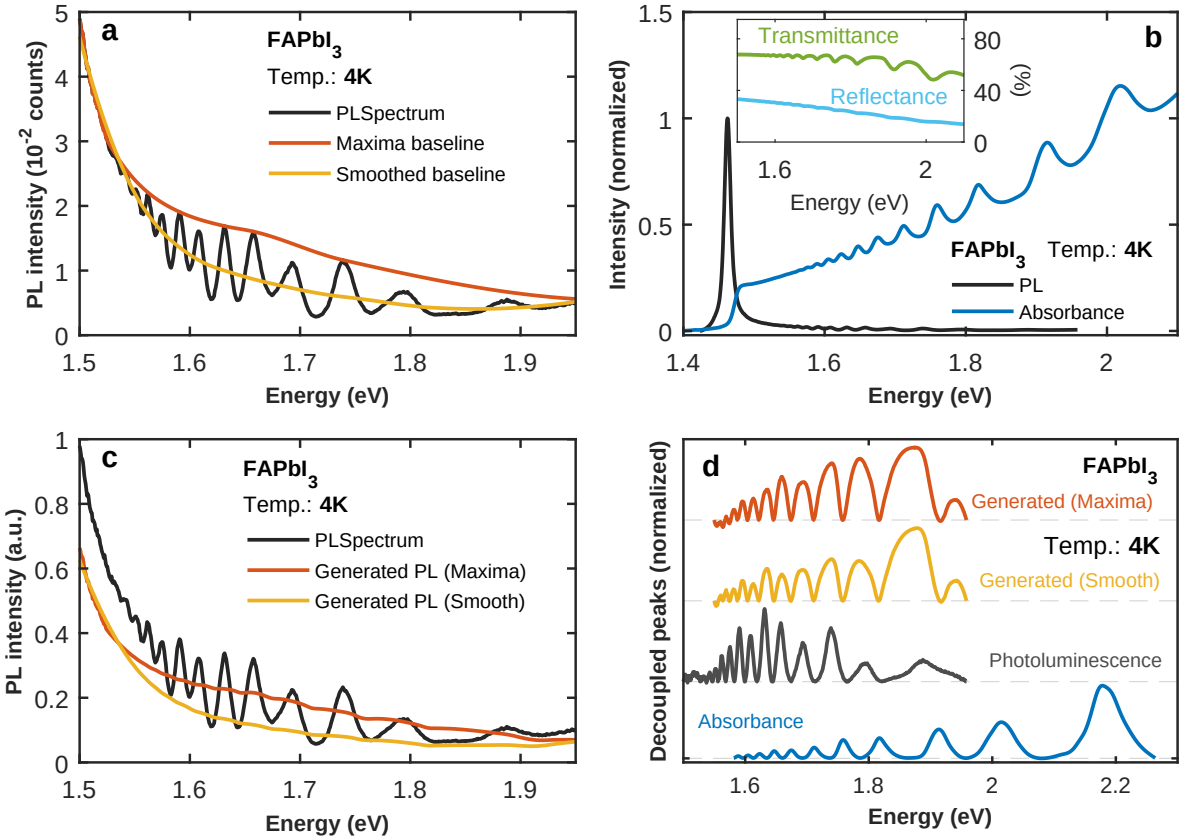


Figure 4.11: Quantitative imitation of the PL peak features observed for IPA-dipped $FAPbI_3$ at 4 K. (**a**) shows the high-energy tail of the 4 K PL spectrum of an IPA-dipped $FAPbI_3$ film with the noticeable PL peak features, along with the hypothetical tails for when no PL peak features would be present. (**b**) shows the full PL, absorption coefficient, reflectance, and transmittance spectra at 4 K. (**c**) shows the generated PL spectra (×250) at 4 K for when the entire $FAPbI_3$ film is used as a filter for a hypothetical smooth PL without any peak features using the two baselines visualized in (**a**). (**d**) shows the decoupled peak features from the experimentally measured absorbance and Pl spectra, as well as the generated PL spectra in (**c**).

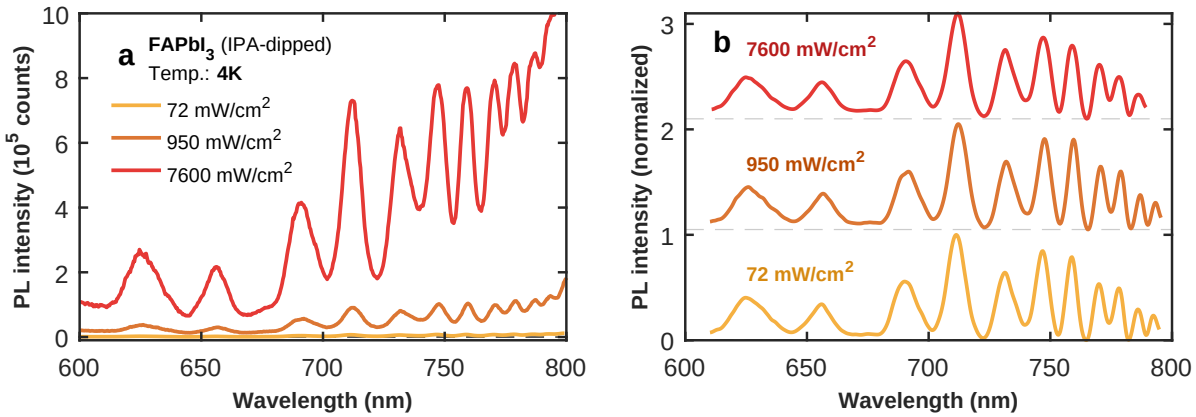


Figure 4.12: Photoluminescence spectra of the PL peak features in $FAPbI_3$ (IPA-dipped) at energies above the main band edge peak under different excitation intensities. (**a**) shows the absolute PL spectra of the IPA-dipped $FAPbI_3$ film at 4 K under difference excitation intensities. (**b**) shows the normalized peaks, decoupled from the PL spectra using a spline baseline fitting, under the different excitation intensities, with subsequent curves vertically offset for visual clarity.

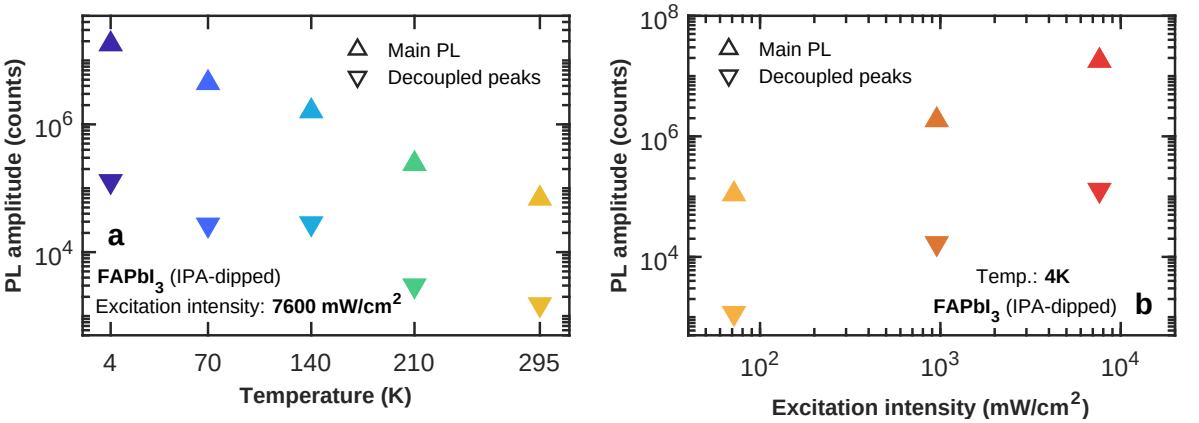


Figure 4.13: PL amplitudes for $FAPbI_3$ films as a function of temperature and excitation intensity. **a**: The temperature dependence and **b**: excitation intensity dependence of the extracted absolute amplitude of the main steady-state PL peak and that of the decoupled peaks is displayed. The amplitude of the decoupled peaks increases for both a reduction in temperature and a rise in excitation intensity, but to a lesser extent when compared to the main PL amplitude variation with temperature and excitation intensity (i.e. the relative amplitude of the decoupled peak features to the main PL decreases for both a reduction in temperature or a rise in excitation intensity.)

from complex selection rules and some moderate phonon bottleneck - which has been observed in perovskite 2D material before, [137] and is possibly enhanced because of lower temperatures.

In fact, the existence of light-emission from these intrinsically quantum-confined states and the agreement of their PL with my primary model can be further corroborated by modeling the relationship between the PL confinement energies (PL peak positions relative to the PL optical bandgap) against their peak index at 4 K, and fitting such a relationship with a quadratic fit (shown in equation A.6). Indeed, this quadratic function fitted the PL confinement energies particularly well and yielded fitting parameters of the same order of magnitude as those obtained from the fitting of the absorbance confinement energies in Section A.5 (displayed in Figure 4.14b).

Charge-carrier dynamics with quantum confinement

The above observations suggest that significant early-time relaxation may occur in quantum confined states of $FAPbI_3$ following photo-excitation. Charge carriers may relax internally within a domain exhibiting quantum confinement, either through inter-level relaxation, or diffusion to lower-energy parts of the domain. They may also funnel away entirely from quantum-confined regions and into the bulk. To probe for such effects, I measured time-resolved photoluminescence at low temperature (4 K) with 40-ps time resolution for different spectral emission regions, as shown in Figure 4.15 (analogous data for IPA-dipped $FAPbI_3$ at room temperature and $FA_{0.57}Cs_{0.43}PbI_3$ at 4 K are shown in Figures A.11 and A.12, respectively). I find that while the main PL peak shows a dispersive decay transient over tens of nanoseconds, the emission arising from the peaks associated with quantum confinement is substantially more rapid. This initial rapid

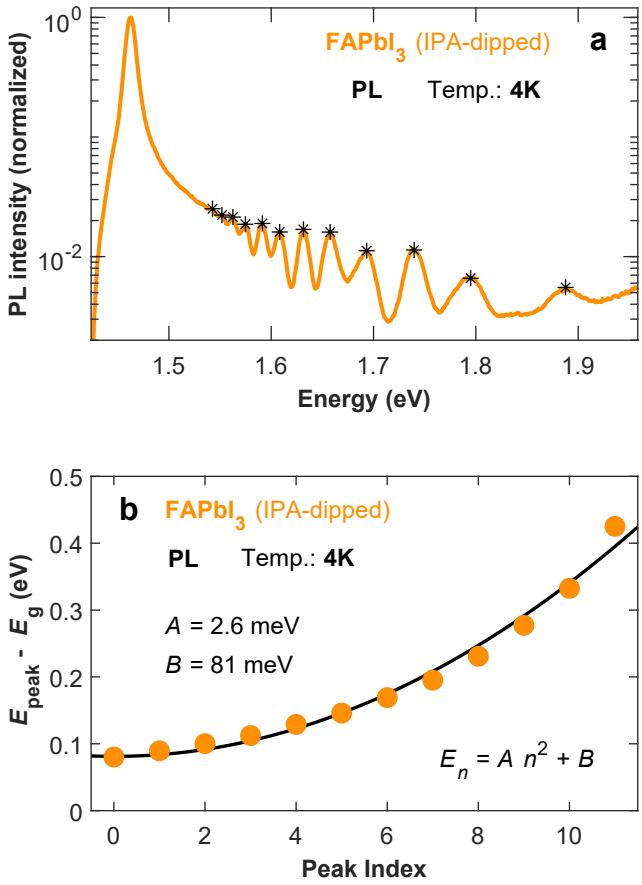


Figure 4.14: Confinement models for the infinite potential well using the PL peak features of IPA-dipped $FAPbI_3$. (**a**) shows the full photoluminescence spectrum of IPA-dipped $FAPbI_3$ at 4 K on a log scale, with the peaks of the PL features visually marked. (**b**) shows the quadratic fit to the PL confinement energies versus peak index, assuming a constant-sized quantum well.

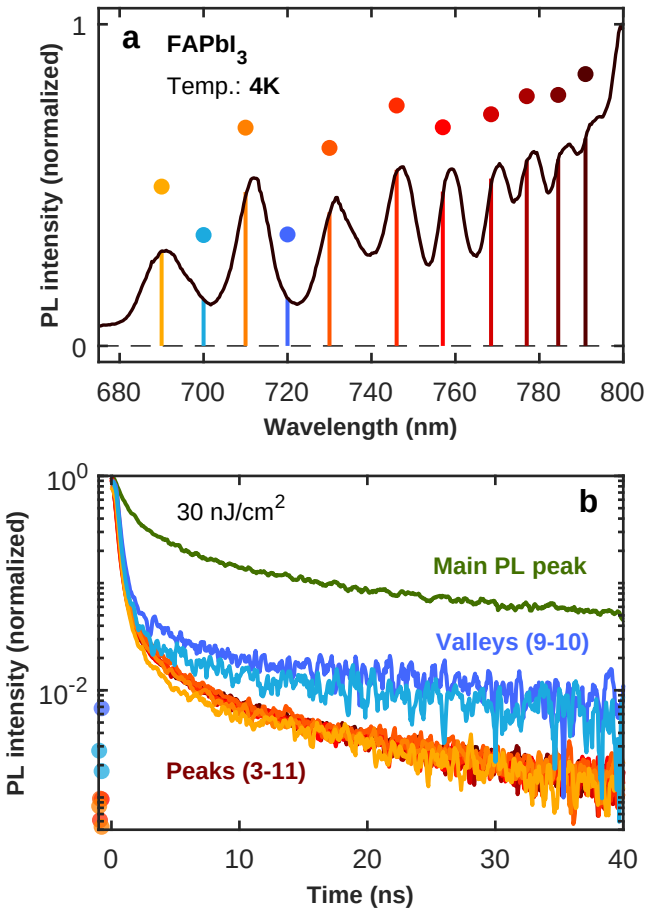


Figure 4.15: Time-resolved photoluminescence of $FAPbI_3$. **a**: High-energy (short-wavelength) tail of the PL spectrum of $FAPbI_3$ (IPA-dipped film) at 4 K. **b**: Time-resolved photoluminescence (TRPL) decay traces recorded at the spectral positions indicated with coloured dots and solid vertical lines in the spectrum shown in (**a**). The PL decay traces were recorded following an excitation by a 398 nm picosecond pulsed diode laser at a repetition rate of 1 MHz for the high-energy tail of the PL spectrum, and a repetition rate of 10 MHz for the peaks and valleys highlighted in (**a**). The numbering of the peaks and valleys were such that the lowest-energy discernible peak and valley were indexed peak #0 and valley #0 respectively.

component is beyond my time-resolution (see Figure A.13) and most likely associated with internal relaxation within the domain but potentially also accelerated by enhanced exciton formation, given that exciton binding energies are enhanced by quantum confinement. [138–142] I note that PL transients recorded in between peaks (i.e. in the valleys) show intermediate behaviour to that of the peaks and bulk emission, most likely owing to limitations on the spectral resolution of my experimental setup. The slow dynamics observed at long times after excitation may therefore mostly be associated with very weak high-energy tails of the bulk emission. Overall, these PL data paint a conclusive picture of quantum emitters being present within regions surrounded by bulk-like $FAPbI_3$.

4.3 Conclusion

Overall, I have shown successful control over the strength of intrinsic quantum confinement exhibited by $FAPbI_3$ perovskite and its derivatives. I have demonstrated that Cs addition allows for the gradual elimination of such confinement effects, which disappear almost entirely as the Cs content in $FA_{1-x}Cs_xPbI_3$ reaches 43%, both at room and low temperature. I postulate that this reduction mostly derives from a decrease in the volume fraction hosting electronic boundaries that cause quantum confinement. I suggest that when such domain walls are caused by either δ_H-phase inclusions or ferroelectric effects, Cs addition may mitigate their formation through either structural effects or its non-polar nature, respectively. I further find that Cs incorporation has a moderate impact on the confinement energy, which gradually reduces by $\sim$4.65% from $FAPbI_3$ (0% Cs) to $FA_{0.71}Cs_{0.29}PbI_3$ (29% Cs) owing to competing changes in effective reduced electron-hole mass and the lattice spacing that defines the length scales of confinement. My observations of the first clear emission features from such quantum confined domains in $FAPbI_3$ reveal features comparable to those found in the corresponding absorption spectra. However, a comparison of emission and absorption spectra, and an analysis of the photoluminescence decay transients, reveal that charge-carriers are likely to undergo rapid relaxation following the initial excitation. Fast initial dynamics are most likely associated with internal charge-carrier relaxation within a given confinement domain, followed by funnelling from such domains into the bulk phase. My study demonstrates that such intrinsic quantum confinement effects can be controlled depending on the desired application. While for photovoltaics devices, charge-carrier extraction may be impeded by the presence of domain walls supporting quantum confinement, for light-emitting applications, such confinement will be advantageous, making such easily-fabricated, self-assembled periodic nanostructures highly desirable. My work allows for an understanding

of the underlying mechanisms influencing quantum confinement in $FAPbI_3$ and FACs mixed-cation perovskite thin films, showing that full elimination of the above-bandgap features through Cs alloying is possible. Further exploring these features and methods of their control, e.g. through strain engineering, tuning crystallization, or multiple A-cation alloying, will be instrumental in fully stabilizing quantum confinement and maximising its utility and potential e.g. for light-emitting applications.

5

Photovoltaic Performance of $FAPbI_3$ Perovskite is Hampered by Intrinsic Quantum Confinement

Contents

5.1 Motivation 104
5.2 Results and discussion 108
5.2.1 Effect of fabrication method on thin film quality, crystallinity and quantum confinement 108
5.2.2 Effect of quantum confinement on photovoltaic performance . . 120
Experimental evidence 120
Literature review 125
5.3 Conclusion 132

In this chapter, I investigate additional methods to achieve control over the intrinsic quantum confinement present in $FAPbI_3$, and probe its relationship with the overall performance of the photovoltaic device through various methods. I begin by exploring three common solution-based film-fabrication methods that offer different nucleation and crystallization control during the fabrication process. In doing so, I show that the suppression (and near total elimination) of quantum confinement and their associated absorption features can be achieved, and that the power conversion efficiencies

(PCEs) and short-circuit current densities of the corresponding devices can be increased, suggesting that quantum confinement hinders charge extraction. To corroborate my findings, I conducted a meta-analysis of literature reports covering 244 articles and 825 photovoltaic devices incorporating $FAPbI_3$ films, which indicated that PCEs rarely exceed a 20% threshold when such absorption features are present. Accordingly, this chapter demonstrates why ensuring the absence of these absorption features should be the first assessment when designing fabrication approaches for high-efficiency FAPbI3 solar cells.

The work presented in this chapter has been published in: **Elmestekawy, K.A.**, Gallant, B.M., Wright, A.D., Holzhey, P., Noel, N.K., Johnston, M.B., Snaith, H.J., and Herz, L.M. 'Photovoltaic Performance of $FAPbI_3$ Perovskite Is Hampered by Intrinsic Quantum Confinement', *ACS energy Letters*, **8(6)**, *2543–2551* (2023) (Ref. [42]).

5.1 Motivation

Metal halide perovskites (MHPs) have experienced tremendous progress in the past decade, reflected by a substantial improvement in the power conversion efficiency (PCE) of perovskite solar cells from a low 3.8% [69] to values now regularly exceeding 26% [6, 70] in just over a decade. These materials owe their excellent optoelectronic properties and photovoltaic (PV) performance to benign defect chemistry, [74, 143–148] high charge-carrier mobilities, [71] long diffusion lengths, [57, 72] low exciton binding energies, [16] and broadly tunable absorption spectra. [73] While many promising MHP compositions have been explored as active layers in photovoltaic devices, those centred around formamidinium lead triiodide ($FAPbI_3$) have arguably emerged amongst the most promising, [9] currently holding the single-junction MHP device efficiency record with a certified power conversion efficiency (PCE) of 26.2%, [6, 7, 70] and being one of the most investigated compositions according to a recent literature survey by Jacobsson et al. [149]. The success of $FAPbI_3$ partly derives from its near-optimal bandgap [9] for single-junction cells [92] and its enhanced stability under elevated temperatures compared to other commonly explored hybrid MHPs based on methylammonium, such as $MAPbI_3$. [150–152] In addition, $FAPbI_3$ importantly offers simplicity of stoichiometry compared with alloyed MHPs containing multi A-site cations or mixed halides, which enhances its resistance against compositional de-alloying and the formation of compositional inhomogeneities that can adversely affect performance. [23, 153–156]

However, one aspect of $FAPbI_3$ requiring careful control is structural stability. At room temperature, the desired perovskite α-phase is only meta-stable and easily deteriorates into a thermodynamically favourable, yellow, non-perovskite 2H (δ)-phase that is not particularly photo-active [33]. Early work demonstrated that partial substitution of

FA with Cs with as little as 5% [29, 33, 103–106] is sufficient to eliminate traces of δ-phase presence in XRD patterns, [30, 31] but such a degree of A-site alloying shifts the band gap to higher energies [29] and has been shown to introduce undesirable compositional inhomogeneities. [157, 158] Recently, a plethora of fabrication methods and optimisation approaches have therefore been developed to attain and stabilize the "unalloyed" perovskite α-phase of $FAPbI_3$. [29, 71, 99–102, 110, 150, 151, 159, 160] These alterations to earlier fabrication methods [9] vary from introducing pre- and post-annealing steps and additive treatments [35, 161] to more elaborate stoichiometric engineering techniques [93, 94, 101], vapor co-deposition [110] and more recently templating and sequential deposition strategies via solution [162] or vapor deposition [160] routes, yielding significant advances in stability and performance.

In addition, one peculiarity specific to $FAPbI_3$ is its propensity to exhibit intrinsic quantum confinement, which has been attributed to the formation of intrinsic nano-structured domains on the length scale of $\sim$10 nm in sub-volumes of nominally bulk films. [40, 41] Evidence for these features has been derived from the presence of peculiar above-bandgap peaks that are superimposed on bulk-like absorption spectra, and that had gone mostly unnoticed and unexplained [9, 29, 90, 91] until recently. [40, 41] Analysis of these absorption peak features has directly pointed towards the presence of electronic quantum confinement, and while these structures have not been imaged directly to date, it has been suggested that they could derive from the presence of thin slices of α-phase $FAPbI_3$ intrinsically self-assembling to form superlattices or quantum wells surrounded by regions acting as energetic barriers, [40] potentially in an attempt to alleviate some of the experienced strain in the lattice. [97] Such energy barriers may constitute inclusions of the δ- or alternative secondary phases forming thin layers undetectable in XRD patterns, with a relatively high Cs content of $\geq$ 40% recently having been found to eliminate

any traces of such quantum confinement. [41] It should be expected that any form of quantum confinement experienced by charge carriers even in small sub-volumes of the absorber layers hinders the unobstructed passage of the photocurrent throughout a solar cell. Surprisingly though, the relationship between the presence of intrinsic quantum confinement features in the absorption spectra of $FAPbI_3$ and the performance of photovoltaic devices based on these layers has not yet been examined. Such an investigation is particularly urgent in the context of the myriad of fabrication protocols developed for $FAPbI_3$, which currently focus relatively narrowly on elimination of δ-phase features in XRD patterns that has, however, been shown to be an inaccurate indicator [40, 41] of whether or not intrinsic quantum confinement will be present.

In this chapter, I unravel the extent to which intrinsic quantum confinement in $FAPbI_3$ affects solar cell performance. I contrast evidence of quantum confinement gathered from features in thin-film optical absorption spectra with photovoltaic performance parameters extracted from devices incorporating the same absorber layers. I directly examine three different fabrication routes as exemplifiers, but to ensure that my findings are generally applicable, I also perform a comprehensive meta-analysis of literature reports across the field. While my three experimentally fabricated $FAPbI_3$ films appear to be compositionally identical, the materials have experienced different crystallization dynamics and therefore are likely to possess different strain environments. Using structural and optical analysis I show that such variations strongly affect the extent to which the $FAPbI_3$ films exhibit domains experiencing intrinsic quantum confinement. I demonstrate a clear positive correlation between the photovoltaic power conversion efficiency and steady-state short-circuit current J_{SC} values of corresponding devices with the absence of peak features in absorption, revealing that intrinsic quantum confinement in $FAPbI_3$ hinders photovoltaic performance. In my meta-analysis of literature reports, I examine photovoltaic PCE data

reported for 825 devices with three-dimensional stoichiometric $FAPbI_3$ films as absorber layers across 244 literature articles, and categorise these according to whether or not intrinsic quantum confinement is evident in thin-film absorption spectra reported alongside. I discover that elimination of these features is highly correlated with the recent performance gains of $FAPbI_3$ solar cells. Importantly, I find that devices incorporating films that possess such features rarely exceed PCE value of 20%, suggesting that such intrinsically formed confinement domains provide inherent barriers that become clearly apparent once all other detriments have been eliminated. Accordingly, I propose that checking for the absence of these absorption features should be the first point of investigation when gauging the effectiveness of a new fabrication approach for $FAPbI_3$ thin films designed to act as photo-absorber layers in high-efficiency solar cells.

5.2 Results and discussion

5.2.1 Effect of fabrication method on thin film quality, crystallinity and quantum confinement

I focus my experimental investigation on stoichiometric $FAPbI_3$ films fabricated using three different solution-based processing routes. The first set of $FAPbI_3$ films (labelled "DMF-DMSO") were fabricated using the standard deposition method based on neat DMF-DMSO (DMF: N,N-dimethylformamide; DMSO: dimethylsulfoxide) solvent utilising "anti-solvent quenching" without any additives aimed at stabilizing the α-phase or slowing down the crystallization process. [9, 150, 151, 159] The second set of $FAPbI_3$ films (labelled "MACl route") resulted from DMF-DMSO solution-casting involving the use of excess MACl (methylammonium chloride) as an additive to induce an intermediate phase which is easily transformed to neat α-phase. [163] MACl thus effectively directs the crystallization process by providing an alternative crystallization pathway, and improving the grain size and crystallographic purity of the fabricated film. [150] Use of this additive has frequently been reported in the literature to stabilize the α-phase and consistently results in devices with enhanced PV performances, with fabrication methods now optimised to ensure the predominant exclusion of MA^+ and Cl^- ions from the crystal structure in order to yield near-stoichiometric $FAPbI_3$ films. [150, 151, 159, 163–165] The third set of $FAPbI_3$ films (labelled "Sequential") was fabricated through a sequential deposition method based on work by Noel et al. [166]. whereby first a 2D perovskite material is deposited, thermally treated, and subsequently converted to the α-$FAPbI_3$ phase by means of an alcoholic solution of formamidinium iodide, analogous to archetypical two-step processing methods of halide perovskites. [162, 167] Such sequential deposition allows for careful curation of a solid-state intermediate phase and initiates formation of high-quality $FAPbI_3$ in its black perovskite α-phase, suppressing inclusions of unintended structures. [159, 162, 166–168] Careful control over the emerging crystal structure can

therefore be attained, which provides the additional opportunity to investigate films fabricated through a significantly more controlled route compared to those of the $FAPbI_3$ films fabricated from neat DMF-DMSO solvent or even MACl-additive routes. [166] The film fabrication was performed by Benjamin M. Gallant and Philippe Holzhey. Further details about each individual fabrication method are presented in Appendix B.2.

Differences in film fabrication methods will directly influence the crystallization dynamics and structural properties of the resulting perovskite, [29, 99–102, 151, 159] which in turn will alter the optoelectronic and photovoltaic performance. I therefore begin by examining the recorded X-ray diffraction (XRD) patterns of the $FAPbI_3$ films, with Figure 5.1 showing the full XRD patterns, and Figure 5.3a showing the relevant region of interest. The good coincidence of the main pseudo-cubic (100) and (200) perovskite peak angles across the three different fabrication methods and their agreement with the expected literature value for α-$FAPbI_3$, [98] highlight that they indeed yield compositionally similar stoichiometric $FAPbI_3$ perovskite, without remnant inclusions of MA or Cl. However, differences between these fabrication methods can still be clearly observed in the XRD patterns. The full-widths at half-maxima (FWHM) of the main (100) and (200) perovskite peaks (displayed in Figure 5.2) reflect the longer-range crystalline order and/or lower microstrain in $FAPbI_3$ films fabricated from the MACl route and sequential deposition method, compared with those for the simple DMF-DMSO route. The scattering intensity of the main α-$FAPbI_3$ phase is orders of magnitude stronger for the MACl and sequential-deposition processed films, indicating increased texture. The XRD patterns further show a relatively small contribution from impurity phases such as PbI_2 and δ-phase $FAPbI_3$ (data are plotted on a logarithmic scale), that seem to show little systematic variation between processing routes, with the films resulting from sequential deposition exhibiting the highest scattering intensity for PbI_2, and those

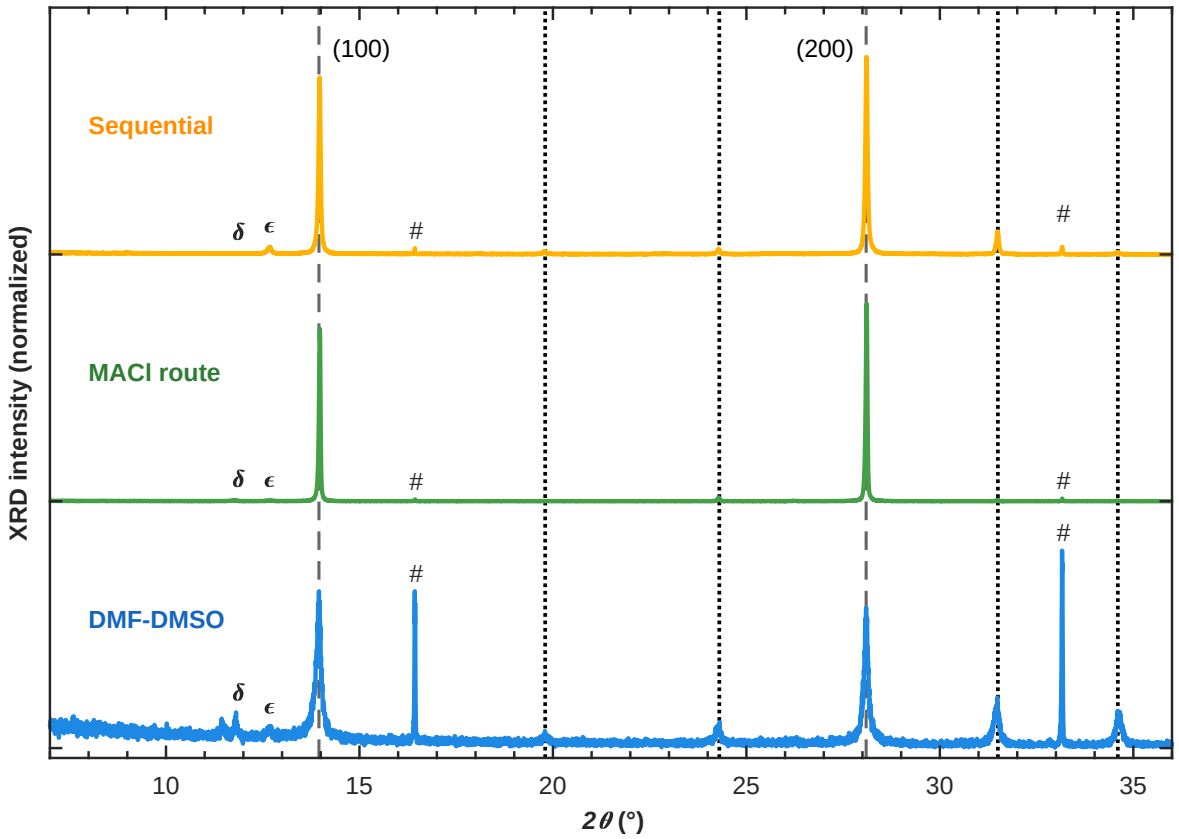


Figure 5.1: Normalized X-ray diffraction (XRD) pattern for $FAPbI_3$ thin films fabricated via DMF-DMSO, MACl route and sequential deposition method. The quartz substrate peak is indexed with #. The main pseudo-cubic α-$FAPbI_3$ peaks ((100) and (200)) are represented by the vertical black dashed lines at the experimentally measured values of 14° and 28.1° respectively. The literature values [98] of the less prominent cubic α-$FAPbI_3$ peaks are indicated by vertical black dotted lines, at 2θ values of $19.8°, 24.3°, 31.5°$, and 34.6°. The PbI_2 peak at 12.7° is indexed with ϵ. [114] The most prominent XRD peak for the non-perovskite δ-$FAPbI_3$ phase appears at 11.8°, [98, 169] and is indexed accordingly.

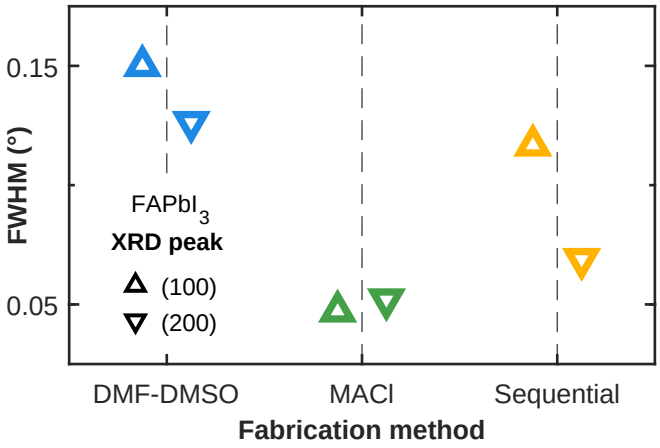


Figure 5.2: Full widths at half maximum (FWHM) of the prominent (100) α-$FAPbI_3$ XRD perovskite peak for $FAPbI_3$ thin films fabricated via DMF-DMSO, MACl route and sequential deposition method. Extracted FWHM of the two most prominent XRD peaks (100), and (200) for the investigated films.

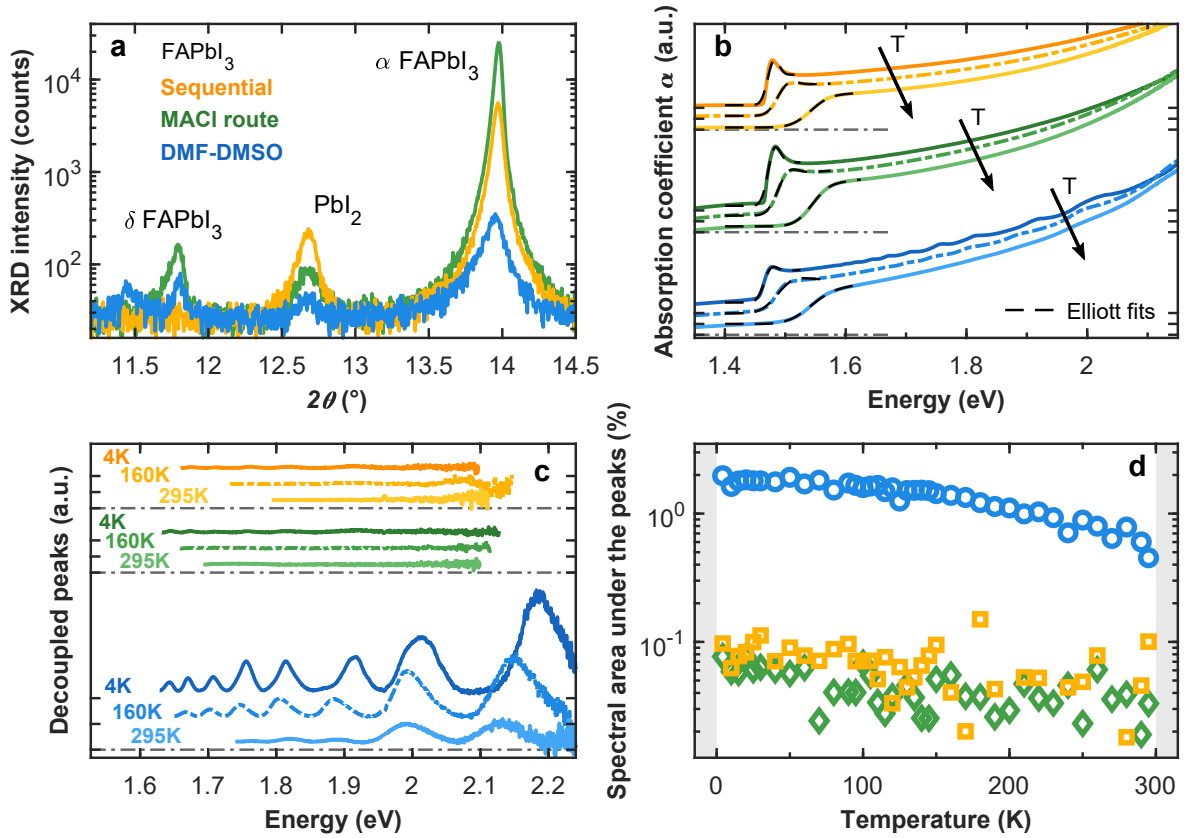


Figure 5.3: Structural and optical properties of stoichiometric $FAPbI_3$ films made from different fabrication methods. **a** Excerpts from recorded X-ray diffraction (XRD) patterns focusing on the pseudo-cubic (100) peak of α-$FAPbI_3$, the main peaks of the non-perovskite δ-$FAPbI_3$ phase, [98] and the peak of PbI_2 precursor residue. [114] Full XRD patterns are displayed in Figure 5.1. **b** Absorption coefficient spectra (colored solid lines) and Elliott fits to the absorption onsets (dashed black lines) of $FAPbI_3$ films fabricated via the "DMF-DMSO" (blue), "MACl route" (green), and "sequential" (yellow) solvent-based methods, recorded at 4 K, 160 K, and 295 K. The spectra recorded at different temperatures and for the different fabrication methods are vertically offset for visual clarity, with the black y-axis ticks marking the zero baseline for each successive curve. A direct comparison of the absorption coefficient spectra is presented in Figure B.3. **c** Peak features decoupled from the underlying, bulk-like absorption spectrum at 4 K, 160 K, and 295 K presented on the same scale. The spectra at different temperatures and for the different fabrication methods are vertically offset for visual clarity, with the black y-axis ticks marking the zero baseline for each successive curve. **d** Spectrally integrated area underneath the absorption peaks shown in (**c**), given as a percentage of the total area under the absorption coefficient spectrum, used to parameterize the occurrence of quantum confinement, and shown as a function of temperature for the differently-fabricated $FAPbI_3$ films. (The fabrication method legend in (**a**) also applies to (**b**), (**c**), and (**d**), and the temperature legend in (**c**) also applies to (**b**).)

derived from the MACl route the highest scattering intensity for the δ-phase $FAPbI_3$. I note however, that the presence of such features has been found to correlate poorly with the strength of absorption peak features, likely because the potential structural barriers causing these effects are too thin to be detectable in XRD. [40]

To further interrogate this apparent increase in the texturing of the films using the MACl route and the sequential deposition approach, I focus my attention on the relative intensities of the main perovskite peaks and those of crystallographic defect phases present in the system. The relative amplitude is a particularly useful parameter to gauge crystalline quality given that the thickness of the films were optimised for each fabrication method, resulting in a difference in thickness across these films which naturally will affect the absolute intensities of the XRD peaks. As expected, the $FAPbI_3$ films fabricated using the MACl additive-based route and sequential deposition method exhibit superior perovskite crystallinity, improved crystallographic purity, better perovskite conversion, and lower relative intensity peaks arising from crystallographic impurities. The significantly lower XRD peak intensity for PbI_2 precursor remnants relative to the main perovskite peak signifies better perovskite conversion for the $FAPbI_3$ films fabricated from the MACl route and sequential deposition method (see Figure 5.3a). The presence of XRD peaks associated with the different hexagonal polymorphs at 11.5° [169], and 11.8° [98, 169] for the $FAPbI_3$ films fabricated via the neat DMF-DMSO route, along with their substantially larger relative intensity with respect to the main perovskite peaks demonstrate the film's relatively poor crystallographic purity and highlight the stronger presence of the δ-phase along with a plethora of other hexagonal polymorphs [169] in such films (see Figure 5.3a). Such poor crystalline quality existing for the films fabricated via the neat DMF-DMSO route is additionally evident from the significantly higher intensity of the quartz substrate peak at $2\theta = 16.22°$ relative to the (100) and (200) main perovskite peaks in the full XRD patterns in Figure 5.1, which is evidence for poor

perovskite conversion even for a 340 nm thick film. These data confirm an increase in crystallinity and a higher degree of orientation in films fabricated through additive-based or sequential deposition approaches.

Top-down and cross-sectional SEM images of the films made from the different fabrication methods are displayed in Figure 5.4 and Figure 5.5 respectively. SEM measurements were performed by Benjamin M. Gallant. The top-down SEM images highlight the surface morphological changes occurring in the absorber layer when the fabrication protocol is varied. While, the cross-sectional SEM images provide accurate measurements of the thicknesses of the films made from the different fabrications methods. They additionally importantly highlight the substantially enlarged and monolithic grain structure for the $FAPbI_3$ thin films fabricated via the MACl route and sequential deposition method, compared to the films made via the neat DMF-DMSO route suffering from intragrain structures, similar to previous reports in the literature. [163, 170]

I proceed by probing how the three different fabrication approaches affect the occurrence of intrinsic quantum confinement in $FAPbI_3$ films. For this purpose, I measured the absorption coefficient spectra at a range of different temperatures from 295 K down to 4 K (displayed in Figure 5.3b) in order to determine the fraction of the absorption spectrum that exhibits the peak features that have been associated with such confinement in the past. [40, 41] While cryogenic temperatures are less relevant to photovoltaic operation, it has recently been shown that they enhance the sharpness and amplitudes of the absorption features, making them easier to discern and evaluate accurately. [40, 41] To analyse the absorption coefficient spectra, I first fitted the onset with Elliott's theory which takes into account the excitonic contribution and Coulombic enhancement to the absorption spectrum [52, 54] (see dashed lines in Figure 5.3b). These

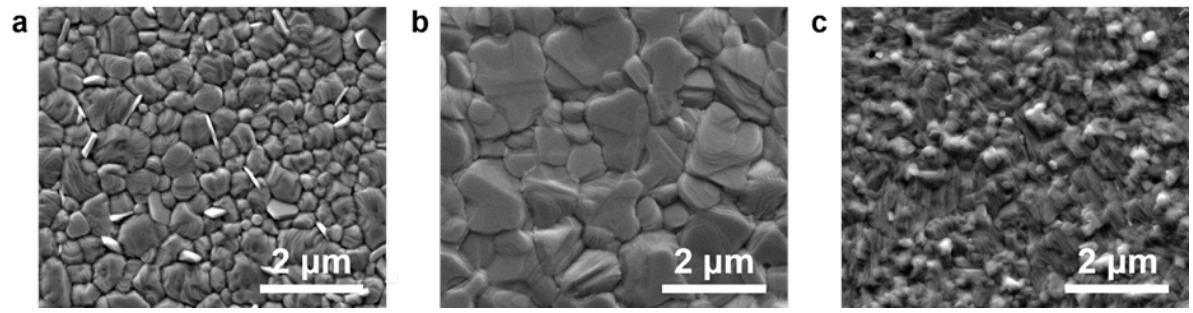


Figure 5.4: Top-down SEM images of photovoltaic devices incorporating the differently-fabricated $FAPbI_3$ films. a. $FAPbI_3$ film made via neat DMF-DMSO route, **b**. $FAPbI_3$ film fabricated through the MACl route, and **c**. $FAPbI_3$ made via the sequential deposition route. SEM measurements were performed by Benjamin M. Gallant.

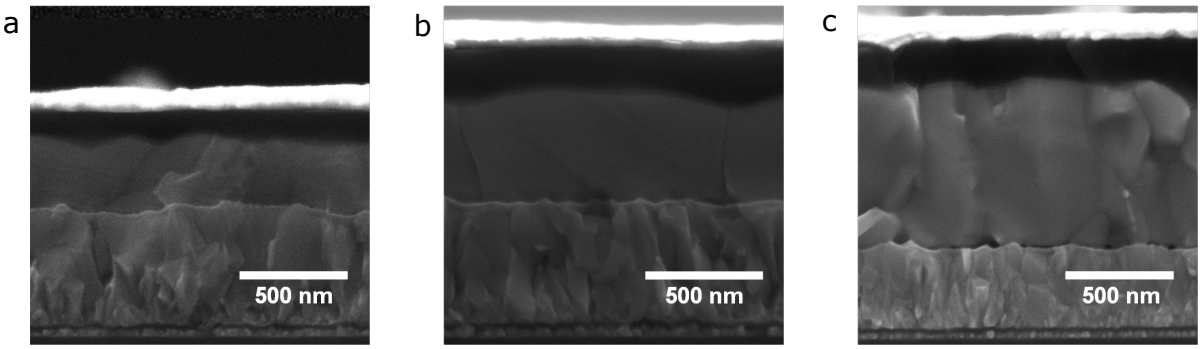


Figure 5.5: Cross-sectional SEM images of photovoltaic devices incorporating the differently-fabricated $FAPbI_3$ films. a. $FAPbI_3$ film made via neat DMF-DMSO route, with an optimal thickness of 340 nm, **b**. $FAPbI_3$ film fabricated through the MACl route, with an optimal thickness of 440 nm, and **c**. $FAPbI_3$ made via the sequential deposition route, with an optimal thickness of 770 nm. This device stack comprises FTO, SnO_2 nanoparticles, perovskite layer with a PEAI surface treatment, Spiro OMeTAD, Au electrodes. SEM measurements were performed by Benjamin M. Gallant.

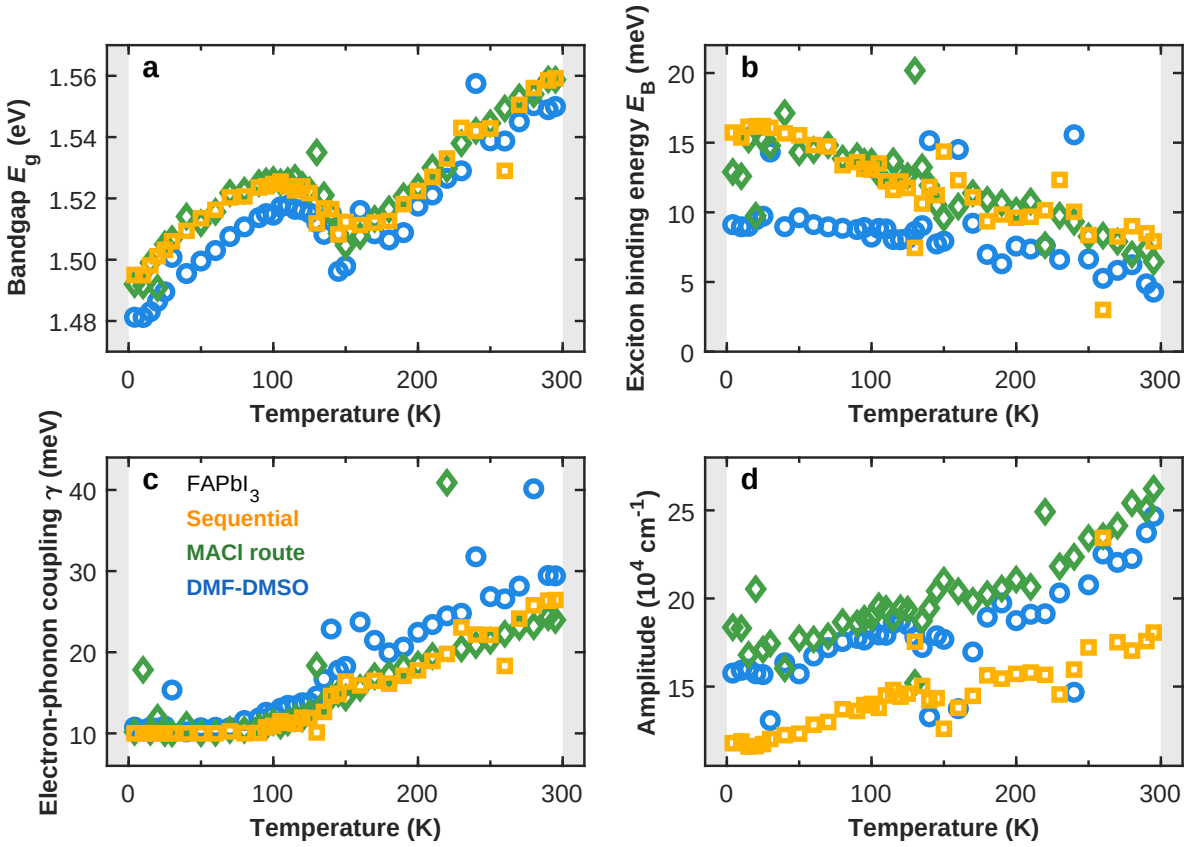


Figure 5.6: Extracted fitted parameters from Elliott fitting of the absorption onset of stoichiometric $FAPbI_3$ thin films fabricated via DMF-DMSO, MACl route and sequential deposition method. The absorption coefficient spectra were fitted with 4 free parameters: E_g representing the optical bandgap, E_b representing the exciton binding energy, γ representing the broadening arising from energetic disorder within the film, and Amp representing the amplitude of the spectrum.

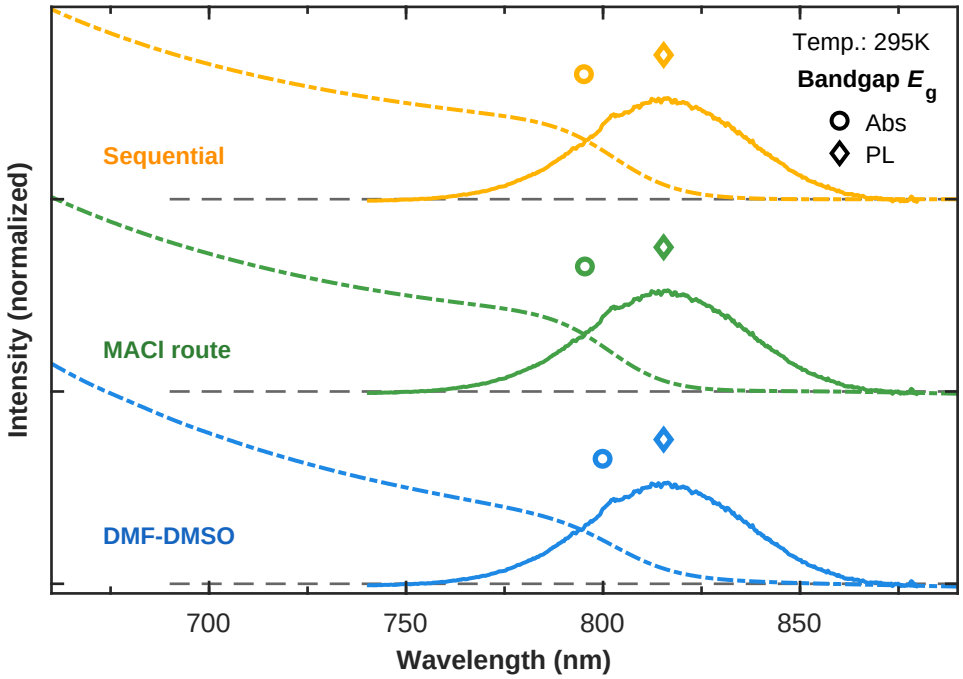


Figure 5.7: Room temperature photoluminescence and absorption coefficient spectra of stoichiometric $FAPbI_3$ films fabricated via DMF-DMSO, MACl route and sequential deposition method. The small peak feature near 800 nm originates from the second-order diffraction of the scattered laser excitation centred at 398 nm.

fits yielded parameters such as the optical bandgap and exciton binding energy (see Figure 5.6) that are very similar in both value and temperature trends for the films made through the three fabrication routes, further highlighting that these films are compositionally similar. Similarly, room-temperature PL peak energies are found to be identical for all three types of $FAPbI_3$ films (see Figure 5.7). As a second step, to determine the contribution to the absorption spectrum arising from quantum confinement, I decoupled the above-bandgap absorption peak features from the underlying, smooth, bulk-like spectrum using the process previously reported. [40, 41] I chose a phenomenological spline baseline connecting all the troughs of the features together, and subtracted this baseline from the full absorption spectrum. The resulting decoupled peaks associated with intrinsic quantum confinement are shown in Figure 5.3c for different $FAPbI_3$ film fabrication methods and temperatures. [40, 41] As a numerical parameter characterising the relative prominence of quantum confinement, I evaluated the area between the experimental absorption coefficient spectrum and the spline baseline connecting the troughs (i.e. the integral over the decoupled peak spectra such as those shown in Figure 5.3c), as a percentage of the overall area under the absorption spectrum. This "spectral area under the peaks" is shown in Figure 5.3d as a function of temperature for the $FAPbI_3$ films processed by the three different methods.

Intriguingly, this analysis reveals that the fabrication method has a profound influence on the prominence of the absorption peak features, despite these all being stoichiometrically similar $FAPbI_3$ films. While $FAPbI_3$ films fabricated from the neat DMF-DMSO method exhibit very prominent absorption peak features, those features are over an order of magnitude lower in amplitude and hardly discernible for the films fabricated through the MACl and sequential deposition routes, even at very low temperatures down to 4 K (Figure 5.3c,d). These differences clearly point towards the crystallization process,

the experienced strain in the system, and/or small inclusions of δ-phase or one of its polymorphs playing a significant role in the self-assembly of domains causing electronic confinement in the perovskite film. Such variations make sense in the context of quantum confinement in $FAPbI_3$ having been proposed to be caused by inclusions of thin layers of δ-phase that act as electronic barrier to the α-phase, possibly to achieve periodic strain relief in the system. [40] Similarly, a range of different hexagonal polytypes have been shown to create peaked absorption features at various energies. [169] The presence of these peaked absorption features in $FAPbI_3$ therefore appear to be direct indicator of crystalline quality. The comparatively uncontrolled crystallization process associated with the neat DMF-DMSO fabrication method is known to result in poorer crystallographic quality of $FAPbI_3$ films and an instability towards reversion into the δ-phase, [71, 101, 150, 151, 159] and these films exhibit strong absorption peak features. In contrast, the MACl additive provides intermediate-phase directed crystallization which yields better control over growth dynamics, while the sequential deposition method nucleates α-phase growth, both of which lead to superior crystalline quality, and, as I show here, a significantly lower propensity towards formation of inferred quantum-confined domains. [163, 171] I therefore demonstrate that thin-film nucleation and crystallization control can regulate and eliminate the quantum confinement experienced in $FAPbI_3$.

5.2.2 Effect of quantum confinement on photovoltaic performance

Experimental evidence

The appearance of domains exhibiting electronic confinement has the potential to hinder charge-carrier extraction in solar cells. I thus proceed by assessing the extent to which the presence of such absorption features affects the performance of photovoltaic devices incorporating $FAPbI_3$ absorber layers fabricated using the neat DMF-DMSO, MACl, and sequential deposition routes. Measurement of photovoltaic performance and device fabrication were performed by Benjamin M. Gallant. Devices were fabricated using a typical n-i-p configuration (FTO/SnO_2/$FAPbI_3$/PEAI/spiro-OMeTAD/Au). Here, the films used are compositionally alike as demonstrated by the structural and optical measurements above, and the device stacks are similar enough that the steady-state J_{SC} should be an accurate reflection of the intrinsic efficiency with which the photo-excited charge carriers move through the film. Some small differences between these films may however exist which may slightly affect their PV properties. The energy landscape of each film and how well their conduction band minimum (CBM) and valence band maximum (VBM) match those of the transport layers may slightly vary across the different fabrication methods because of the difference in lattice distortions present in the crystal. The tilting of the perovskite octahedra or the slight change in the lattice parameter caused by a contraction or an expansion as a result of extra stress or relief in the system can cause a change in the orbital overlap of the Pb and I ions which would slightly change the positions of the CBM and VBM [31, 117], changing the energetic alignment with the transport layers, and yet still resulting in similar bandgaps. However, a better-matched perovskite band alignment with the transport layers would mainly result in an improvement in the steady-state V_{OC}, maintaining the validity of this method of using the steady-state J_{SC} as an accurate gauge of how unobstructed the photocurrent

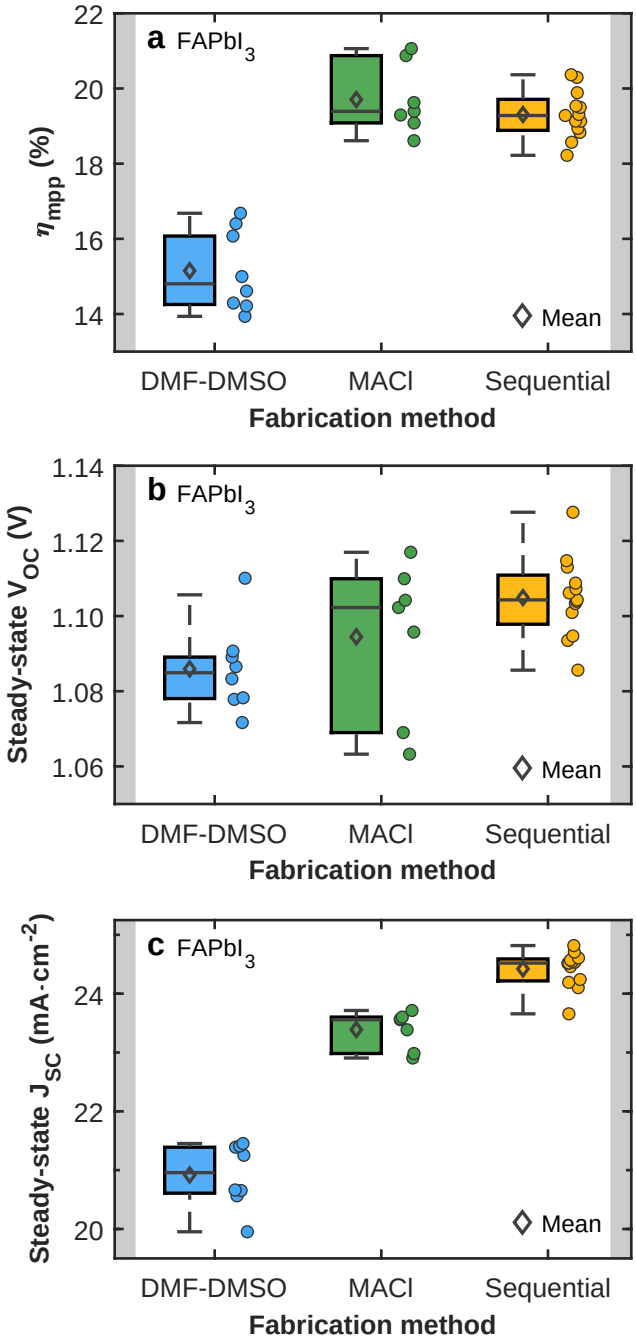


Figure 5.8: Performance parameters for photovoltaic devices incorporating $FAPbI_3$ films made from different fabrication methods. Box and scatter plots showing the steady-state photovoltaic parameters for devices based on $FAPbI_3$ absorber layers fabricated through the "DMF-DMSO" (blue), "MACl route" (green), and "sequential" (yellow) solvent-based methods; **a** maximum power point tracked power conversion efficiency (η_{mpp}), **b** steady-state open-circuit voltage (V_{OC}), and **c** steady-state short-circuit current density J_{SC}. The scatter points represent the different device pixels investigated. A comparison of the performance parameters for photovoltaic devices incorporating $FAPbI_3$ films of different thicknesses fabricated via the "DMF-DMSO" route is displayed in Figure 5.9. Photovoltaic performance was measured by Benjamin M. Gallant.

is. Therefore, the main difference in PV performance parameters should be associated with the properties of each $FAPbI_3$ photo-absorber layer. Accordingly, the steady-state short-circuit current density (J_{SC}) of optimized devices can be treated as a parameter to gauge how efficient and unobstructed the charge-carrier motion is throughout the MHP layer. Full details of device fabrication and more detailed comparisons of the performance parameters for these devices are presented in Appendix B.7.

A direct comparison of photovoltaic performance parameters for devices incorporating stoichiometric $FAPbI_3$ films made with the three different fabrication methods is displayed in Figure 5.8 and Figures B.4 - B.7. The PCEs and steady-state J_{SC} values exhibit a notable improvement for $FAPbI_3$ films fabricated through the MACl route and sequential deposition method, compared with the neat DMF-DMSO method. I note that the MACl route and sequential deposition procedure have been shown to result in improved interfacial alignment with the employed transport layers and trap passivation [172–174] that are likely to be responsible for the slight increase in steady-state open-circuit voltage (V_{OC}) of the corresponding devices I observe here (Figure 5.8b). However, such improvements would not be expected to also cause a significant enhancement to the charge-carrier extraction capabilities, and yet, devices incorporating films fabricated through the MACl and sequential deposition routes possess a substantially higher steady-state J_{SC} than those made from the neat DMF-DMSO protocol. Instead, these improvements in steady-state J_{SC} with the MACl route and sequential deposition approach appear to be correlated with the removal of the absorption peak features for these types of absorber layers I reported above. Such quantum confinement domains thus appear to induce significantly lower stabilsied J_{SC} as a clear indication of poor charge-carrier extraction, consistent with the emergence of high-energy potential barriers obstructing transport across the film.

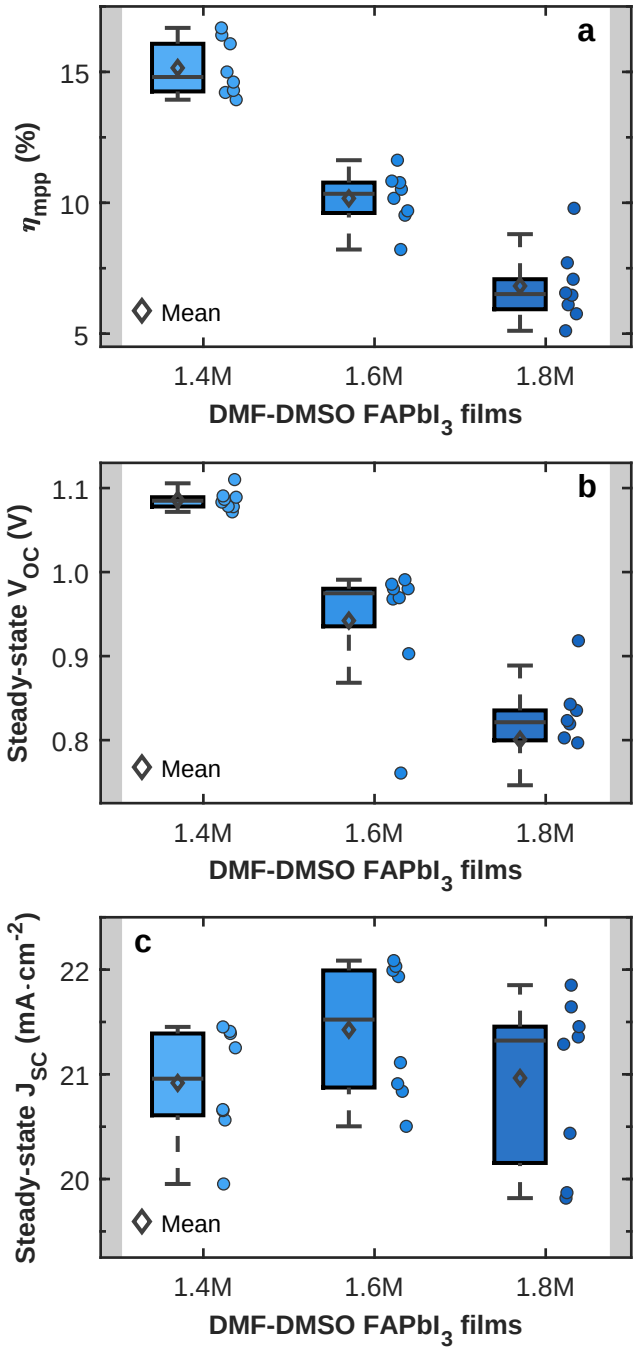


Figure 5.9: Performance of photovoltaic devices incorporating $FAPbI_3$ absorber layers made from the neat DMF-DMSO route using different FAI precursor molar concentrations that resulted in different film thicknesses. Box and scatter plots showing the photovoltaic device parameters obtained from $J-V$ curves for $FAPbI_3$ films made from the neat DMF-DMSO route using different FAI precursor molar concentrations that resulted in different film thicknesses; **a**. Maximum power point tracked power conversion efficiency, **b**. Steady-state V_{OC}, and **c**. Steady-state J_{SC}. The scatter points represent the different pixels investigated. Photovoltaic performance was measured by Benjamin M. Gallant.

It is worth noting that for each $FAPbI_3$ film fabrication type, the absorber layer thickness was optimized for best performance, yielding 340 nm, 440 nm, and 770 nm for the neat DMF-DMSO, MACl, and sequential deposition routes, respectively (see SEM images in Figures 5.4 - 5.5, and Figure B.2 in Appendix B.4). [166] While I acknowledge that generally, increasing the thickness of the perovskite layer will result in increased light absorption and hence, current generation, that expected increase in current generation might not be sufficient to explain the observed significant increase in steady-state J_{SC} for solar cells incorporating $FAPbI_3$ layers fabricated through the MACl route and sequential deposition method, compared to those made via the neat DMF-DMSO route. Therefore, to investigate in more detail this major increase observed in steady-state J_{SC}, a comparison was conducted of photovoltaic parameters for films made via the neat DMF-DMSO route, but with different molar concentrations of FAI, resulting in films with different thicknesses. As shown in Figure B.2, the resulting thickness values of the perovskite films are 340 nm, 450 nm, and 440 nm for 1.4 M, 1.6 M, and 1.8 M FAI precursor solutions respectively. Figure 5.9 demonstrates that devices with thicker $FAPbI_3$ films perform substantially worse when compared to the 1.4 M-FAI $FAPbI_3$ film with 340 nm thickness (which represented the value for which the power conversion efficiency was optimised) with the V_{OC} and η_{mpp} for the thicker devices representing the main culprits behind the worsened PV performance. These results could reflect a more defective perovskite-transport layer interface, possibly caused by an increased surface roughness, or too rapid a crystallization process resulting from the higher concentration $FAPbI_3$ precursor solution used, which naturally supersaturates earlier in the deposition process.

More intriguingly, the steady-state J_{SC} values have a different dependence on the precursor concentration and film thickness than V_{OC} values. As discussed in Section B.4, the thickness of the $FAPbI_3$ films are 340 nm, 450 nm, and 440 nm for the 1.4 M, 1.6 M, and 1.8 M precursor solutions respectively, and the steady-state J_{SC} seems to

generally follow the same variation in thickness. This suggests that these devices are, to a small extent, limited by the thickness of the photo-absorber layer. However, the comparison between the 440 nm-thick $FAPbI_3$ film made from the neat DMF-DMSO route (shown in Figure 5.9), and the equally-thick film made via the MACl route (Figure 5.8) sheds more light on the main factor limiting the charge-carrier extraction. Even with the increase in stabilsied J_{SC} owing to the use of a thicker $FAPbI_3$ film from the neat DMF-DMSO method, its value still lags behind that obtained for the film made from the MACl route by ca. $2\,mAcm^{-2}$. It is therefore clear the devices made with $FAPbI_3$ films of similar thicknesses, processed with and without the MACl additive, still possessed a substantial difference in their steady-state J_{SC} values. As such, I conclude that the thickness variations in the optimised devices do not affect my general conclusions.

Literature review

My analysis suggests that the quantum confinement present in $FAPbI_3$-rich films heavily depends on the fabrication method and is detrimental to the performance of the associated photovoltaic device. To examine whether these findings hold more generally beyond the investigated fabrication methods, I conducted a meta-analysis across a wide range of literature reports. The meta-study was carried out by correlating reported PCE values of $FAPbI_3$ solar cells with the presence or absence of quantum confinement, as determined from the analysis described and used above of the presence of peak features in the absorption spectra of corresponding films. Selection was effectively limited to devices whose photo-active layer was reported to be $FAPbI_3$ three-dimensional perovskite thin films, i.e. I excluded any reports where additives or treatments were proven to be fully incorporated into the crystal structure such that they changed the stoichiometry. As a result, 244 unique publications were included in the meta-study, and a total of 825

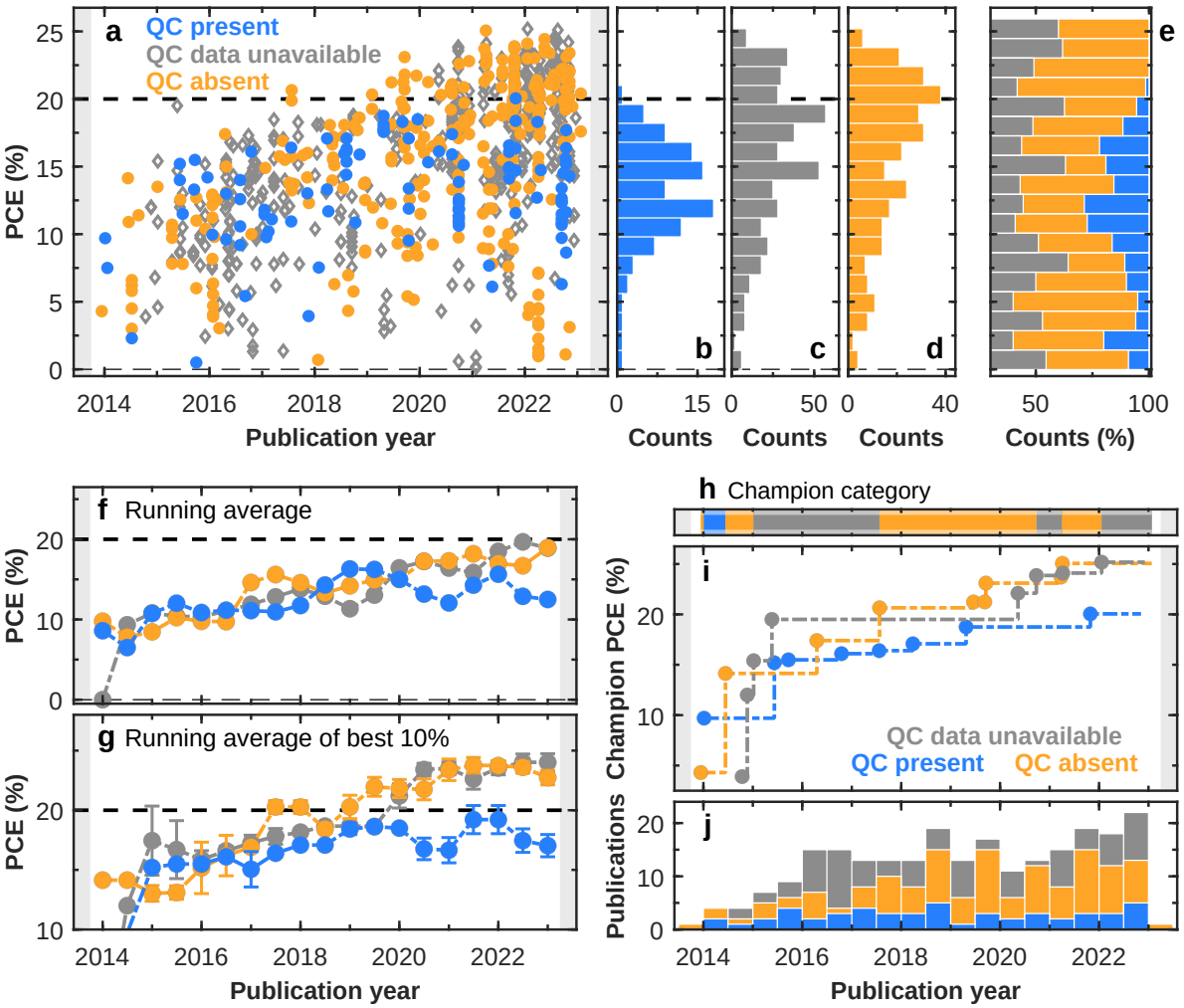


Figure 5.10: Meta-analysis of photovoltaic device performance and presence of absorbance features for $FAPbI_3$ thin films extracted from literature. **a** Reported PCE values of single-junction solar cells whose photo-absorber layers compromise stoichiometric bulk $FAPbI_3$ thin films, plotted as a function of publication year, visualized for three categories of $FAPbI_3$ films; films with above-bandgap "quantum confinement (QC)" absorption features present (labelled as "QC present", blue), films for which absorption spectra were unavailable or of insufficient quality or spectral range (labelled as "QC data unavailable", grey), and films for which absorption data showed no discernible peak features, or features below a certain low threshold (labelled as "QC absent", orange), see Appendix B.8 for full details. **b**, **c**, **d** The total time-integrated device count for each PCE range across the "QC present", "QC data unavailable", and "QC absent" categories, respectively. **e** The relative contribution of each category to the available device data for every PCE range, integrated over the years of publication. **f**, **g** Running average of PCE values recorded for all devices reported in literature, and for the best 10% of devices respectively, for each category with an averaging window of one year. **h** The time evolution of the absorber film category associated with the highest PCE $FAPbI_3$ devices. **i** The time evolution of the highest PCE device for each absorber film category. **j** Distribution of the number of unique publications with data on solar cell performance for $FAPbI_3$ films as a function of publication year divided into the three absorber film categories. (The color legend in **a** also applies to **b-j**.)

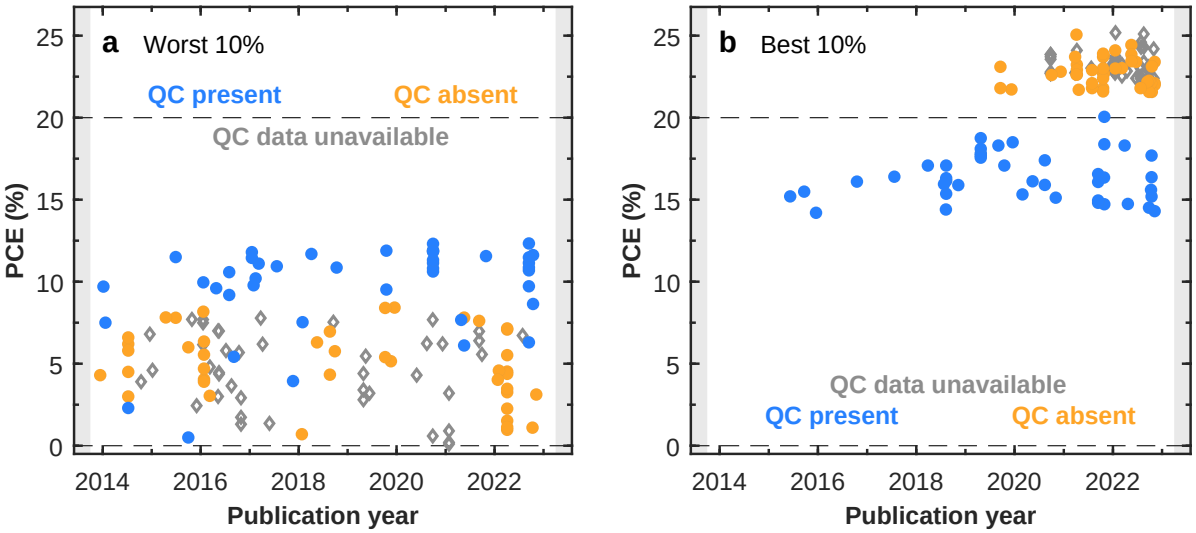


Figure 5.11: Meta-study of device performance and absorbance features of $FAPbI_3$ thin films. Scatter plot of the devices with the lowest (**a**) and highest (**b**) 10% PCE data for each category.

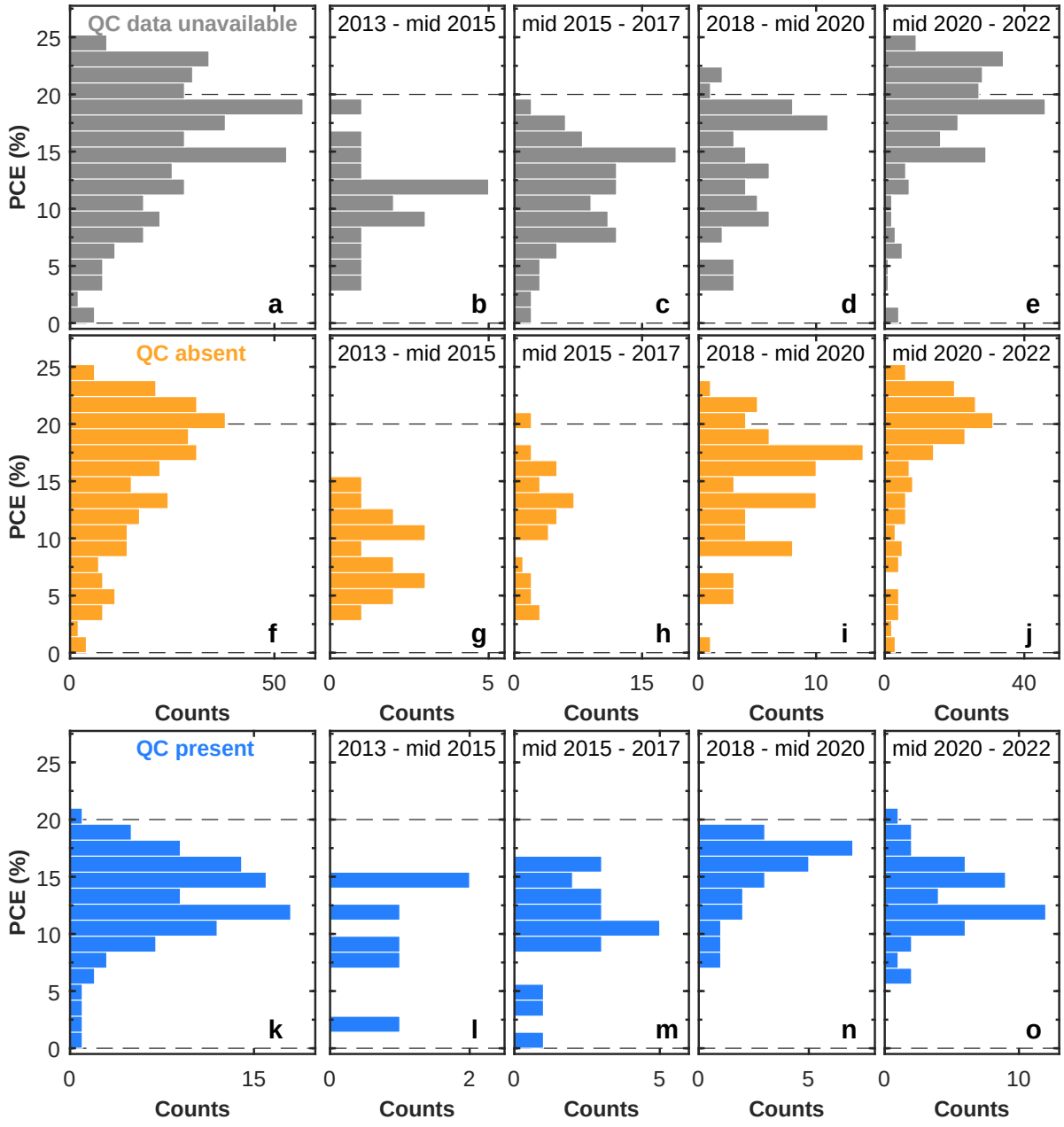


Figure 5.12: Meta-study of device performance and absorbance features of $FAPbI_3$ thin films. Spread of the time-integrated PCE values in Main Figure 5.10a, for devices in the "QC data unavailable", "QC absent", and "QC present" categories.

device performance reports, providing statistically significant correlation data between PV performance and the presence of quantum confinement (QC). The PV performance data were either the batch-averages across many reported devices, or data corresponding to the champion cell if an average was not reported. Overall, the very large number of devices and published reports on the $FAPbI_3$ composition (see also Figure 5.10j) is directly reflective of the historical and continued interest in this thermally-stable composition. To assess the correlation between photovoltaic performance and the presence of quantum confinement, I divided the parameters associated with different devices into three unique categories. First, solar cells whose corresponding photo-absorber layer either possessed easily-discernible above-bandgap absorption features or features above a certain minimum threshold were labelled “QC present" and amounted to 100 devices. Second, solar cells with no apparent visible features or features below the threshold were labelled “QC absent” and amounted to 302 devices. Finally, when absorption spectra were absent in the publication reporting the PV performance, or were too noisy to allow conclusion of presence or absence of features, this was labelled “QC data unavailable" and amounted to 423 devices. I note that only about half (48.7%) of the reported device performance parameters come with sufficient absorption data. While this still provides us with ample available data (402 device reports) to retrieve statistically significant correlations, it highlights that insufficient attention has been devoted to these absorption features and their relevance to photovoltaic device performance to date. Full details on the nuances of my meta-study can be found in Appendix B.8.

The results from my meta-analysis are visualized in a range of different scatter plots in Figures 5.10 - 5.12 and Figures B.8 - B.15. At first sight, it is apparent that PCE values of $FAPbI_3$ solar cells follow a clear upward trajectory of continuous enhancement of PV properties over time, culminating in the highest certified PCE for a

MHP single junction of 25.7% [7, 175] for this composition (Figure 5.10a). Examining device performance according to the three categories of quantum confinement (present, absent, data unavailable) it also becomes clear that such QC effects have been present since the first realization of working $FAPbI_3$ PV devices, and that the simple running average of the PCE follows a similar upward trajectory (see Figure 5.10f). This unrelenting enhancement demonstrates the intense interest invested by the field in this composition and highlights the success of current research in tackling some major hurdles such as reducing defect concentration, improving crystallinity, interface quality, and charge extraction layers. However, more recently, noticeable differences have started to emerge as devices are breaking through the 20% PCE ceiling - reflective of a region where quantum confinement appears to become the decisive factor.

Such evidence for QC features in absorption restricting performance near the Shockley-Queisser limit can be seen in the meta-data in a number of forms. First, Figure 5.10a shows that since 2019, any meaningful progress in PCE values of devices in the “QC present" category (blue dots) has stalled, with a maximum of only 20.05% attained, compared with 25.06% for the “QC absent" and 25.18% for the “QC data unavailable" category, suggesting that an intrinsic barrier exists for efficient charge-carrier extraction and PV performance for devices employing films possessing these peculiar QC features. The time-integrated PCE spread in Figure 5.10b,c,d clearly highlights an abundance of devices in the “QC absent" and “QC data unavailable" categories with PCE values regularly exceeding the 20% mark, while devices in the “QC present" category very rarely approach that threshold. This is further illustrated in Figures 5.10h,i which show that both the “QC absent" and “QC data unavailable" categories also dominate the champion performance since 2014. Finally, Figure 5.10g provides a temporal evolution of the running average of the best 10% of all devices within each of the three categories showing that even for such averages across the top end of the performance spectrum, the “QC

absent" and “QC data unavailable" categories clearly outrun the performance of devices in the “QC present" category. Overall, these meta-data clearly reflect the stagnation in the PV enhancement of the devices in the “QC present" category, and the futility of attempts to improve the PCE of a device beyond 20% without attempting to suppress these absorption peak features. Based on this established correlation, a necessary but insufficient condition to obtain devices with efficiencies exceeding ∼20% is to ensure the absence of any above-bandgap QC features in the absorption spectrum. I note that, in fact, most of the recent literature-reported attempts to alter the fabrication method of this promising composition with the aim of optimising its photovoltaic performance have inadvertently been suppressing these peculiar absorption features. [94, 99, 165, 176–185] However, the lack of comment on such features in literature reports, and an absence of absorption spectra in over half of the reports I examined, clearly show that little attention has to date been paid to this simple design and validation criterion. Accordingly, I propose that a first point for investigating a new fabrication protocol for $FAPbI_3$ films to be incorporated into solar cells should be to discern the presence or absence of these peak features in the thin-film absorption spectrum. Such simple assessment can ascertain whether there is a tendency for the fabricated $FAPbI_3$ films to include electronic barriers that are too thin to be detectable in XRD patterns, but that may still inhibit charge-carrier extraction, and whose elimination will thus pave the way for high-performance solar cells.

5.3 Conclusion

In conclusion, my work has shown that to realize the highest performing solar cells based on the attractive $FAPbI_3$ perovskite, quantum confinement needs to be fully eliminated from within the thin-film layer, most likely because it impedes charge-carrier transport and hence restrains the maximum attainable steady-state J_{SC} values. I have conclusively demonstrated this finding through two approaches. First, I have examined a set of stoichiometric $FAPbI_3$ films with varying degrees of quantum confinement induced by means of three different solution-based film fabrication processes. Those methods capable of reducing the strain, directing and controlling crystallization, and thus increasing perovskite crystalline quality strongly suppressed the quantum confinement features and clearly enhanced the solar cell performance parameters, in particular obtainable steady-state J_{SC} values. Second, I have performed a meta-analysis across 244 publications, analysing 825 occurrences of PCE data from $FAPbI_3$ solar cells in order to search for correlations with the presence or absence of the quantum confinement features evident from peaks in the matching absorption spectra. My meta-study reveals that for $FAPbI_3$ solar cells to break through the 20% PCE ceiling, quantum confinement effects should be absent from the film.

These conclusions clearly highlight simple checks for peaked absorption features as an easy step in the development of new thin-film fabrication procedures aimed at delivering efficient photovoltaic cells based on $FAPbI_3$. I note that the presence or absence of phase impurities, such as the δ-phase, in XRD patterns is unlikely to be as conclusive, because even $FAPbI_3$ films with strong absorption peak features have at times been found to display no discernible δ-phase peak in XRD. [40] These electronic barriers may thus offer too few lattice planes to allow sufficiently sharp deflection of x-rays,

leading to insufficiently sharp XRD peaks that cannot easily be detected. The alternative criterion I propose here, i.e. an examination of the absorption spectrum, is a simple and experimentally-straightforward approach already accessible in the vast majority of research laboratories. This approach should therefore be an easy and powerful means to gauge the effectiveness of any newly-developed treatment method for $FAPbI_3$ thin-film absorber layers. Overall, my findings will accelerate power conversion efficiencies of the most commercially viable MHP on the last stretch towards the maximum theoretical attainable efficiencies for single-junction photovoltaic devices.

6

Charge-carrier dynamics in quantum confined perovskites

Contents

6.1 Motivation 136
6.2 Results and discussion 138
6.2.1 3-dimensional $FAPbI_3$ 138
6.2.2 2-dimensional perovskites 147
6.3 Conclusion 158

In this chapter, I investigate the dynamics of charge carriers within different sample sets of perovskite semiconductors experiencing different types and strengths of quantum confinement.

The work presented in this chapter is a combination of a couple of projects currently in the peer-review stage (Gallant, B.M., Holzhey, P., Smith, J.A., Choudhary, S., **Elmestekawy, K.A.**, Caprioglio, P., Levine, I., Sheader, A., Yang, F., Toolan, D.T.W., Kilbride, R.C., Zaininger, A.K.A., Ball, J.M., Christoforo, G., Noel, N., Herz, L.M., Kubicki, D.J., and Snaith, H.J. 'From 2D to 3D: A Green Solvent System for Templated Sequential Deposition of Perovskite Solar Cells', *Nature Energy.*) and (Zanetta, A., Larini, V., Toniolo, F., Vishal, B., Vikram, **Elmestekawy, K.A.**, Du, J., Scardina, A.,

Faini, F., Pica, G., Pirota, V., Marras, S., Ding, C., Yildirim, B., Babics, M., Ugur, E., Aydin, E., Ma, C., Doria, F., Loi, M.A., De Bastiani, M., Herz, L.M., Portale, G., De Wolf, S., Islam, S., and Grancini, G. 'Breaking Transport Limits by Vertically Orienting Low-Dimensional Perovskites: The Oath to High Efficiency Wide Band Gap Perovskite Solar Cell', *Nature Energy.*).

6.1 Motivation

In the previous two experimental chapters, I have both demonstrated the ability to control the intrinsic quantum confinement in $FAPbI_3$ and FA-rich MHP compositions through different fabrication protocols, and correlated the presence of quantum confinement with an inherent limitation on the maximum achievable PCE of a PV device made out of that composition. In this chapter, I aim to expand my investigation of quantum confinement in its many forms in MHPs and explore how it can affect the optoelectronic and charge-carrier transport properties of the semiconductor.

In the first part of this chapter, I analyze the optoelectronic properties of the same films studied in Chapter 5. Namely, a DMF-DMSO $FAPbI_3$ film fabricated using the historically standard deposition method (labelled "DMF-DMSO"), [9, 150, 151, 159], a DMF-DMSO $FAPbI_3$ film fabricated with an excess of MACl to improve the crystalline quality of the perovskite crystal (labelled "MACl route"), [150, 151, 159, 163–165] and a $FAPbI_3$ film fabricated through a sequential deposition method to have better control over the intermediate phases and crystallization route (labelled "Sequential"). [159, 162, 166–168] This analysis portrays how the fabrication method of a 3-dimensional semiconductor and the presence or absence of the intrinsic quantum confinement in $FAPbI_3$ are able to affect the charge-carrier transport properties and the optoelectronic quality of the emerging semiconductor.

In the second half of this chapter, I extend the analysis conducted for the 3-dimensional films with intrinsic quantum confinement to 2-dimensional perovskite semiconductors with much stronger quantum confinement. As discussed in Chapter 2.2.3, 2-dimensional perovskites are fabricated with strong quantum confinement in mind; a large insulating organic molecule is used in place of the A-site cation in the standard ABX_3 perovskite structure. These long-chained organic molecules are too large to fit within the perovskite

structure and effectively act as insulators separating the conductive perovskite octahedral slabs. The ratio of large organic spacer molecules to the typical small A-site cations determines the dimensionality of the semiconductor; such that the semiconductor can be considered as fully 2-dimensional when no small A-site cations exist, 3-dimensional when no large spacer molecules exist, and quasi-2-dimensional for any ratio in between.

Additionally, the strength of the quantum confinement in these 2-dimensional material and the plausibility of charge-carrier transport across the insulating layers (inter-slab charge-carrier transport) both depend on the length of the insulating organic molecule and the dielectric mismatch between the conductive slabs and the spacer molecules. [15, 24, 25] However, due to the extreme sensitivity of inter-slab charge-carrier transport (whether it is charge-carrier tunnelling or Förster resonance energy transfer) on the potential barrier width and the typical length of the organic molecules used for the fabrication of these 2-dimensional perovskite semiconductors, inter-slab charge-carrier transport can be effectively dismissed and ignored for such semiconductors studied in this chapter. [24–26]

The contrast offered by studying the optoelectronic and photo-induced conductivity across samples experiencing different forms and strengths of quantum confinement offers invaluable insights into how quantum confinement affects charge-carrier transport properties. Such an analysis can be conducted by utilising time-resolved spectroscopy experiments that probe charge-carrier dynamics. Optical-pump terahertz-probe (OPTP experiments are described in Chapter 3.4) and time-resolved photoluminescence (described in Chapter 3.3) are two such techniques that can be used to non-invasively probe the photo-induced conductivity of free charge carriers, study the charge-carrier recombination dynamics, and estimate the lifetimes and diffusion lengths of the charge carriers in the studied material.

6.2 Results and discussion

6.2.1 3-dimensional $FAPbI_3$

Although there is a plethora of fabrication methods that yield compositionally nearly-identical $FAPbI_3$ films, they still hold significant sway on the emerging crystalline quality, optoelectronic property, and photovoltaic performance of the perovskite crystal. As such, in Chapter 5, I have demonstrated the dependence of intrinsic quantum confinement, crystalline quality, and photovoltaic performance on these fabrication methods for a small sample set representing the different families of fabrication protocols. I expand this investigation on fabrication method by exploring its relationship with quantum confinement and optoelectronic properties of the same sample set in this chapter. The 3-dimensional $FAPbI_3$ films were fabricated by Benjamin M. Gallant and Philippe Holzhey. Further details about each individual fabrication method are presented in Appendix B.2.

The main difference in the absorption spectrum of the films resulting from the three different fabrication methods is mainly in the above-bandgap absorption features indicative of quantum confinement (absorption spectra are visualized in Figure 6.1). As discussed in more details in Chapter 5, the "DMF-DMSO" film is the sole $FAPbI_3$ film in this sample set that demonstrates observable features in its room-temperature absorption spectrum and that exhibits strong quantum confinement behaviour. While the presence of these quantum confined nanodomains was shown to set an intrinsic limit to the photovoltaic PCE, other extrinsic factors such as the film's crystallinity, morphology, or high trap density prevalence at the grain boundaries may have similarly strong (if not stronger) effects on the operational optoelectronic properties of the material.

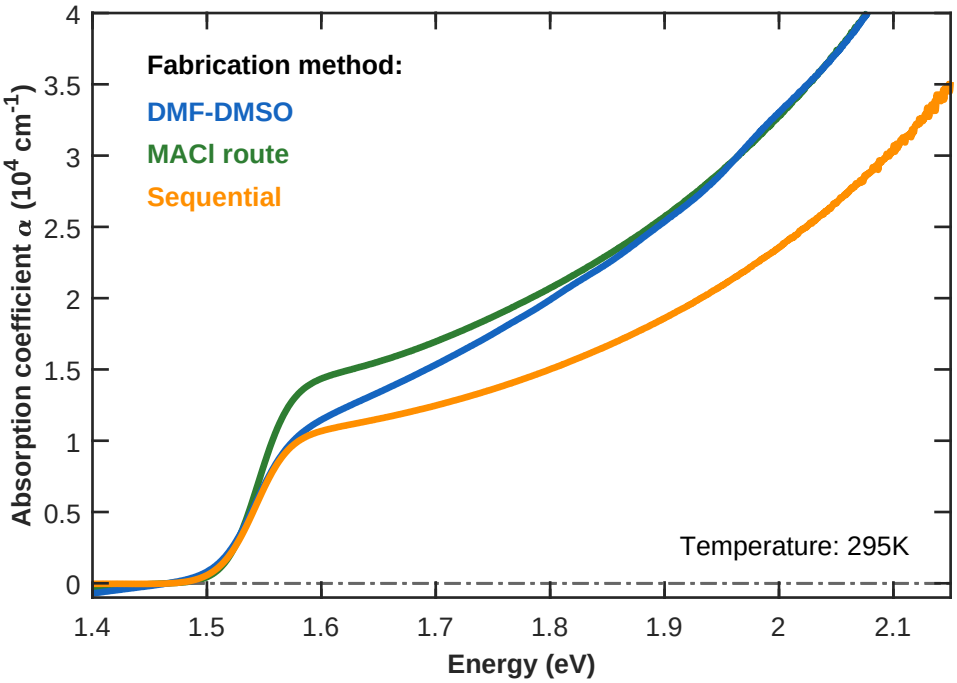


Figure 6.1: Absorption spectrum for $FAPbI_3$ thin films fabricated via the DMF-DMSO, MACl route and sequential deposition method.

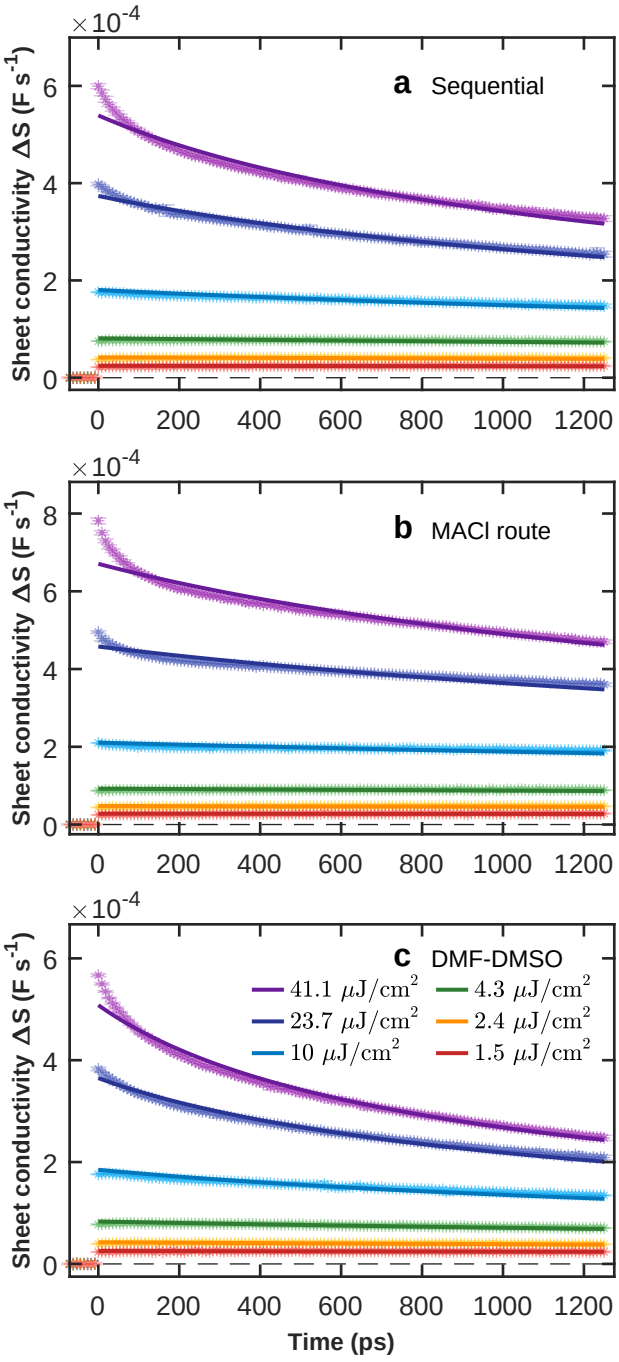


Figure 6.2: Photo-induced sheet conductivity for $FAPbI_3$ thin films fabricated via the DMF-DMSO, MACl route and sequential deposition method. The excitation fluence (excitation intensity per laser pulse) was varied in order to probe the different charge-carrier recombination regimes, and globally fit the photoconductivity traces to estimate the effective sum mobility ($\Phi\mu$) and the bimolecular recombination rate constant (k_2). Scattered points represent the measured data, while the solid lines represent the global fits for each fabrication method. (Legend in (**c**) also applies to (**a**), and (**b**).)

Therefore, in order to begin such an investigation, I measure the temporal evolution of the material's photo-induced conductivity (photoconductivity) to probe the local charge-carrier dynamics. The density of photo-generated charge carriers from the amplified pump laser beam used in the OPTP experiments makes the bimolecular recombination pathway the dominant recombination pathway based on the rate equation shown in Equation 6.1, and makes these experiments particularly sensitive to changes in the k_2 rate constant. [63, 66]

$$\frac{dn}{dt} = -k_1 n - k_2 n^2 - k_3 n^3. \tag{6.1}$$

Accordingly, the measured sheet photoconductivity (ΔS) traces at different excitation fluences (excitation intensity per laser pulse) can then be globally fitted using Equation 6.2 to extract estimates for the bimolecular recombination rate constant (k_2), while the initial photoconductivity values can be used to estimate the effective sum mobilities ($\Phi\mu$) using Equation 6.3.

$$\frac{d\left(\Delta S\right)}{dt} = -k_1\left(\Delta S\right) - \Phi k_2 \cdot C\left(\Delta S\right)^2, \tag{6.2}$$

where Φ is the branching ratio of free charge carriers to photons absorbed, C is the proportionality constant given as $\tilde{n}_o \,/\, (\Delta S_0)$, and $\tilde{n}_o$ is the absorbed photon density.

$$\Phi\mu = \frac{A_{\text{eff}} hc}{Ee\lambda\left(1 - R_{\text{pump}} - T_{\text{pump}}\right)} \cdot \Delta S, \tag{6.3}$$

where A_{eff} is the effective area of overlap between the optical pump and THz probe, $(1 - R_{\text{pump}} - T_{\text{pump}})$ is the fraction of the pump pulse absorbed by the sample, $\frac{hc}{\lambda}$ and E are the photon and pulse energy of the pump beam, such that $\frac{E\lambda}{hc} = N_{\text{photon}}$ is the number of photons in a pump pulse.

As can be seen in Figure 6.2 and 6.5a, such an analysis yields very similar dynamics, similar $\Phi\mu$ and k_2 within their error bounds, and generally similar intrinsic local charge-carrier behaviour across this sample set. This is indeed what is expected given the

similarity in strength and shape of the absorption spectrum around the band edge for these compositionally-similar films. The strength of the absorption onset is reflective of both the oscillator strength of the band edge transition and the local intrinsic trends for charge-carrier dynamics and k_2 recombination rates. [54] Therefore, the observed trends from the absorption spectrum should predict those measured from the photoconductivity measurements. Indeed, the "MACl route" film possesses a stronger absorption coefficient value at the absorption onset and similarly exhibits a small deviation in its estimated effective sum mobility and bimolecular recombination rate from the rest of the sample set, with that small difference in the measured mobility values accounted for by considering the changes in its local environment such as in the improved crystallinity, morphology, or grain size.

In order to complement the OPTP experiment, time-resolved photoluminesnce measurements were carried out at different laser excitation fluences and displayed in Figure 6.3. The PL transients corresponding to the lowest excitation fluence (displayed in Figure 6.4) are best reflective of the recombination regime where monomlecular trap-mediated recombination dominate as predicted by the rate equation (Equation 6.1) for low densities of photo-generated charge carriers. Accordingly, they were fitted with a stretched exponential model using Equation 6.4 to account for the spatial distribution and temporal evolution of the trap density throughout the film. [16]

$$I = I_0 e^{\left(\frac{t}{\tau_{\text{char}}}\right)^{\beta}}, \tag{6.4}$$

where I is the PL signal, τ_{char} is the characteristic lifetime corresponding to the time taken for the PL intensity to drop to I_0/e, and β is the distribution coefficient used to account for the higher-order recombination still present in the film, the time-dependent nature of the available trap density and its spatial inhomogeneity. [58, 59] The extracted

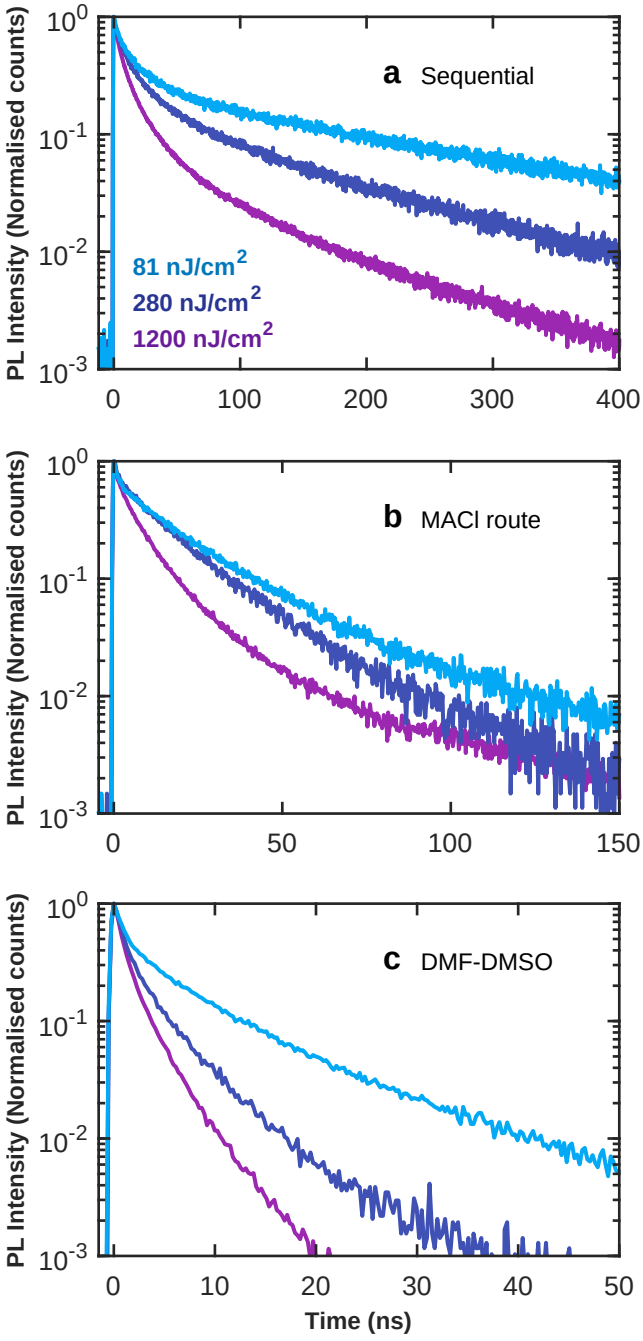


Figure 6.3: Excitation fluence-dependent time-resolved PL measurements for $FAPbI_3$ thin films fabricated via the DMF-DMSO, MACl route and sequential deposition method.

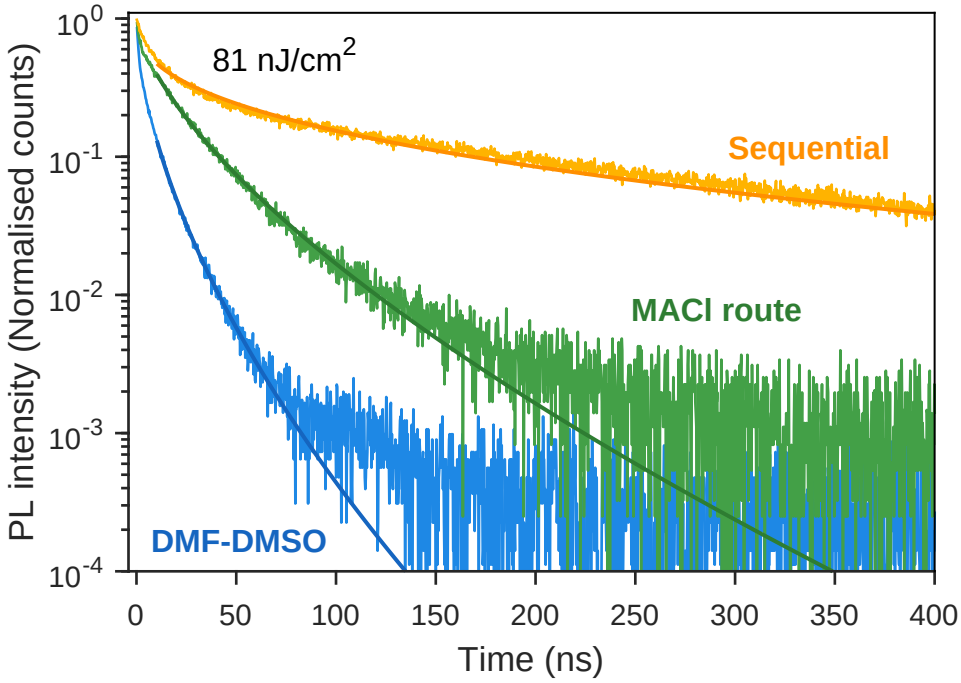


Figure 6.4: Low excitation fluence time-resolved PL transients for $FAPbI_3$ thin films fabricated via the DMF-DMSO, MACl route and sequential deposition method. PL transients measured at the lowest excitation fluence of 81 nJ/cm^2 to probe the monomolecular recombination regime and extract lifetime estimates based on stretched exponential fits. Solid dark lines represent the stretched exponential fits to the measured data.

charge-carrier lifetimes (τ_{eff}) and diffusion length (L_{D}) shown in Figure 6.5 are therefore the optimal parameters to assess the differences in the prevalence of crystallographic defects, trap densities, or other extrinsic properties of the films.

The massive improvement in the lifetimes of the charge carriers by nearly an order of magnitude as the fabrication method is optimised from the "DMF-DMSO" method to the "MACl route" method to the "Sequential" fabrication method, implies a strong enhancement in many extrinsic properties of these films. These enactments could be in the form of an improvement to the crystalline quality, a reduction in the presence of defects and other crystallographic phases, a suppression of the intrinsic quantum confinement, and a passivation of the present traps, all of which could be responsible for the elongation of the charge-carrier diffusion length, lifetimes, and for the general improvement in the charge-carrier transport properties of these film. However, due to the fabrication method not affecting the intrinsic local environment of the film, the intrinsic charge-carrier transport properties, such as the effective sum mobility, and bimolecular recombination rate, are retained across the sample set.

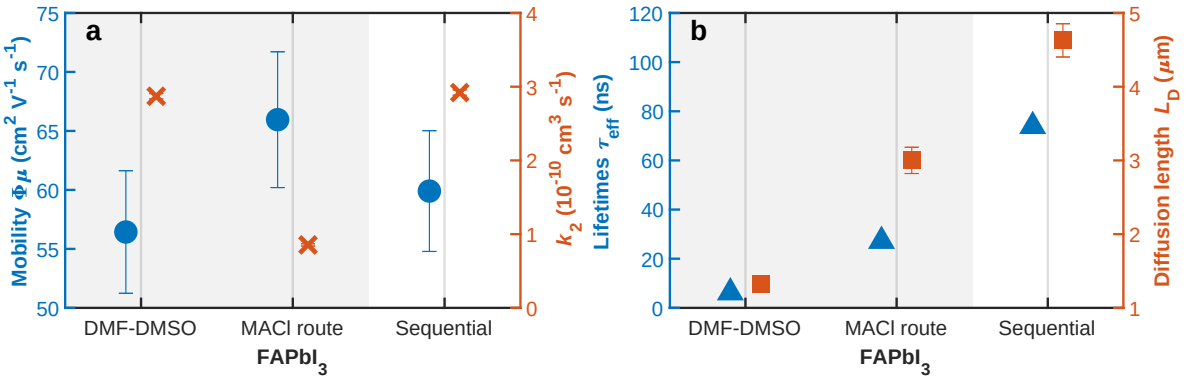


Figure 6.5: Optoelectronic parameters for $FAPbI_3$ thin films fabricated via the DMF-DMSO, MACl route and sequential deposition method. a Effective sum mobilities ($\Phi\mu$) and bimolecular recombination rate constant (k_2) extracted from the initial values of the photoconductivity traces and the global fits to the full transients using Equation 3.15 and 3.17 respectively. b Effective charge-carrier lifetime (τ_{eff}) extracted from stretched exponential fits to the measured PL transients using Equation 3.10. Diffusion length (L_{D}) calculated from all other extracted parameters using Equation 3.9.

6.2.2 2-dimensional perovskites

A similar analysis on the photoconductivity of 2-dimensional perovskite semiconductors can be conducted in order to obtain deeper insights into the preferred orientation of the conductive 2-dimensional slabs, and the type of charge carriers present in the film. To do so, 2-dimensional perovskite semiconductors employing the same large organic spacer molecule of $N(CH_3)_3$ (TMA: trimethylamine) were fabricated using two different fabrication and crystallization techniques in order to promote and encourage a preferential growth orientation for the 2-dimensional conductive slabs. Film fabrication was performed by Valentina Larini. Further information on the fabrication method is presented in Appendix C. The resultant films are quasi 2-dimensional perovskite semiconductors with opposing orientations for the conductive slabs. When the conductive slabs are orientated such that they are in the plane of the substrate, they are labelled "Horizontal", while when they are oriented perpendicular to the substrate, they are labelled "Vertical". These opposing orientations in tandem with photoconductivity measurements have the potential to corroborate the successful creation of opposing preferential growth orientation and shed light on the type of charge-carrier transport within this type of 2-dimensional semiconductors. For consistency, the samples with their different preferential orientation are grouped into different categories labelled "A", "B", or "C", depending on the amount and duration of light they have been exposed to, for an easier comparison between the orientations.

To confirm the formation of the 2-dimensional perovskite, I measured the absorption spectrum of the two different orientation, as displayed in Figure 6.6. Both orientations show a strong absorption peak centered around $\sim 2.18\,\mathrm{eV}$, which indicates that the majority of the film is composed of the same 2-dimensional perovskite. The presence of ordered 2-dimensional perovskite is additionally corroborated in a grazing wide-angle

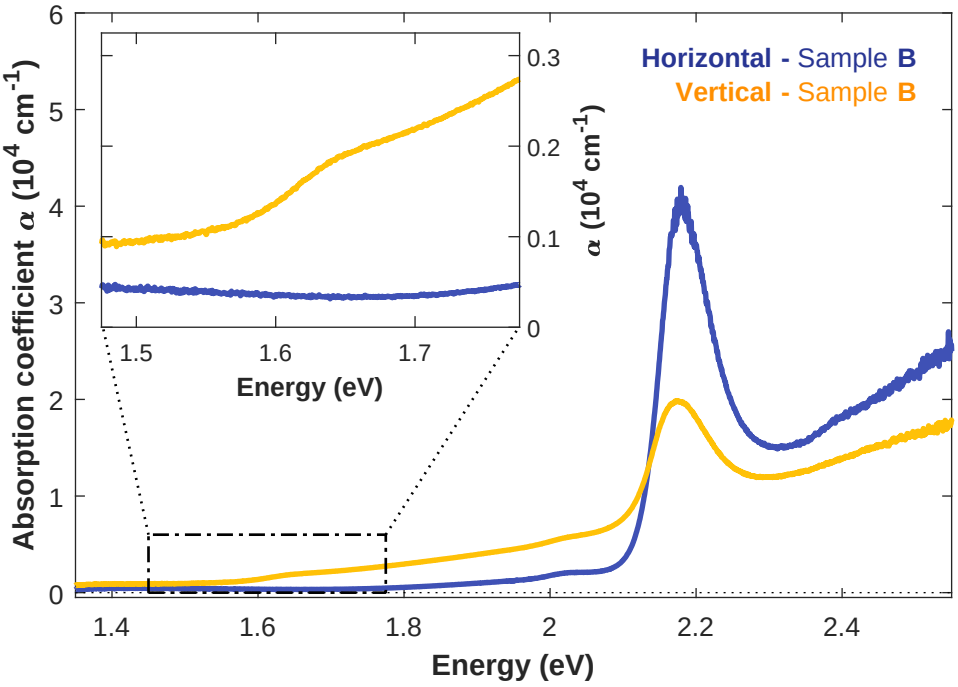


Figure 6.6: Absorption spectrum of the 2-dimensional perovskite semiconductors. The inset represents the energetic range corresponding to a 3-dimensional absorption onset for a 3-dimensional MA-rich perovskite film.

X-ray scattering patterns displayed in Figure 6.7.

The typical periodicity of the perovskite octahedra ((100) family of lattice planes centered around q_z and q_r = 0.9-1 Å) [186, 187] will still be present in the 2-dimensional perovskite, albeit with a strong preferential orientation. For instance, for the "Vertical" orientation, due to the spacer molecules forcing the conductive perovskite octahedral slabs to be oriented perpendicular to the substrate, the family of lattice planes (100) corresponding to the typical perovskite octahedral periodicity will be preferentially parallel to the substrate and should result in a GIWAXS pattern centered around q_z = 0.9-1 Å, q_r = 0 Å, and form weak spots around q_r = 0.9-1 Å, q_z = 0 Å. While for the "Horizontal" orientation, that family of lattice planes (100) will have its reciprocal vector exclusively pointing in the plane of the substrate and should form diffraction spots around q_r = 0.9-1 Å, q_z = 0 Å only. Both of these predictions are what I observe in the GIWAXS pattern, confirming the formation of preferentially oriented 2-dimensional perovskites. Additional strong low q_z and q_y peaks can be seen in the GIWAXS patterns which could be attributed to longer-range periodicities within the semiconductor and organic molecule, and additional ring-like features can be seen which could be due to the weak presence of other orientations or quasi 2-dimensional and 3-dimensional phases. Linear and logarithmic scales of the same GIWAXS patterns are displayed in Figures C.3 and C.2 respectively.

The existence of any lower-energy compositions and higher-dimensionality structures within the film, regardless of how much sub volume of the film they occupy could present a problem for probing the charge-carrier dynamics within the 2-dimensional structure, as charge carriers typically quickly funnel to such lower-energy phases within a few nanoseconds. However, the time range studied in my photoconductivity measurements

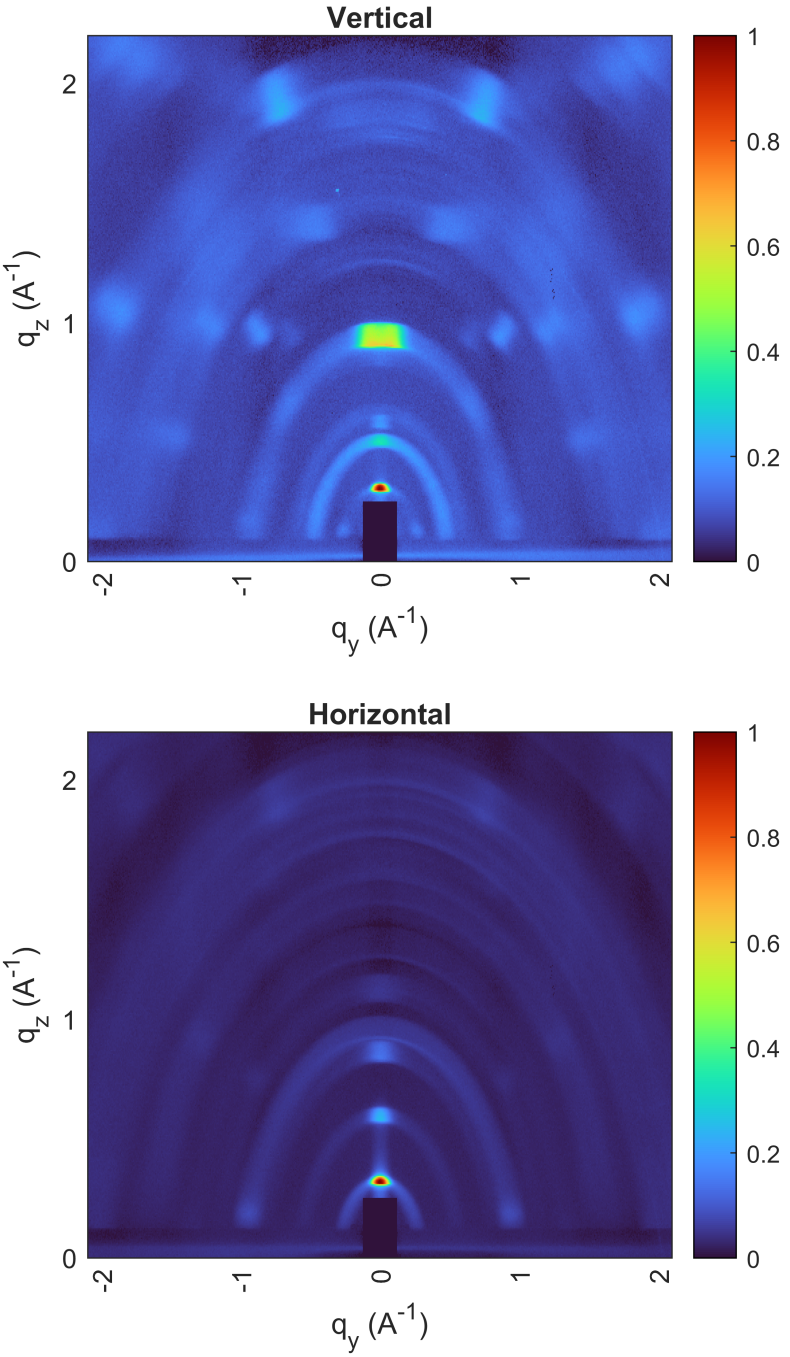


Figure 6.7: Grazing wide-angle X-ray scattering (GIWAXS) patterns of the 2-dimensional perovskite semiconductors. Square-root scaling of the GIWAXS patterns are displayed in order to highlight the differences between the two perovskite orientation. The linear and logarithmic GIWAXS patterns are displayed in Figures C.3 and C.2 respectively.

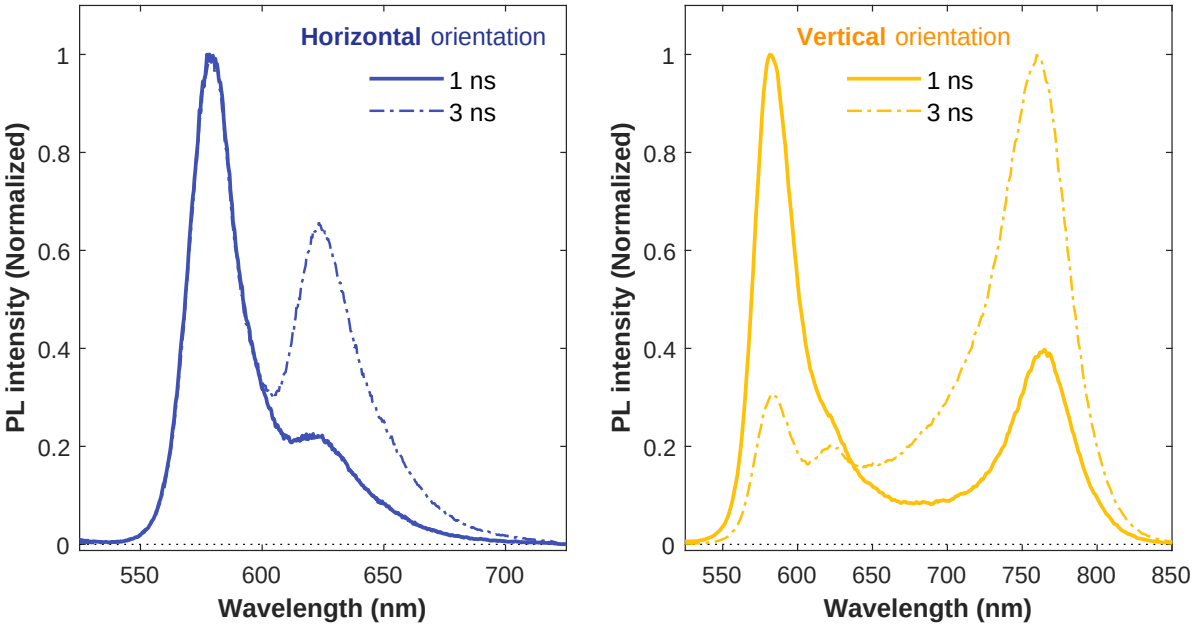


Figure 6.8: Photoluminesnce (PL) spectrum of the 2-dimensional perovskite semiconductors. Early time (1 ns post photo-excitation) PL of both orientations is dominated by emission from the purely 2-dimensional phase.

only extends up to 1.25 ns post laser excitation. Therefore, to discern which phase the charge carriers are in in that time window, the temporal evolution of the photoluminescence spectrum is explored, which is displayed in Figure 6.8. PL measurements were performed by Jiaxing Du. Within the first 1 ns, most of the PL emission is centered around ∼ 580 nm for both orientations, which implies that the emission originates from the radiative recombination of electron-hole pairs within the higher-energy 2-dimensional structure and that most of the charge carriers have not yet funneled into the higher-dimensionality and lower-energy phases during the time range of the optical-pump terahertz-probe (OPTP) experiments.

An analysis of the photo-induced conductivity between these two orthogonal orientations can be extremely useful in understanding the type of charge-carrier transport within these 2-dimensional semiconductors, in gauging the strength of the quantum confinement between the conductive slabs, and in corroborating their preferential growth orientation. The probing terahertz (THz) beam used in this experiment is polarized in the plane of the sample and substrate. Therefore, upon reaching a conductive material, the incident THz beam will induce the free charge carriers to oscillate along its polarization direction in a plane parallel to the substrate. Accordingly, depending on the geometry and confinement strength of the 2-dimensional semiconductor, the induced charge-carrier motion can be significantly hindered (such as in the case of conductive material perpendicular to the substrate and THz polarization) or completely unhindered (for conductive material parallel to the substrate and THz polarization). The measured photo-induced sheet conductivity and extracted effective sum mobilities ($\Phi\mu$) are displayed in Figures 6.9 and 6.10 respectively. I additionally note that the extraction of effective sum mobility estimates is done from the early-time photoconductivity values, which further highlights that the photoconductivity analysis is nearly exclusively reflective of charge-carrier

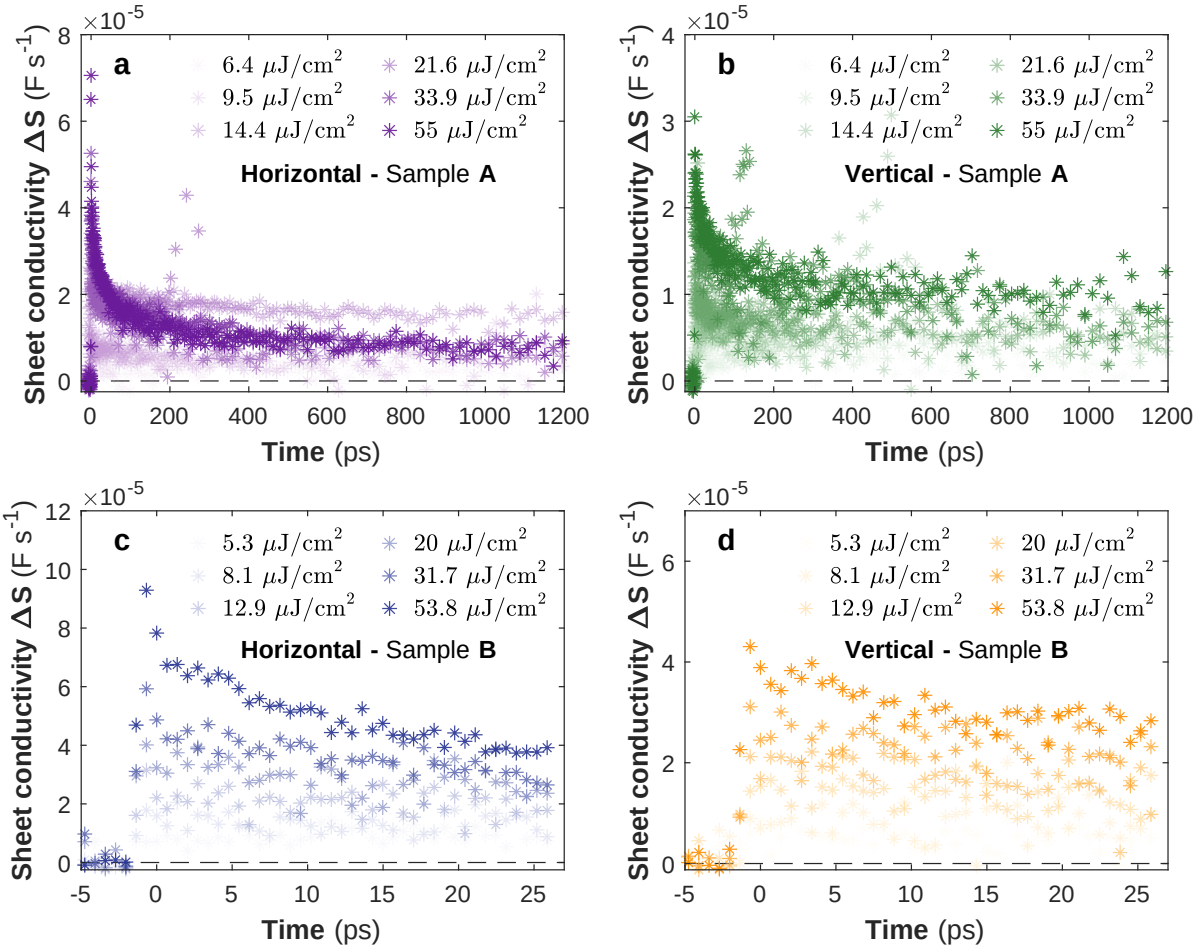


Figure 6.9: Photo-induced sheet conductivity dynamics of the 2-dimensional perovskite semiconductors. The excitation fluence (excitation intensity per laser pulse) was varied in order to probe the different charge-carrier recombination regimes, and extract a more accurate estimate for the effective sum mobility ($\Phi\mu$) from the early-time photoconductivity signal. The samples labelled "A" and "B" were exposed to the amplified laser for different durations and therefore have degraded to different extents.

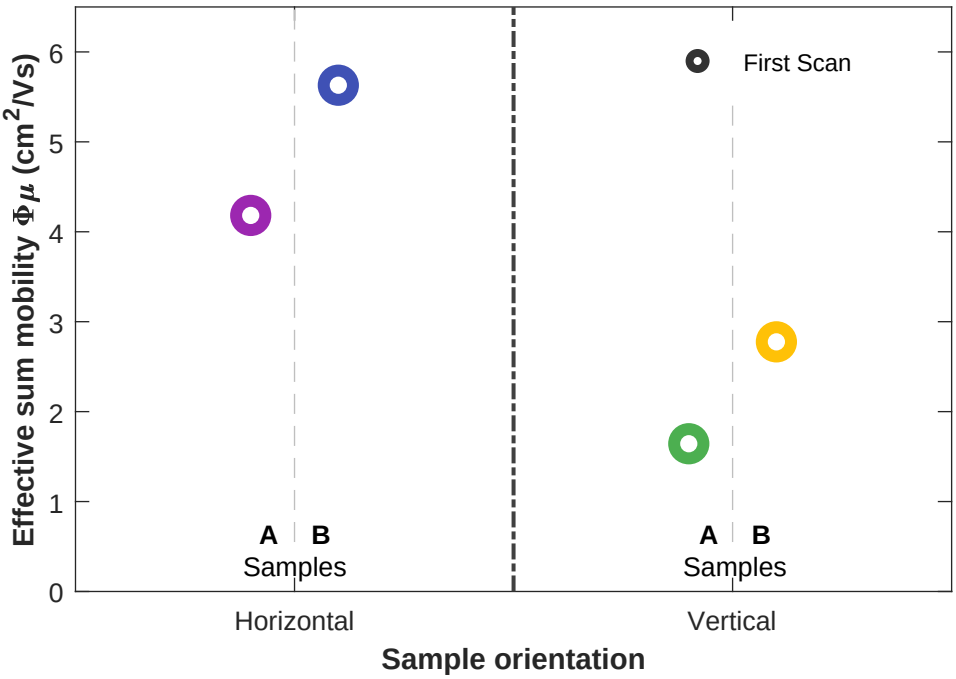


Figure 6.10: Effective sum mobility estimates for the 2-dimensional perovskite semiconductors. The samples labelled "A" and "B" were exposed to the amplified laser for different durations and therefore have degraded to different extents.

dynamics within the 2-dimensional semiconductor. The samples labelled "A" and "B" were exposed to the amplified laser for different durations and have therefore degraded to different extents. Nonetheless, for the same exposure time, the extracted effective sum mobilities for the "Horizontal" samples (4.2 cm^2/Vs and 5.6 cm^2/Vs for samples A and B respectively) are nearly double that of the "Vertical" samples (1.6 cm^2/Vs and 2.8 cm^2/Vs for samples A and B respectively) in complete agreement with what is expected. The mobility value of the "Horizontal" sample reflects the true intrinsic effective mobility of that 2-dimensional perovskite semiconductor, as the conductive slabs should be parallel to the substrate and the induced motion of the free charge carriers should not experience the confinement created by the organic spacer molecules. On the other hand, the "Vertical" sample has its conductive slabs perpendicular to the substrate, therefore, the free charge carriers in half of its grains will have their induced motion blocked due to the confinement and the other half will experience unhindered motion, resulting in half the photoconductivity and mobility values.

Additionally, the fact that the values of the effective mobilities precisely follow the geometry arguments of the conductive slabs, suggests that the only possible charge-carrier motion is the motion within the conductive slabs (intra-slab motion), and that charge-carrier tunnelling or energy transfer across the insulating layers (inter-slab motion) is effectively impossible in these material.

It is worth noting that the photoconductivity dynamics observed in Figure 6.9 can be simply explained in terms of exciton formation. The very fast reduction in photoconductivity signal is reflective of equally fast exciton formation (a charge-neutral and non-conductive electron-hole bound state) which are invisible to my photoconductivity measurements. Additionally, the presence of a non-zero tail in the photoconductivity signal after exciton formation, and an excitation fluence dependence of the photoconductivity

transients, are both expected from previous analyses of confined semiconductors, which reflect the presence of remnant free charge carriers as predicted by the Saha equation. [24, 188, 189]

An interesting consequence of this analysis was the observation of different operational stability for the different orientations. After prolonged exposure to the amplified laser, the mobility anisotropy between the two orientations seemed to gradually disappear until both mobility values equilibrated to values less than $2\,\mathrm{cm}^2/\mathrm{Vs}$. However, this apparent anisotropy disappearance can be simply explained in terms of different degradation speeds. The "Horizontal" sample consistently degraded faster than the "Vertical" sample, consistently ablating off its substrates at the end of the stability measurements, while the "Vertical" sample showed little signs of ablation. This selective loss of material for one of the orientations better explains the apparent anisotropy disappearance and highlights the importance of further studies investigating the operational stability of 2-dimensional semiconductors.

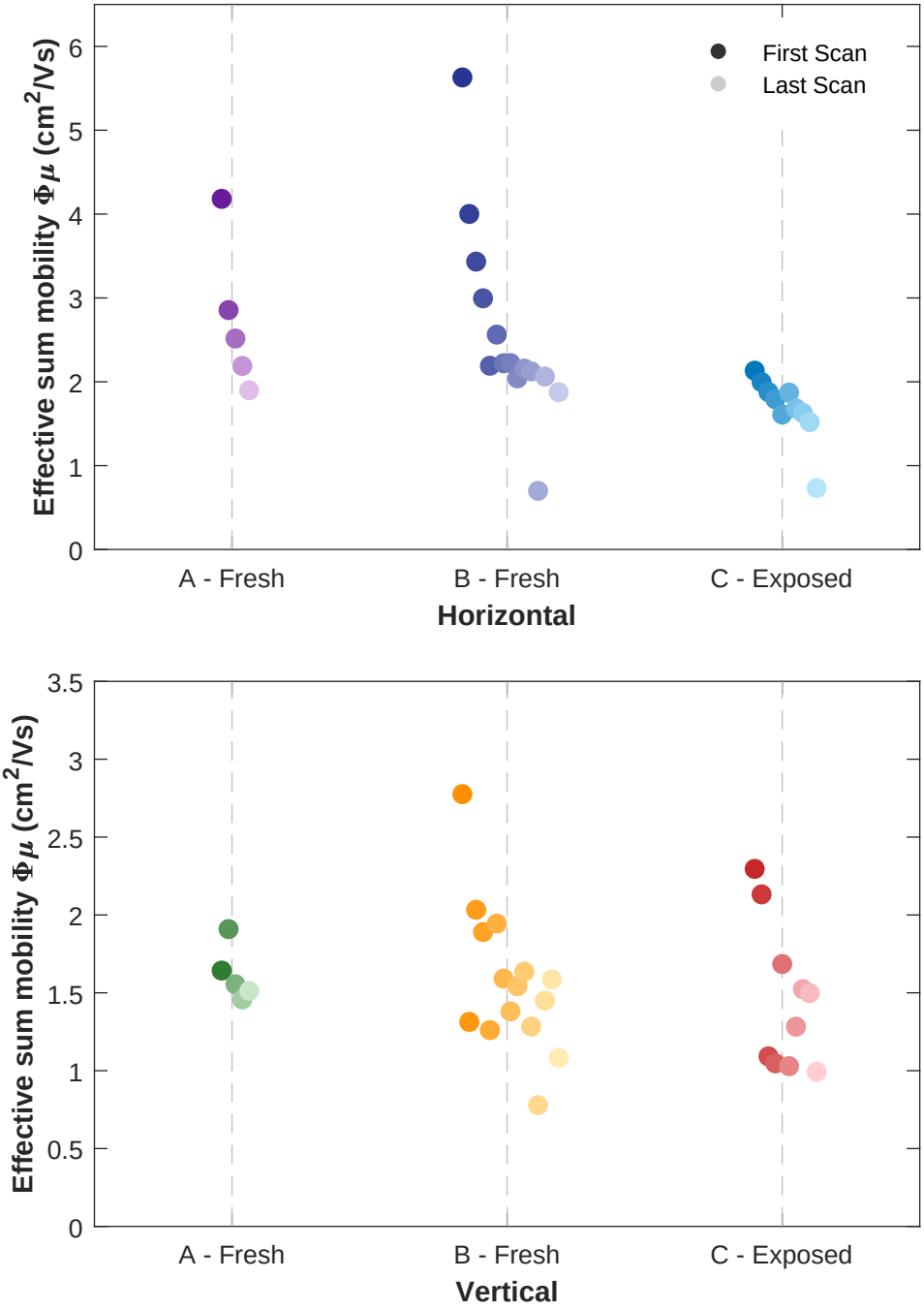


Figure 6.11: Stability of the effective sum mobility estimates for the 2-dimensional perovskite semiconductors. The samples labelled "A" and "B" were exposed to the amplified laser for different durations and therefore have degraded to different extents, and the "C" samples were exposed to the X-ray source to measure their GIWAXS patterns before the OPTP experiments. The lighter shade scatter plots represents mobility estimates extracted after prolonged exposure to the amplified laser and degradation.

6.3 Conclusion

In conclusion, I have analyzed the charge-carrier dynamics and investigated the optoelectronic properties and its relationship with quantum confinement in perovskite semiconductors experiencing different types and strengths of quantum confinement.

In the first half of this chapter, I study 3-dimensional $FAPbI_3$ MHP films demonstrating different amounts of the intrinsic quantum confinement attributable to that composition. Through photo-induced conductivity measurements, I find that the intrinsic optoelectronic variables (such as the effective mobility, and k_2 recombination rate) and local charge-carrier transport properties of these compositionally-similar films to be similar. While time-resolved photoluminescence measurements shed light on the significant differences in the extrinsic properties of these samples; highlighting that as the fabrication method is more optimised, the crystallinity, presence of defects, tendency to form quantum confined domains, and other significant extrinsic properties can be controlled to optimise the optoelectronic properties of the emerging semiconductor.

In the second half of this chapter, I investigate the charge-carrier dynamics of preferentially-oriented 2-dimensional perovskite semiconductors with photoconductivity measurements. By analyzing the combination of the known polarization of the THz probing beam along with the geometry of the conductive slabs, I am able to extract the true intrinsic effective sum mobility of this 2-dimensional perovskite composition, corroborate the existence of preferentially-oriented conductive slabs through the observation of different mobility values for the different orientation agreeing with geometry arguments, and confirm that the dominant charge-carrier motion in these 2-dimensional semiconductor is band-like and is within the 2-dimensional conductive slabs rather than across the insulating organic layers.

7

Conclusion and Outlook

This thesis has focused on understanding quantum confinement in its many forms in metal halide perovskites, on unraveling methods of controlling its prominence, and its effect on the optoelectronic properties and photovoltaic performance of the whole semiconductor. Different theoretical models of quantum confinement such as the infinite quantum well model and the periodic superlattice of finite potential barriers were explored in Chapter 2, along with a detailed introduction and foundation for examples of how they manifest in perovskite semiconductors such as in the formamidinium lead triiodide ($FAPbI_3$) perovskite composition in the form of intrinsic quantum confinement and in perovskite compositions whose A-site cation was substituted for a large long-chained organic molecule in the form of 2-dimensional electronic confinement.

To be able to gauge the strength of such quantum confinement and probe its effects on the semiconductor, Chapter 3 provided the necessary details on the experimental setups and data analysis required for such an assessment. Absorption spectroscopy was shown to be important in understanding the energetic landscape of the semiconductor and distinguish the different compositions and phases present within a semiconductor and estimate the sub-volume of the film they occupy. It was additionally shown to be vital in

discerning the presence or absence of the intrinsic quantum confinement phenomenon in $FAPbI_3$ and FA-rich metal halide perovskites (MHPs). The algorithm of decoupling the peak features can be simply applied to any composition or fabrication method in order to gauge the prominence of the quantum confinement and quantitatively compare its presence across any sample set. Complementary experimental technique used to probe the crystallographic purity of the semiconductor and assess the radiative efficiency and emission spectral profile, such as X-ray diffraction (XRD) and photoluminescence (PL) were also presented in Chapter 3. This chapter additionally discussed the theory and experimental setup of both time-resolved PL and photo-induced conductivity measurements. Both of which can be used to non-invasively probe the charge-carrier dynamics, and extract estimates for the effective sum mobility, charge-carrier lifetimes and diffusion lengths, and recombination rate constants.

In Chapter 4, the possibility of controlling the strength of the experienced quantum confinement in thermally evaporated $FAPbI_3$ film was explored. This was done by partially substituting FA with Cs in an attempt to change the bandstructure, increase the stability of the photo-active α-$FAPbI_3$ phase, reduce any crystallographic defects and faults, and suppress the formation of other $FAPbI_3$ polymorphs - all of which could be the culprits behind the tendency of the $FAPbI_3$ composition to self assemble into these confined nanodomains. The successful gradual suppression of quantum confinement as the partial inclusion of Cs was increased until quantum confinement and its effects were completely eliminated confirmed that such precise control over the quantum confinement is possible, and provided additional insights into the fundamental physics governing the intrinsic quantum confinement of this composition. Additionally PL emission occupying the same energetic range from these nanodomains was observed for the pure $FAPbI_3$ film under cryogenic temperatures, which highlights the importance of further investigation into the various ways of precisely controlling this intriguing phenomenon in order to amplify or

suppress its effects according to one's need and according to the future applications of the $FAPbI_3$ composition into either light-emitting devices or photovoltaic devices.

Chapter 5 expanded on the work presented in Chapter 4, by exploring different methods of controlling the intrinsic quantum confinement. Similar control over the quantum confinement was demonstrated to be possible while still retaining compositional similarity across the investigated sample set. This was achieved by employing different fabrication methods that result in drastically different crystallization processes within the perovskite crystal, resulting in diverging quantum confinement behaviour. The historically traditional "DMF-DMSO" method exhibited strong quantum confinement behaviour, while the additive ("MACl route") and the templating ("Sequential") methods demonstrated little to zero quantum confinement behaviour. To complement this observation, the relationship between the presence of quantum confinement and photovoltaic performance was investigated through both experiments and a meta-study of the field. The experimental observations highlighted that both the extractable charge-carrier current density (J_{SC}) and power conversion efficiencies (PCEs) are significantly enhanced for the "MACl route" and "sequential" fabrication methods where quantum confinement and its effects were heavily suppressed. This was corroborated using the meta-study which conclusively showed that an intrinsic PCE ceiling of 20% exists for photovoltaic (PV) devices made out of $FAPbI_3$ films possessing features indicative of quantum confinement. These conclusions highlight the importance of checking the absorption spectrum for the presence of quantum confinement as the first point of investigation for the validity of a composition or fabrication method to yield highly-efficient FA-rich MHPs.

Finally, in Chapter 6, an investigation into the relationship between quantum confinement and charge-carrier dynamics was carried out in two parts. In the first half of this chapter, charge-carrier dynamics of the same sample set of 3-dimensional $FAPbI_3$ film used in Chapter 5 were investigated. The investigation concluded that

these compositionally-similar films share the same intrinsic local charge-carrier transport properties such as the effective sum mobility ($\Phi\mu$) and bimolecular recombination rate constant (k_2). On the other hand, their extrinsic properties such as the prevalence of crystallographic defects and strain, abundance of $FAPbI_3$ polymorphs, and quantum confinement behaviour have a dramatic impact on the charge-carrier dynamics as demonstrated by the divergence of their charge-carrier lifetimes and diffusion lengths calculated from time-resolved PL measurements. In the second half of this chapter, 2-dimensional perovskite semiconductors with orthogonal preferential growth orientation were studied. The combination of the orthogonal orientation of the conductive 2-dimensional slabs and the known polarization of the probing terahertz (THz) beam, allowed for an analysis of their charge-carrier transport properties. An estimate of the true effective sum mobility ($\Phi\mu$) of this composition was obtained for the "Horizontal" orientation, whose conductive slabs are aligned with the THz polarization. While, the "Vertical" orientation possessed $\Phi\mu$ values half those of the "Horizontal" orientation in exact agreement with what is expected based on geometrical arguments. This observed charge-carrier transport anisotropy confirms the successful growth of orthogonal preferential orientations, confirms that charge-carrier transport is dominated by charge-carrier transport within the conductive slabs (intra-slab band-like transport) and that charge-carrier transport across the insulating layers (inter-slab hopping-like transport) can effectively be completely ignored in such perovskite compositions. This investigation additionally shed light on the difference in the operational stability of the different orientations of this 2-dimensional perovskite, as the "Horizontal" orientation ablated and degraded on a much faster timescale than the "Vertical" sample, which highlights the need for further research on lower-dimensional perovskites and specifically 2-dimensional perovskites, especially since the successful growth of the 2-dimensional conductive slabs in an orientation that can connect the electron and hole transport layers ("Vertical"

samples) could open the doors for such quantum confined material to be more widely used in PV devices.

Appendices

A

Supplementary Analysis of Control of intrinsic quantum confinement in formamidinium lead triiodide 4

Contents

A.1 Sample fabrication 166
A.2 X-ray diffraction 167
A.2.1 XRD spectra 167
A.3 Steady-state photoluminescence 169
A.4 Absorption measurements 171
A.4.1 Elliott fitting 173
A.4.2 Tauc plots 176
A.4.3 Baseline fitting and peak indexing 178
A.4.4 Temperature-dependent study of the absorbance spectra 179
A.5 Theoretical models 182
A.5.1 Infinite quantum well 182
A.5.2 Krönig-Penney potential 183
A.6 Temperature-dependent study of steady-state PL 184
A.6.1 $FA_{0.57}Cs_{0.43}PbI_3$ 186
A.7 Time-resolved PL (TRPL) 189

This appendix provides details of sample preparation and characterisation relevant to Chapter 4. It also describes methods used for data fitting in Chapter 4 and presents additional data to back the conclusions made in that chapter.

A.1 Sample fabrication

In a modified Kurt J. Lesker dual source evaporation system, lead (II) iodide PbI_2 (Ultradry, 99.999%, metals basis) and formamidinium iodide FAI (Dyesol, GreatCellSolar Materials) were heated in separate crucibles until each of them evaporated. During evaporation the pressure in the chamber was 10^{-6} mbar. The evaporation temperature for FAI was 150°C, and PbI_2 was evaporated at 300°C. The vapors condensed on rotating substrates to ensure uniform coating. Film evaporation was performed by Kilian B. Lohmann. The evaporated $FAPbI_3$ films were then annealed on a hot plate at 170°C for 3-5 minutes to ensure the formation of the photo-active perovskite α-$FAPbI_3$ phase, which was visually confirmed by the change in the films' physical appearance to the expected black color. The films have a thickness of 100 nm as measured using a Bruker Dektak XTL Stylus profilometer. Cesium acetate ($CsCH_3COO$) (99.9% purity, Sigma-Aldrich) was dissolved in IPA to make dipping solutions with differing $CsCH_3COO$ concentrations (0.2, 0.5, 1, 5, and 7.5 mg/mL). Following the procedure outlined by Jiang et al. [113], we dipped the films in the prepared solutions for 3 seconds to induce cation exchange between the FA^+ and Cs^+ ions, dried the films with a N_2 gun, and proceeded with annealing the dipped films on a hot plate at 170°C for a further 20 minutes to ensure the complete evaporation of the $FACH_3COO$ byproduct from the dipping process. Solution preparation, film annealing and storage between measurements were all done in a N_2-filled, moisture-, and O_2-controlled glove box.

The films were always re-annealed on a hot plate at 170°C for 3-5 minutes before any new measurements on the samples were undertaken to reconvert any newly-formed δ_H-phase (induced by the exposure to moisture) to the black α-phase and to ensure good film crystallinity.

A.2 X-ray diffraction

A.2.1 XRD spectra

The XRD patterns were measured in air using a Panalytical X'pert powder diffractometer with a copper X-ray source (Cu-Kα X-rays with a wavelength of 1.5418 Å).
The XRD patterns were then corrected for tilt by shifting the 2θ-axis, such that the z-cut quartz reference peaks at $2\theta = 16.433°$ were all aligned for the films on quartz substrates. The films deposited on sapphire substrates were shifted similarly to have their sapphire reference peak aligned at $2\theta = 20.553°$.

The extracted peak position and FWHM of each XRD peak that was studied were obtained manually using a smoothing algorithm to find the associated maximum, and the full widths at half maximum after the background were subtracted.

The increase in the FWHM of the XRD perovskite peaks with higher Cs-acetate concentrations (shown in Figure A.2) is at odds with the improvement in crystallinity of the film and the enlargement of the grain size, which had previously been reported for the addition of Cs in the literature. [31] This increase in FWHM, indicating a reduction in crystallographic purity, can be explained by the non-uniformity of the Cs cation exchange across the thickness of the film, and the formation of $CsPbI_3$, [29] both of which will increase in prominence when a higher $CsCH_3COO$ dipping concentration is used. [113] This conclusion is supported by the observation of a prominent non-perovskite δ_O-$CsPbI_3$ XRD peak for the highest Cs concentration film, presented in Figure 4.1.

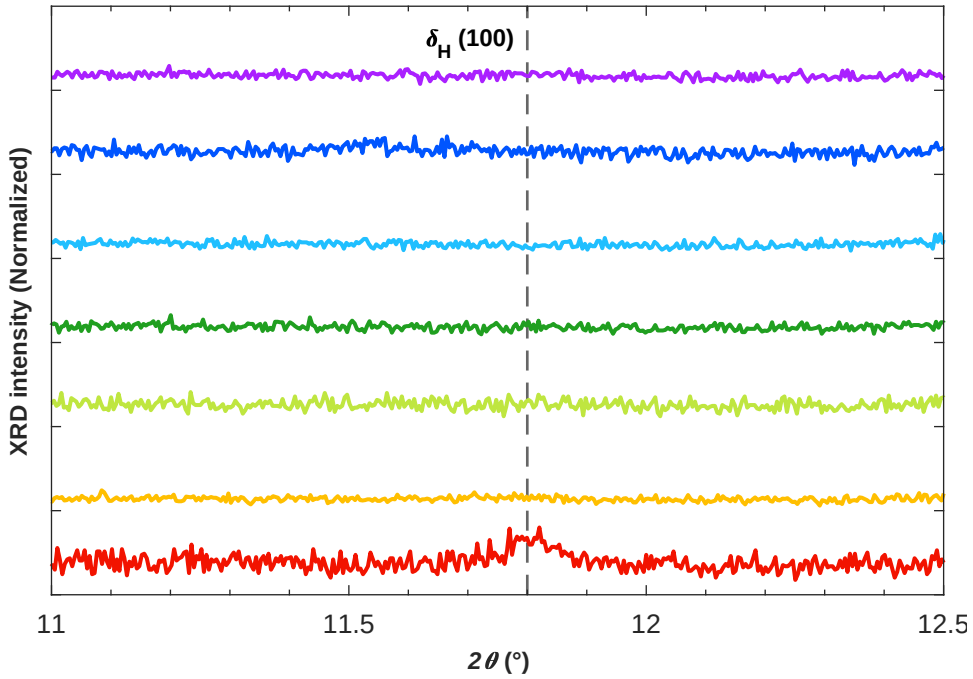


Figure A.1: X-ray diffraction (XRD) pattern magnified around the hexagonal non-perovskite δ_H-FAPbI$_3$ phase for the investigated FA$_{1-x}$Cs$_x$PbI$_3$ films. The extracted position of the most prominent δ_H-FAPbI$_3$ peak (100) [190, 191] is indicated by a vertical black dashed line. An observable peak is only found for the neat FAPbI$_3$ film. The labels for the different colored solid lines is included in Figure 4.1.

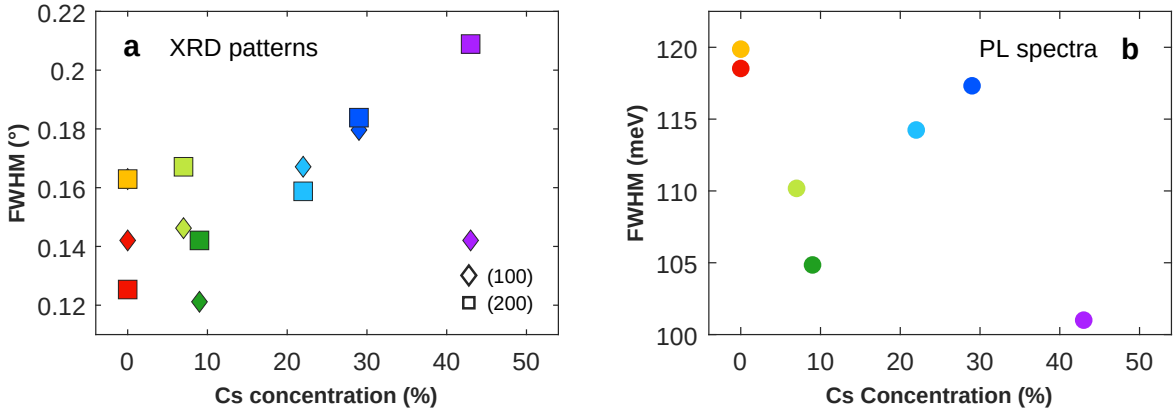


Figure A.2: Full widths at half maximum (FWHM) of the prominent XRD perovskite peaks and the PL peaks for FA$_{1-x}$Cs$_x$PbI$_3$, as a function of Cs content. a: Extracted FWHM of the two most prominent XRD peaks (100), and (200) for the investigated films, represented with diamond and square markers respectively. **b**: Extracted FWHM of the main peak in the PL spectra.

A.3 Steady-state photoluminescence

A 398 nm diode laser (PicoHarp, LDH-D-C-405M) was used to photo-excite the samples, on a continuous wave setting at an intensity of 75.5 mW/cm^2. The resultant PL was collected and coupled into a grating spectrometer (Princeton Instruments, SP-2558), which directed the spectrally dispersed PL onto a silicon iCCD (intensified charge coupled device, PI-MAX4, Princeton Instruments). The samples were mounted in a vacuum cell under low pressure ($\sim 10^{-2}$ mbar).

The PL peak position and full width at half maximum (FWHM) were obtained manually using a smoothing algorithm to smooth the measured data and find the maximum, and the full width at half maximum after the background had been subtracted. The PL amplitude is seen to decrease for the films with increasing Cs content, suggesting an increase in the trap density within the film and an increased prevalence of nonradiative monomolecular charge-carrier recombination. This could be explained by the fabrication method used in this study: the composition differential throughout the thickness of the film for higher Cs films could create a tail of deep trap states, and the solution-induced cation exchange could also be introducing Cs interstitials and leading to the creation of more trap states in the film.

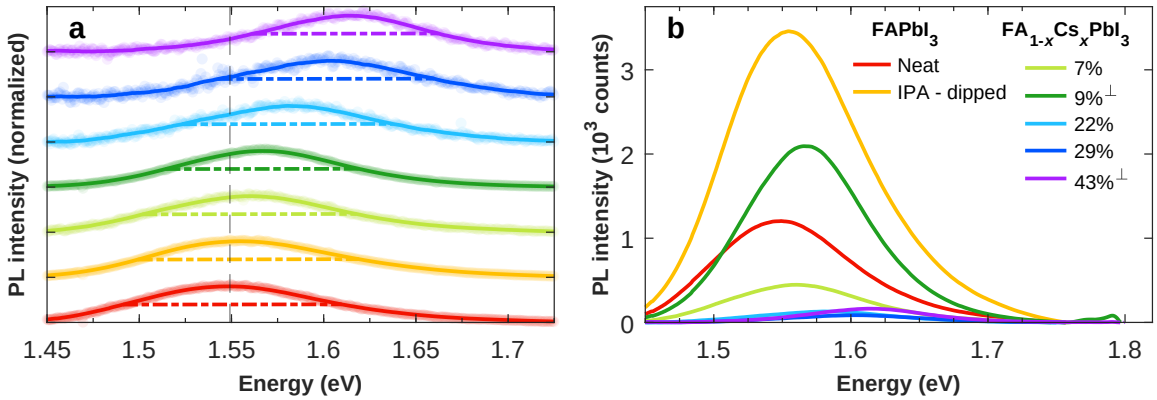


Figure A.3: Photoluminescence spectra of the $FA_{1-x}Cs_xPbI_3$ films. a: Normalized PL spectra (scatter points) for the different films, with smoothed versions of the spectra shown as solid lines. For visual clarity, the spectra are vertically offset, the full-width-half-maximum (FWHM) is represented by the horizontal dashed lines, and the PL peak of the neat film is represented by the vertical dashed line. (**b**) shows the unnormalized, smoothed PL spectra. The PL amplitude is observed to decrease for the films with increasing Cs content. (The legend in (**b**) also applies to (**a**). Films are evaporated on quartz or sapphire (indicated by $^{\perp}$) substrates).

A.4 Absorption measurements

Reflectance (R) and transmittance (T) spectra were measured using a Fourier transform infrared (FTIR) spectrometer (Bruker Vertex 80v), configured with a tungsten halogen lamp illumination source, a CaF_2 beamsplitter and a silicon detector. The absorption coefficient (α) spectrum of each sample can then be obtained using the relationship

$$\alpha = -\frac{1}{d} \cdot \log_{10}\left(\frac{T}{1-R}\right), \tag{A.1}$$

where d is the film thickness (100 nm). The measured transmittance and reflectance spectra of the $FAPbI_3$ (Neat) film at 4 K, along with the calculated absorption coefficient spectra is displayed in Figure A.4.

The samples were all mounted in a gas-exchange helium cryostat (Oxford Instruments, OptistatCF2) in a helium atmosphere for the room-temperature measurements (where the outer vacuum chamber was pumped down to low pressures ($< 5 \times 10^{-5}$ mbar)) and for the temperature-dependent study, where the temperature was varied between 4 K and 295 K in either 5 K or 10 K increments.

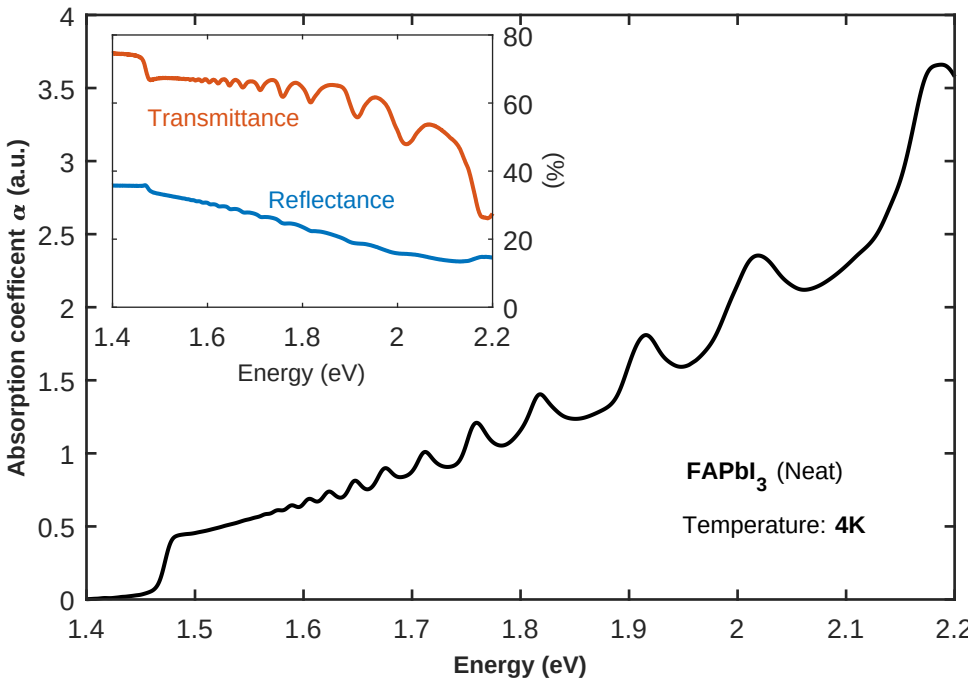


Figure A.4: Absorption coefficient spectra of the $FAPbI_3$ (Neat) film. Absorption coefficient spectrum of the $FAPbI_3$ (Neat) film at 4 K, calculated from the measured transmittance and reflectance spectra shown in the inset.

A.4.1 Elliott fitting

The onset in the absorption coefficient spectrum was fitted using Elliott's model that accurately describes the absorption of a semiconductor near its band edge. [52]

The theory expresses the energy-dependent absorption as:

$$\alpha(E) = \alpha_{\mathrm{X}}(E) + \alpha_{\mathrm{C}}(E). \tag{A.2}$$

The bound exciton contribution α_{X} has the form:

$$\alpha_{\mathrm{X}}(E) = \frac{b_0}{E} \sum_{n=1}^{\infty} \frac{4\pi E_{\mathrm{B}}^{3/2}}{n^3} \delta\left(E - \left[E_{\mathrm{g}} - \frac{E_{\mathrm{B}}}{n^2}\right]\right), \tag{A.3}$$

where b_0 is a constant of proportionality that incorporates the electric dipole transition matrix element between the valence and conduction band. α_{X} is formed of the weighted sum of contributions from the exciton states with positive integer quantum number n and energies $E_{\mathrm{g}} - \frac{E_{\mathrm{B}}}{n^2}$, where E_{g} is the bandgap energy and E_{B} is the exciton binding energy.

Here, the contribution from the electron-hole continuum states $\alpha_{\mathrm{C}}(E)$ has the form

$$\alpha_{\mathrm{C}}(E) = \frac{b_0}{E} \left[\frac{2\pi\sqrt{\frac{E_{\mathrm{B}}}{E-E_{\mathrm{g}}}}}{1 - \exp(-2\pi\sqrt{\frac{E_{\mathrm{B}}}{E-E_{\mathrm{g}}}})}\right] c_0^{-1} \mathrm{JDoS}(E), \tag{A.4}$$

where the joint density of states is given by $\mathrm{JDoS}(E) = c_0\sqrt{E - E_{\mathrm{g}}}$ for $E > E_{\mathrm{g}}$ and 0 otherwise, and the joint density of states constant $c_0 = \frac{1}{(2\pi)^2}\left(\frac{2\mu}{\hbar^2}\right)^{3/2} \times 2$, where μ is the reduced effective mass of the electron-hole system. The term in square brackets is the Coloumbic enhancement factor, which increases the absorption from the continuum states above the square-root form of the JDoS for a direct-gap semiconductor as a result of the Coloumbic attraction between the unbound electrons and holes.

The linear combination of the contributions from the excitonic and continuum states, $\alpha(E)$, is then convolved with a normal distribution - representing the homogeneous broadening caused by electron-phonon coupling. The broadening is mathematically denoted by $g(E) = \mathcal{N}(0, \gamma^2) = \frac{1}{\sqrt{2\pi}\gamma} e^{-\frac{x^2}{2\gamma^2}}$.

The bandgap energy (E_g), amplitude (Amp), and electron-phonon coupling strength (γ) are freely fitted to yield the values shown in Table A.1. The exciton binding energy (E_B) was globally fixed to 2 meV, based on $FAPbI_3$ room-temperature values (calculated from Elliott fits to the absorption onsets) from the literature, [40, 111] and the reported experimental invariance of E_B with the $FA_{1-x}Cs_x$ A-cation ratio (measured from magneto optical studies) at lower temperatures. [122, 123]

Cs concentration	E_g (eV)	E_B (meV)	γ (meV)	*Amp* (a.u.)
0% (Neat)	1.554	2	32.3	18.6
0% (IPA-dipped)	1.558	2	33.9	15.5
7%	1.564	2	31.5	19.6
9%	1.568	2	34.4	23.3
21%	1.590	2	32.2	27.1
29%	1.601	2	30.4	27.2
43%	1.612	2	43.1	34.0

Table A.1: Parameters extracted from Elliott fits to the absorption onsets of $FA_{1-x}Cs_xPbI_3$ films. The absorption coefficient spectra were fitted with 3 free parameters: E_g representing the optical bandgap, γ representing the electron-phonon coupling, and *Amp* representing the amplitude of the spectrum. The exciton binding energy E_B was globally fixed to a value of 2 meV. [40, 111, 122, 123]

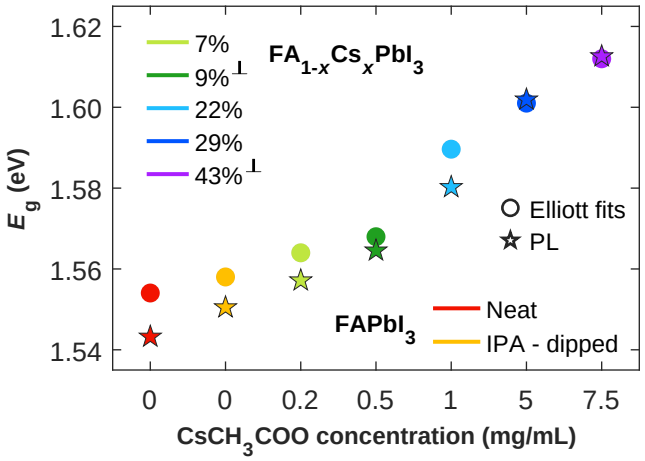


Figure A.5: Optical bandgap of $FA_{1-x}Cs_xPbI_3$ films. The optical bandgap for all $FA_{1-x}Cs_xPbI_3$ films extracted either from room-temperature steady-state PL spectra (star markers), or from the Elliott fits to the absorbance onset (circle markers). The Stokes shift is the difference between the absorbance-extracted bandgap and the PL-extracted bandgap. The small difference between the absorbance and PL bandgaps also suggests limited photon recycling and reabsorption events, which would otherwise cause an observable red-shift of the PL spectrum and peak.

A.4.2 Tauc plots

Tauc plots are frequently used in the literature to extract the bandgap of perovskite polycrystalline thin films including $FA_{1-x}Cs_xPbI_3$ films, [29, 30] yet their validity is somewhat questionable. The Tauc relationship was derived for amorphous semiconductors and its apparent close proximity to the actual perovskite bandgap is dependent on some of the errors from its assumptions cancelling out each other. [53]

Despite its deficiencies, I here apply this relationship to my data in order to make a comparison with a literature value of the bandgap of a similar material, [117] which was however obtained using Tauc plots and an integrating sphere to account for scattered light. The extracted bandgaps I obtain from Tauc plots to the absorption onsets of $FA_{1-x}Cs_xPbI_3$ are noticeably smaller than the optical bandgaps which were extracted from PL and Elliott fits, which would indeed imply an unlikely negative Stokes shift. However, they generally follow the same trend of a widening bandgap for the films dipped in the higher $CsCH_3COO$ concentration solutions.

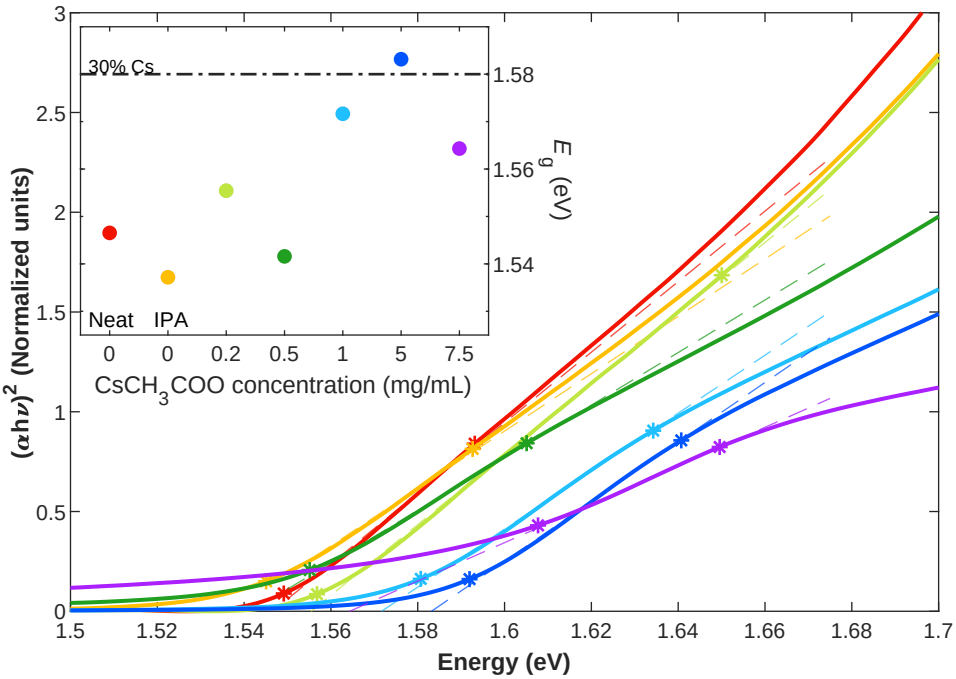


Figure A.6: Tauc plots to onsets of the squared absorbance spectra of $FA_{1-x}Cs_xPbI_3$ films. $(\alpha h\nu)^2$ (solid lines), and the linear fits (dashed lines) used for bandgap extraction for direct bandgap semiconductors according to the Tauc method. The inset shows the variation of the Tauc-extracted bandgaps, E_g, across the different Cs concentrations used for dipping $FAPbI_3$ films and a literature Tauc-extracted bandgap for an $FA_{0.7}Cs_{0.3}PbI_3$ film shown by the black dot-dash line. [117]

A.4.3 Baseline fitting and peak indexing

The Elliott fitting is only applicable to the absorption onset near the band edge, where the electronic band structure can be assumed to be parabolic and isotropic, transitions can be assumed to be between one valence and one conduction band, and the electric dipole transition matrix assumed to be independent of photon energy. [54] Therefore to decouple the peak features from the standard absorption coefficient spectrum at energies higher than the bandgap, I used a phenomenological fit to extract the peaks and quantify their behaviour.

The positions of the troughs in the experimental absorption coefficient data were obtained by subtracting a smoothed “central fit" line from the measured spectrum to result in a spectrum showing only the peak feature, from which the minimas (corresponding to the troughs) could be more readily extracted. Subsequently, interpolating a cubic spline between the experimental data at the energies of these troughs, resulted in the spline baseline fit I used to decouple the peak features from the underlying absorption coefficient data.

It is worth noting that because the dimensionality of confinement has not been conclusively determined, the peak-decoupling procedure implemented in this study potentially eliminates any underlying density of state contributions that may be associated with the quantum confinement. For instance, for an infinite-quantum-well confinement in all three dimensions, the density of states will have peak-like behaviour similar to what I extract from the decoupling mechanism. Alternatively, for a one-dimensional or a two-dimensional electronic confinement, the density of states will have additional continuum states associated with the electronic free motion in the other non-confined dimensions, states that would be removed when using this decoupling mechanism and would result in the same peak-like features I observe. This makes an accurate estimate of the confinement dimensionality even more difficult.

A.4.4 Temperature-dependent study of the absorbance spectra

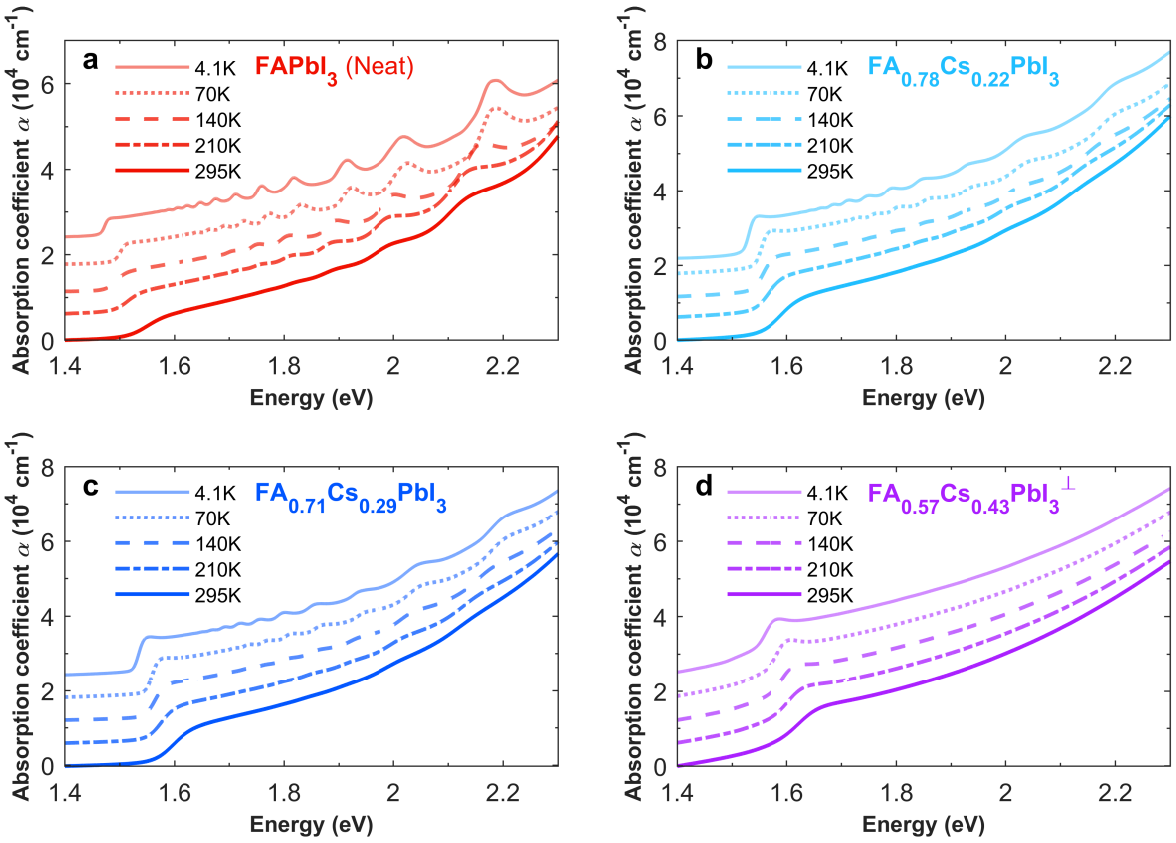


Figure A.7: Temperature-dependent absorption coefficient spectra of $FA_{1-x}Cs_xPbI_3$. **a**: $FAPbI_3$ (Neat), **b**: $FA_{0.78}Cs_{0.22}PbI_3$, **c**: $FA_{0.71}Cs_{0.29}PbI_3$, **d**: $FA_{0.57}Cs_{0.43}PbI_3$. Films are evaporated on either quartz or sapphire (indicated by $^{\perp}$) substrates.

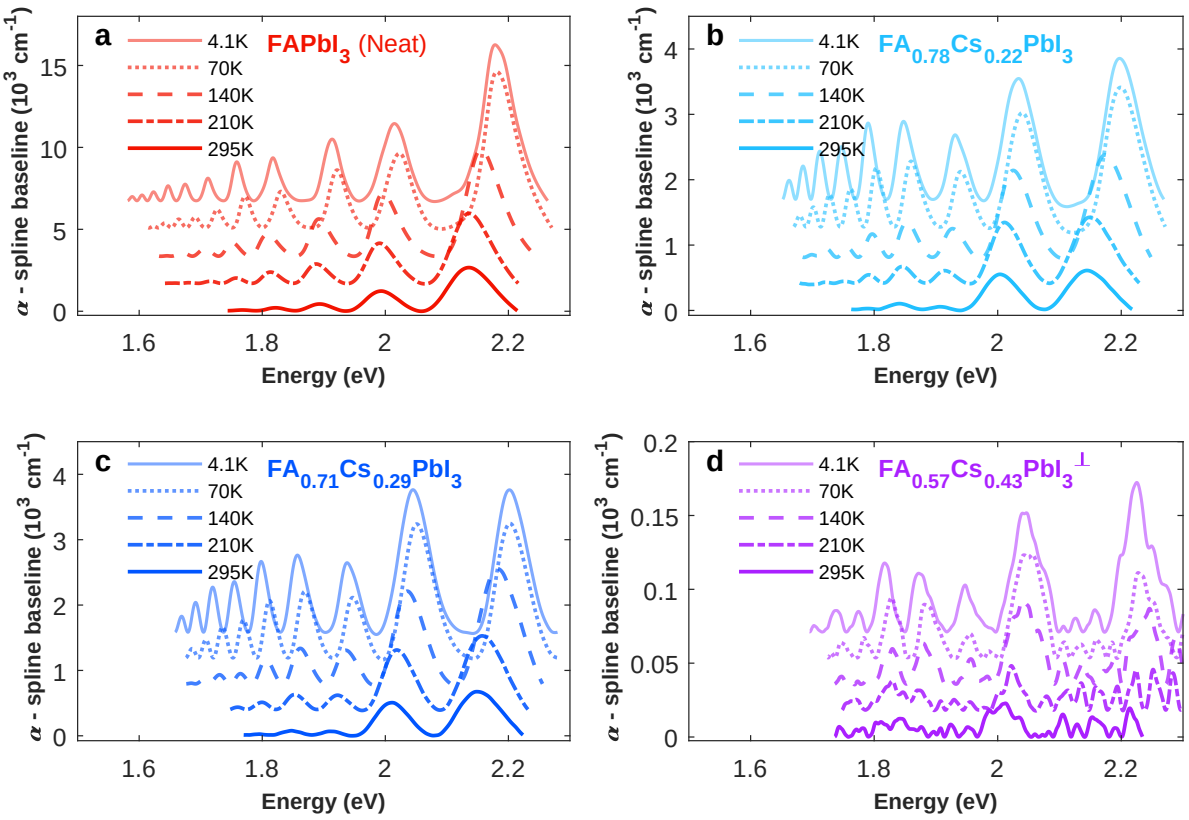


Figure A.8: Temperature-dependent above-bandgap peaks features of $FA_{1-x}Cs_xPbI_3$. The peaks are decoupled from the absorption coefficient spectra in the same way as described in the main text. **a**: $FAPbI_3$ (Neat), **b**: $FA_{0.78}Cs_{0.22}PbI_3$, **c**: $FA_{0.71}Cs_{0.29}PbI_3$, **d**: $FA_{0.57}Cs_{0.43}PbI_3$. Films are evaporated on either quartz or sapphire (indicated by $^{\perp}$) substrates.

A.5 Theoretical models

A.5.1 Infinite quantum well

The infinite quantum well provides an easy and straightforward method, albeit only an approximation to the real scenario, to analyse the peak behaviour and obtain simple analytic solutions that can be a good approximation to the deep states within the quantum well.

Assuming a perfectly parabolic electronic density of states for a confined system in an infinite quantum well, the confinement energy of the n^{th} peak is given by

$$E_n = \frac{\hbar^2}{8\mu^* L^2} \sum_{i=1}^{d_{\text{conf}}} n_i^2, \tag{A.5}$$

where μ^* is the reduced effective mass of the electron and hole in the material - defined as $\frac{1}{\mu^*} = \frac{1}{m_e^*} + \frac{1}{m_h^*}$, L is the quantum well width, and d_{conf} is the dimensionality of confinement.

I fit the 4 K confinement energies extracted from the absorbance spectra against their peak indices with a one-dimensional infinite quantum well model (shown in Figure 4.8) given by

$$E_n = A(n - n_0)^2 + B, \tag{A.6}$$

where A is a constant of proportionality $\left(\frac{\hbar^2}{8\mu^* L^2}\right)$, n_0 is the peak index at which the quadratic relation starts (lowest discernible peak $n_0 = 0$ for the neat $FAPbI_3$ film at 4 K), and B is the energy shift of the confined ground state from the bulk bandgap, which could be a result of a different bandgap within the confined regions owing to the lattice strain, and was fixed to the freely fitted value obtained from the $FAPbI_3$ fit across the different samples.

A.5.2 Krönig-Penney potential

The Krönig-Penney model offers a more realistic model to be used, in which the quantum confinement is the result of a periodic potential barrier of finite height, perhaps originating from periodic δ_{H}-$FAPbI_3$ phase inclusions for lattice strain relaxation. The simple Krönig-Penney approach can be applied here to a superlattice of periodically arranged finite quantum wells and has been shown to yield similar results to those obtained from a infinite quantum well for modelling the quantum confinement being investigated in this study. [40]

A.6 Temperature-dependent study of steady-state PL

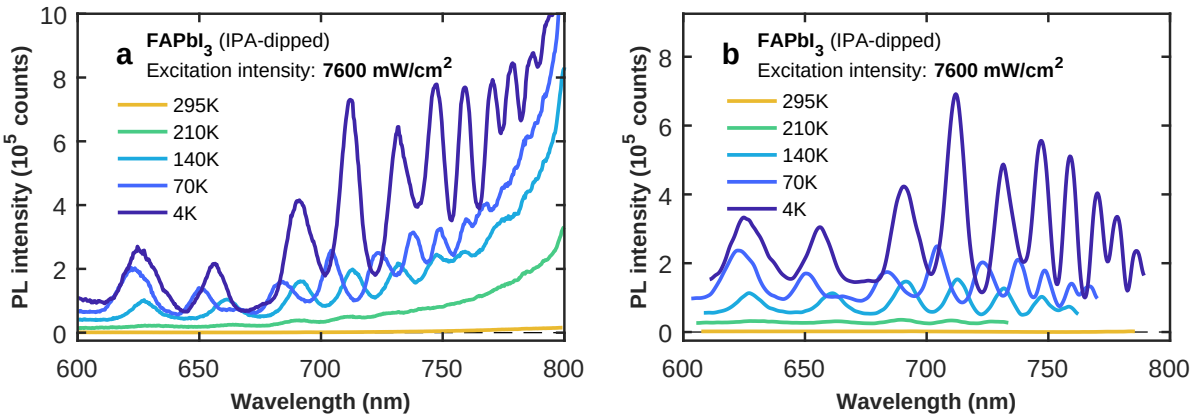


Figure A.9: Photoluminescence spectra of the PL peak features in $FAPbI_3$ (IPA-dipped) at energies above the main band edge peak at different temperatures. (**a**) shows the absolute PL spectra of the IPA-dipped $FAPbI_3$ film at different temperatures for a laser excitation intensity of $7600\,\mathrm{mW/cm^2}$. (**b**) shows the absolute peaks, decoupled from the PL spectra using a spline baseline fitting, for a laser excitation intensity of $7600\,\mathrm{mW/cm^2}$, with subsequent curves vertically offset by 0.25×10^5 counts.

A.6.1 $FA_{0.57}Cs_{0.43}PbI_3$

It is worth noting that for the low-temperature (4 K) steady-state PL of the $FA_{0.57}Cs_{0.43}PbI_3$ film, two main PL peaks were observed (as can be seen in Figure A.10), where the higher intensity peak corresponds to the bandgap extracted from the absorption coefficient spectrum for the same film at 4 K. This can be explained by bandtail recombination expected for metal-halide perovskites at low temperatures, as explained in previous work. [192] The method we implemented of inducing partial substitution of FA with Cs both results in a spatial variation of the bandgap of the material across its thickness (i.e. a composition differential across the film exists), and creates comparatively a larger number of deep trap states than those present in the control film - corroborated by the reduction in PL amplitude with increasing Cs concentration present in the film (as displayed in Figure A.3 and Figure 4.1 respectively). This creates a tail of deep trap states in the 43% Cs film, that would be difficult for the charge carriers to escape from with the limited thermal energy available at 4 K. Additionally, at these low temperature, fewer phonons will be available to mediate non-radiative recombinations from sub-gap trap states, resulting in the emergence of a visible bandtail peak in the PL spectrum, as observed here. It has previously been claimed that bandtail emissions at low temperatures, photon recycling and reabsorption, [193, 194] strong recombination due to excitons bound to surface defects, [195] or segregation of the different compositions throughout the films (causing two main different compositions and PL peaks - especially for those films dipped in higher concentrations of cs-acetate) can cause the formation of two main PL peaks. I can first rule out excitonic emission, since the expected E_B from the PL peak separation does not match that obtained from the Elliott fits. Similarly photon recycling can be ruled out as a source for the second peak, because of its very limited influence on the PL spectrum of these 100 nm thin films - as discussed above. Although the prevalence of ionic motion in metal halide perovskites with temperature is complicated (owing to both

the strength of entropic mixing and speed of ionic motion decreasing with a reduction in temperature), [33] the absence of two onsets or an additional feature in the absorption coefficient spectrum of this composition at 4 K (displayed in Figure A.7) can conclusively rule out cation segregation as an explanation. As a result, I conclude that the second PL peak arises from the existence of a tail of trap states causing prominent strong bandtail radiative recombination - as observed and explained before for metal-halide perovskites, [192] and inorganic semiconductors.

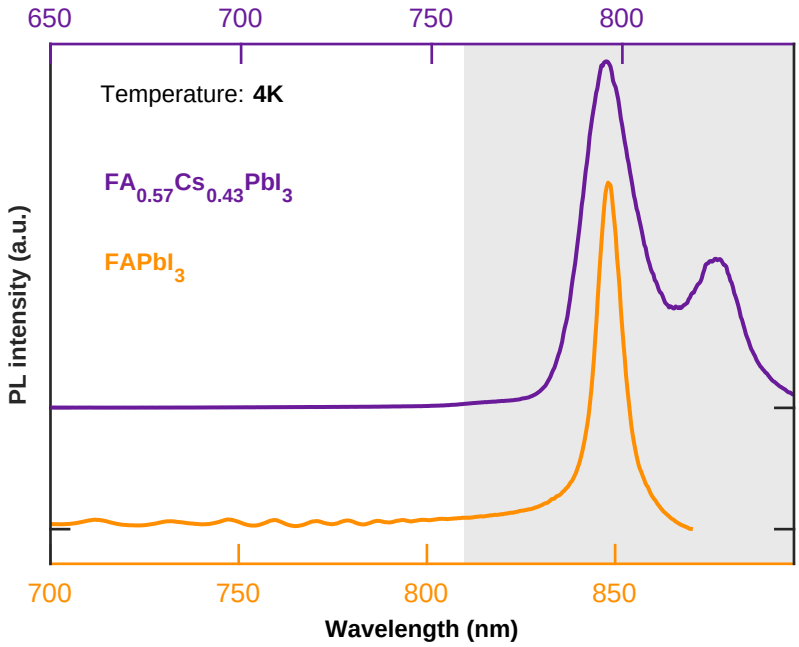


Figure A.10: Photoluminescence spectra at 4 K of $FA_{1-x}Cs_xPbI_3$ films. Photoluminescence (PL) spectra of an $FAPbI_3$ (IPA dipped) and a $FA_{0.57}Cs_{0.43}PbI_3$ film at a temperature of 4 K showcasing the presence and absence, respectively, of above-bandgap peak features. The two spectra are vertically offset for visual clarity. The appearance of a second PL peak for the $FA_{0.57}Cs_{0.43}PbI_3$ film is due to the existence of a tail of deep trap states, which is further discussed in section **??**

A.7 Time-resolved PL (TRPL)

TRPL of the thin films was measured using TCSPC (time-correlated single photon counting) following excitation by a 398 nm picosecond pulsed diode laser at a repetition rate of 1, 5, or 10 MHz (PicoHarp, LDH-D-C-405M), depending on the trace and to avoid wrap around and pile up. The resultant PL was collected and coupled into a grating spectrometer (Princeton Instruments, SP-2558), which directed the spectrally dispersed PL onto a photon-counting detector (PDM series from MPD), whose timing was controlled with a PicoHarp300 TCSPC event timer. The transients were recorded at the wavelengths corresponding to the main PL peak, and the observed PL peak features and valleys to probe the charge-carrier dynamics of the confined and unconfined regions.

The time-resolved PL traces of the $FAPbI_3$ (IPA-dipped) film at room temperature and the $FA_{0.57}Cs_{0.43}PbI_3$ film at 4 K are shown in Figures A.11 and A.12 respectively. The PL decay traces for both show a different dependence to what is observed for the decay traces of the PL peak features for the $FAPbI_3$ (IPA-dipped) film at 4 K.

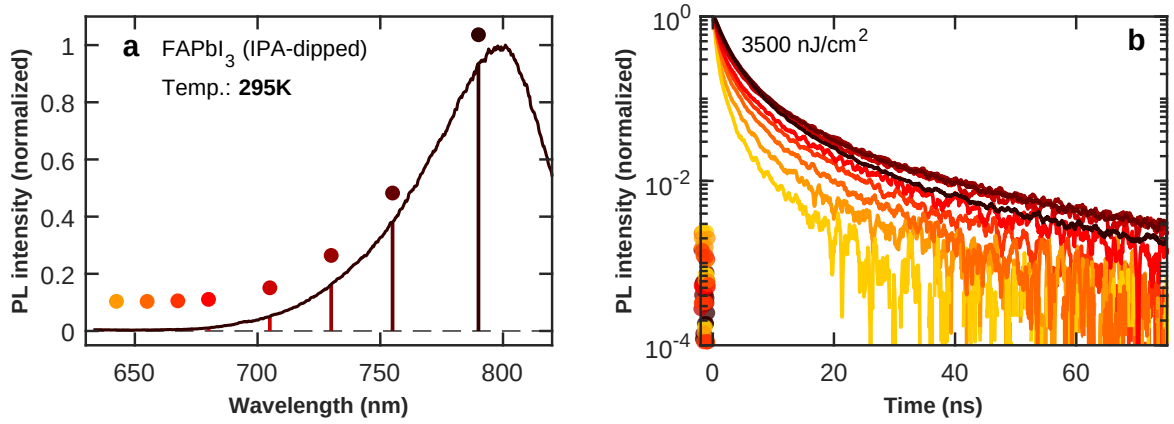


Figure A.11: Steady-state and time-resolved photoluminescence of the IPA-dipped $FAPbI_3$ film at room temperature PL spectra of the IPA-dipped $FAPbI_3$ film at **a**: 295 K for the region expected to show high-energy peak features, and **b**: the corresponding time-resolved photoluminescence (TRPL) decay traces recorded at the wavelength of the peaks represented by the solid vertical lines and dots in (**a**).

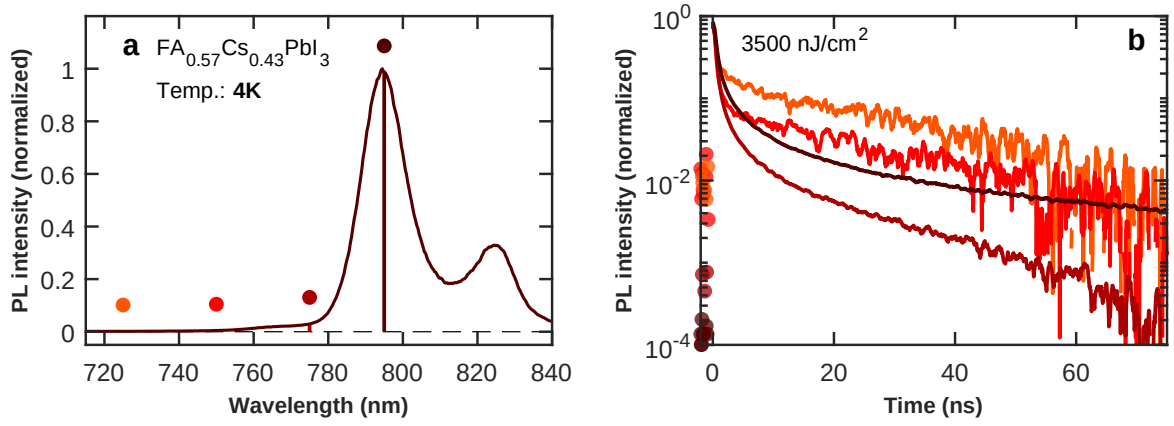


Figure A.12: Steady-state and time-resolved photoluminescence for the $FA_{0.57}Cs_{0.43}PbI_3$ film at 4 K PL spectra of the $FA_{0.57}Cs_{0.43}PbI_3$ film at **a**: 4 K for the region expected to show high-energy peak features, and **b**: the corresponding time-resolved photoluminescence (TRPL) decay traces recorded at the wavelengths of the peaks represented by the solid vertical lines and dots in (**a**).

Instrument Response Function

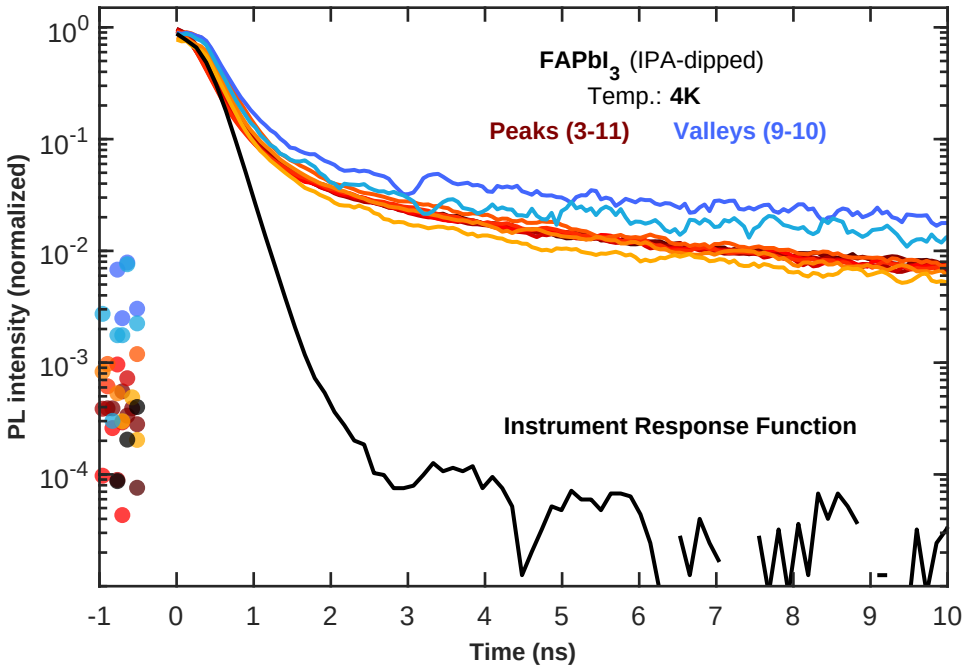


Figure A.13: IRF and time-resolved PL decay traces for $FAPbI_3$ at early times after excitation. The IRF sets the intrinsic temporal resolution of the experimental setup being used in this study. The early-time similarity between the IRF trace and the PL decay traces make a distinction between the charge-carrier dynamics of the quantum-confined states (peaks) and the non-confined regions (valleys) difficult, especially at early time. It also prohibits time resolution of some of the relaxation pathways likely to occur at very early times, such as internal relaxation within the quantum well and its domains.

B

Supplementary Analysis of Photovoltaic Performance of $FAPbI_3$ Perovskite is Hampered by Intrinsic Quantum Confinement [5]

Contents

B.1 Materials . . . 195
B.2 Fabrication . . . 196
B.2.1 For material characterization: . . . 196
B.2.2 For perovskite solar cell fabrication: . . . 196
"DMF-DMSO" Method . . . 197
"MACl route" . . . 197
"Sequential deposition" . . . 198
B.3 X-ray diffraction (XRD) . . . 200
B.3.1 Synchrotron X-ray data . . . 201
B.4 Scanning electron microscopy (SEM) . . . 203
B.5 Absorption measurements . . . 205
B.5.1 Elliott fitting . . . 207
B.5.2 Baseline fitting . . . 209
B.5.3 Temperature dependence of the absorbance spectra . . . 209
B.5.4 Definitions . . . 210
B.6 Photoluminescence . . . 211
B.7 Photovoltaic performance . . . 212
B.8 meta-analysis of literature reports . . . 217
B.8.1 Additional figures displaying results of meta-analysis: . . . 219

This appendix provides details of sample preparation and characterisation relevant

to Chapter 5. It also describes methods used for the meta literature survey in Chapter 5 and presents additional data to back the conclusions made in that chapter.

B.1 Materials

Fluorine-doped tin oxide (FTO) coated glass substrates (8 or 15 $\Omega\,cm^{-2}$, AMG), z-cut quartz substrates (UQG Optics Ltd, 13 mm diameter), tin (IV) oxide (15 wt. % in H_2O colloidal dispersion, Alfa Aesar), lead(II) iodide (99.99%, trace metal basis, Tokyo Chemical Industries), aluminium oxide nanoparticles (20 wt. % in isopropyl alcohol, Sigma Aldrich), methylammonium iodide (>99.99%, Greatcell Solar Materials), formamidinium iodide (>99.99%, Greatcell Solar Materials), phenethylammonium iodide (>99%, Greatcell Solar Materials), spiro-OMeTAD (2,2',7,7'-Tetrakis(N,N-di-p-methoxyphenylamino)-9,9'-spirobifluoren, >99.5%, Luminescence Technology Corp.), FK209 Co(III) TFSI salt (tris(2-(1H-pyrazol-1-yl)-4-tert-butylpyridine)cobalt(III) tri[bis(trifluoromethane)sulfonimide], 98%, Sigma Aldrich), bis(trifluoromethylsulfonyl)amine lithium salt (99.95%, Sigma Aldrich), gold pellets (99.999%, Kurt J. Lesker Company).

n-butylamine (99.5%, Sigma Aldrich), n-butanol (anhydrous, 99.8%, Sigma Aldrich), 2-propanol (anhydrous, 99.5%, Sigma Aldrich), chlorobenzene (anhydrous, 99.8%, Sigma Aldrich), acetonitrile (anhydrous, 99.8%, Sigma Aldrich), 4-tert-butylpyridine (98%, Sigma Aldrich).

Prior to use, all FTO-coated and quartz substrates were scrubbed with an aqueous 2 vol% Decon 90 solution, rinsed with deionised water, sonicated in acetone and subsequently sonicated in 2-propanol before being dried in a stream of N_2 gas.

All other non-aqueous chemicals were stored in a N_2-filled glovebox before use and protected from exposure to light.

B.2 Fabrication

Film fabrication was performed by Benjamin M. Gallant and Philippe Holzhey.

B.2.1 For material characterization:

A solution was prepared with 1:150 (vol:vol) aluminium oxide nanoparticles and anhydrous isopropyl alcohol. The solution was allowed to stir overnight prior to use. 80 μL of this solution was spin-coated dynamically on top of UV-ozone treated (15 minutes) z-cut quartz substrates, and annealed for 10 minutes at 100°C. This process was carried out in ambient air. Subsequently a $FAPbI_3$ perovskite layer was deposited through either of the three methods described in the solar cell fabrication methods below.

B.2.2 For perovskite solar cell fabrication:

Fluorine-doped tin oxide (FTO) substrates (30 mm × 30 mm, 15 Ωcm^{-2}) were cleaned (scrubbed and ultrasonicated) with a solution of decon 90 (3 vol%) in deionised water, then rinsed and ultrasonicated sequentially with deionised water, acetone and isopropyl alcohol, then dried in a stream of N_2 gas.

A colloidal suspension of tin oxide nanoparticles (400 μL) was diluted with ultrapure water (2,600 μL). In an atmosphere containing minimum moisture (<5% relative humidity), 200 μL of this solution was placed statically on a UV-ozone treated (15 minutes) substrate coated with a fluorine-doped tin oxide layer (15 Ω cm^{-2}), then spun at 4,000 rpm (with an initial acceleration of 1,000 rpm s^{-1}) for 30 seconds before being immediately annealed at 150°C for 30 minutes in the same environment. The substrates were allowed to cool, then immediately subjected to a further 15 minutes of UV-ozone treatment before being immediately used in the following processing step.

One of three protocols was used for each of the $FAPbI_3$ perovskite thin films:

"DMF-DMSO" Method

Stoichiometric FAI and PbI_2 were dissolved in a 4:1 mixture of DMF:DMSO (DMF: N,N-dimethylformamide; DMSO: dimethylsulfoxide) at 1.4 M concentration. 150 μL of this solution was dispensed statically on top of the SnO_2 layer (for PSC devices) or Al_2O_3 nanoparticle-coated z-cut quartz substrate (for material characterisation) under an atmosphere of air controlled to 18-24% relative humidity. The substrate was spun at 6,000 rpm (with an initial acceleration of 12,000 rpm s^{-1}) for 35 seconds. At 10 seconds into this procedure, 800 μL of diethyl ether antisolvent was dispensed slowly onto the spinning substrate. The substrate was then heated in ambient air at 150°C for 10 minutes. This protocol is adapted from that described by Kim et al.. [163]

"MACl route"

Stoichiometric FAI and PbI_2 were dissolved in a 4:1 mixture of DMF-DMSO at 1.8 M concentration, along with a 40 mol% excess of MACl. 150 μL of this solution was dispensed statically on top of the SnO_2 layer (for PSC devices) or Al_2O_3 nanoparticle-coated z-cut quartz substrate (for material characterisation) under an atmosphere of air controlled to 18-24% relative humidity. The substrate was spun at 6,000 rpm (with an initial acceleration of 12,000 rpm s^{-1}) for 35 seconds. At 10 seconds into this procedure, 800 μL of diethyl ether antisolvent was dispensed slowly onto the spinning substrate. The substrate was then heated in ambient air at 150°C for 10 minutes. This protocol is adapted from that described by Kim et al., [163] which reports minimal inclusion of any MA^+ or Cl^- ions in the resulting $FAPbI_3$ film. Additionally, similar fabrication methods reported in the literature have evidenced minuscule amounts of MA^+ ions (likely in the bulk of the film) [94, 163] or Cl^- ions (likely at the lower interface in contact with the substrate) [181, 196] being incorporated. Such trace inclusions are highly unlikely to have

any effect on the structure and electronic bandstructure, as apparent from absorption onsets reported for across the three fabrication methods.

"Sequential deposition"

Lead iodide (1.266 mmol, 583.5 mg) and methylammonium iodide (1.139 mmol, 181.1 mg) were mixed with n-butylamine (1.899 mmol, 187.6 μL) and the ether solvent (1,500 μL) and agitated until all solids were fully dissolved, in a modified version of the process reported by Noel et al.. [166] 50 μL of this solution was spin-coated dynamically on top of the SnO_2 layer (in PSC devices) or Al_2O_3 nanoparticle-coated z-cut quartz substrate (for material characterisation) at 2,500 rpm for 45 seconds. The substrates were immediately annealed at 70°C for 10 minutes. After cooling, the substrates were coated with 350 μL of a 0.1 M solution of formamidinium iodide (0.500 mmol, 86.0 mg) dissolved in n-butanol (5,000 μL). After 45 seconds of static soaking, the substrates were spun at 4,000 rpm (with an initial acceleration of 1,000 rpm s^{-1}) for 45 seconds, then immediately annealed for 10 minutes at 70°C, followed by 30 minutes at 180°C.

In all cases, the substrates were allowed to cool, then a 20 mM solution of phenethylammonium iodide (0.200 mmol, 49.8 mg) in 2-propanol (10,000 μL) was spin-coated dynamically on top at 5,000 rpm for 45 seconds, in a N_2-containing glovebox.

A solution of spiro-OMeTAD (0.070 mmol, 85.8 mg) dissolved in chlorobenzene (1,000 μL) and doped with 8.4 μL of a 0.250 M solution of tris(2-(1H-pyrazol-1-yl)-4-tert-butylpyridine)cobalt(III) tri[bis(trifluoromethane)sulfonimide] in acetonitrile, 19.4 μL of a 1.8 M solution of
bis(trifluoromethylsulfonyl)amine lithium salt in acetonitrile, and tert-butyl pyridine

(0.231 mmol, 38.0 μL) was spin-coated on the PEAI-passivated substrates dynamically at 2,500 rpm for 30 seconds, in a N_2-containing glovebox.

Finally, 80 nm of gold was evaporated on top of the substrates at an initial rate of 0.1 As^{-1} at a pressure $<2\times10^{-6}$ torr.

B.3 X-ray diffraction (XRD)

XRD patterns were measured in air using a Panalytical X'pert powder diffractometer with a copper X-ray source (Cu-Kα X-rays with a wavelength of 1.5418 Å).
The XRD patterns were then corrected for tilt by shifting the 2θ-axis, such that the z-cut quartz reference peaks at $2\theta = 16.433°$ were all aligned for the films on quartz substrates.

The extracted peak positions and full widths at half maximum (FWHM) of the pseudo-cubic (100) perovskite XRD peak of α-$FAPbI_3$ were obtained by using the extracted fitting parameters from pseudo-Voigt fits.

B.3.1 Synchrotron X-ray data

Synchrotron XRD measurement was performed by Nakita K. Noel. Synchrotron X-ray scattering data was acquired at the Stanford Synchrotron Radiation Lightsource (SSRL) at beamline 11-3. The samples were measured at an incident angle of 3° and an incident X-ray energy of 12.7 keV. A Rayonix MX225 2D detector was used for data collection and a LaB_6 standard was used to calibrate the sample to detector distance. The data were integrated over the full azimuthal range using GSAS-II. Peaks were fitted with a Voigt function.

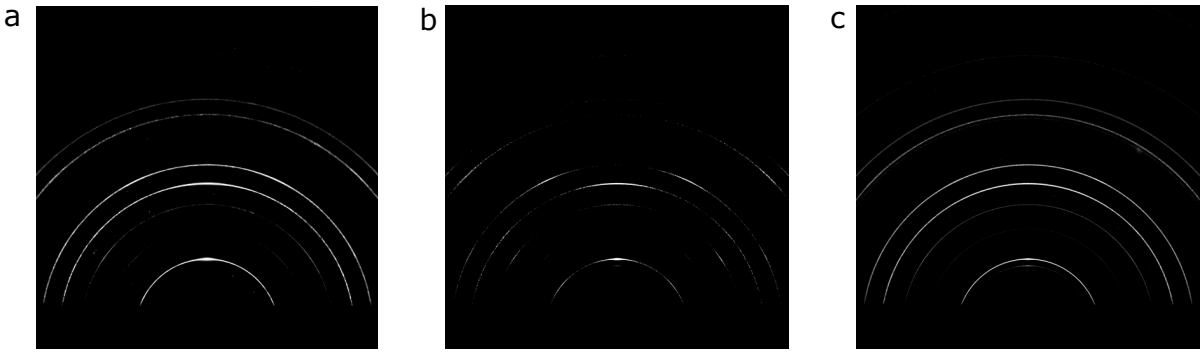


Figure B.1: Grazing-incidence wide angle X-ray scattering of $FAPbI_3$ thin films fabricated via a. DMF-DMSO, b. MACl route and c. sequential deposition method.

B.4 Scanning electron microscopy (SEM)

SEM measurements were performed by Benjamin M. Gallant. A FEI Quanta 600 FEG Environmental Scanning Electron Microscope (ESEM) was employed to investigate perovskite layer morphology. Accelerating voltages between 4-15 kV were employed for various analyses. For cross-sectional SEM images the substrates were partially scored post-deposition, then snapped along the score line. Images were acquired from snapped regions that had not been directly scored.

Employing different concentration of the $FAPbI_3$ precursor solution for the films made via the neat DMF-DMSO method resulted in films of different thicknesses. The film thickness increase as the precursor concentration increases from 1.4 M to 1.6 M, followed by a noticeable decrease when the precursor concentration further to 1.8 M, which could be a result of incomplete conversion of $FAPbI_3$ to the perovskite phase and the expected fast nucleation associated with higher precursor and colloid concentrations. By contrast, $FAPbI_3$ fabricated via the MACl route gives optimal performance when a 1.8 M precursor solution is employed.

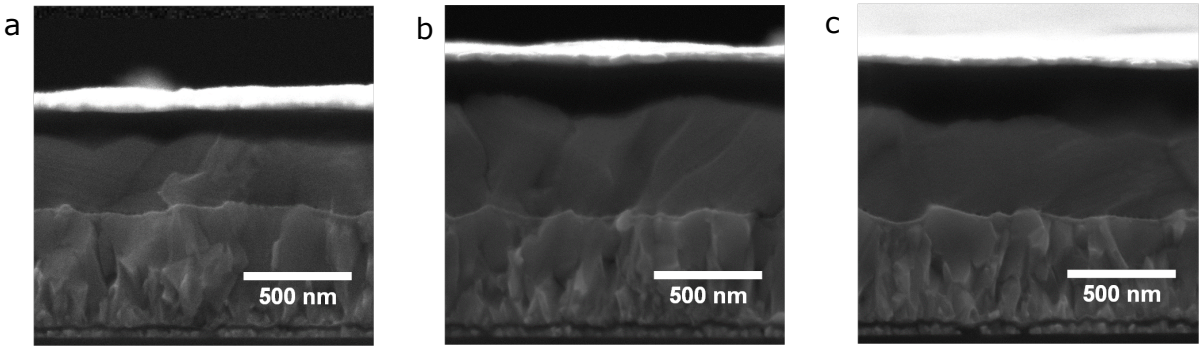


Figure B.2: Cross-sectional SEM images of the devices incorporating $FAPbI_3$ films made via the neat DMF-DMSO route, with different molar concentrations of FAI. **a**. 1.4 M (resulting in $FAPbI_3$ thickness of 340 nm) **b**. 1.6 M (resulting in $FAPbI_3$ thickness of 450 nm), and **c**. 1.8 M (resulting in $FAPbI_3$ thickness of 440 nm). This device stack comprises FTO, SnO_2 nanoparticles, perovskite layer with a PEAI surface treatment, Spiro OMeTAD, Au electrodes.

B.5 Absorption measurements

Reflectance (R) and transmittance (T) spectra were measured using a Fourier transform infrared (FTIR) spectrometer (Bruker Vertex 80v), configured with a tungsten halogen lamp illumination source, a CaF_2 beamsplitter and a silicon detector. The absorption coefficient (α) spectrum of each thin-film sample is then obtained using the relationship

$$\alpha = -\frac{1}{d} \cdot \log_{10}\left(\frac{T}{1-R}\right)$$

where d is the film thickness.

The samples were all mounted in a gas-exchange helium cryostat (Oxford Instruments, OptistatCF2) for the room-temperature measurements (where the outer vacuum chamber was pumped down to low pressures ($< 5 \times 10^{-5}$ mbar) and for the temperature-dependent study, where the temperature was varied between 4 K and 295 K in either 5 K or 10 K increments.

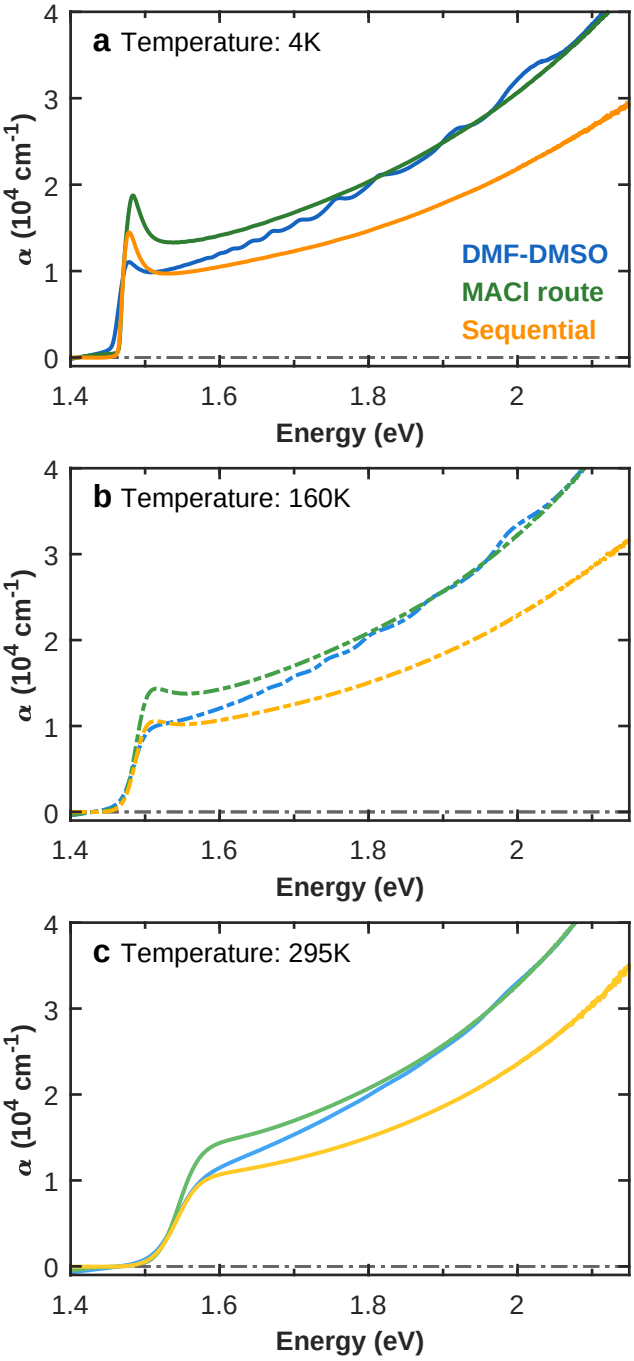


Figure B.3: Absorption coefficient spectra of $FAPbI_3$ thin films fabricated via DMF-DMSO, MACl route and sequential deposition method at a. 4 K, b. 160 K, and c. 295 K.

B.5.1 Elliott fitting

The onset in the absorption coefficient spectrum is fitted using Elliott's model that describes the absorption of a semiconductor near its band edge. [52]

The theory expresses the energy-dependent absorption as:

$$\alpha(E) = \alpha_{\mathrm{X}}(E) + \alpha_{\mathrm{C}}(E)$$

The bound exciton contribution α_{X} has the form:

$$\alpha_{\mathrm{X}}(E) = \frac{b_0}{E} \sum_{n=1}^{\infty} \frac{4\pi E_{\mathrm{b}}^{3/2}}{n^3} \delta\left(E - \left[E_{\mathrm{g}} - \frac{E_{\mathrm{b}}}{n^2}\right]\right)$$

where b_0 is a constant of proportionality that incorporates the electric dipole transition matrix element between the valence and conduction band. α_{X} is formed of the weighted sum of contributions from the exciton states with positive integer quantum number n and energies $E_{\mathrm{g}} - \frac{E_{\mathrm{b}}}{n^2}$, where E_{g} is the band gap energy and E_{b} is the exciton binding energy.

Here, the contribution from the electron-hole continuum states $\alpha_{\mathrm{C}}(E)$ has the form

$$\alpha_{\mathrm{C}}(E) = \frac{b_0}{E} \left[\frac{2\pi\sqrt{\frac{E_{\mathrm{b}}}{E-E_{\mathrm{g}}}}}{1 - \exp(-2\pi\sqrt{\frac{E_{\mathrm{b}}}{E-E_{\mathrm{g}}}})}\right] c_0^{-1} \mathrm{JDoS}(E)$$

where the joint density of states is given by $\mathrm{JDoS}(E) = c_0\sqrt{E - E_{\mathrm{g}}}$ for $E > E_{\mathrm{g}}$ and 0 otherwise, and the joint density of states constant $c_0 = \frac{1}{(2\pi)^2}\left(\frac{2\mu}{\hbar^2}\right)^{3/2} \times 2$, where μ is the reduced effective mass of the electron-hole system. The term in square brackets is the Coloumbic enhancement factor, which increases the absorption from the continuum states above the square-root form of the JDoS for a direct-gap semiconductor as a result of the Coloumbic attraction between the unbound electrons and holes.

The linear combination of the contributions from the excitonic and continuum states, $\alpha(E)$, is then convolved with a broadening normal distribution function - representing the homogeneous broadening caused by electron-phonon coupling, disorder and local

fluctuations of the stoichiometry of the material. The broadening is mathematically denoted by $g(E) = \mathcal{N}(0, \sigma_{\mathrm{T}}^2)$.

B.5.2 Baseline fitting

Elliott fitting is only applicable to the absorption onset near the band edge, therefore to decouple the oscillatory features from the standard absorption coefficient spectrum at energies higher than the bandgap, I used a phenomenological fit to extract the peaks and quantify their behaviour, as described in previous works.[40,41]

A smoothing algorithm is applied to the peaked features of the absorption spectrum and subsequently subtracted from the absorption spectrum to result in purely the contributions from the peak features, whose minima correspond to the troughs observed in the experimental data. Interpolating a cubic spline between the experimental data at the energies of the minima, resulted in the baseline fit I used to decouple the peak features from the underlying absorption coefficient data resembling the bulk material.

It should be noted that this procedure also eliminates any possible additional density-of-state contributions associated with the quantum confinement.

B.5.3 Temperature dependence of the absorbance spectra

A reduction in temperature is expected to increase the prominence of the studied absorption features and by association the strength of the electronic quantum confinement. This experienced increase in confinement strength may arise from the lattice contraction and subsequent reduction in confinement length scale, and a decrease in electron-phonon coupling and thermal fluctuations. [40, 41] In addition, the increased prominence may derive from a growth in the material volume experiencing confinement as the formation of the potentially-confining δ-phase becomes more prominent at lower temperatures. [33, 40, 41]

B.5.4 Definitions

In my quantitative analysis of the quantum confinement and behaviour of the peaks, I utilise the confinement energy and spectral area under the peaks. I define the confinement energy associated with a given peak as the peak energy position of the decoupled peak minus the Elliott-extracted band gap of the material. Meanwhile, the spectral area under the peaks is defined as the spectral area between the experimental absorption coefficient data and baseline fit, stated as a percentage of the spectral area under my experimental data (integrated between the first and last detectable minima of the oscillatory peak features).

B.6 Photoluminescence

A 398 nm diode laser (PicoHarp, LDH-D-C-405M) was used to photo-excite the samples, on a continuous wave setting at an intensity of 67.3 mW/cm^2. The resultant PL was collected and coupled into a grating spectrometer (Princeton Instruments, SP-2558), which directed the spectrally dispersed PL onto a silicon iCCD (intensified charge coupled device, PI-MAX4, Princeton Instruments). The samples were mounted in a vacuum cell under low pressure ($\sim 10^{-2}$ mbar).

The optical bandgap was extracted by finding the energy corresponding to the maximum intensity of the room-temperature PL spectra of the $FAPbI_3$ films is shown in Figure 5.7, and is further proof that the $FAPbI_3$ thin films fabricated via DMF-DMSO, MACl route and sequential deposition method are of essentially the same composition.

I note that similar low-temperature PL spectra of a $FAPbI_3$ film exhibiting strong quantum confinement have previously been reported, [41] with steady-state PL peaks falling at similar energies to those of corresponding peaks in the absorption spectra, and time-resolved PL showing differences between bulk and confined phases. [41]

B.7 Photovoltaic performance

Device fabrication and photovoltaic performance measurements were performed by Benjamin M. Gallant and Philippe Holzhey. Current-voltage (J–V) and maximum power point (MPP) measurements were carried out using a 2400 series source meter by Keithley Instruments in ambient air both under light (simulated AM 1.5 irradiance generated by a Wavelabs SINUS-220 simulator) and in the dark. The active area of the solar cell was masked with a black-anodised metal aperture to 0.25 cm^2, within a light-tight holder. Device areas are determined based on the aperture area of a mask that covers the solar cell during measurement. These masks have been measured precisely using optical microscopy (area is correct $\pm\dot{0}.5\%$). [197] The “forward" J–V scans were measured from forward bias to short-circuit and the “backward" scans were from short-circuit to forward bias, both at a scan rate of 245 mVs^{-1}. Active MPP tracking measurements using a gradient descent algorithm were performed for at least 30 s to obtain the steady-state power conversion efficiency. Active MPP tracking measurements (η_{mpp}) using a gradient descent algorithm were performed for at least 30 s to obtain the steady-state power conversion efficiency. Steady-state open-circuit voltage (V_{OC}) measurements were performed by illuminating the PSCs and extracting no charge carriers ($J = 0\,mAcm^{-2}$) and measuring the potential difference across the cell until it no longer evolved over time (10-250 s). Subsequently for each PSC, a steady-state short-circuit current (J_{SC}) measurement was made by illuminating the PSCs and holding the applied bias at 0 V and measuring the current density output over time until it no longer evolved over time (5-20 s). Some cells exhibited improvement over multiple measurements, in which case the peak performance was reported. This typically took two to five J–V scan plus MPP tracking iterations for the highest efficiency cells, in a measurement time of around 2–5 minutes. The intensity of the solar simulator was set periodically such that the

short-circuit current density from a KG3-filtered Si reference photodiode (Fraunhofer ISE) matched its 1-sun certified value. A local measurement of the intensity before each batch of solar cell measurements were performed by integrating the spectrum obtained from the solar simulator's internal spectrometer. By taking the ratio of this internal intensity measurement to one obtained at the time of calibration we determined the equivalent irradiance at the time of measurement. For the data presented in this publication, this gave values ranging from 0.990-1.005 suns equivalent, which have been applied to the calculation of power conversion efficiencies for each individual measurement. The spectral mismatch factor was estimated to be 1.022 according to a previously reported method. [197] This has also been applied to calculate power conversion efficiencies. We estimate the systematic error of this setup to be on the order of $\pm 5\%$ (relative).

EQE spectra of two sample solar cells incorporating $FAPbI_3$ films produced through the MACl route and the sequential deposition approach are presented in Figure B.7 together with their corresponding *J-V* characteristics. We note that the integrated J_{SC} values for both PSCs presented are somewhat lower than those exacted from the *J-V* characteristics of the same cell or found from a steady-state J_{SC} measurement. A similar disparity has been reported by a number of research groups, and was recently described and summarised in detail in a Viewpoint from Saliba and Etgar, [198] and observed by Lin et al. [199] and Schutt et al. [200]. In these examples the difference between the integrated J_{SC} measured via EQE and the steady-state J_{SC} extracted from *J-V* characteristics is of similar magnitude to that observed in this chapter. We further calibrated the solar simulator, by carrying out a stabilised J_{SC} measurement (whereby the bias across the solar cell is held at 0 V until the extracted current stabilises) to confirm that current densities extracted from *J-V* characteristics do not over- or underestimate J_{SC}, which is of particular concern for PSCs in the n-i-p configuration given that these devices are

prone to hysteretic behaviour. Accordingly, the steady-state J_{SC} values presented in our chapter are precise to an acceptable degree of error.

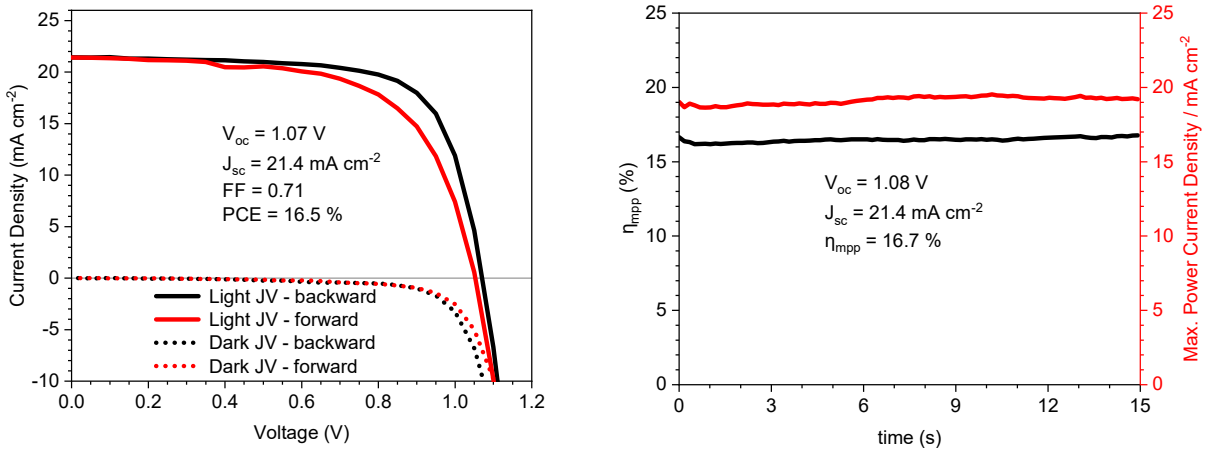


Figure B.4: $J-V$ **characteristics and maximum power tracked power output plots of the champion cell incorporating an** $FAPbI_3$ **layer fabricated via the neat DMF-DMSO route.**

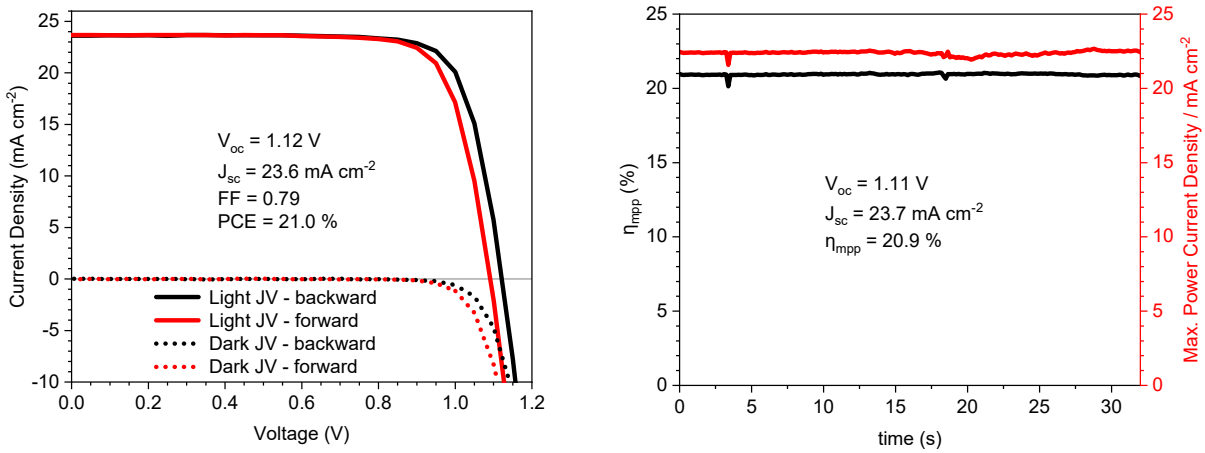


Figure B.5: $J-V$ **characteristics and maximum power tracked power output plots of the champion cell incorporating an** $FAPbI_3$ **layer fabricated via the MACl route.**

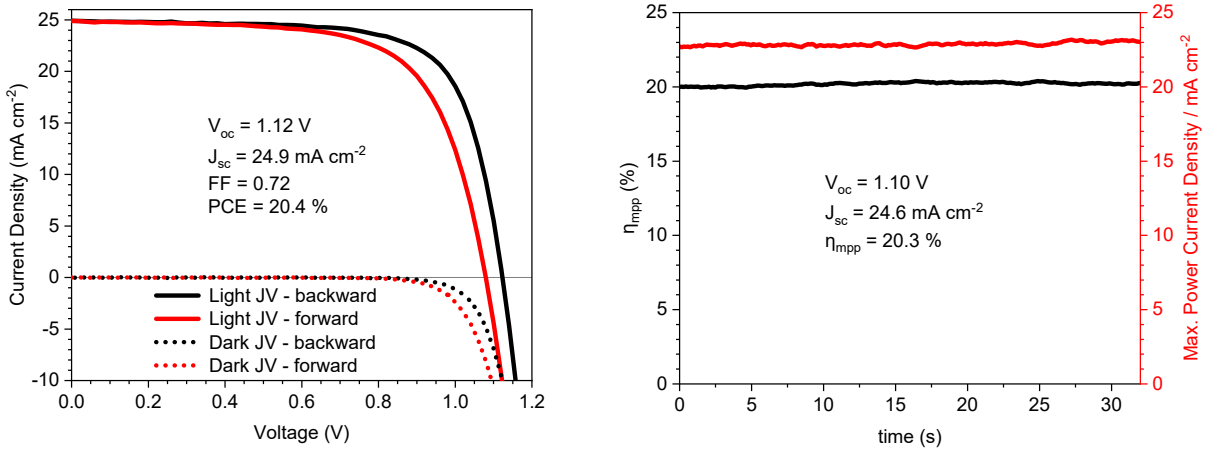


Figure B.6: $J-V$ **characteristics and maximum power tracked power output plots of the champion cell incorporating an** $FAPbI_3$ **layer fabricated via the sequential deposition route.**

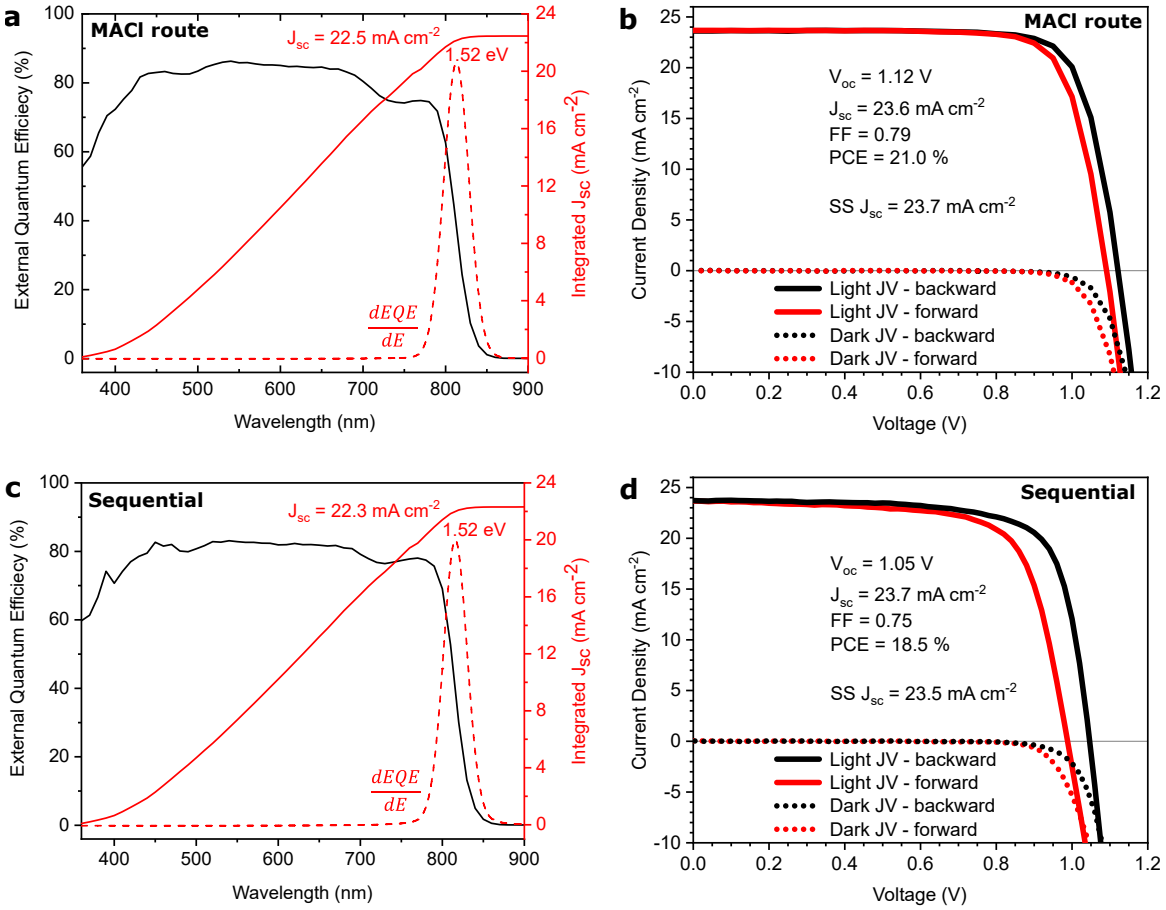


Figure B.7: "EQE spectra and $J-V$ characteristics of two sample solar cells incorporating a $FAPbI_3$ layer fabricated either via the (a,b) MACl route or (c, d) the sequential deposition route. We note that these devices represent randomly selected examples rather than champion cells from within the batch.

B.8 meta-analysis of literature reports

For my meta-study of literature reports covering photovoltaic applications with $FAPbI_3$ as absorber layer, I searched for relevant publications as follows:

- For reports with publication dates up to and until the 31^{st} of December 2019, I utilised the open-access Perovskite Database Project, [149] which reports photovoltaic devices incorporating perovskites as their photo-absorber layer and the performance for their corresponding PV devices. This dynamic database is thorough and comprehensive up to the chosen date of the 31^{st} of December 2019, with some additional sporadic entries beyond that from authors choosing to upload PV performance data for their devices after the release of the database.

- For reports from the $1st$ of January 2020, I searched the "Web of Science" [201] global citation database by entering "Formamidinium" as the search term in the abstract or title of all published scientific reports, as a starting point to obtain a similarly comprehensive overview of the field working on fabricating solar cells incorporating $FAPbI_3$.

Any publications not reporting PV performance data for solar cells incorporating $FAPbI_3$ films were excluded from my meta-study. For publications with such data available, the typical PCE values recorded in this chapter were either the averaged PCE values determined across a batch of many solar cell devices, or alternatively the champion PCE value of the solar cell if the averaged value is not reported, both during a reverse scan. I note that the field has evolved since the earliest publications I included (i.e. from December 2013 onwards) towards improved device reporting standards, however, in order to include many of the early studies, listing of reports where solely champion efficiencies are reported, was essential.

I note that Figure 5.10 in Chapter 5 and Figure B.15 show good continuity between the numbers of reports across the transition time (2019 to 2020) between the two search methods, suggesting that these searches cover the field sufficiently comprehensively.

Subsequently, I placed a couple of criteria on the photovoltaic devices allowed to be incorporated into the meta-analysis. First, the photo-absorber layer had to be a stoichiometric $FAPbI_3$ film, i.e. I did not include absorbers for which additives had been fully incorporated into the perovskite or treatments that would change its claimed composition away from $FAPbI_3$. For example, additives such as HI, MACl, and Cl were accepted, while others, such as MAI, MABr and CsI, were discarded. Second, any $FAPbI_3$ films of lower dimensionality were excluded from this meta-study.

The accepted devices were then categorized into three categories: If the absorption spectra were unavailable, or if the clear determination of the presence or absence of the absorption features was deemed impossible with the data presented, then the devices associated with these spectra were categorized into “QC data unavailable". This difficulty in discerning the existence of these features can stem from the absorption spectra being too noisy, from the plotted absorption spectra not covering the energetic range where these features typically exist and are prominent (e.g. shown absorption range only covering the onset where these features are weak), or from the plots being too crowded with overlaid absorption spectra of multiple films being studied to allow for clear data extraction and analysis. However, if the absorption spectra were smooth and clear enough for an accurate evaluation, then the films, and associated photovoltaic devices, were either categorized into “QC present", or “QC absent". On numerous occasions, the films were easily categorized by eye into one of these two categories if the absorption features were clearly detectable, or if it was clearly apparent that no modulations or features existed. When this was not the case, the data were extracted from the published absorption spectra using the DigitizeIt software and the analysis of decoupling any existing features

and calculating the spectra area under the peaks was carried out as described above. Accordingly, if the absorption spectrum of a $FAPbI_3$ film had a spectral area under the peaks exceeding the assigned threshold value of 1% of the full spectral area, then the features were deemed as “QC present", otherwise they were deemed as “QC absent".

I note that owing to the wide variety of reported processing methods used to fabricate $FAPbI_3$ films, I was unable to disentangle correlations between the appearance of the features and any given fabrication method or solvents used. It is practically impossible to obtain clusters of data covering identical fabrication methods because approaches vary so widely, making it impossible to extract any statistically significant information out of such an analysis.

B.8.1 Additional figures displaying results of meta-analysis:

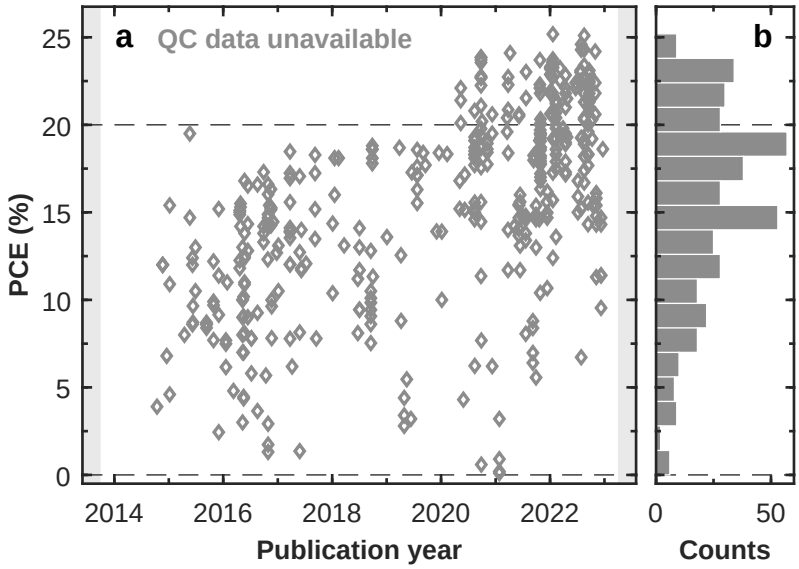


Figure B.8: Meta-study of device performance and absorbance features of $FAPbI_3$ thin films categorised as "QC data unavailable". **a**. Scatter plot of all device data. **b**. Percentage spread of the time-integrated PCE data in **a**.

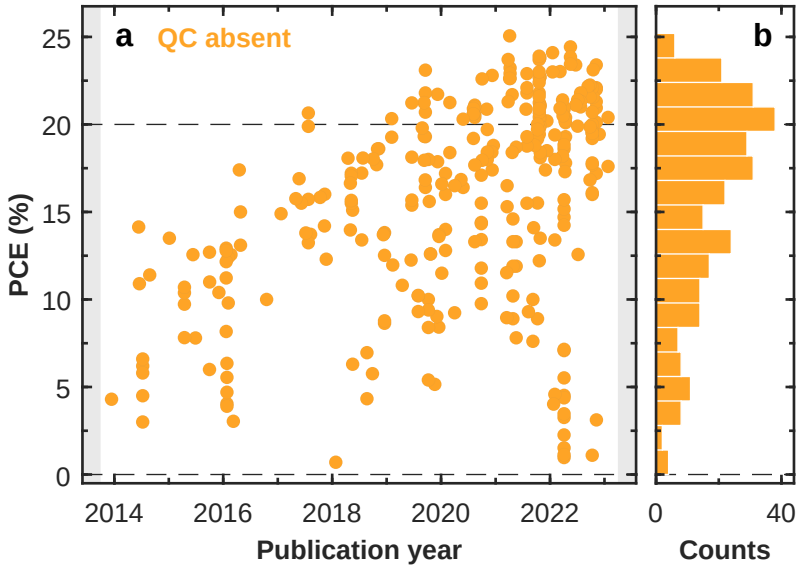


Figure B.9: Meta-study of device performance and absorbance features of $FAPbI_3$ thin films categorised as "QC absent". **a**. Scatter plot of all device data. **b**. Percentage spread of the time-integrated PCE data in **a**.

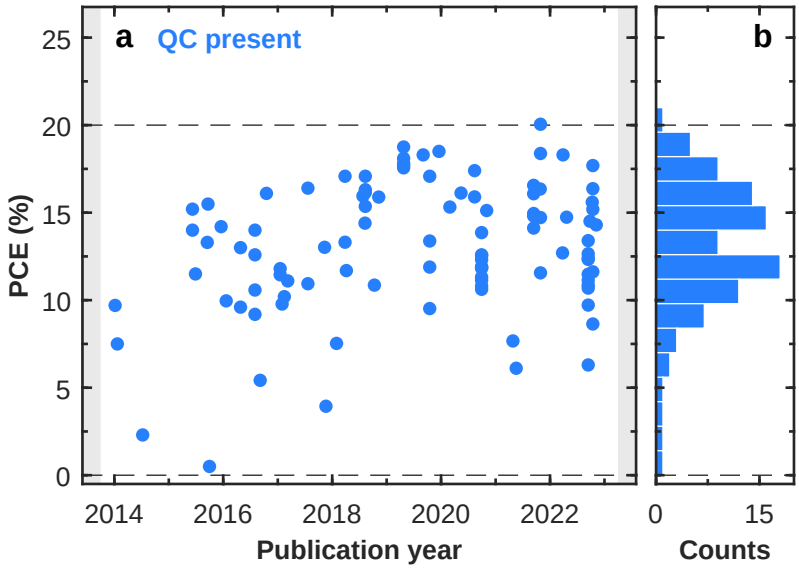


Figure B.10: Meta-study of device performance and absorbance features of $FAPbI_3$ thin films categorised as "QC present". a. Scatter plot of all device data. **b**. Percentage spread of the time-integrated PCE data in **a**.

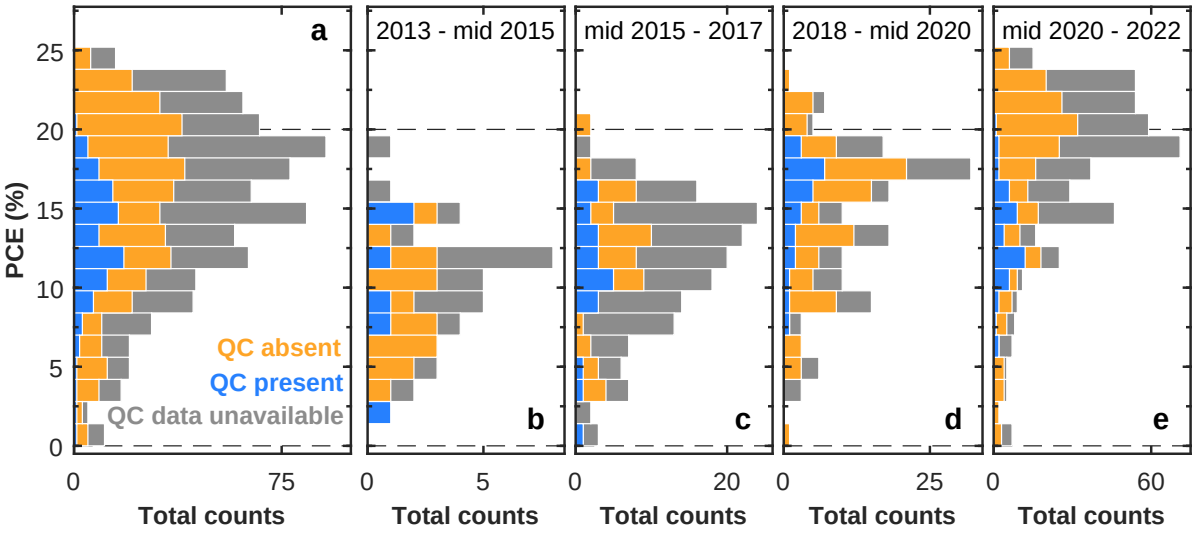


Figure B.11: Meta-study of device performance and absorbance features of $FAPbI_3$ thin films. a. Total counts spread of the total time-integrated PCE values presented in Main Figure 5.10a. Total counts spread of the 18-months time-integrated PCE values presented in Main Figure 5.10a from 2013 - mid 2015 (**b**), mid 2015 - 2017 (**c**), 2018 - mid 2020 (**d**), and mid 2020 - 2022 (**e**).

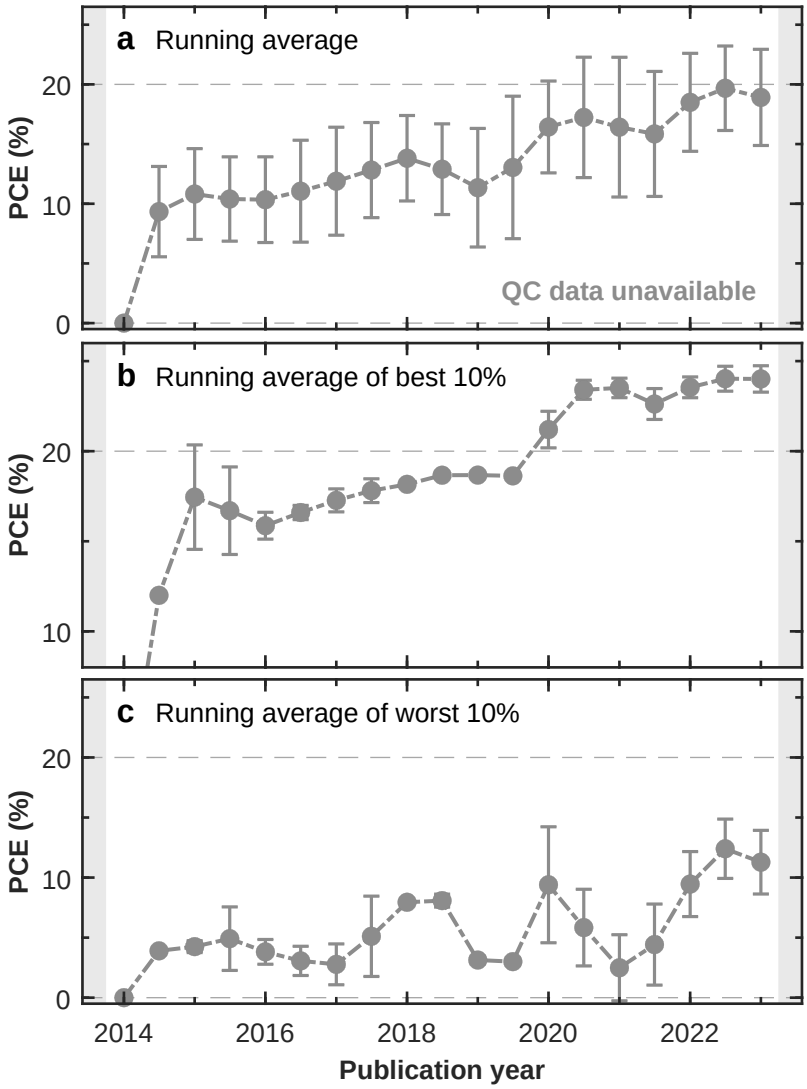


Figure B.12: Meta-study of device performance and absorbance features of $FAPbI_3$ thin films categorised as "QC data unavailable". Running average of total (**a**), highest 10% (**b**), and lowest 10% (**c**) PCE values for devices of each category with a one year time window. Error bars represent one standard deviation.

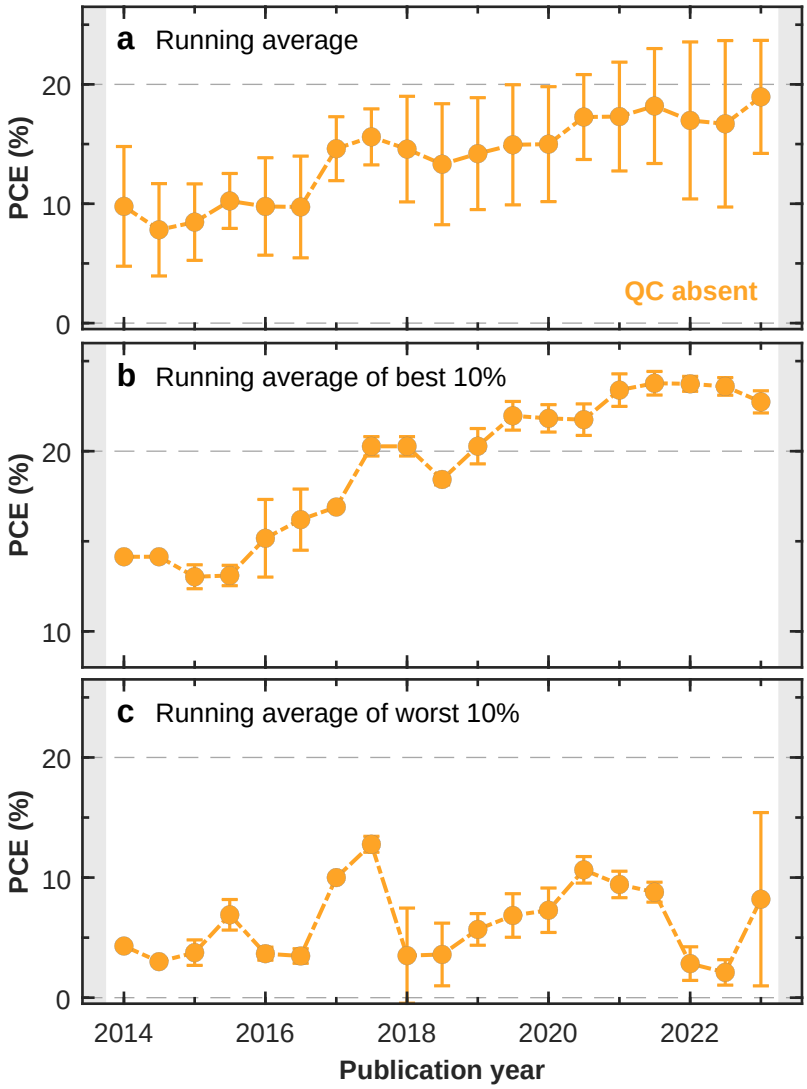


Figure B.13: Meta-study of device performance and absorbance features of $FAPbI_3$ thin films categorised as "QC absent". Running average of total (**a**), highest 10% (**b**), and lowest 10% (**c**) PCE values for devices of each category with a one year time window. Error bars represent one standard deviation.

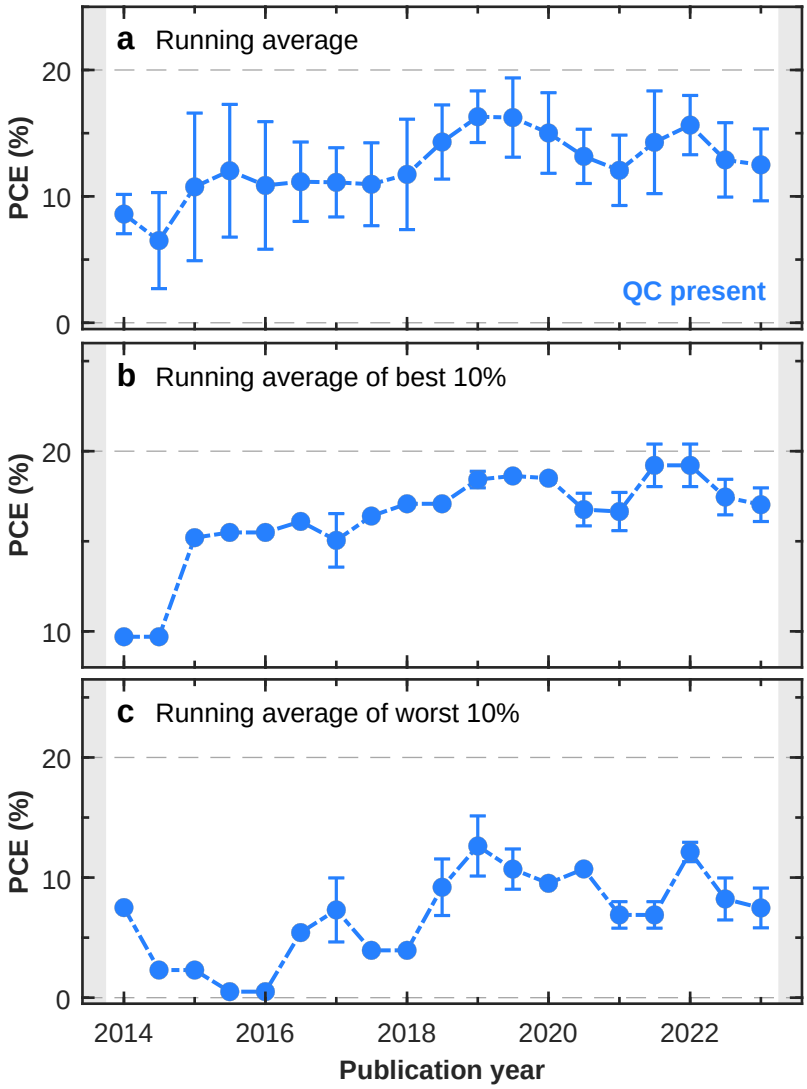


Figure B.14: Meta-study of device performance and absorbance features of $FAPbI_3$ thin films categorised as "QC present". Running average of total (**a**), highest 10% (**b**), and lowest 10% (**c**) PCE values for devices of each category with a one year time window. Error bars represent one standard deviation.

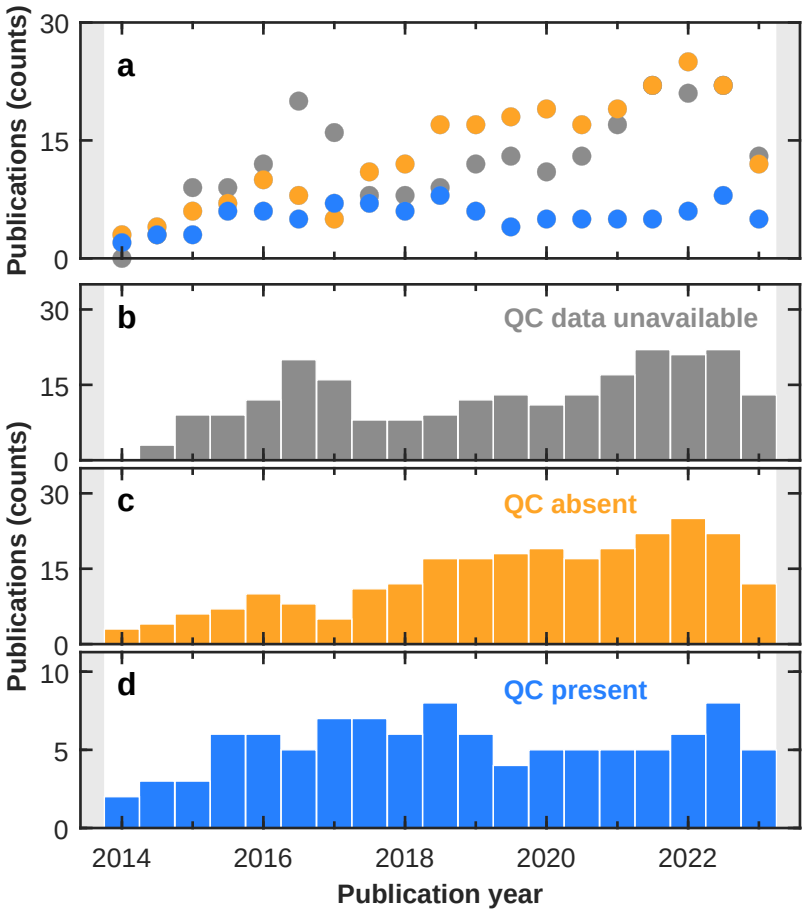


Figure B.15: Meta-study of device performance and absorbance features of $FAPbI_3$ thin films. a. Unique publication counts for each category with a one year time window. Unique publication counts for devices in the "QC data unavailable" (**b**), "QC absent" (**c**), and "QC present" (**d**) categories.

C

Supplementary Analysis of charge-carrier dynamics in quantum confined perovskites 6

Contents

C.1 2-dimensional perovskites 228
C.1.1 Fabrication 228
C.1.2 Absorption measurements 229
C.1.3 Grazing incidence wide-angle X-ray scattering (GIWAXS) . . . 231
C.1.4 Photoluminescence (PL) 234

This appendix provides details of sample preparation and characterisation relevant to Chapter 6.

C.1 2-dimensional perovskites

C.1.1 Fabrication

The film fabrication was performed by Valentina Larini. The "Horizonta" samples were prepared by stoichiometrically dissolving trimethylamine iodide (TMAI), methylammonium iodide (MAI), and lead iodide (PbI_2) powders in N,N-dimethylformamide (DMF) to get a 0.7 M precursor solution. While, in order to fabricate the "vertical" samples, a proper amount of methylammonium chloride (MACl) was included in the formulation, partially replacing MAI. Subsequently, the thin films were prepared by spin-coating the precursor solution at 4000 rpm, adding toluene as an antisolvent, and annealing the resultant thin film at 100°C for 30 minutes.

C.1.2 Absorption measurements

Reflectance (R) and transmittance (T) spectra were measured using a Fourier transform infrared (FTIR) spectrometer (Bruker Vertex 80v), configured with a tungsten halogen lamp illumination source, a CaF_2 beamsplitter and a silicon detector. The absorption coefficient (α) spectrum of each thin-film sample is then obtained using the relationship

$$\alpha = -\frac{1}{d} \cdot \log_{10}\left(\frac{T}{1-R}\right)$$

where d is the film thickness.

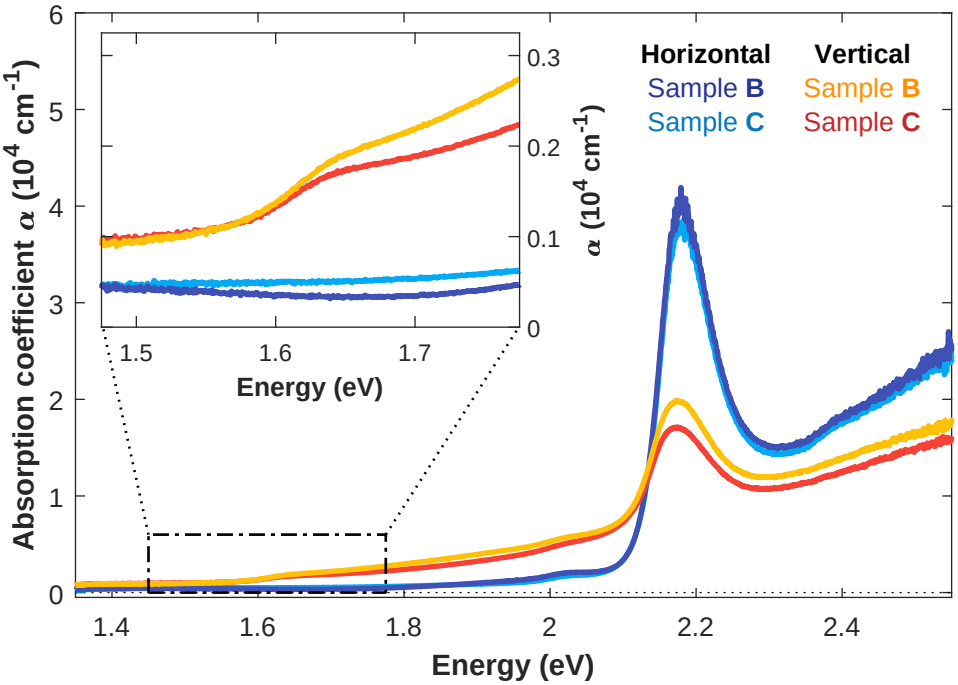


Figure C.1: Absorption spectrum of the 2-dimensional perovskite semiconductors. The inset represents the energetic range corresponding to a 3-dimensional absorption onset for a 3-dimensional MA-rich perovskite film. The samples labelled "B" and "C" were exposed to the amplified laser for different durations and therefore have degraded to different extents.

C.1.3 Grazing incidence wide-angle X-ray scattering (GIWAXS)

The 2-dimensional XRD patterns were measured using a Rigaku Smartlab X-ray diffractometer using the Cu-Kα X-ray source and a HyPix-3000 2D X-ray detector in a Bragg-Brentano reflection geometry.

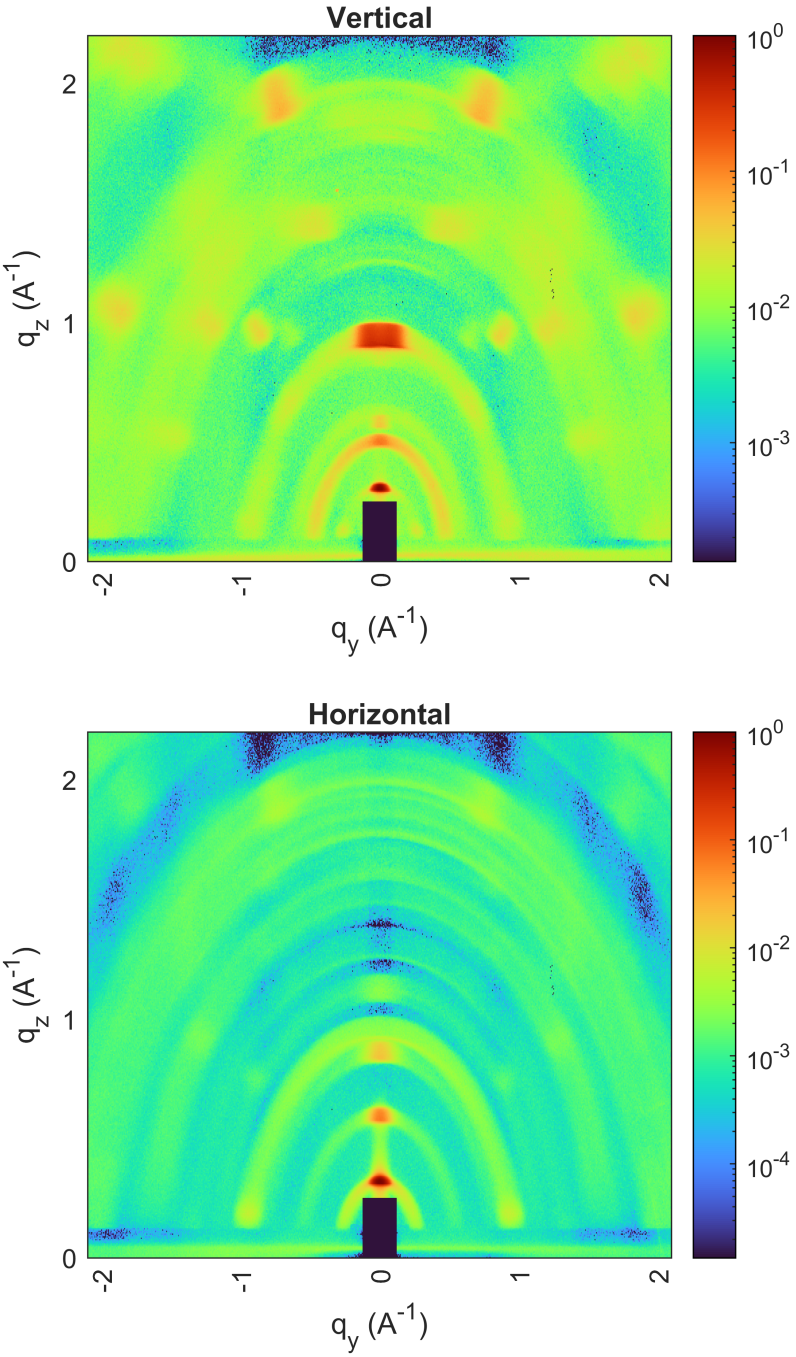


Figure C.2: Logarithmic scaling of the grazing wide-angle X-ray scattering (GIWAXS) patterns of the 2-dimensional perovskite semiconductors.

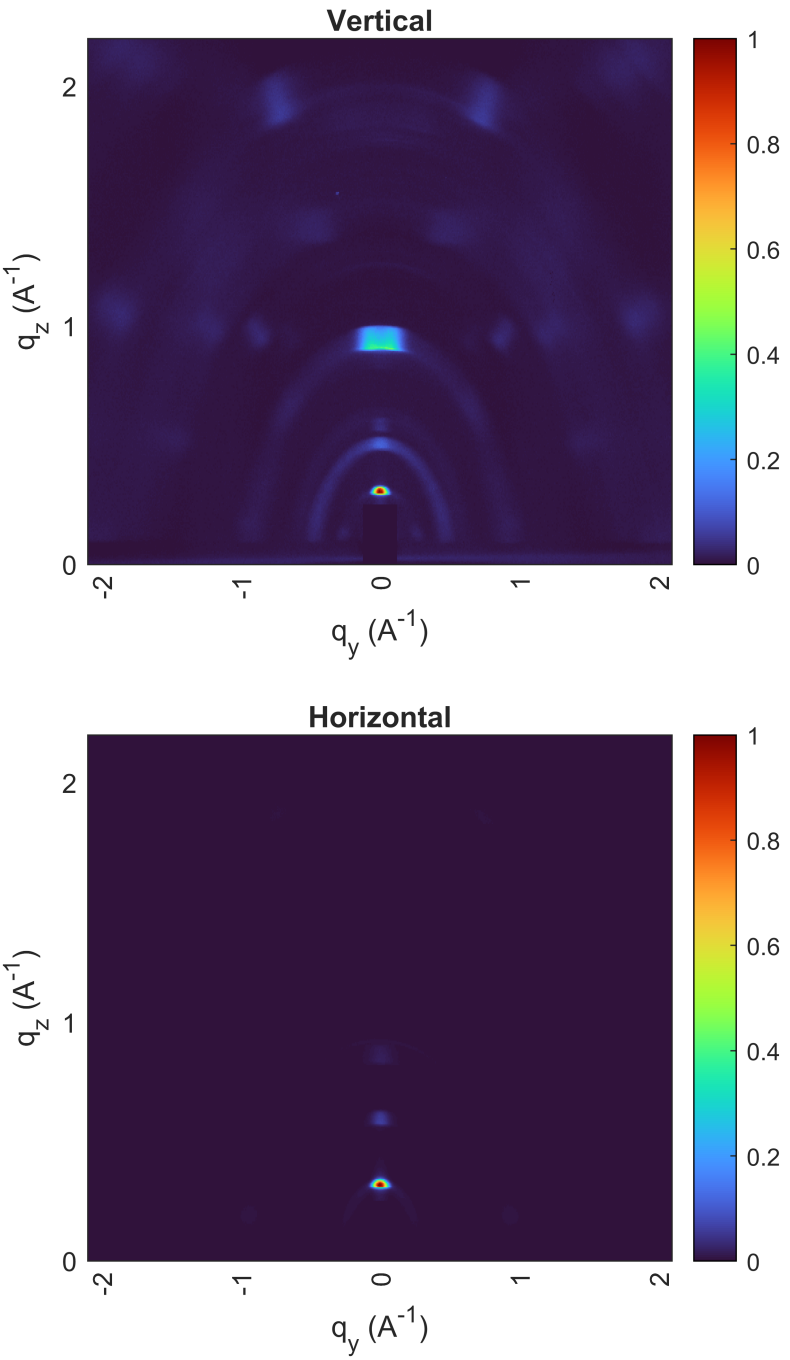


Figure C.3: Linear scaling of the grazing wide-angle X-ray scattering (GIWAXS) patterns of the 2-dimensional perovskite semiconductors.

C.1.4 Photoluminescence (PL)

A 398 nm diode laser (PicoHarp, LDH-D-C-405M) was used to photo-excite the samples, on a continuous wave setting at. The resultant PL was collected and coupled into a grating spectrometer (Princeton Instruments, SP-2558), which directed the spectrally dispersed PL onto a silicon iCCD (intensified charge coupled device, PI-MAX4, Princeton Instruments). The samples were mounted in a vacuum cell under low pressure ($\sim 10^{-2}$ mbar). PL measurements were performed by Jiaxing Du.

References

[1] United Nations, D. o. E. and Social Affairs, P. D. 'World Population Prospects 2022: Summary of Results'. https://www.un.org/development/desa/pd/sites/www.un.org.development.desa.pd/files/undesa_pd_2022_wpp_key-messages.pdf. (accessed 2024-04-19).

[2] IEA, D. o. E. and Social Affairs, P. D. 'World Energy Outlook 2023'. https://www.iea.org/reports/world-energy-outlook-2023. (accessed 2024-04-19).

[3] IPCC. 'AR6 Synthesis Report: Climate Change 2023'. https://www.ipcc.ch/report/ar6/syr/. (accessed 2024-04-19).

[4] Kabir, E.; Kumar, P.; Kumar, S.; Adelodun, A. A. and Kim, K.-H. 'Solar energy: Potential and future prospects'. *Renewable and Sustainable Energy Reviews*, 2018, **82**, 894–900.

[5] Chapin, D. M.; Fuller, C. S.; Pearson, G. L. *et al.* 'A new silicon p-n junction photocell for converting solar radiation into electrical power'. *Journal of applied physics*, 1954, **25**, 676.

[6] Green, M. A.; Dunlop, E. D.; Yoshita, M.; Kopidakis, N.; Bothe, K.; Siefer, G. and Hao, X. 'Solar cell efficiency tables (Version 63)'. *Progress in Photovoltaics: Research and Applications*, 2024, **32**, 3–13.

[7] 'NREL Best Research-Cell Efficiency Chart, 2024'. https://www.nrel.gov/pv/cell-efficiency.html. (accessed 2024-04-19).

[8] Nayak, P. K.; Mahesh, S.; Snaith, H. J. and Cahen, D. 'Photovoltaic solar cell technologies: analysing the state of the art'. *Nature Reviews Materials*, 2019, **4**, 269.

[9] Eperon, G. E.; Stranks, S. D.; Menelaou, C.; Johnston, M. B.; Herz, L. M. and Snaith, H. J. 'Formamidinium lead trihalide: a broadly tunable perovskite for efficient planar heterojunction solar cells'. *Energy & Environmental Science*, 2014, **7**, 982–988.

[10] Eperon, G. E.; Hörantner, M. T. and Snaith, H. J. 'Metal halide perovskite tandem and multiple-junction photovoltaics'. *Nature Reviews Chemistry*, 2017, **1**, 0095.

[11] Song, Z.; Chen, C.; Li, C.; Awni, R. A.; Zhao, D. and Yan, Y. 'Wide-bandgap, low-bandgap, and tandem perovskite solar cells'. *Semiconductor Science and Technology*, 2019, **34**, 093001.

[12] Baikie, T.; Fang, Y.; Kadro, J. M.; Schreyer, M.; Wei, F.; Mhaisalkar, S. G.; Graetzel, M. and White, T. J. 'Synthesis and crystal chemistry of the hybrid perovskite $(CH_3NH_3)PbI_3$ for solid-state sensitised solar cell applications'. *Journal of Materials Chemistry A*, 2013, **1**, 5628–5641.

[13] Simon, S. H. *The Oxford solid state basics*. OUP Oxford, 2013.

[14] Hook, J. R. and Hall, H. E. *Solid state physics*. John Wiley & Sons, 2013.

[15] Peter, Y. and Cardona, M. *Fundamentals of semiconductors: physics and materials properties*. Springer Science & Business Media, 2010.

[16] Herz, L. M. 'Charge-carrier dynamics in organic-inorganic metal halide perovskites'. *Annual review of physical chemistry*, 2016, **67**, 65–89.

[17] Blundell, S. J. and Blundell, K. M. *Concepts in thermal physics*. Oup Oxford, 2010.

[18] Jones, R. A. *Soft condensed matter*. Vol. 6. Oxford University Press, 2002.

[19] Fox, M. *Optical properties of solids*. Vol. 3. Oxford university press, 2010.

[20] Bera, S.; Saha, A.; Mondal, S.; Biswas, A.; Mallick, S.; Chatterjee, R. and Roy, S. 'Review of defect engineering in perovskites for photovoltaic application'. *Materials Advances*, 2022, **3**, 5234–5247.

[21] Goldschmidt, V. M.; Barth, T. F.; Lunde, G. and Zachariasen, W. H. 'Geochemische Verteilungsgesetze der Elemente: 7. Die Gesetze der Krystallochemie'. *Videnskapsselskapet (Kristiania). Matematisk-Naturvidenskapelig Klasse: Skrifter; 1926, 2*. I Kommission Hos Jacob Dybwad, 1926.

[22] Peña, M. A. and Fierro, J. L. 'Chemical structures and performance of perovskite oxides'. *Chemical reviews*, 2001, **101**, 1981–2018.

[23] Knight, A. J. and Herz, L. M. 'Preventing phase segregation in mixed-halide perovskites: a perspective'. *Energy & Environmental Science*, 2020, **13**, 2024–2046.

[24] Motti, S. G.; Kober-Czerny, M.; Righetto, M.; Holzhey, P.; Smith, J.; Kraus, H.; Snaith, H. J.; Johnston, M. B. and Herz, L. M. 'Exciton Formation Dynamics and Band-Like Free Charge-Carrier Transport in 2D Metal Halide Perovskite Semiconductors'. *Advanced Functional Materials*, 2023, **33**, 2300363.

[25] Kober-Czerny, M.; Motti, S. G.; Holzhey, P.; Wenger, B.; Lim, J.; Herz, L. M. and Snaith, H. J. 'Excellent Long-Range Charge-Carrier Mobility in 2D Perovskites'. *Advanced Functional Materials*, 2022, **32**, 2203064.

[26] Li, W.; Sidhik, S.; Traore, B.; Asadpour, R.; Hou, J.; Zhang, H.; Fehr, A.; Essman, J.; Wang, Y.; Hoffman, J. M. *et al.* 'Light-activated interlayer contraction in two-dimensional perovskites for high-efficiency solar cells'. *Nature nanotechnology*, 2022, **17**, 45–52.

[27] Motti, S. G.; Crothers, T.; Yang, R.; Cao, Y.; Li, R.; Johnston, M. B.; Wang, J. and Herz, L. M. 'Heterogeneous photon recycling and charge diffusion enhance charge transport in quasi-2D lead-halide perovskite films'. *Nano letters*, 2019, **19**, 3953–3960.

[28] Guo, Z.; Wang, J. and Yin, W.-J. 'Atomistic origin of lattice softness and its impact on structural and carrier dynamics in three dimensional perovskites'. *Energy & Environmental Science*, 2022, **15**, 660–671.

[29] Lee, J.-W.; Kim, D.-H.; Kim, H.-S.; Seo, S.-W.; Cho, S. M. and Park, N.-G. 'Formamidinium and cesium hybridization for photo-and moisture-stable perovskite solar cell'. *Advanced Energy Materials*, 2015, **5**, 1501310.

[30] Masi, S.; Gualdrón-Reyes, A. F. and Mora-Sero, I. 'Stabilization of Black Perovskite Phase in $FAPbI_3$ and $CsPbI_3$'. *ACS Energy Letters*, 2020, **5**, 1974–1985.

[31] Ghosh, D.; Smith, A. R.; Walker, A. B. and Islam, M. S. 'Mixed A-cation perovskites for solar cells: atomic-scale insights into structural distortion, hydrogen bonding, and electronic properties'. *Chemistry of Materials*, 2018, **30**, 5194–5204.

[32] Galle, M. H.; Li, J.; Frantsuzov, P. A.; Basché, T. and Scheblykin, I. G. 'Self-Healing Ability of Perovskites Observed via Photoluminescence Response on Nanoscale Local Forces and Mechanical Damage'. *Advanced Science*, 2023, **10**, 2204393.

[33] Chen, T.; Foley, B. J.; Park, C.; Brown, C. M.; Harriger, L. W.; Lee, J.; Ruff, J.; Yoon, M.; Choi, J. J. and Lee, S.-H. 'Entropy-driven structural transition and kinetic trapping in formamidinium lead iodide perovskite'. *Science advances*, 2016, **2**, e1601650.

[34] Du, T.; Macdonald, T. J.; Yang, R. X.; Li, M.; Jiang, Z.; Mohan, L.; Xu, W.; Su, Z.; Gao, X.; Whiteley, R. *et al.* 'Additive-Free, Low-Temperature Crystallization of Stable α-$FAPbI_3$ Perovskite'. *Advanced Materials*, 2022, **34**, 2107850.

[35] McMeekin, D. P.; Wang, Z.; Rehman, W.; Pulvirenti, F.; Patel, J. B.; Noel, N. K.; Johnston, M. B.; Marder, S. R.; Herz, L. M. and Snaith, H. J. 'Crystallization Kinetics and Morphology Control of Formamidinium–Cesium Mixed-Cation Lead Mixed-Halide Perovskite via Tunability of the Colloidal Precursor Solution'. *Advanced Materials*, 2017, **29**, 1607039.

[36] Chen, Y.; Lei, Y.; Li, Y.; Yu, Y.; Cai, J.; Chiu, M.-H.; Rao, R.; Gu, Y.; Wang, C.; Choi, W. *et al.* 'Strain engineering and epitaxial stabilization of halide perovskites'. *Nature*, 2020, **577**, 209–215.

[37] Nelson, J. A. *The physics of solar cells*. World Scientific Publishing Company, 2003.

[38] Protesescu, L.; Yakunin, S.; Bodnarchuk, M. I.; Krieg, F.; Caputo, R.; Hendon, C. H.; Yang, R. X.; Walsh, A. and Kovalenko, M. V. 'Nanocrystals of cesium lead halide perovskites ($CsPbX_3$, X = Cl, Br, and I): novel optoelectronic materials showing bright emission with wide color gamut'. *Nano letters*, 2015, **15**, 3692–3696.

[39] 'n-dimensional Volume of a Euclidean Ball'. https://dlmf.nist.gov/5.19#E4. (accessed 2024-04-19).

[40] Wright, A. D.; Volonakis, G.; Borchert, J.; Davies, C. L.; Giustino, F.; Johnston, M. B. and Herz, L. M. 'Intrinsic quantum confinement in formamidinium lead triiodide perovskite'. *Nature Materials*, 2020, **19**, 1201–1206.

[41] Elmestekawy, K. A.; Wright, A. D.; Lohmann, K. B.; Borchert, J.; Johnston, M. B. and Herz, L. M. 'Controlling Intrinsic Quantum Confinement in Formamidinium Lead Triiodide Perovskite through Cs Substitution'. *ACS nano*, 2022, **16**, 9640–9650.

[42] Elmestekawy, K. A.; Gallant, B. M.; Wright, A. D.; Holzhey, P.; Noel, N. K.; Johnston, M. B.; Snaith, H. J. and Herz, L. M. 'Photovoltaic Performance of $FAPbI_3$ Perovskite Is Hampered by Intrinsic Quantum Confinement'. *ACS Energy Letters*, 2023, **8**, 2543–2551.

[43] Bockelmann, U and Bastard, G. 'Phonon scattering and energy relaxation in two-, one-, and zero-dimensional electron gases'. *Physical Review B*, 1990, **42**, 8947.

[44] Alivisatos, A.; Harris, T.; Carroll, P.; Steigerwald, M. and Brus, L. 'Electron–vibration coupling in semiconductor clusters studied by resonance Raman spectroscopy'. *The Journal of Chemical Physics*, 1989, **90**, 3463–3468.

[45] Hooker, S. and Webb, C. *Laser physics*. Vol. 9. Oxford University Press, 2010.

[46] Stoumpos, C. C.; Cao, D. H.; Clark, D. J.; Young, J.; Rondinelli, J. M.; Jang, J. I.; Hupp, J. T. and Kanatzidis, M. G. 'Ruddlesden–Popper hybrid lead iodide perovskite 2D homologous semiconductors'. *Chemistry of Materials*, 2016, **28**, 2852–2867.

[47] Smith, I. C.; Hoke, E. T.; Solis-Ibarra, D.; McGehee, M. D. and Karunadasa, H. I. 'A layered hybrid perovskite solar-cell absorber with enhanced moisture stability'. *Angewandte Chemie*, 2014, **126**, 11414–11417.

[48] Wang, Z.; Lin, Q.; Chmiel, F. P.; Sakai, N.; Herz, L. M. and Snaith, H. J. 'Efficient ambient-air-stable solar cells with 2D–3D heterostructured butylammonium-caesium-formamidinium lead halide perovskites'. *Nature Energy*, 2017, **2**, 17135.

[49] Milot, R. L.; Sutton, R. J.; Eperon, G. E.; Haghighirad, A. A.; Martinez Hardigree, J.; Miranda, L.; Snaith, H. J.; Johnston, M. B. and Herz, L. M. 'Charge-carrier dynamics in 2D hybrid metal–halide perovskites'. *Nano letters*, 2016, **16**, 7001–7007.

[50] 'Introduction to FTIR spectroscopy'. https://www.newport.com/n/introduction-to-ftir-spectroscopy. (accessed 2024-04-19).

[51] Soroush, M. and Lau, K. K. *Dye-Sensitized Solar Cells: Mathematical Modelling, and Materials Design and Optimization*. Academic Press, 2019.

[52] Elliott, R. 'Intensity of optical absorption by excitons'. *Physical Review*, 1957, **108**, 1384.

[53] Zanatta, A. 'Revisiting the optical bandgap of semiconductors and the proposal of a unified methodology to its determination'. *Scientific reports*, 2019, **9**, 1–12.

[54] Davies, C. L.; Filip, M. R.; Patel, J. B.; Crothers, T. W.; Verdi, C.; Wright, A. D.; Milot, R. L.; Giustino, F.; Johnston, M. B. and Herz, L. M. 'Bimolecular recombination in methylammonium lead triiodide perovskite is an inverse absorption process'. *Nature Communications*, 2018, **9**, 1–9.

[55] 'Introduction to Gated Intensified Cameras (iCCD Cameras)'. https://andor.oxinst.com/learning/view/article/intensified-ccd-cameras. (accessed 2024-04-19).

[56] Ulatowski, A. M.; Wright, A. D.; Wenger, B.; Buizza, L. R.; Motti, S. G.; Eggimann, H. J.; Savill, K. J.; Borchert, J.; Snaith, H. J.; Johnston, M. B. *et al.* 'Charge-carrier trapping dynamics in bismuth-doped thin films of $MAPbBr_3$ perovskite'. *The Journal of Physical Chemistry Letters*, 2020, **11**, 3681–3688.

[57] Stranks, S. D.; Eperon, G. E.; Grancini, G.; Menelaou, C.; Alcocer, M. J.; Leijtens, T.; Herz, L. M.; Petrozza, A. and Snaith, H. J. 'Electron-hole diffusion lengths exceeding 1 micrometer in an organometal trihalide perovskite absorber'. *Science*, 2013, **342**, 341–344.

[58] Longo, G.; Mahesh, S.; Buizza, L. R.; Wright, A. D.; Ramadan, A. J.; Abdi-Jalebi, M.; Nayak, P. K.; Herz, L. M. and Snaith, H. J. 'Understanding the performance-limiting factors of $Cs_2AgBiBr_6$ double-perovskite solar cells'. *ACS energy letters*, 2020, **5**, 2200–2207.

[59] Savill, K. J.; Ulatowski, A. M.; Farrar, M. D.; Johnston, M. B.; Snaith, H. J. and Herz, L. M. 'Impact of tin fluoride additive on the properties of mixed tin-lead iodide perovskite semiconductors'. *Advanced Functional Materials*, 2020, **30**, 2005594.

[60] Yamada, Y.; Nakamura, T.; Endo, M.; Wakamiya, A. and Kanemitsu, Y. 'Photocarrier recombination dynamics in perovskite $CH_3NH_3PbI_3$ for solar cell applications'. *Journal of the American Chemical Society*, 2014, **136**, 11610–11613.

[61] Yamada, Y.; Endo, M.; Wakamiya, A. and Kanemitsu, Y. 'Spontaneous defect annihilation in $CH_3NH_3PbI_3$ thin films at room temperature revealed by time-resolved photoluminescence spectroscopy'. *The journal of physical chemistry letters*, 2015, **6**, 482–486.

[62] O'Connor, D. *Time-correlated single photon counting*. Academic press, 2012.

[63] Joyce, H. J.; Boland, J. L.; Davies, C. L.; Baig, S. A. and Johnston, M. B. 'A review of the electrical properties of semiconductor nanowires: insights gained from terahertz conductivity spectroscopy'. *Semiconductor Science and Technology*, 2016, **31**, 103003.

[64] Spies, J. A.; Neu, J.; Tayvah, U. T.; Capobianco, M. D.; Pattengale, B.; Ostresh, S. and Schmuttenmaer, C. A. 'Terahertz spectroscopy of emerging materials'. *The Journal of Physical Chemistry C*, 2020, **124**, 22335–22346.

[65] Nahata, A.; Weling, A. S. and Heinz, T. F. 'A wideband coherent terahertz spectroscopy system using optical rectification and electro-optic sampling'. *Applied physics letters*, 1996, **69**, 2321–2323.

[66] Ulatowski, A. M.; Herz, L. M. and Johnston, M. B. 'Terahertz conductivity analysis for highly doped thin-film semiconductors'. *Journal of Infrared, Millimeter, and Terahertz Waves*, 2020, **41**, 1431–1449.

[67] Cullity, B. D. *Elements of X-ray Diffraction*. Addison-Wesley Publishing, 1956.

[68] Lohmann, K. B.; Patel, J. B.; Rothmann, M. U.; Xia, C. Q.; Oliver, R. D.; Herz, L. M.; Snaith, H. J. and Johnston, M. B. 'Control over crystal size in vapor deposited metal-halide perovskite films'. *ACS energy letters*, 2020, **5**, 710–717.

[69] Kojima, A.; Teshima, K.; Shirai, Y. and Miyasaka, T. 'Organometal halide perovskites as visible-light sensitizers for photovoltaic cells'. *Journal of the American Chemical Society*, 2009, **131**, 6050–6051.

[70] Zhou, J.; Tan, L.; Liu, Y.; Li, H.; Liu, X.; Li, M.; Wang, S.; Zhang, Y.; Jiang, C.; Hua, R. *et al.* 'Highly efficient and stable perovskite solar cells via a multifunctional hole transporting material'. *Joule*, 2024.

[71] Rehman, W.; McMeekin, D. P.; Patel, J. B.; Milot, R. L.; Johnston, M. B.; Snaith, H. J. and Herz, L. M. 'Photovoltaic mixed-cation lead mixed-halide perovskites: links between crystallinity, photo-stability and electronic properties'. *Energy & Environmental Science*, 2017, **10**, 361–369.

[72] Wehrenfennig, C.; Eperon, G. E.; Johnston, M. B.; Snaith, H. J. and Herz, L. M. 'High charge carrier mobilities and lifetimes in organolead trihalide perovskites'. *Advanced Materials*, 2014, **26**, 1584–1589.

[73] Green, M. A.; Ho-Baillie, A. and Snaith, H. J. 'The emergence of perovskite solar cells'. *Nature photonics*, 2014, **8**, 506–514.

[74] Stoumpos, C. C. and Kanatzidis, M. G. 'Halide Perovskites: poor Man's high-performance semiconductors'. *Advanced Materials*, 2016, **28**, 5778–5793.

[75] Yuan, M.; Quan, L. N.; Comin, R.; Walters, G.; Sabatini, R.; Voznyy, O.; Hoogland, S.; Zhao, Y.; Beauregard, E. M.; Kanjanaboos, P. *et al.* 'Perovskite energy funnels for efficient light-emitting diodes'. *Nature nanotechnology*, 2016, **11**, 872–877.

[76] Sadhanala, A.; Ahmad, S.; Zhao, B.; Giesbrecht, N.; Pearce, P. M.; Deschler, F.; Hoye, R. L.; Gödel, K. C.; Bein, T.; Docampo, P. *et al.* 'Blue-green color tunable solution processable organolead chloride–bromide mixed halide perovskites for optoelectronic applications'. *Nano letters*, 2015, **15**, 6095–6101.

[77] Wang, N.; Cheng, L.; Ge, R.; Zhang, S.; Miao, Y.; Zou, W.; Yi, C.; Sun, Y.; Cao, Y.; Yang, R. *et al.* 'Perovskite light-emitting diodes based on solution-processed self-organized multiple quantum wells'. *Nature Photonics*, 2016, **10**, 699–704.

[78] Chin, X. Y.; Perumal, A.; Bruno, A.; Yantara, N.; Veldhuis, S. A.; Martínez-Sarti, L.; Chandran, B.; Chirvony, V.; Lo, A. S.-Z.; So, J. *et al.* 'Self-assembled hierarchical nanostructured perovskites enable highly efficient LEDs via an energy cascade'. *Energy & Environmental Science*, 2018, **11**, 1770–1778.

[79] Kim, Y.-H.; Cho, H.; Heo, J. H.; Kim, T.-S.; Myoung, N.; Lee, C.-L.; Im, S. H. and Lee, T.-W. 'Multicolored organic/inorganic hybrid perovskite light-emitting diodes'. *Advanced Materials*, 2015, **27**, 1248–1254.

[80] Xing, G.; Mathews, N.; Lim, S. S.; Yantara, N.; Liu, X.; Sabba, D.; Grätzel, M.; Mhaisalkar, S. and Sum, T. C. 'Low-temperature solution-processed wavelength-tunable perovskites for lasing'. *Nature materials*, 2014, **13**, 476–480.

[81] Yakunin, S.; Protesescu, L.; Krieg, F.; Bodnarchuk, M. I.; Nedelcu, G.; Humer, M.; De Luca, G.; Fiebig, M.; Heiss, W. and Kovalenko, M. V. 'Low-threshold amplified spontaneous emission and lasing from colloidal nanocrystals of caesium lead halide perovskites'. *Nature Communications*, 2015, **6**, 1–9.

[82] Zhang, Q.; Ha, S. T.; Liu, X.; Sum, T. C. and Xiong, Q. 'Room-temperature near-infrared high-Q perovskite whispering-gallery planar nanolasers'. *Nano letters*, 2014, **14**, 5995–6001.

[83] Righetto, M.; Giovanni, D.; Lim, S. S. and Sum, T. C. 'The photophysics of Ruddlesden-Popper perovskites: A tale of energy, charges, and spins'. *Applied Physics Reviews*, 2021, **8**, 011318.

[84] Buizza, L. R.; Crothers, T. W.; Wang, Z.; Patel, J. B.; Milot, R. L.; Snaith, H. J.; Johnston, M. B. and Herz, L. M. 'Charge-Carrier Dynamics, Mobilities, and Diffusion Lengths of 2d–3d Hybrid Butylammonium–Cesium–Formamidinium Lead Halide Perovskites'. *Advanced Functional Materials*, 2019, **29**, 1902656.

[85] Motti, S. G.; Krieg, F.; Ramadan, A. J.; Patel, J. B.; Snaith, H. J.; Kovalenko, M. V.; Johnston, M. B. and Herz, L. M. '$CsPbBr_3$ Nanocrystal Films: Deviations from Bulk Vibrational and Optoelectronic Properties'. *Advanced Functional Materials*, 2020, **30**, 1909904.

[86] Gramlich, M.; Lampe, C.; Drewniok, J. and Urban, A. S. 'How Exciton–Phonon Coupling Impacts Photoluminescence in Halide Perovskite Nanoplatelets'. *The Journal of Physical Chemistry Letters*, 2021, **12**, 11371–11377.

[87] Giovanni, D.; Righetto, M.; Zhang, Q.; Lim, J. W. M.; Ramesh, S. and Sum, T. C. 'Origins of the long-range exciton diffusion in perovskite nanocrystal films: photon recycling vs exciton hopping'. *Light: Science & Applications*, 2021, **10**, 1–9.

[88] Polavarapu, L.; Nickel, B.; Feldmann, J. and Urban, A. S. 'Advances in Quantum-Confined Perovskite Nanocrystals for Optoelectronics'. *Advanced Energy Materials*, 2017, **7**, 1700267.

[89] Fu, Y.; Zhu, H.; Chen, J.; Hautzinger, M. P.; Zhu, X.-Y. and Jin, S. 'Metal halide perovskite nanostructures for optoelectronic applications and the study of physical properties'. *Nature Reviews Materials*, 2019, **4**, 169–188.

[90] Lv, S.; Pang, S.; Zhou, Y.; Padture, N. P.; Hu, H.; Wang, L.; Zhou, X.; Zhu, H.; Zhang, L.; Huang, C. *et al.* 'One-step, solution-processed formamidinium lead trihalide ($FAPbI_{(3-x)}Cl_x$) for mesoscopic perovskite–polymer solar cells'. *Physical Chemistry Chemical Physics*, 2014, **16**, 19206–19211.

[91] Pang, S.; Hu, H.; Zhang, J.; Lv, S.; Yu, Y.; Wei, F.; Qin, T.; Xu, H.; Liu, Z. and Cui, G. '$NH_2CH{=}NH_2PbI_3$: an alternative organolead iodide perovskite sensitizer for mesoscopic solar cells'. *Chemistry of Materials*, 2014, **26**, 1485–1491.

[92] Shockley, W. and Queisser, H. J. 'Detailed balance limit of efficiency of p-n junction solar cells'. *Journal of applied physics*, 1961, **32**, 510–519.

[93] Kim, M.; Jeong, J.; Lu, H.; Lee, T. K.; Eickemeyer, F. T.; Liu, Y.; Choi, I. W.; Choi, S. J.; Jo, Y.; Kim, H.-B. *et al.* 'Conformal quantum dot-SnO_2 layers as electron transporters for efficient perovskite solar cells'. *Science*, 2022, **375**, 302–306.

[94] Jeong, J.; Kim, M.; Seo, J.; Lu, H.; Ahlawat, P.; Mishra, A.; Yang, Y.; Hope, M. A.; Eickemeyer, F. T.; Kim, M. *et al.* 'Pseudo-halide anion engineering for α-$FAPbI_3$ perovskite solar cells'. *Nature*, 2021, **592**, 381–385.

[95] Utzat, H.; Sun, W.; Kaplan, A. E.; Krieg, F.; Ginterseder, M.; Spokoyny, B.; Klein, N. D.; Shulenberger, K. E.; Perkinson, C. F.; Kovalenko, M. V. *et al.* 'Coherent single-photon emission from colloidal lead halide perovskite quantum dots'. *Science*, 2019, **363**, 1068–1072.

[96] Rainò, G.; Becker, M. A.; Bodnarchuk, M. I.; Mahrt, R. F.; Kovalenko, M. V. and Stöferle, T. 'Superfluorescence from lead halide perovskite quantum dot superlattices'. *Nature*, 2018, **563**, 671–675.

[97] McKenna, K. P. 'Electronic properties of {111} twin boundaries in a mixed-ion lead halide perovskite solar absorber'. *ACS Energy Letters*, 2018, **3**, 2663–2668.

[98] Stoumpos, C. C.; Malliakas, C. D. and Kanatzidis, M. G. 'Semiconducting tin and lead iodide perovskites with organic cations: phase transitions, high mobilities, and near-infrared photoluminescent properties'. *Inorganic Chemistry*, 2013, **52**, 9019–9038.

[99] Kim, G.; Min, H.; Lee, K. S.; Yoon, S. M.; Seok, S. I. *et al.* 'Impact of strain relaxation on performance of α-formamidinium lead iodide perovskite solar cells'. *Science*, 2020, **370**, 108–112.

[100] Syzgantseva, O. A.; Saliba, M.; Grätzel, M. and Rothlisberger, U. 'Stabilization of the perovskite phase of formamidinium lead triiodide by methylammonium, Cs, and/or Rb doping'. *The journal of physical chemistry letters*, 2017, **8**, 1191–1196.

[101] McMeekin, D. P.; Sadoughi, G.; Rehman, W.; Eperon, G. E.; Saliba, M.; Hörantner, M. T.; Haghighirad, A.; Sakai, N.; Korte, L.; Rech, B. *et al.* 'A mixed-cation lead mixed-halide perovskite absorber for tandem solar cells'. *Science*, 2016, **351**, 151–155.

[102] Andaji-Garmaroudi, Z.; Abdi-Jalebi, M.; Guo, D.; Macpherson, S.; Sadhanala, A.; Tennyson, E. M.; Ruggeri, E.; Anaya, M.; Galkowski, K.; Shivanna, R. *et al.* 'A Highly Emissive Surface Layer in Mixed-Halide Multication Perovskites'. *Advanced Materials*, 2019, **31**, 1902374.

[103] Eperon, G. E.; Beck, C. E. and Snaith, H. J. 'Cation exchange for thin film lead iodide perovskite interconversion'. *Materials Horizons*, 2016, **3**, 63–71.

[104] Saliba, M.; Matsui, T.; Seo, J.-Y.; Domanski, K.; Correa-Baena, J.-P.; Nazeeruddin, M. K.; Zakeeruddin, S. M.; Tress, W.; Abate, A.; Hagfeldt, A. *et al.* 'Cesium-containing triple cation perovskite solar cells: improved stability, reproducibility and high efficiency'. *Energy & Environmental science*, 2016, **9**, 1989–1997.

[105] Yi, C.; Luo, J.; Meloni, S.; Boziki, A.; Ashari-Astani, N.; Grätzel, C.; Zakeeruddin, S. M.; Röthlisberger, U. and Grätzel, M. 'Entropic stabilization of mixed A-cation ABX 3 metal halide perovskites for high performance perovskite solar cells'. *Energy & Environmental Science*, 2016, **9**, 656–662.

[106] Li, Z.; Yang, M.; Park, J.-S.; Wei, S.-H.; Berry, J. J. and Zhu, K. 'Stabilizing perovskite structures by tuning tolerance factor: formation of formamidinium and cesium lead iodide solid-state alloys'. *Chemistry of Materials*, 2016, **28**, 284–292.

[107] Wozny, S.; Yang, M.; Nardes, A. M.; Mercado, C. C.; Ferrere, S.; Reese, M. O.; Zhou, W. and Zhu, K. 'Controlled humidity study on the formation of higher efficiency formamidinium lead triiodide-based solar cells'. *Chemistry of Materials*, 2015, **27**, 4814–4820.

[108] Pool, V. L.; Dou, B.; Van Campen, D. G.; Klein-Stockert, T. R.; Barnes, F. S.; Shaheen, S. E.; Ahmad, M. I.; Van Hest, M. F. and Toney, M. F. 'Thermal engineering of $FAPbI_3$ perovskite material via radiative thermal annealing and in situ XRD'. *Nature communications*, 2017, **8**, 1–8.

[109] Long, M.; Zhang, T.; Xu, W.; Zeng, X.; Xie, F.; Li, Q.; Chen, Z.; Zhou, F.; Wong, K. S.; Yan, K. *et al.* 'Large-grain formamidinium $PbI_{3-x}Br_x$ for high-performance perovskite solar cells via intermediate halide exchange'. *Advanced Energy Materials*, 2017, **7**, 1601882.

[110] Borchert, J.; Milot, R. L.; Patel, J. B.; Davies, C. L.; Wright, A. D.; Martinez Maestro, L.; Snaith, H. J.; Herz, L. M. and Johnston, M. B. 'Large-area, highly uniform evaporated formamidinium lead triiodide thin films for solar cells'. *ACS Energy Letters*, 2017, **2**, 2799–2804.

[111] Davies, C. L.; Borchert, J.; Xia, C. Q.; Milot, R. L.; Kraus, H.; Johnston, M. B. and Herz, L. M. 'Impact of the organic cation on the optoelectronic properties of formamidinium lead triiodide'. *The journal of physical chemistry letters*, 2018, **9**, 4502–4511.

[112] Rothmann, M. U.; Kim, J. S.; Borchert, J.; Lohmann, K. B.; O'Leary, C. M.; Sheader, A. A.; Clark, L.; Snaith, H. J.; Johnston, M. B.; Nellist, P. D. *et al.* 'Atomic-scale microstructure of metal halide perovskite'. *Science*, 2020, **370**, eabb5940.

[113] Jiang, Y.; Leyden, M. R.; Qiu, L.; Wang, S.; Ono, L. K.; Wu, Z.; Juarez-Perez, E. J. and Qi, Y. 'Combination of Hybrid CVD and Cation Exchange for Upscaling Cs-Substituted Mixed Cation Perovskite Solar Cells with High Efficiency and Stability'. *Advanced Functional Materials*, 2018, **28**, 1703835.

[114] Trots, D. and Myagkota, S. 'High-temperature structural evolution of caesium and rubidium triiodoplumbates'. *Journal of Physics and Chemistry of Solids*, 2008, **69**, 2520–2526.

[115] Filip, M. R.; Eperon, G. E.; Snaith, H. J. and Giustino, F. 'Steric engineering of metal-halide perovskites with tunable optical band gaps'. *Nature Communications*, 2014, **5**, 1–9.

[116] Sutton, R. J.; Filip, M. R.; Haghighirad, A. A.; Sakai, N.; Wenger, B.; Giustino, F. and Snaith, H. J. 'Cubic or orthorhombic? Revealing the crystal structure of metastable black-phase $CsPbI_3$ by theory and experiment'. *ACS Energy Letters*, 2018, **3**, 1787–1794.

[117] Prasanna, R.; Gold-Parker, A.; Leijtens, T.; Conings, B.; Babayigit, A.; Boyen, H.-G.; Toney, M. F. and McGehee, M. D. 'Band gap tuning via lattice contraction and octahedral tilting in perovskite materials for photovoltaics'. *Journal of the American Chemical Society*, 2017, **139**, 11117–11124.

[118] Rehman, W.; Milot, R. L.; Eperon, G. E.; Wehrenfennig, C.; Boland, J. L.; Snaith, H. J.; Johnston, M. B. and Herz, L. M. 'Charge-carrier dynamics and mobilities in formamidinium lead mixed-halide perovskites'. *Advanced Materials*, 2015, **27**, 7938–7944.

[119] Parrott, E. S.; Green, T.; Milot, R. L.; Johnston, M. B.; Snaith, H. J. and Herz, L. M. 'Interplay of structural and optoelectronic properties in formamidinium mixed tin–lead triiodide perovskites'. *Advanced Functional Materials*, 2018, **28**, 1802803.

[120] Kim, H.-S. and Park, N.-G. 'Soft Lattice and Phase Stability of α-$FAPbI_3$'. *Advanced Energy Materials*, 2400089.

[121] Wright, A. D.; Verdi, C.; Milot, R. L.; Eperon, G. E.; Pérez-Osorio, M. A.; Snaith, H. J.; Giustino, F.; Johnston, M. B. and Herz, L. M. 'Electron–phonon coupling in hybrid lead halide perovskites'. *Nature Communications*, 2016, **7**, 1–9.

[122] Galkowski, K.; Mitioglu, A.; Miyata, A.; Plochocka, P.; Portugall, O.; Eperon, G. E.; Wang, J. T.-W.; Stergiopoulos, T.; Stranks, S. D.; Snaith, H. J. *et al.* 'Determination of the exciton binding energy and effective masses for methylammonium and formamidinium lead tri-halide perovskite semiconductors'. *Energy & Environmental Science*, 2016, **9**, 962–970.

[123] Yang, Z.; Surrente, A.; Galkowski, K; Miyata, A.; Portugall, O; Sutton, R.; Haghighirad, A.; Snaith, H.; Maude, D.; Plochocka, P *et al.* 'Impact of the halide cage on the electronic properties of fully inorganic cesium lead halide perovskites'. *ACS Energy Letters*, 2017, **2**, 1621–1627.

[124] Prathapani, S.; Bhargava, P. and Mallick, S. 'Electronic band structure and carrier concentration of formamidinium–cesium mixed cation lead mixed halide hybrid perovskites'. *Applied Physics Letters*, 2018, **112**, 092104.

[125] Ashari-Astani, N.; Meloni, S.; Salavati, A. H.; Palermo, G.; Grätzel, M. and Rothlisberger, U. 'Computational characterization of the dependence of halide perovskite effective masses on chemical composition and structure'. *The Journal of Physical Chemistry C*, 2017, **121**, 23886–23895.

[126] Zhao, J.; Deng, Y.; Wei, H.; Zheng, X.; Yu, Z.; Shao, Y.; Shield, J. E. and Huang, J. 'Strained hybrid perovskite thin films and their impact on the intrinsic stability of perovskite solar cells'. *Science advances*, 2017, **3**, eaao5616.

[127] Freestone, B. G.; Smith, J. A.; Piana, G.; Kilbride, R. C.; Parnell, A. J.; Sortino, L.; Coles, D. M.; Ball, O. B.; Martsinovich, N.; Thompson, C. J. *et al.* 'Low-dimensional emissive states in non-stoichiometric methylammonium lead halide perovskites'. *Journal of Materials Chemistry A*, 2019, **7**, 11104–11116.

[128] Kirchartz, T.; Markvart, T.; Rau, U. and Egger, D. A. 'Impact of small phonon energies on the charge-carrier lifetimes in metal-halide perovskites'. *The Journal of Physical Chemistry Letters*, 2018, **9**, 939–946.

[129] Trimpl, M. J.; Wright, A. D.; Schutt, K.; Buizza, L. R.; Wang, Z.; Johnston, M. B.; Snaith, H. J.; Müller-Buschbaum, P. and Herz, L. M. 'Charge-carrier trapping and radiative recombination in metal halide perovskite semiconductors'. *Advanced Functional Materials*, 2020, **30**, 2004312.

[130] Herz, L.; Phillips, R.; Le Ru, E. and Murray, R. 'Time-Resolved Photoluminescence Cross-Correlation Measurements on InAs Quantum Dots'. *physica status solidi (a)*, 2002, **190**, 565–569.

[131] Heinrichsdorff, F; Grundmann, M; Stier, O; Krost, A and Bimberg, D. 'Influence of In/Ga intermixing on the optical properties of InGaAs/GaAs quantum dots'. *Journal of crystal growth*, 1998, **195**, 540–545.

[132] Brunner, K; Bockelmann, U; Abstreiter, G; Walther, M; Böhm, G; Tränkle, G and Weimann, G. 'Photoluminescence from a single GaAs/AlGaAs quantum dot'. *Physical review letters*, 1992, **69**, 3216.

[133] Goni, A.; Born, H; Heitz, R; Hoffmann, A; Thomsen, C; Heinrichsdorff, F and Bimberg, D. 'Magnetoluminescence study of annealing effects on the electronic structure of self-organized InGaAs/GaAs quantum dots'. *Japanese Journal of Applied Physics*, 2000, **39**, 3907.

[134] Sosnowski, T.; Norris, T.; Jiang, H; Singh, J; Kamath, K and Bhattacharya, P. 'Rapid carrier relaxation in $In_{0.4}Ga_{0.6}As$/GaAs quantum dots characterized by differential transmission spectroscopy'. *Physical Review B*, 1998, **57**, R9423.

[135] Urayama, J.; Norris, T. B.; Singh, J. and Bhattacharya, P. 'Observation of phonon bottleneck in quantum dot electronic relaxation'. *Physical review letters*, 2001, **86**, 4930.

[136] Reed, M.; Bate, R.; Bradshaw, K; Duncan, W.; Frensley, W.; Lee, J. and Shih, H. 'Spatial quantization in GaAs–AlGaAs multiple quantum dots'. *Journal of Vacuum Science & Technology B: Microelectronics Processing and Phenomena*, 1986, **4**, 358–360.

[137] Jia, X.; Jiang, J.; Zhang, Y.; Qiu, J.; Wang, S.; Chen, Z.; Yuan, N. and Ding, J. 'Observation of enhanced hot phonon bottleneck effect in 2D perovskites'. *Applied Physics Letters*, 2018, **112**, 143903.

[138] Dyksik, M.; Wang, S.; Paritmongkol, W.; Maude, D. K.; Tisdale, W. A.; Baranowski, M. and Plochocka, P. 'Tuning the Excitonic Properties of the 2D $(PEA)_2(MA)_{n-1}Pb_nI_{3n+1}$ Perovskite Family via Quantum Confinement'. *The Journal of Physical Chemistry Letters*, 2021, **12**, 1638–1643.

[139] Bohn, B. J.; Tong, Y.; Gramlich, M.; Lai, M. L.; Doblinger, M.; Wang, K.; Hoye, R. L.; Muller-Buschbaum, P.; Stranks, S. D.; Urban, A. S. *et al.* 'Boosting tunable blue luminescence of halide perovskite nanoplatelets through postsynthetic surface trap repair'. *Nano letters*, 2018, **18**, 5231–5238.

[140] Li, Q. and Lian, T. 'Ultrafast charge separation in two-dimensional $CsPbBr_3$ perovskite nanoplatelets'. *The Journal of Physical Chemistry Letters*, 2019, **10**, 566–573.

[141] Blancon, J.-C.; Stier, A. V.; Tsai, H.; Nie, W.; Stoumpos, C. C.; Traore, B.; Pedesseau, L; Kepenekian, M.; Katsutani, F.; Noe, G. *et al.* 'Scaling law for excitons in 2D perovskite quantum wells'. *Nature communications*, 2018, **9**, 1–10.

[142] Gramlich, M.; Swift, M. W.; Lampe, C.; Lyons, J. L.; Döblinger, M.; Efros, A. L.; Sercel, P. C. and Urban, A. S. 'Dark and Bright Excitons in Halide Perovskite Nanoplatelets'. *Advanced Science*, 2022, **9**, 2103013.

[143] Herz, L. M. 'Charge-carrier mobilities in metal halide perovskites: fundamental mechanisms and limits'. *ACS Energy Letters*, 2017, **2**, 1539–1548.

[144] Yin, W.-J.; Shi, T. and Yan, Y. 'Unusual defect physics in $CH_3NH_3PbI_3$ perovskite solar cell absorber'. *Applied Physics Letters*, 2014, **104**, 063903.

[145] Kim, J.; Lee, S.-H.; Lee, J. H. and Hong, K.-H. 'The role of intrinsic defects in methylammonium lead iodide perovskite'. *The Journal of Physical Chemistry Letters*, 2014, **5**, 1312–1317.

[146] Azpiroz, J. M.; Mosconi, E.; Bisquert, J. and De Angelis, F. 'Defect migration in methylammonium lead iodide and its role in perovskite solar cell operation'. *Energy & Environmental Science*, 2015, **8**, 2118–2127.

[147] Yin, W.-J.; Shi, T. and Yan, Y. 'Unique properties of halide perovskites as possible origins of the superior solar cell performance'. *Advanced Materials*, 2014, **26**, 4653–4658.

[148] Stoumpos, C. C. and Kanatzidis, M. G. 'The renaissance of halide perovskites and their evolution as emerging semiconductors'. *Accounts of ChemicalResearch*, 2015, **48**, 2791–2802.

[149] Jacobsson, T. J.; Hultqvist, A.; García-Fernández, A.; Anand, A.; Al-Ashouri, A.; Hagfeldt, A.; Crovetto, A.; Abate, A.; Ricciardulli, A. G.; Vijayan, A. *et al.* 'An open-access database and analysis tool for perovskite solar cells based on the FAIR data principles'. *Nature Energy*, 2022, **7**, 107–115.

[150] An, Y.; Hidalgo, J.; Perini, C. A. R.; Castro-Mendez, A.-F.; Vagott, J. N.; Bairley, K.; Wang, S.; Li, X. and Correa-Baena, J.-P. 'Structural Stability of Formamidinium-and Cesium-Based Halide Perovskites'. *ACS Energy Letters*, 2021, **6**, 1942–1969.

[151] Lee, J.-W.; Tan, S.; Seok, S. I.; Yang, Y. and Park, N.-G. 'Rethinking the A cation in halide perovskites'. *Science*, 2022, **375**, eabj1186.

[152] Conings, B.; Drijkoningen, J.; Gauquelin, N.; Babayigit, A.; D'Haen, J.; D'Olieslaeger, L.; Ethirajan, A.; Verbeeck, J.; Manca, J.; Mosconi, E. *et al.* 'Intrinsic thermal instability of methylammonium lead trihalide perovskite'. *Advanced Energy Materials*, 2015, **5**, 1500477.

[153] Bercegol, A.; Ramos, F. J.; Rebai, A.; Guillemot, T.; Puel, J.-B.; Guillemoles, J.-F.; Ory, D.; Rousset, J. and Lombez, L. 'Spatial inhomogeneity analysis of cesium-rich wrinkles in triple-cation perovskite'. *The Journal of Physical Chemistry C*, 2018, **122**, 23345–23351.

[154] Chatterjee, R.; Pavlovetc, I. M.; Aleshire, K.; Hartland, G. V. and Kuno, M. 'Subdiffraction infrared imaging of mixed cation perovskites: Probing local cation heterogeneities'. *ACS Energy Letters*, 2018, **3**, 469–475.

[155] Barrier, J.; Beal, R. E.; Gold-Parker, A.; Vigil, J. A.; Wolf, E.; Waquier, L.; Weadock, N. J.; Zhang, Z.; Schelhas, L. T.; Nogueira, A. F. *et al.* 'Compositional heterogeneity in $Cs_yFA_{1-y}Pb(Br_xI_{1-x})_3$ perovskite films and its impact on phase behavior'. *Energy & Environmental Science*, 2021, **14**, 6394–6405.

[156] Knight, A. J.; Borchert, J.; Oliver, R. D.; Patel, J. B.; Radaelli, P. G.; Snaith, H. J.; Johnston, M. B. and Herz, L. M. 'Halide segregation in mixed-halide perovskites: influence of A-site cations'. *ACS Energy Letters*, 2021, **6**, 799–808.

[157] Mundt, L. E.; Zhang, F.; Palmstrom, A. F.; Xu, J.; Tirawat, R.; Kelly, L. L.; Stone, K. H.; Zhu, K.; Berry, J. J.; Toney, M. F. *et al.* 'Mixing matters: nanoscale heterogeneity and stability in metal halide perovskite solar cells'. *ACS Energy Letters*, 2021, **7**, 471–480.

[158] Schelhas, L. T.; Li, Z.; Christians, J. A.; Goyal, A.; Kairys, P.; Harvey, S. P.; Kim, D. H.; Stone, K. H.; Luther, J. M.; Zhu, K. *et al.* 'Insights into operational stability and processing of halide perovskite active layers'. *Energy & Environmental Science*, 2019, **12**, 1341–1348.

[159] Liu, Z.; Liu, P.; Li, M.; He, T.; Liu, T.; Yu, L. and Yuan, M. 'Efficient and Stable FA-Rich Perovskite Photovoltaics: From Material Properties to Device Optimization'. *Advanced Energy Materials*, 2022, **12**, 2200111.

[160] Lin, D.; Gao, Y.; Zhang, T.; Zhan, Z.; Pang, N.; Wu, Z.; Chen, K.; Shi, T.; Pan, Z.; Liu, P. *et al.* 'Vapor Deposited Pure α-$FAPbI_3$ Perovskite Solar Cell via Moisture-Induced Phase Transition Strategy'. *Advanced Functional Materials*, 2022, **32**, 2208392.

[161] Chen, H.; Chen, Y.; Zhang, T.; Liu, X.; Wang, X. and Zhao, Y. 'Advances to high-performance black-phase $FAPbI_3$ perovskite for efficient and stable photovoltaics'. *Small Structures*, 2021, **2**, 2000130.

[162] Burschka, J.; Pellet, N.; Moon, S.-J.; Humphry-Baker, R.; Gao, P.; Nazeeruddin, M. K. and Grätzel, M. 'Sequential deposition as a route to high-performance perovskite-sensitized solar cells'. *Nature*, 2013, **499**, 316–319.

[163] Kim, M.; Kim, G.-H.; Lee, T. K.; Choi, I. W.; Choi, H. W.; Jo, Y.; Yoon, Y. J.; Kim, J. W.; Lee, J.; Huh, D. *et al.* 'Methylammonium chloride induces intermediate phase stabilization for efficient perovskite solar cells'. *Joule*, 2019, **3**, 2179–2192.

[164] Wang, Z.; Zhou, Y.; Pang, S.; Xiao, Z.; Zhang, J.; Chai, W.; Xu, H.; Liu, Z.; Padture, N. P. and Cui, G. 'Additive-modulated evolution of $HC(NH_2)_2PbI_3$ black polymorph for mesoscopic perovskite solar cells'. *Chemistry of Materials*, 2015, **27**, 7149–7155.

[165] Ye, F.; Ma, J.; Chen, C.; Wang, H.; Xu, Y.; Zhang, S.; Wang, T.; Tao, C. and Fang, G. 'Roles of MACl in Sequentially Deposited Bromine-Free Perovskite Absorbers for Efficient Solar Cells'. *Advanced Materials*, 2021, **33**, 2007126.

[166] Noel, N. K.; Wenger, B.; Habisreutinger, S. N. and Snaith, H. J. 'Utilizing nonpolar organic solvents for the deposition of metal-halide perovskite films and the realization of organic semiconductor/perovskite composite photovoltaics'. *ACS Energy Letters*, 2022, **7**, 1246–1254.

[167] Yang, W. S.; Noh, J. H.; Jeon, N. J.; Kim, Y. C.; Ryu, S.; Seo, J. and Seok, S. I. 'High-performance photovoltaic perovskite layers fabricated through intramolecular exchange'. *Science*, 2015, **348**, 1234–1237.

[168] Bu, T.; Li, J.; Li, H.; Tian, C.; Su, J.; Tong, G.; Ono, L. K.; Wang, C.; Lin, Z.; Chai, N. *et al.* 'Lead halide-templated crystallization of methylamine-free perovskite for efficient photovoltaic modules'. *Science*, 2021, **372**, 1327–1332.

[169] Gratia, P.; Zimmermann, I.; Schouwink, P.; Yum, J.-H.; Audinot, J.-N.; Sivula, K.; Wirtz, T. and Nazeeruddin, M. K. 'The many faces of mixed ion perovskites: unraveling and understanding the crystallization process'. *ACS Energy Letters*, 2017, **2**, 2686–2693.

[170] Cho, C.; Feldmann, S.; Yeom, K. M.; Jang, Y.-W.; Kahmann, S.; Huang, J.-Y.; Yang, T. C.-J.; Khayyat, M. N. T.; Wu, Y.-R.; Choi, M. *et al.* 'Efficient vertical charge transport in polycrystalline halide perovskites revealed by four-dimensional tracking of charge carriers'. *Nature Materials*, 2022, 1–8.

[171] Dutta, N. S.; Noel, N. K. and Arnold, C. B. 'Crystalline nature of colloids in methylammonium lead halide perovskite precursor inks revealed by cryo-electron microscopy'. *The Journal of Physical Chemistry Letters*, 2020, **11**, 5980–5986.

[172] Byranvand, M. M. and Saliba, M. 'Defect Passivation of Perovskite Films for Highly Efficient and Stable Solar Cells'. *Solar RRL*, 2021, **5**, 2100295.

[173] Jiang, Q.; Zhao, Y.; Zhang, X.; Yang, X.; Chen, Y.; Chu, Z.; Ye, Q.; Li, X.; Yin, Z. and You, J. 'Surface passivation of perovskite film for efficient solar cells'. *Nature Photonics*, 2019, **13**, 460–466.

[174] Wolff, C. M.; Caprioglio, P.; Stolterfoht, M. and Neher, D. 'Nonradiative recombination in perovskite solar cells: the role of interfaces'. *Advanced Materials*, 2019, **31**, 1902762.

[175] Park, J.; Kim, J.; Yun, H.-S.; Paik, M. J.; Noh, E.; Mun, H. J.; Kim, M. G.; Shin, T. J. and Seok, S. I. 'Controlled growth of perovskite layers with volatile alkylammonium chlorides'. *Nature*, 2023, **616**, 724–730.

[176] Lu, H.; Liu, Y.; Ahlawat, P.; Mishra, A.; Tress, W. R.; Eickemeyer, F. T.; Yang, Y.; Fu, F.; Wang, Z.; Avalos, C. E. *et al.* 'Vapor-assisted deposition of highly efficient, stable black-phase $FAPbI_3$ perovskite solar cells'. *Science*, 2020, **370**.

[177] Hui, W.; Chao, L.; Lu, H.; Xia, F.; Wei, Q.; Su, Z.; Niu, T.; Tao, L.; Du, B.; Li, D. *et al.* 'Stabilizing black-phase formamidinium perovskite formation at room temperature and high humidity'. *Science*, 2021, **371**, 1359–1364.

[178] Park, B.-w.; Kwon, H. W.; Lee, Y.; Lee, D. Y.; Kim, M. G.; Kim, G.; Kim, K.-j.; Kim, Y. K.; Im, J.; Shin, T. J. *et al.* 'Stabilization of formamidinium lead triiodide α-phase with isopropylammonium chloride for perovskite solar cells'. *Nature Energy*, 2021, **6**, 419–428.

[179] Zhu, J.; Park, S.; Gong, O. Y.; Sohn, C.; Li, Z.; Zhang, Z.; Jo, B.; Kim, W.; Han, G. S.; Kim, D. H. *et al.* 'Formamidine disulfide oxidant as a localised electron scavenger for> 20% perovskite solar cell modules'. *Energy & Environmental Science*, 2021, **14**, 4903–4914.

[180] Jeong, S.; Seo, S.; Yang, H.; Park, H.; Shin, S.; Ahn, H.; Lee, D.; Park, J. H.; Park, N.-G. and Shin, H. 'Cyclohexylammonium-Based 2D/3D Perovskite Heterojunction with Funnel-Like Energy Band Alignment for Efficient Solar Cells (23.91%)'. *Advanced Energy Materials*, 2021, **11**, 2102236.

[181] Min, H.; Lee, D. Y.; Kim, J.; Kim, G.; Lee, K. S.; Kim, J.; Paik, M. J.; Kim, Y. K.; Kim, K. S.; Kim, M. G. *et al.* 'Perovskite solar cells with atomically coherent interlayers on SnO_2 electrodes'. *Nature*, 2021, **598**, 444–450.

[182] Zhang, D.; Li, H.; Riaz, A.; Sharma, A.; Liang, W.; Wang, Y.; Chen, H.; Vora, K.; Yan, D.; Su, Z. *et al.* 'Unconventional direct synthesis of Ni_3N/Ni with N-vacancies for efficient and stable hydrogen evolution'. *Energy & Environmental Science*, 2022, **15**, 185–195.

[183] Zhao, L.; Li, Q.; Hou, C.-H.; Li, S.; Yang, X.; Wu, J.; Zhang, S.; Hu, Q.; Wang, Y.; Zhang, Y. *et al.* 'Chemical Polishing of Perovskite Surface Enhances Photovoltaic Performances'. *Journal of the American Chemical Society*, 2022, **144**, 1700–1708.

[184] Haris, M. P. U.; Kazim, S. and Ahmad, S. 'Microstrain and Urbach Energy Relaxation in $FAPbI_3$-Based Solar Cells through Powder Engineering and Perfluoroalkyl Phosphate Ionic Liquid Additives'. *ACS Applied Materials & Interfaces*, 2022, **14**, 24546–24556.

[185] Chao, L.; Xia, Y.; Duan, X.; Wang, Y.; Ran, C.; Niu, T.; Gu, L.; Li, D.; Hu, J.; Gao, X. *et al.* 'Direct and stable α-phase formation via ionic liquid solvation for formamidinium-based perovskite solar cells'. *Joule*, 2022, **6**, 2203–2217.

[186] Steele, J. A.; Solano, E.; Hardy, D.; Dayton, D.; Ladd, D.; White, K.; Chen, P.; Hou, J.; Huang, H.; Saha, R. A. *et al.* 'How to GIWAXS: Grazing Incidence Wide Angle X-Ray Scattering Applied to Metal Halide Perovskite Thin Films'. *Advanced Energy Materials*, 2023, **13**, 2300760.

[187] Tan, W. L. and McNeill, C. R. 'X-ray diffraction of photovoltaic perovskites: Principles and applications'. *Applied Physics Reviews*, 2022, **9**.

[188] Saha, M. N. 'On a physical theory of stellar spectra'. *Proceedings of the Royal Society of London. Series A, Containing Papers of a Mathematical and Physical Character*, 1921, **99**, 135–153.

[189] Sarritzu, V.; Sestu, N.; Marongiu, D.; Chang, X.; Wang, Q.; Loi, M. A.; Quochi, F.; Saba, M.; Mura, A. and Bongiovanni, G. 'Perovskite excitonics: primary exciton creation and crossover from free carriers to a secondary exciton phase'. *Advanced Optical Materials*, 2018, **6**, 1700839.

[190] Weber, O. J.; Ghosh, D.; Gaines, S.; Henry, P. F.; Walker, A. B.; Islam, M. S. and Weller, M. T. 'Phase behavior and polymorphism of formamidinium lead iodide'. *Chemistry of Materials*, 2018, **30**, 3768–3778.

[191] Constantinos, S; Christos, M; Mercouri, K *et al.* 'Semiconducting tin and lead iodide perovskites with organic cations: phase transitions, high mobilites and near-infrared photoluminescent properties'. *Inorg. Chem*, 2013, **52**, 9019–9038.

[192] Wright, A. D.; Milot, R. L.; Eperon, G. E.; Snaith, H. J.; Johnston, M. B. and Herz, L. M. 'Band-Tail Recombination in Hybrid Lead Iodide Perovskite'. *Advanced Functional Materials*, 2017, **27**, 1700860.

[193] Schötz, K.; Askar, A. M.; Peng, W.; Seeberger, D.; Gujar, T. P.; Thelakkat, M.; Köhler, A.; Huettner, S.; Bakr, O. M.; Shankar, K. *et al.* 'Double peak emission in lead halide perovskites by self-absorption'. *Journal of Materials Chemistry C*, 2020, **8**, 2289–2300.

[194] Chen, Y.; Wang, T.; Li, Z.; Li, H.; Ye, T.; Wetzel, C.; Li, H. and Shi, S.-F. 'Communicating two states in perovskite revealed by time-resolved photoluminescence spectroscopy'. *Scientific Reports*, 2018, **8**, 1–7.

[195] Priante, D.; Dursun, I.; Alias, M. S.; Shi, D.; Melnikov, V.; Ng, T. K.; Mohammed, O. F.; Bakr, O. and Ooi, B. S. 'The recombination mechanisms leading to amplified spontaneous emission at the true-green wavelength in $CH_3NH_3PbBr_3$ perovskites'. *Applied Physics Letters*, 2015, **106**, 081902.

[196] Kang, D.-H.; Lee, S.-U. and Park, N.-G. 'Effect of Residual Chloride in $FAPbI_3$ Film on Photovoltaic Performance and Stability of Perovskite Solar Cell'. *ACS Energy Letters*, 2023, **8**, 2122–2129.

[197] Snaith, H. J. 'How should you measure your excitonic solar cells?' *Energy & Environmental Science*, 2012, **5**, 6513–6520.

[198] Saliba, M. and Etgar, L. 'Current density mismatch in perovskite solar cells'. *ACS Energy Letters*, 2020, **5**, 2886–2888.

[199] Lin, Y.-H.; Sakai, N.; Da, P.; Wu, J.; Sansom, H. C.; Ramadan, A. J.; Mahesh, S.; Liu, J.; Oliver, R. D.; Lim, J. *et al.* 'A piperidinium salt stabilizes efficient metal-halide perovskite solar cells'. *Science*, 2020, **369**, 96–102.

[200] Schutt, K.; Nayak, P. K.; Ramadan, A. J.; Wenger, B.; Lin, Y.-H. and Snaith, H. J. 'Overcoming zinc oxide interface instability with a methylammonium-free perovskite for high-performance solar cells'. *Advanced Functional Materials*, 2019, **29**, 1900466.

[201] *Web of Science*. https://clarivate.com/webofsciencegroup/solutions/web-of-science/. Accessed: 2023-02-28.